Seismological structure of the Carpathian-Pannonian region of central Europe

Benjamin David Edward Dando

Submitted in accordance with the requirements for the degree of Doctor of Philosophy

The University of Leeds

School of Earth and Environment

November 2010

Acknowledgements

Firstly, I would like to thank my supervisors Graham Stuart and Greg Houseman. Their encouragement was unwavering, and the knowledge they shared and the advice they gave was invaluable.

In Hungary, Endre Hegedüs and the team at ELGI were always welcoming and provided excellent support to the Carpathian Basins Project. In particular, Attila Kovács who managed the Hungarian operation, was great company on the numerous service trips; the stops in Villány were always appreciated. In Austria, Ewald Brückl and the team at TU-Wien were fantastically well organised and I always enjoyed the service trips with Helmut Hausmann and Walter Loderer. In Serbia, Slavica Radovanović at the Seismological Survey of Serbia was a generous host and provided a great support team.

Thank you to all the individuals who provided the sites for the seismometers. In servicing, the offers of strongly brewed coffee were greatly appreciated. The home-made wine and schnapps also went down particularly well, even first thing in the morning.

I would also like to thank the staff at SEIS-UK in Leicester. Alex Brisbourne gave training in their procedures and data management. Together with Anna Horleston and Dave Hawthorn, they provided essential advice over the phone, whenever I was confronted by strange error messages in the field.

Nick Rawlinson provided me with his tomography and adaptive stacking software, and I benefited from numerous discussions with him. His clear programming helped me enormously. Useful discussions were also had with Ian Bastow, who provided me with John VanDecar's tomography code and advice on its use. Talks with György Hetényi were always beneficial, and Sebastian Rost provided sound advice. Michael Behm is thanked for providing data from his crustal model and Marek Grad kindly gave me early access to the European Moho map.

My time in Leeds was made enjoyable by many people, but especially Carl, Paddy, Ian, Tom and Matt(y). Thanks also to Sheona, Lucky, Hannah, Babs, Julia and Fran for their tolerance and some great office banter, ensuring entertainment throughout.

A big thank you to Alice who has been fantastic and provided me with a near-constant supply of home-made brownies and cookies whilst writing-up. Thanks also to my family for their continual support.

Data from permanent seismological stations were provided by Geofon, the GFZ Seismological Data Archive, ORFEUS, IRIS and the Hungarian Academy of Sciences, Geodetical and Geophysical Research Institute. The Carpathian Basins Project was funded by a NERC standard grant (NE/C004574/1) and I undertook this work whilst on a NERC studentship (NER/S/J/2006/14333).

Abstract

The extensional Pannonian Basin is set within the convergent arc of the Alpine-Carpathian mountain system in central Europe. Various models have been proposed as mechanisms to drive extension within this collisional setting. As part of the Carpathian Basins Project (CBP), a temporary network of 56 broadband seismometers was deployed. With a further 44 permanent broadband seismometers, tomographic inversion of P and S-wave relative arrival-time residuals from teleseismic earthquakes, reveal the velocity structure of the mantle to a depth of 850 km throughout the Carpathian-Pannonian region.

The tomographic models reduce the P-wave rms residual by 71% from 0.446 s to 0.130 s, and the S-wave rms residual by 59% from 1.513 s to 0.624 s. The effect of applying a deterministic crustal correction on the relative arrival-time residuals is tested using a crustal velocity model derived from previous crustal seismic experiments, but I show that the use of a station term parameter in the inversion provides a robust method of correcting for near-surface velocity variations in this experiment.

At shallow sub-lithospheric depths several localised slower regions are imaged, which correlate with extensional depocentres and regional volcanics, and are interpreted as upwelling asthenosphere. Beneath the Eastern Alps, I image a high velocity structure, which continues east beneath the Pannonian Basin with depth and into the mantle transition zone (MTZ). The fast anomaly in the MTZ is distributed laterally as far as the Carpathians, the Dinarides and the Eastern Alps.

The high velocity mantle material linking the structure beneath the Pannonian Basin with the Eastern Alps indicates a once continuous continental collision zone. Eastward extrusion from the Adria collision and detachment of the continental lithosphere beneath the Carpathians resulted in asthenospheric upwelling, which may have provided the driving force for extension of the Pannonian Basin.

Contents

List of Figures

List of Tables

Chapter 1

Introduction

1.1 Overview

The Carpathian-Pannonian system is one of the key structural features of the European continent and has been intensively studied over the past three decades (e.g. Horváth, 1993; Royden et al., 1983a). The present structure of the Carpathian-Pannonian system (figure 1.1) is the result of Cretaceous to Miocene convergence as the southern margin of the European plate collided with a series of continental fragments and the Tethys Ocean closed (Ustaszewski et al., 2008). Anti-clockwise rotation and northward indentation of the Adriatic microplate were accompanied by lateral extrusion of an East Alpine block, uplift of the Carpathians and eastward extension of the Pannonian Basin up to the Mid-Miocene (Horváth et al., 2006). Several hypotheses have been proposed to explain the uplift of the Carpathians and extension of the Pannonian Basin. These include extension driven by a mantle plume or active upwelling (e.g. Huismans et al., 2001; Stegena et al., 1975), subduction and roll-back along the Carpathian margin (e.g. Horváth, 1993; Royden et al., 1983a), mantle flow due to escape tectonics from the Alpine collision (Kovács & Szabó, 2008) and gravitational instability of the lithospheric mantle producing synchronous convergence in the Carpathians, and thinning of the lithosphere in the basin (Houseman & Gemmer, 2007).

In this thesis, I provide additional control on models for the formation of the Pannonian Basin, using seismic tomography. As part of the Carpathian Basins Project (CBP) a temporary seismological network was deployed, consisting of 56 broadband seismometers, across Austria, Hungary and Serbia (figure 1.2) for 16 months from 2006–2007. This deployment was made possible by the co-operation of the University of Leeds, Eötvös

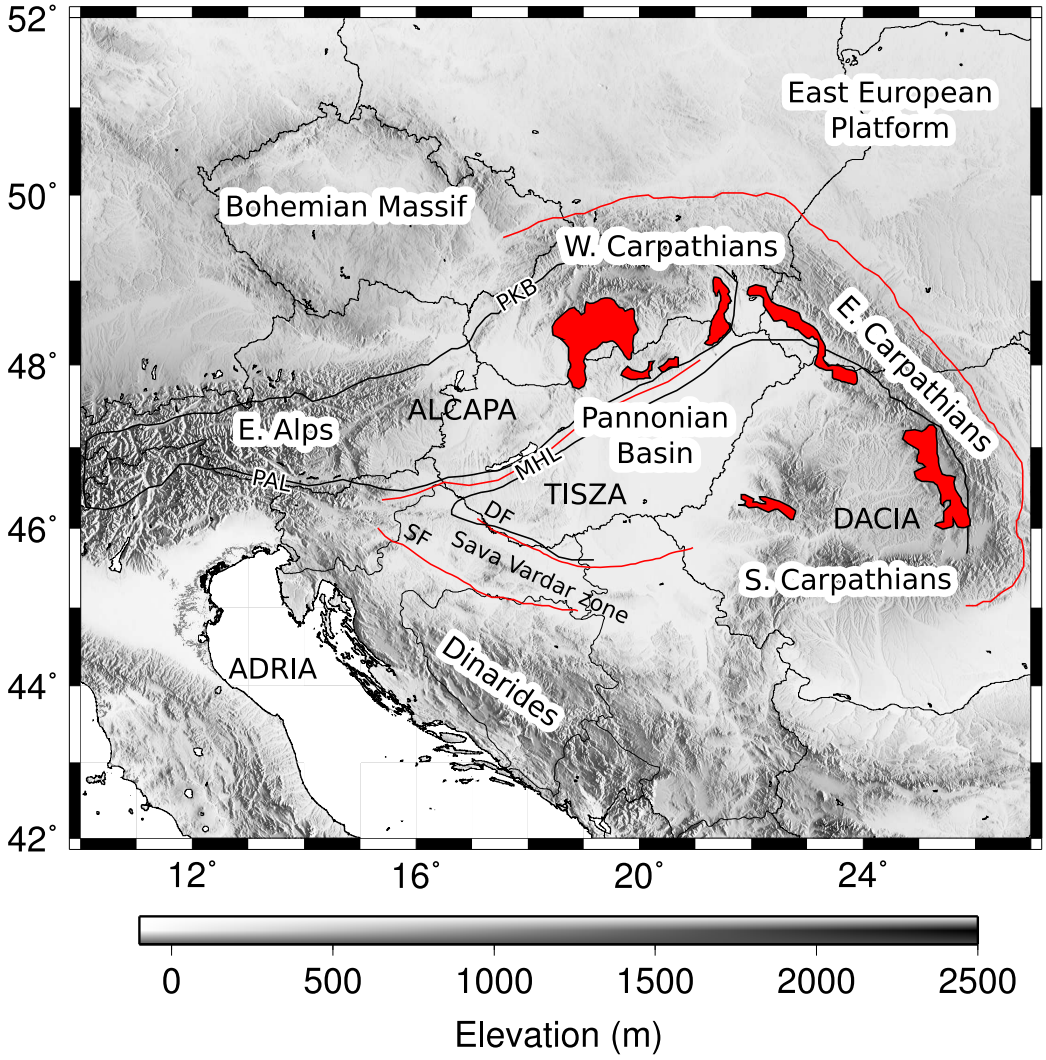

Figure 1.1: Topographic map of the Carpathian-Pannonian region, with the main structural features. The red shaded areas show the main outcrops of Middle Miocene to sub-recent magmatic rocks after Kovács et al. (2007). PKB - Pieniny Klippen Belt; PAL - Periadriatic Line; MHL - Mid-Hungarian Line; DF - Drava Fault; SF - Sava Fault.

Loránd Geophysical Institute in Hungary, the Technical University of Vienna in Austria, the Seismological Survey of Serbia, with support of SEIS-UK and major funding from the UK Natural Environment Research Council. Using CBP data together with data from a further 44 permanent stations, I have imaged the upper-mantle velocity structure beneath the Carpathian-Pannonian region to a depth of 850 km by inversion of P and S-wave relative arrival-time residuals of teleseismic events. This dataset enables new regional-scale tomographic images of the mantle beneath the Pannonian Basin and adjacent Carpathian mountain belt. The spatial resolution of these images is significantly improved on earlier tomographic solutions (Chang et al., 2010; Koulakov et al., 2009; Piromallo & Morelli, 2003; Wortel & Spakman, 2000), allowing new insights into the processes that produced the basin.

1.2 The Carpathian-Pannonian system

1.2.1 Tectonic setting

The uplift of the Carpathians, Eastern Alps and Dinarides, which surround the Pannonian Basin, began in the Cretaceous as a result of collision between the Adriatic microplate and the European continent (Royden et al., 1982). The inner Carpathian region consists of two microplates: an eastern Alpine, Alcapa (Alpine-Carpathian-Pannonian) terrain, which was extruded from the Late Eocene (Csontos et al., 1992) along the Pieniny Klippen Belt to the north and the Mid-Hungarian shear zone to the south (Fig. 1.1), and the Tisza-Dacia terrain, which was extruded at a slower rate, causing dextral shearing along the Mid-Hungarian shear zone (Márton & Fodor, 1995). The extrusion was accompanied by extension and anti-clockwise rotation of Alcapa and clockwise rotation of Tisza-Dacia (Csontos & Nagymarosy, 1998). The two units were juxtaposed at the beginning of the Miocene when the formation of the Pannonian Basin started, and have since acted as a single unit (Csontos et al., 1992; Horváth et al., 2006).

The extension of the previously thickened crust and lithosphere (Stegena et al., 1975) occurred from the mid to late Miocene (Horváth, 1995), to form the Pannonian Basin, presumably accompanied by mantle upwelling. The basin consists of a set of small, deep sub-basins, separated by relatively shallow basement blocks; the Neogene-Quaternary sediments, in some of these sub-basins, exceed 7 km in thickness (Kilényi et al., 1991). In the northern part of the Pannonian Basin and in the East Carpathians (Fig. 1.1)

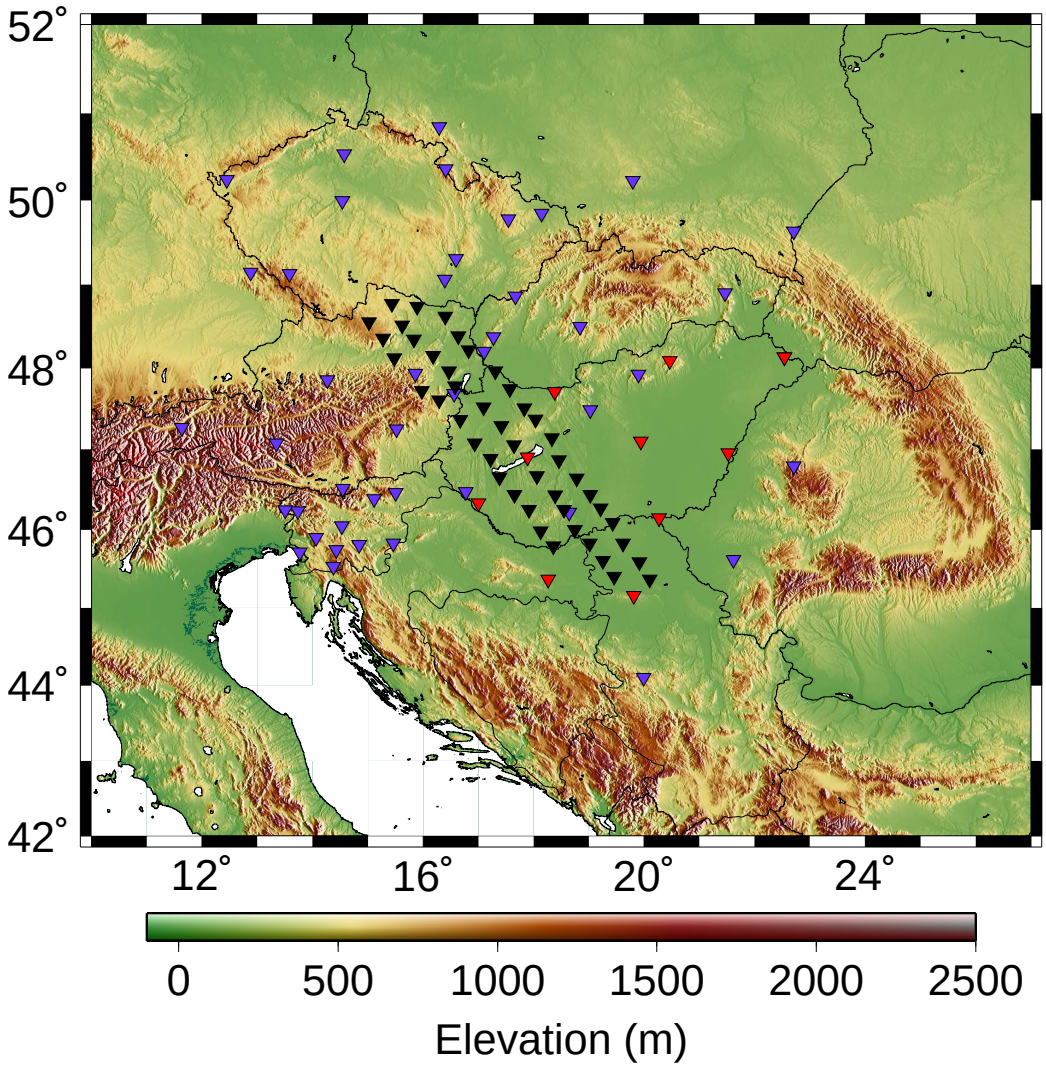

Figure 1.2: Distribution of broadband stations used in the study. Black triangles are the Carpathian Basins Project (CBP) 30 s period instruments, red triangles are the CBP 100 s period instruments and purple triangles are the permanent broadband seismological stations used in this study.

Miocene calc-alkaline volcanics, thought to be related to back-arc spreading and eastwards retreat of a subduction zone, accompanied basin subsidence and underthrusting in the Carpathian mountains (Lexa & Konečný, 1998). Later, alkaline basalts erupted in the Pannonian Basin itself, due to extension and asthenospheric up-doming. Heat flow in the Pannonian Basin is above average (∼90 mW m^{-2}) and contrasts with values of about 60 mW m^{-2} in the Carpathians (Tari et al., 1999).

The present day compressive stress field, observed within the Pannonian Basin, is thought to be the result of the continued convergence of the Adriatic microplate and the European plate by about 3 mm per year (Grenerczy & Kenyeres, 2006), causing inversion of pre-existing extensional faults and reactivation of shear zones (e.g. Bada et al., 2007; Gerner et al., 1999).

The tectonic evolution of the Carpathian-Pannonian region is summarised as follows:

1. Late Oligocene (∼ 23 Ma) to Early Miocene pre-rift thickening with NW-SE compression from continental extrusion (Frisch et al., 1998; Huismans et al., 2002; Ratschbacher et al., 1991)

2. Neogene thrusting in the Western Carpathians from around 20 Ma (Kováčs et al., 1998; Oszcypko, 2006), reaching units in the Eastern Carpathians at 17 Ma (Matenco & Bertotti, 2000; Săndulescu, 1988).

3. The initiation of extension and sedimentation in the Pannonian Basin begins at times estimated variously between 20.5 Ma and 17 Ma (e.g. Bérczi et al., 1988; Corver et al., 2009; Horváth, 1995; Horváth & Tari, 1999; Huismans et al., 2001; Nagymarosy & Müller, 1988), with an initial transtensional regime progressing to pure E-W extension (Huismans et al., 2002).

4. The synrift phase of basin development continued until the middle Miocene, while a postrift phase characterised by downwarping of the lithosphere and thermal subsidence (Corver et al., 2009) finished in the early Pliocene (Bada et al., 2001).

5. Post-rift subsidence was followed by gradual structural inversion of the Pannonian Basin during Late Pliocene to present day (Corver et al., 2009; Horváth & Cloetingh, 1996; Huismans et al., 2002).

1.2.2 Models of formation

An early model for the development of the Pannonian Basin by Stegena et al. (1975), inferred the presence of a mantle diapir, generated by subduction of the Carpathian flysch towards the Pannonian region. In this model, the diapir eroded the base of the crust leading to isostatic subsidence and basin formation. A later and more commonly cited model for the driving force behind Pannonian extension is the subduction of oceanic lithosphere along the Carpathian margin and slab roll-back, which resulted in asthenospheric upwelling and rifting (e.g. Horváth, 1993; Nemcock et al., 1998; Royden et al., 1983a; Wortel & Spakman, 2000). In this model, extension finally ended with the complete consumption of oceanic lithosphere, followed by slab detachment beneath the Carpathians, and a gradual increase in horizontal compressive stress in the Neogene (Bada et al., 2007; Horváth et al., 2006). The slab roll-back model has dominated structural and geological interpretations of this region in recent decades, but alternative ideas have been proposed: Kovács & Szabó (2008) challenged the presence of a subduction margin along the Western Carpathians and explained the extension by mantle flow associated with eastward extrusion from the Alpine compression; Huismans et al. (2001) rule out the presence of a deep mantle plume as suggested by earlier authors (e.g. Stegena et al., 1975) but do suggest a role for active asthenospheric upwelling, thinning the lithosphere and driving extension, triggered by an initial phase of passive rifting caused by the regular back-arc extension model; Houseman & Gemmer (2007) proposed a model where collapse of over-thickened continental lithosphere triggered the development of a gravitational downwelling of the mantle lithosphere beneath the Carpathians and synchronous extension of the Pannonian Basin.

1.2.3 Volcanism

The history of volcanism and the associated mantle xenoliths in the Carpathian-Pannonian Basin have provided a strong basis for some of the geodynamic and tectonic models of the region (e.g. Chalot-Prat & Boullier, 1997; Chalot-Prat & Girbacea, 2000; Downes et al., 1995; Kovács et al., 2007; Seghedi et al., 2004; Wilson & Downes, 2006). Kovács et al. (2007) classify the igneous rocks of the region into five suites: 1) Miocene-Pleistocene alkali mafic extrusions; 2) middle Miocene to sub-recent calc-alkaline volcanic rocks and their related intrusions; 3) late Oligocene-early Miocene calc-alkaline volcanic rocks and tuffs and their intrusions; 4) late Eocene-early Oligocene acidic-intermediate intrusives

with local volcanic successions; 5) Eocene plutonic rocks. The alkaline volcanism, which occurred sporadically from 17-0.5 Ma, and is older in the western part of the Pannonian Basin and younger in the central region, was partly contemporaneous with the calc-alkaline volcanism related with subduction (Wilson & Downes, 2006). However, Huismans et al. (2001) indicate the first occurrence of alkaline basaltic magmatism is around 11.5 Ma, and link the onset with a second phase of rifting, which they suggest provides evidence for active asthenospheric upwelling after the effect of subduction roll-back has ceased. Timing of the calc-alkaline magmatism in the Inner Carpathians shows an eastwards migration with time (Pecskay et al., 1995), which is usually cited as evidence of progressive slab detachment of the subducted slab (e.g. Wortel & Spakman, 2000). The middle Miocene calc-alkaline magmatic rocks which show the subduction-related geochemical characteristics (e.g. Downes et al., 1995; Harangi et al., 1995; Kovács & Szabó, 2008), also show evidence of a crustal component, which has been suggested as contamination from the subducting oceanic slab and the associated sediments (Seghedi et al., 2004). Harangi et al. (1995) provide two possible alternatives for the crustal component, which include assimilation from crustal wall rocks as the magma ascends and derivation of small volumes of ultrapotassic liquids from ancient recycled subducted material frozen in the lithosphere. However, Chalot-Prat & Girbacea (2000) also show how the crustal component could represent contamination from delaminated continental European lithosphere. The argument that recent subduction is implied by the calc-alkaline volcanism is also questioned by Kovács & Szabó (2008), due to the mantle's ability to preserve previous geodynamic settings. They cite examples of volcanism within the Basin and Range in the USA, Southern Sonora in Mexico, Anatolia in Turkey, and the Eastern Rift in Morocco, as all showing subduction related geochemical signatures with otherwise no evidence of recent subduction. In the case of the Pannonian Basin, Kovács & Szabó (2008) argue that the enrichment of the mantle was from previous subduction of the Budva-Pindos or Vardar oceans along the Sava-Vardar Zone (figure 1.1) during the Mesozoic-Paleogene, rather than recent subduction along the Carpathians. In their interpretation, recent melting was triggered by the extension caused by the asthenospheric flow from extrusion and rotation of the Alcapa microplate.

1.3 Previous geophysical work

The first heat flow map for the Carpathian-Pannonian region was produced by Dövényi et al. (1983), with a comprehensive heat flow compilation including the region produced by Hurtig et al. (1992). More recently maps produced by Lenkey et al. (2002) and Pospíšil et al. (2006) show heat flow ranging from 50 to 130 mW m^{-2} within the Pannonian Basin, with an average of 100 mW m^{-2} (Lenkey et al., 2002). Elevated heat flow occurs in a central zone up to 300 km wide, trending NW-SE, corresponding with areas of thin lithosphere and shallow Moho depths (Pospíšil et al., 2006). In the Carpathians and Bohemian Massif, heat flow varies between 50–70 mW m^{-2} (Lenkey et al., 2002), which is close to the mean value for the continental crust at 65 mW m^{-2} (Pollack et al., 1993). There is also a correlation of the high heat flow with the volcanic regions. Although the high temperatures and heat flow around an intrusion have been shown to dissipate in a few million years (e.g Fowler & Nisbit, 1982; Horváth et al., 1986), the deeper source of the volcanism in the lower crust or mantle is still providing elevated heat flow (Lenkey et al., 2002) in these parts of the Pannonian.

Since 1997, central Europe has been covered extensively by controlled-source refraction and wide-angle reflection seismic experiments, including the CELEBRATION 2000 and ALP2002 projects (Guterch et al., 2003; 2004). Behm et al. (2007a) and Behm et al. (2007b), used these data to produce a new seismic model of the Eastern Alps, showing three crustal blocks with significantly different depths to the Moho. Interpretation of the region by Brückl et al. (2007) identifies the three blocks as the Adriatic microplate, the European plate and a Pannonian fragment. From Adria to the Pannonian fragment, an upward jump of ∼10 km (from ∼37 km to 27–29 km) in the depth of the Moho is observed. They interpret the development and thinning of the Pannonian fragment as a consequence of escape tectonics due to the Adria collision, and also speculate on possible underthrusting of Adriatic mantle below the Pannonian fragment (Brückl et al., 2007). The model reveals no significant differences in the crustal structure between the Alcapa and Tisza-Dacia blocks, providing confidence that they can be considered as a single unit (Csontos et al., 1992; Horváth et al., 2006). Posgay et al. (2008), however, observe a reduction in velocity and decrease in crustal thickness from Alcapa to the Tisza block in their profile crossing the Mid-Hungarian shear zone.

Structure of the lithosphere in the Pannonian Basin is also revealed by the CELEBRA-

TION 2000 and ALP2002 projects and shows a relatively simple crustal structure (Grad et al., 2007). From a seismic refraction line crossing the Western Carpathians, Grad et al. (2006) counters geological interpretation of southward dipping subduction beneath the Carpathians, with images of the Pannonian mantle at very low angles dipping northwards beneath the Carpathians. They interpret these images as showing either 'old' subduction of the lithosphere under the East European craton (EEC) in the Jurassic-Lower Cretaceous; a 'crocodile' structure produced by Carpatho-Pannonian upper crust obducted over crystalline crust of Variscan-EEC origin, with Carpathian-Pannonian mantle lithosphere underthrusting the cratonic crust; or thinning of the Pannonian lithosphere due to extension with southward subduction of the EEC in the Miocene (figure 1.3). Using the multiple refraction lines from the CELEBRATION 2000 project, which cross the Western Carpathians, Środa (2010) interprets the structure as either 'old' northward subduction of oceanic lithosphere or delamination of the Alcapa continental lithosphere, producing the 'crocodile' structure.

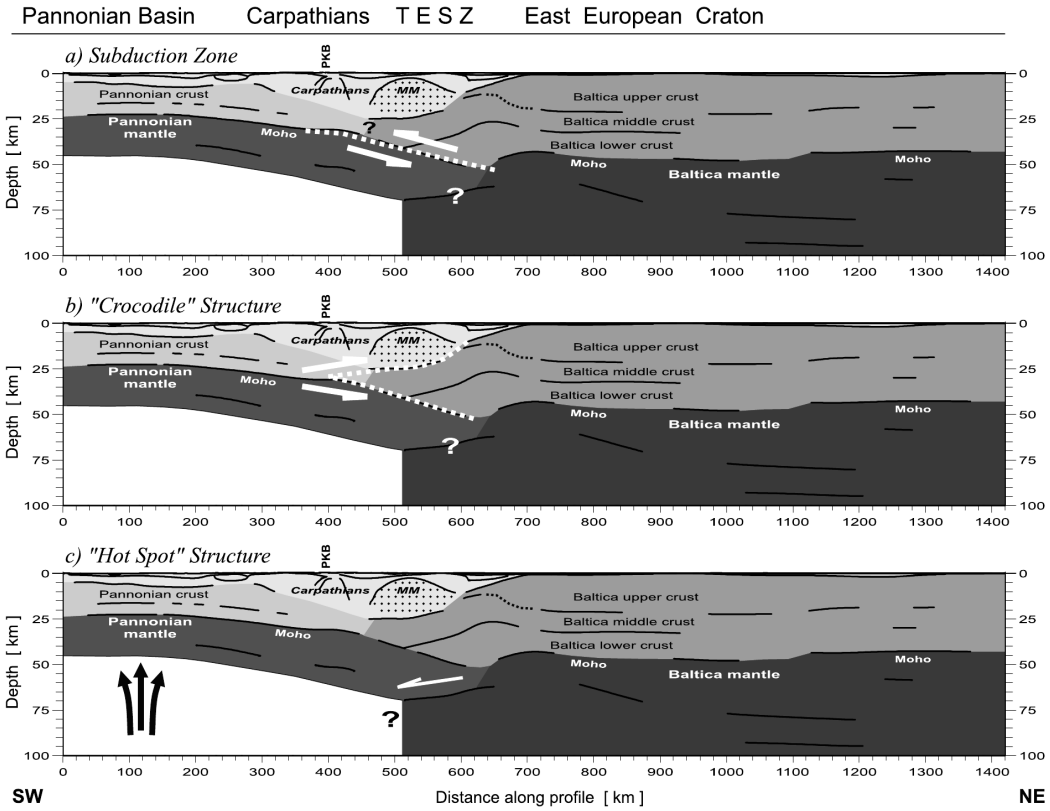

Figure 1.3: Three alternative models based on the lithospheric structure beneath the Western Carpathians: a) 'old' subduction of the lithosphere under the East European craton (EEC) in the Jurassic-Lower Cretaceous; b) a 'crocodile' structure produced by Carpatho-Pannonian upper crust obducted over crystalline crust of Variscan-EEC origin with Carpathian-Pannonian mantle lithosphere underthrusting the cratonic crust; c) thinning of the Pannonian lithosphere due to extension with southward subduction of the EEC in the Miocene. After Grad et al. (2006).

In addition to the active source seismic experiments, the crustal thickness has also been investigated with receiver function analyses (e.g. Diehl et al., 2005; Geissler et al., 2008; Hétenyi & Bus, 2007). A compilation of these various geophysical measurements was used to produced the most up to date map of the European Moho by Grad et al. (2009): in the Carpathian-Pannonian region crustal thickness varies between 24–30 km in the Pannonian Basin; 29–37 km in the Western Carpathians; up to 43 km beneath the SE Carpathians; 31–48 km in the Eastern Alps; 39 km in the Dinarides; and up to 38 km in the Bohemian Massif.

Regional crustal earthquakes were used by Wéber (2002) to measure P_n - a head-wave that travels along the base of the Moho - travel-times beneath the Pannonian Basin to invert for P_n velocity. The results show an average P_n velocity of 7.9 km s^{-1} with a range of $\pm$0.3 km s^{-1}, compared with the average continental P_n velocity of 8.1 km s^{-1}.

The first model of lithospheric thickness in the Carpathian-Pannonian region was produced from teleseismic P-wave arrival-time residuals by Babuška et al. (1987) and Babuška & Plomerová (1988). The lithospheric thickness model has since been developed with further geophysical datasets (e.g. Ádám, 1996; Horváth, 1993; Horváth et al., 2006; Posgay et al., 1995) and shows lithospheric thicknesses from around 50 km in the basin to 140 km or more beneath the East European platform. Integrated modelling of the thermal structure of the lithosphere from five transects, which cross the Western Carpathians, Bohemian Massif and the Pannonian Basin, and using surface heat flow, gravity and topography have revealed more details of the lithospheric structure (Zeyen et al., 2002). Similar modelling by Bielik et al. (2010); Dérerová et al. (2006) and Tašárová et al. (2009), using constraints from the CELEBRATION 2000 project have shown lithospheric thicknesses (e.g. figure 1.4) of up to 240 km beneath the Eastern Carpathians and its foreland, compared to 100 to 120 km beneath the Western Carpathians (Bielik et al., 2010). In contrast with the earlier thinner estimates based on magnetotelluric data (e.g. Ádám, 1996; Horváth, 1993; Horváth et al., 2006; Lenkey et al., 2002), Bielik et al. (2010) estimated lithospheric thickness beneath the Pannonian Basin to be no less than 70 km. In the Eastern Alps Tašárová et al. (2009) model the lithospheric thickness at 160 km, and 140 km beneath the Bohemian Massif.

Seismic tomography has previously been used to image the upper-mantle of the Pannonian region. The slab roll-back model described by Wortel & Spakman (2000) is based on the regional tomography of Bijwaard & Spakman (2000). They image a slow upper-

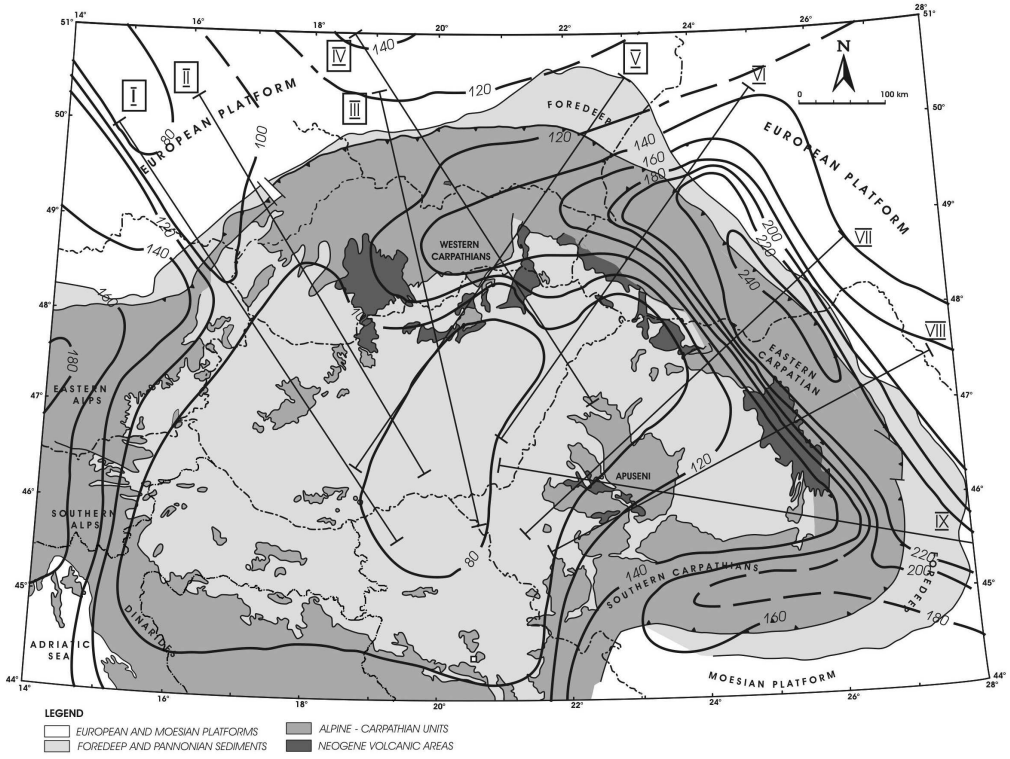

Figure 1.4: Map of lithospheric thickness in the Carpathian-Pannonian region, after Dérerová et al. (2006). Transects show the locations of modelling by Dérerová et al. (2006) and Zeyen et al. (2002).

mantle for the Pannonian region overlying a fast mantle transition zone (MTZ) (figure 1.5). They interpreted the fast MTZ to be the result of subduction of oceanic material along the Carpathian margin since 16 Ma. Based on the history of volcanism they also interpreted the progressive detachment of an east Carpathian slab starting at 10 Ma in the north and culminating today beneath the SE Carpathian region of Vrancea (Wortel & Spakman, 2000). Piromallo & Morelli (2003) obtained better resolved images in their tomographic study of the Alpine-Mediterranean region and also imaged fast material within the MTZ beneath southern and central Europe, which they interpreted as remnant Tethyan oceanic lithosphere. Chang et al. (2010) used both body and surface waves to produce S-wave velocity maps, from which they inferred hot upwelling mantle in the top 200 km under the Pannonian Basin from low asthenospheric velocities, which extend into the MTZ to the north-east, beneath the East-European platform.

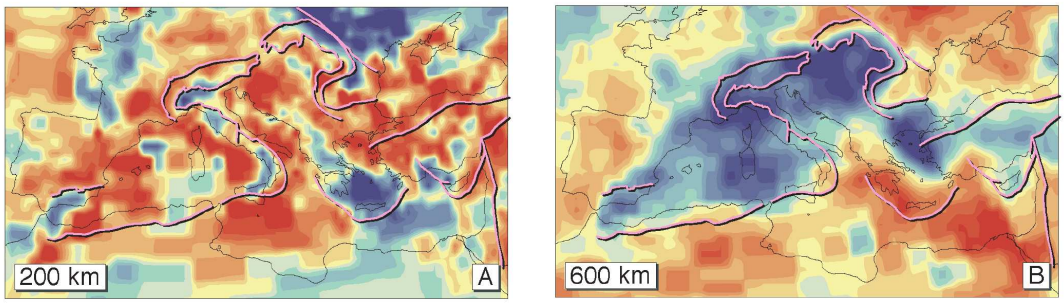

Figure 1.5: Two depth slices through the P-wave tomographic model of Bijwaard & Spakman (2000). Red shows slow anomalies relative to *ak135* (Kennett et al., 1995); blue shows fast anomalies relative to *ak135*. After Wortel & Spakman (2000).

Receiver functions have been used to determine the depth and thickness of the MTZ beneath the Carpathian-Pannonian region (Hetényi et al., 2009) and the greater Alpine region (Lombardi et al., 2009). These studies show a relatively flat 410 km discontinuity with a depression of the 660 km discontinuity by up to 40 km under the Pannonian Basin and the Alps. The thickened MTZ is indicative of cold, dense material within the transition zone, consistent with the higher velocities imaged by tomography (e.g. Piromallo & Morelli, 2003; Wortel & Spakman, 2000).

1.4 Thesis outline

This thesis contains 8 chapters, including this introduction.

Chapter 2 describes the seismic experiment, providing information on the seismological stations, their deployment and servicing, and the data recorded. The method for

determining arrival-time residuals is described and analyses of these data presented.

Chapter 3 describes the methodology used in the inversion of the relative arrival-time residuals. Details are given of the parameterisation of the tomographic model, and the inversion method of VanDecar et al. (1995) is tested against the iterative non-linear inversion method of Rawlinson et al. (2006) using synthetic travel-time data.

Chapter 4 presents the results from the P-wave tomography and shows the effect of regularisation, model depth extent and the use of station terms on the results. Various sensitivity tests are also presented using synthetic data to assess the resolution of the tomographic model, and an analysis of the final solution residuals to examine the data fit to the model.

Chapter 5 presents the results from the S-wave tomography, the regularisation, and tests on the use of station terms. Sensitivity tests for S-wave tomography are presented and the differences in resolution between the P and S inversions are shown.

Chapter 6 assesses the effect of using an *a priori* crustal correction on the P-wave arrival-time residuals. Seismic velocities and crustal thicknesses derived from previous crustal studies are used to compute corrections on mantle velocity anomaly maps. These inversions are in order to examine the effect of variation of crustal structure compared with free parameter inversions using station terms.

Chapter 7 discusses the tomography results and their relation to previous work in the region. Simplified synthetic model data are used to test the resolution of the data and assess the reliability of the tomographic inversion. The effect of topography on the 660 km discontinuity is also discussed, using synthetic models to illustrate the effect.

Chapter 8 provides some concluding remarks as well as suggestions for possible future work in the region.

Chapter 2

Seismic networks and earthquake data

2.1 Overview

To provide constraints on the seismic structure of the Carpathian-Pannonian region, the Carpathian Basins Project (CBP) deployed two temporary networks of broadband seismometers, providing unprecedented coverage of the Pannonian Basin. A regional broadband network (RBB) was deployed from September 2005 until August 2007, and consisted of 10 Guralp CMG-3T(D) 120 s seismometers. Deployed throughout the Pannonian Basin, this network covered gaps in the permanent station distribution in Hungary and Serbia. The second high resolution network (HST) of 46 Guralp CMG-6TD 30 s seismometers was deployed as a three line array running NW-SE through Austria, western Hungary and northern Serbia, and operated from May 2006 to August 2007. In addition to the temporary networks, data were also used from 44 permanent broadband stations, throughout the region (figure 2.1).

2.2 Carpathian Basins Project network

The regional broadband (RBB) network was designed to provide station coverage throughout the Pannonian Basin and has a mean minimum station spacing of 113 km. The RBB network consisted of 9 Guralp CMG-3T (analogue) seismometers and 1 CMG-3TD (digital) seismometer, which have a frequency response of 0.02 s (50 Hz) to 120 s (0.008 Hz). The single digital station used a Guralp Storage and Acquisition Module (SAM) data logger. For the analogue stations, an external Nanometrics Taurus data logging

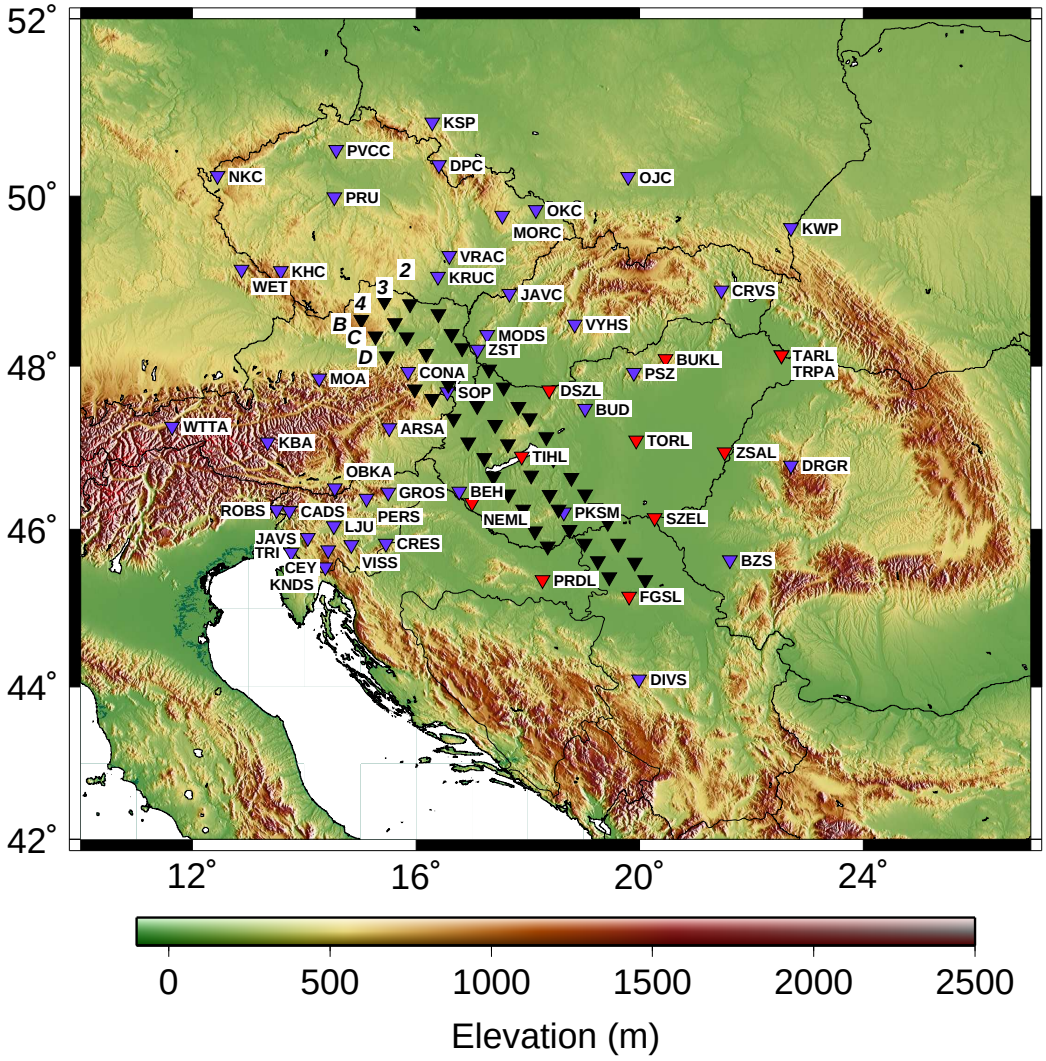

Figure 2.1: Station location map. The red triangles show the RBB temporary network; the black triangles show the temporary 3-line HST network, operating for 16 months from March 2006; the blue triangles show the permanent broadband stations used. The naming convention for the HST network is based on the position in the array, where each line is named 2, 3, 4 and the along line position varies from B to S (as shown). E.g. the most north-westerly station in the array is named CBP4B and the most south-easterly station is CBP2S.

system recorded and digitised the data for 5 stations, and the remaining four stations used Nanometrics Orion data loggers and digitisers (table 2.1). All stations recorded at 100 s.p.s.

Station	Latitude	Longitude	Elevation (km)	Sensor	Data Logger
NEML	46.3322	17.0013	0.230	CMG-3T	Orion
DSZL	47.7071	18.3827	0.240	CMG-3T	Orion
TIHL	46.9000	17.8879	0.211	CMG-3T	Orion
TORL	47.0977	19.9374	0.111	CMG-3T	Orion
FGSL	45.1574	19.8104	0.520	CMG-3TD	SAM
BUKL	48.0866	20.4626	0.556	CMG-3T	Taurus
SZEL	46.1446	20.2727	0.124	CMG-3T	Taurus
TARL	48.1318	22.5402	0.138	CMG-3T	Taurus
ZSAL	46.9530	21.5270	0.110	CMG-3T	Taurus
PRDL	45.3660	18.2670	0.197	CMG-3T	Taurus

Table 2.1: List of stations for the RBB network. The coordinates use the WGS 84 reference frame from a handheld GPS device.

The HST (High resolution Seismic Tomography) array comprised of 46 Guralp CMG-6TD sensors, with a frequency response of 0.02 s (50 Hz) to 30 s (0.03 Hz). It was deployed on a NW-SE trend, traversing the extensional and structural features of the Vienna and western Pannonian Basin and was designed to cross the mid-Hungarian shear zone. The stations were positioned along 3 parallel lines, with approximately 40 km between each line and have a mean minimum station spacing along line of 28 km. These seismometers have an internal flash memory, so no external data logger was required. Sampling was set at 100 s.p.s., although this was reduced to 50 s.p.s. for some replacement sensors.

Deployment of the HST network took place in three phases, depending on country. In March 2006 the first phase took place, with fifteen stations deployed in Austria. The second phase, was the deployment of the 25 Hungarian stations in May 2006, with the final six stations deployed in July 2006 in Serbia.

The installation for both networks was similar at each site; a pit up to 1 m deep was dug, and lined with a plastic container. A compacted layer of sand and a concrete plinth was placed at the bottom as a stable base and good couple for the seismometer to the ground. The seismometer was aligned to magnetic north and levelled. One 20 W solar panel, mounted on a wooden frame was used to charge a single 12 V battery, powering the CMG-6TD sensor. A GPS antenna was mounted on the frame, in clear view of the sky. The battery, solar regulator and breakout box were stored in a plastic box dug into

Station	Latitude	Longitude	Elevation (km)
CBP2C	48.7399	15.8968	0.284
CBP2D	48.6199	16.4029	0.296
CBP2E	48.3839	16.6409	0.175
CBP2F	48.2126	16.8282	0.144
CBP2G	47.9596	17.3103	0.125
CBP2H	47.7439	17.5694	0.113
CBP2I	47.5098	17.8345	0.187
CBP2J	47.3673	18.0317	0.260
CBP2K	47.1375	18.3317	0.146
CBP2L	46.8658	18.4543	0.130
CBP2M	46.6414	18.7829	0.138
CBP2N	46.4373	19.0231	0.100
CBP2O	46.2669	19.2147	0.136
CBP2P	46.0838	19.4297	0.136
CBP2Q	45.8233	19.6201	0.114
CBP2R	45.5857	19.9122	0.086
CBP2S	45.3631	20.1012	0.092
CBP3B	48.7739	15.4372	0.564
CBP3C	48.5145	15.6230	0.359
CBP3D	48.3435	15.8338	0.186
CBP3E	48.1471	16.1790	0.353
CBP3F	47.9586	16.4658	0.192
CBP3G	47.7774	16.5818	0.183
CBP3H	47.5217	17.0944	0.128
CBP3I	47.2874	17.4185	0.148
CBP3J	47.0508	17.6474	0.528
CBP3L	46.6667	18.0567	0.166
CBP3M	46.4317	18.3923	0.154
CBP3N	46.2464	18.5535	0.174
CBP3O	45.9941	18.7466	0.094
CBP3P	45.8261	19.0149	0.099
CBP3Q	45.6063	19.2541	0.095
CBP3R	45.3991	19.4587	0.096
CBP4B	48.5499	15.0170	0.750
CBP4C	48.3542	15.2735	0.664
CBP4D	48.1152	15.4738	0.306
CBP4F	47.7202	15.9780	0.541
CBP4G	47.6076	16.2917	0.746
CBP4H	47.3662	16.6709	0.240
CBP4I	47.0760	16.9371	0.206
CBP4J	46.8865	17.2198	0.224
CBP4K	46.6539	17.3847	0.136
CBP4L	46.4350	17.6506	0.165
CBP4M	46.2454	17.9176	0.158
CBP4N	45.9783	18.1270	0.165
CBP4O	45.7850	18.3540	0.102

Table 2.2: List of stations for the HST network. The coordinates use the WGS 84 reference frame obtained from the on-site GPS antenna.

the ground. A typical CMG-6TD installation is shown in figure 2.2.

Figure 2.2: Typical site configuration: a mounted solar panel and GPS antenna, connecting to a battery, solar regulator and breakout box in a plastic box. The seismometer in the foreground is covered with a plastic container and buried.

2.2.1 Network management and quality control

The 8 GB internal flash memory of the CMG-6TD sensors allowed 5 months recording before data were overwritten ($\sim$ 50 MB per day). In practice, service runs took place every 4 months to account for high noise at some stations and for quality control. A summary of service runs is shown in table 2.3. Extraction of the sensors took place on the final service run between 5th August 2007–22nd August 2007. A huddle test of all seismometers (in each country) was performed to check for discrepancies with the timing and to test the equipment.

	Austria	**Hungary**	**Serbia**
Deployment	11–20/04/2006	8–11/05/2006	12–16/07/2006
Service 1	06–08/06/2006	10–13/07/2006	12–13/10/2006
Service 2	09–10/11/2006	06–09/11/2006	23–24/01/2007
Service 3	11–13/12/2006	25–28/03/2006	26/04/2006
Service 4	22–24/04/2007	05–07/08/2007	07–08/08/2007
Service 5	20–22/08/2007	n/a	n/a

Table 2.3: Summary of deployments, service runs and extraction dates for the HST array.

In addition to the collection of data, service runs were needed for quality control pro-

cedures. The operational status for each site was checked in terms of battery voltage, GPS status, seismometer mass positions, recording status, and real-time velocity offsets. Appendix A lists the procedure for the service runs and shows the GPS continuity for the CMG-6TD stations. The most common problems related to hardware failure of the firewire download system, and electrical faults in the breakout boxes, which resulted in either the loss of a GPS lock, or power. Sensors were also routinely re-levelled on service runs, due to unstable mass positions. Flooding of the box containing the electrical equipment also occurred in a few cases, with consequent power loss.

2.3 Permanent stations

To provide improved seismological images of the whole Carpathian-Pannonian region, data from permanent stations were also obtained (table 2.4). Available stations were searched from IRIS[1], the GFZ Seismological Data archive[2], and ORFEUS[3], resulting in 44 permanent stations contributing data for the study.

2.4 Seismic noise

With the region of interest focussed in and around a sedimentary basin, the majority of seismic stations were not installed on bedrock. Station locations varied from isolated farm land, to back-gardens, and in several cases in relatively quiet buildings (with the extremes of next door to a band rehearsal room or next to a 40 m tower). Power spectral density (PSD) plots of ground acceleration at each CMG-6TD station, were produced to compare the ambient noise levels at different sites, with the standard low and high noise models (NLNM and NHNM respectively) of Peterson (1993). Thirty days were selected, over the recording period, which contained no seismic events with $M_w \geq 5.5$. The instrument response was removed from the time series for the selected data, with a PSD produced for each hour-long time segment. The individual PSDs were then ordered into frequency distributions by binning the data into 1 dB intervals, normalising by the number of PSDs and constructing the probability density function as described by McNamara & Boaz (2005).

The ambient noise for three stations in the HST array is shown in figure 2.3. The plots

[1] http://www.iris.edu/SeismiQuery/
[2] http://geofon.gfz-potsdam.de/geofon/
[3] http://www.orfeus-eu.org/

Station Code	Network	Sensor	Latitude	Longitude	Elevation (km)
OKC	CZ	CMG-3ESP	49.8375	18.1472	0.272
DPC	CZ	STS-1	50.3583	16.4111	0.760
PRU	CZ	STS-2	49.9883	14.5417	0.302
PVCC	CZ	STS-2	50.5282	14.5690	0.311
KRUC	CZ	STS-2	49.0619	16.3952	0.341
VRAC	CZ	STS-2	49.3084	16.5933	0.470
NKC	CZ	STS-2	50.2331	12.4479	0.546
KHC	CZ	STS-2	49.1309	13.5782	0.700
JAVC	CZ	STS-2	48.8591	17.6707	0.828
KWP	GE	STS-2	49.6314	22.7075	0.448
MORC	GE	STS-2	49.7766	17.5428	0.740
PSZ	GE	STS-2	47.9184	19.8944	0.940
WET	GR	STS-2	49.1440	12.8782	0.613
TRPA	HU	STS-2	48.1304	22.5391	0.113
PKSM	HU	STS-2	46.2119	18.6413	0.170
BUD	HU	STS-2	47.4836	19.0239	0.196
SOP	HU	STS-2	47.6833	16.5583	0.260
BEH	HU	STS-2	46.4703	16.7756	0.310
TRI	MN	STS-1	45.7090	13.7640	0.161
DIVS	MN	STS-1	44.0981	19.9917	1.000
MOA	OE	STS-2	47.8495	14.2659	0.572
ARSA	OE	STS-2	47.2505	15.5232	0.577
CONA	OE	STS-2	47.9288	15.8628	1.046
OBKA	OE	STS-2	46.5092	14.5489	1.075
KBA	OE	STS-2	47.0784	13.3447	1.721
WTTA	OE	STS-2	47.2638	11.6363	1.764
OJC	PL	STS-2	50.2195	19.7984	0.300
KSP	PL	STS-2	50.8428	16.2931	0.353
DRGR	RO	KS-2000	46.7917	22.7111	0.923
BZS	RO	STS-2	45.6167	21.6167	0.260
ZST	SK	Kirnos	48.1961	17.1025	0.250
CRVS	SK	STS-2	48.9022	21.4614	0.476
VYHS	SK	STS-2	48.4940	18.8361	0.480
MODS	SK	STS-2	48.3730	17.2770	0.520
ROBS	SL	CMG-40T	46.2445	13.5094	0.250
LJU	SL	CMG-40T	46.0438	14.5273	0.396
VISS	SL	CMG-40T	45.8033	14.8393	0.399
CRES	SL	CMG-40T	45.8260	15.4578	0.431
CEY	SL	CMG-40T	45.7388	14.4267	0.579
CADS	SL	CMG-40T	46.2280	13.7370	0.750
PERS	SL	CMG-40T	46.3809	15.1167	0.795
GROS	SL	CMG-40T	46.4610	15.5018	0.930
KNDS	SL	CMG-40T	45.5280	14.3770	1.010
JAVS	SL	CMG-40T	45.8934	14.0643	1.120

Table 2.4: List of 44 permanent stations used in this study.

show similar results along the HST array. The typical noise level increases past the NHNM of Peterson (1993) at periods greater than 20 s. Below this, in the body-wave frequency band ($\sim$ 0.5–20 s), the ambient noise is still relatively high but generally beneath the NHNM.

2.5 Teleseismic earthquake recordings

Using the IRIS Archive Data Center, the Bulletin of the International Seismological Centre was searched for global earthquakes between 11/04/2006 to 22/08/2007 with magnitude $M_w \geq 5.5$. From the 745 earthquakes (figure 2.4) published in the Bulletin, events within the teleseismic distance range ($30 < \Delta < 100^\circ$) were extracted from the dataset. For both the P and S-wave tomography, the extracted events were searched for a consistent arrival across at least 30 stations. Events masked by aftershocks, emergent signals or poor signal to noise ratio were discarded. In the P-wave tomography, 225 usable events were found to produce a dataset consisting of 15853 P-wave arrival-times from 100 stations. In the S-wave-tomography, 124 usable events were found to produce a dataset of 8016 S-wave arrival-times from 99 stations (station ZST yielded no usable S-waves). Hypocentral information can be found in appendix B.

2.6 Determination of arrival-times

2.6.1 Absolute arrival-time residuals

Although, the relative arrival-times between stations are used in the tomography, the absolute arrival-times also provide significant information and put the regional tomography into context. To assess how anomalous the Carpathian-Pannonian region is, absolute travel-times were picked for P-waves at each station used in the final P-wave tomography - 15853 arrival-times from 225 events. The first arrival-time picking was semi-automated using the adaptive stacking method (Rawlinson & Kennett, 2004). The first onset of energy was manually picked from the stacked trace for each event. The individual station pick could then be determined automatically from the adaptive stacking derived time-shifts. Figure 2.5a shows a mean absolute residual relative to *iasp91* (Kennett & Engdahl, 1991) of -1.458 s, indicating the region is anomalously fast. Poupinet et al. (2003) found absolute P-wave residuals on continental lithosphere stations ranged from -1.5–1.5 s, with stations on stable continents (eliminating stations on rifts, in volcanic regions, in moun-

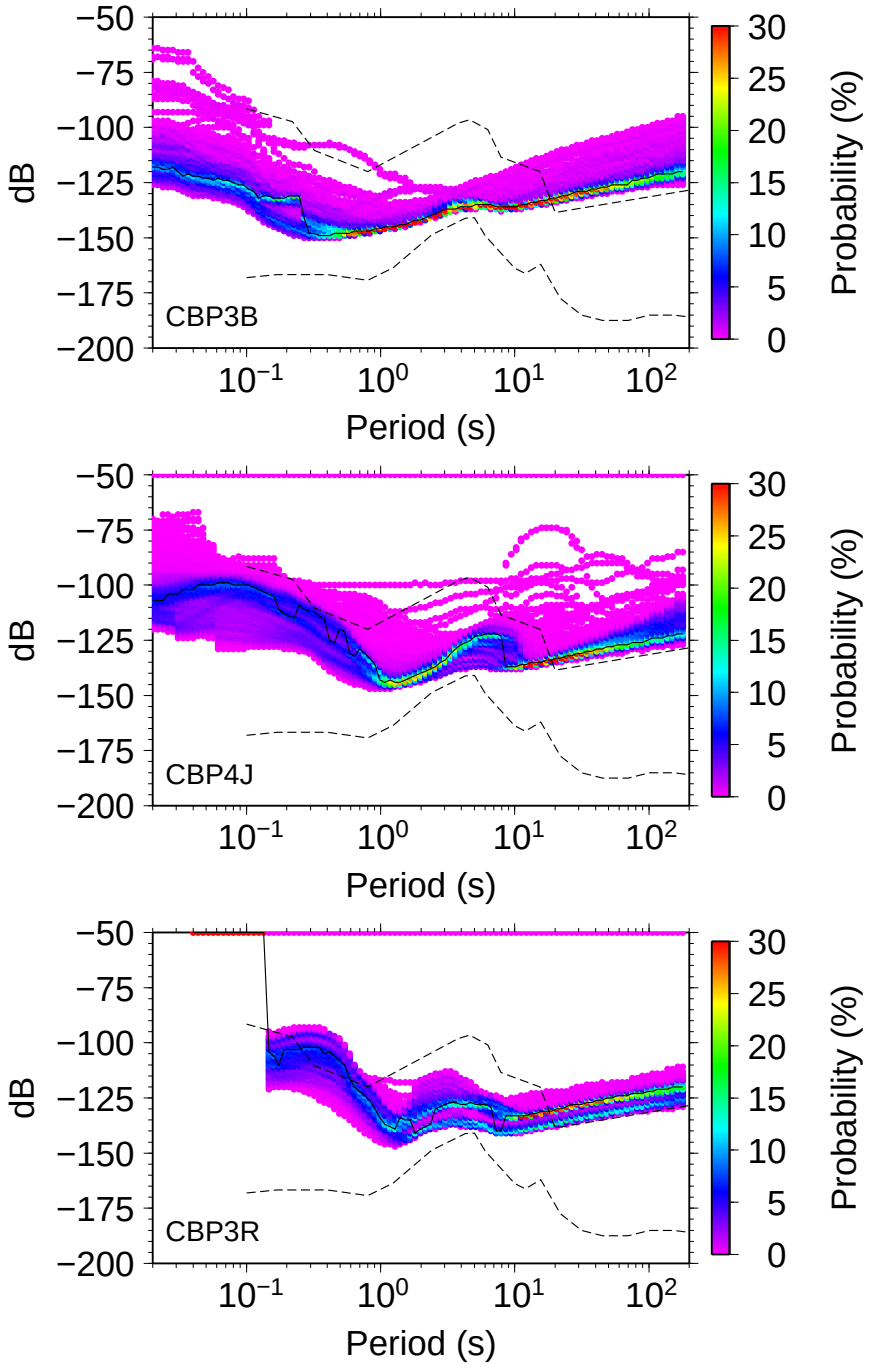

Figure 2.3: Power spectral density plots of the vertical components over a seismically quiet period. The stations show typical ambient noise along the temporary HST array from north-west (CBP3B) to south-east (CBP3R). The dashed lines show the high and low noise model of Peterson (1993). The modal value is shown as a solid black line.

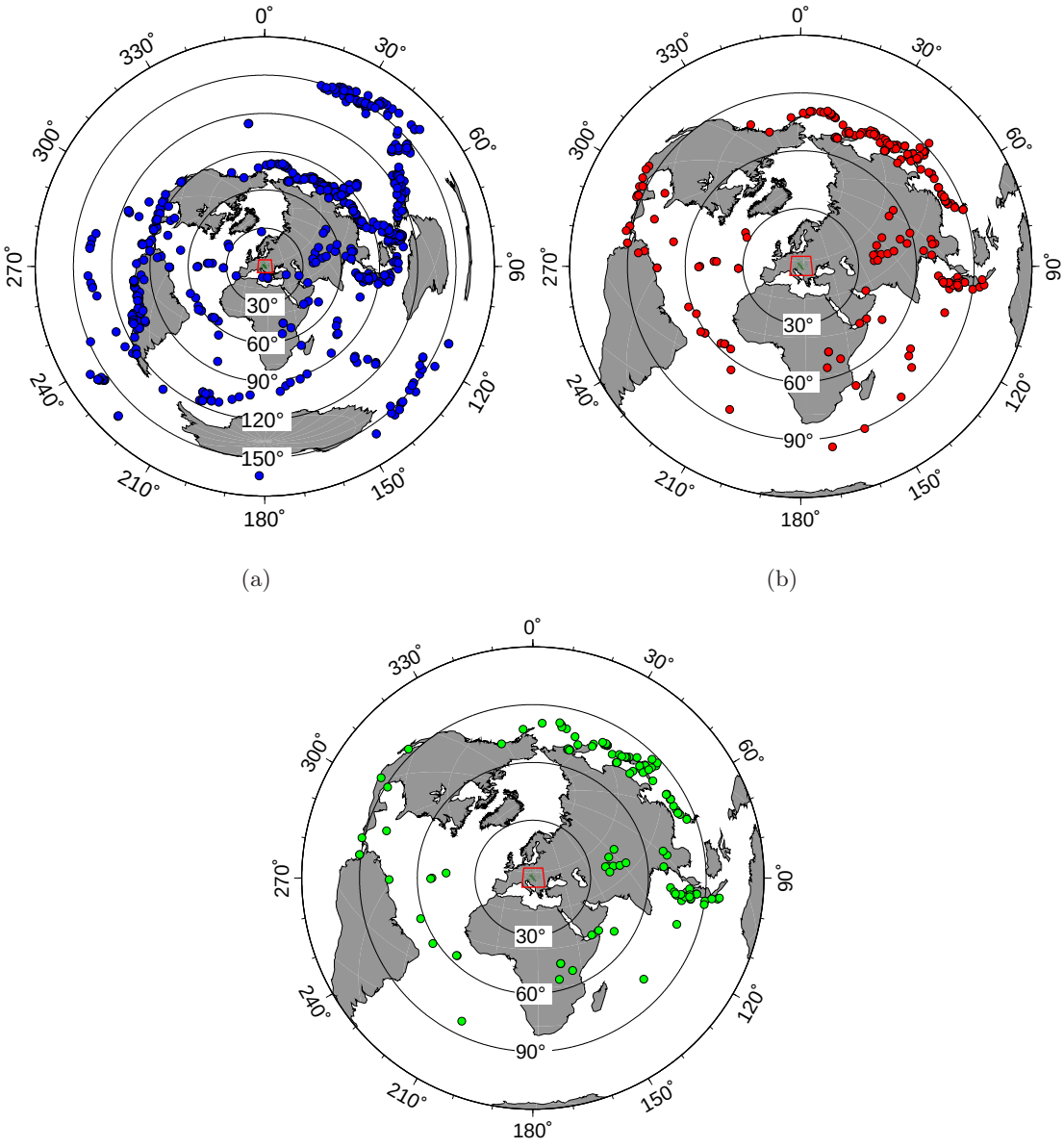

(a) (b)

(c)

Figure 2.4: Azimuthal projection of events recorded from 11/04/2006 to 22/08/2007 with magnitude $M_w \geq 5.5$. Hypocentral information is from the Bulletin of the International Seismological Centre. (a) all seismicity - 745 events; (b) events used for the P-wave tomography - 225 events; (c) events used for the S-wave tomography - 124 events. The stations are located in the centre of each plot.

tain belts or where surface waves have shown large upper-mantle anomalies) limited to -1.3–0 s. In figure 2.5b, the mean absolute residual for each event is relatively consistent, with little variation with distance and back-azimuth. Plots of the absolute residuals at individual stations were also produced (e.g. figure 2.5c), showing the residual pattern at each station. We should observe a similar variation within the relative arrival-time residuals. Figure 2.6 shows the mean absolute residuals at each station from four different source regions again highlighting the anomalously fast structure of the region.

2.6.2 Relative arrival-time residuals

Global travel-time tomography uses absolute travel-time residuals to determine absolute perturbations in wave-speed, relative to a reference model. However, absolute residuals suffer from errors in both source origin time and mis-location (e.g. Engdahl et al., 1998; Piromallo & Morelli, 2003). Additionally, the picking of absolute times can be inherently difficult, with the onset of energy often emergent, resulting in large errors from picks. In order to mitigate the effects of large scale heterogeneity outside the local volume and source effects, I use relative arrival-time residuals. These measure the difference in arrival-time between each station, relative to a zero mean across the network. For teleseismic events ($\Delta > 30°$), rays travel similar paths, only diverging in the region beneath the stations. The relative arrival-time residuals, thus, reveal the variation of the velocity within this region. The depth extent of crossing ray-paths is determined by the aperture of the network, which reaches 888 km (between stations DIVS and NKC) for the selected station distribution.

Recording teleseismic events on a regional network means that the arriving waveform is relatively similar at each station. This lends itself to using cross-correlation techniques to determine any time-lag between stations. To determine the relative arrival-time residuals, I use the multi-channel cross-correlation (MCCC) method of VanDecar & Crosson (1990).

A significant disadvantage of the MCCC method is the need for an initial pick for every trace. Phase-picking algorithms, for example the STA/LTA (short-term averaging/long-term averaging) method (e.g. Coppens, 1985; Kanasewich, 1981), which work on single traces, would not reliably be able to locate the onset of major energy consistently across an array, due to variable signal to noise. Even with advances in phase-picking algorithms, where seismograms are modelled with an autoregressive model (e.g. Leonard & Kennett, 1999; Morita & Hamaguchi, 1984; Sleeman & van Eck, 1999), manually picking the

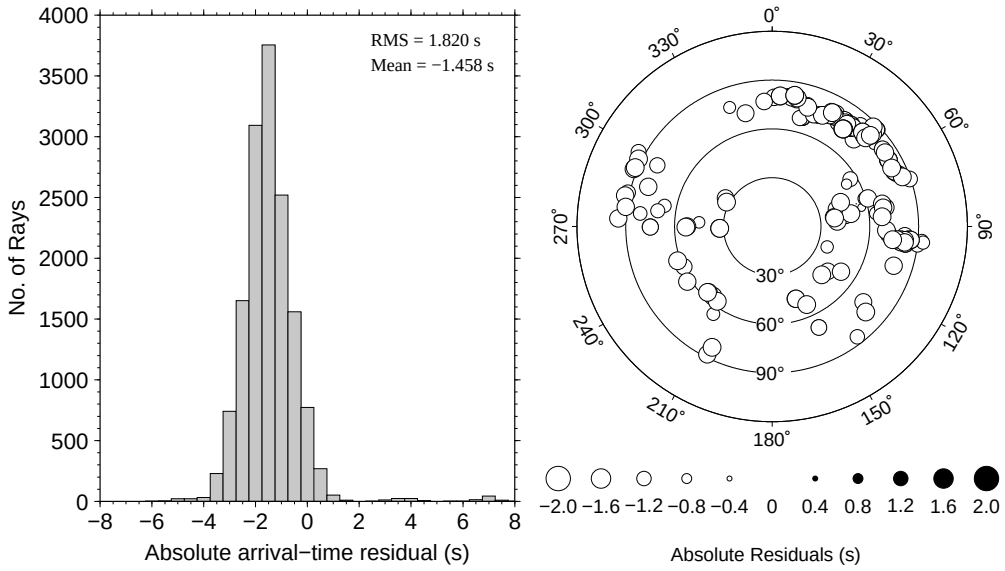

(a) (b)

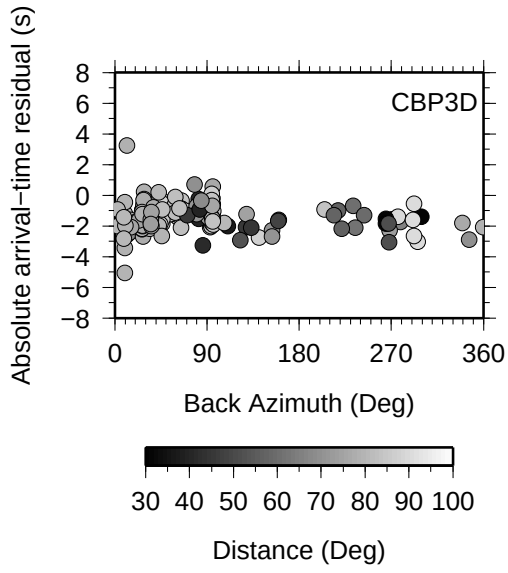

(c)

Figure 2.5: Absolute travel-time residuals relative to *iasp91*: (a) histogram of all residuals; (b) mean residuals for each event plotted as a function of distance and back-azimuth from the centre of the network; (c) residuals at a single station, CBP3D (48.34° N, 15.83° E)

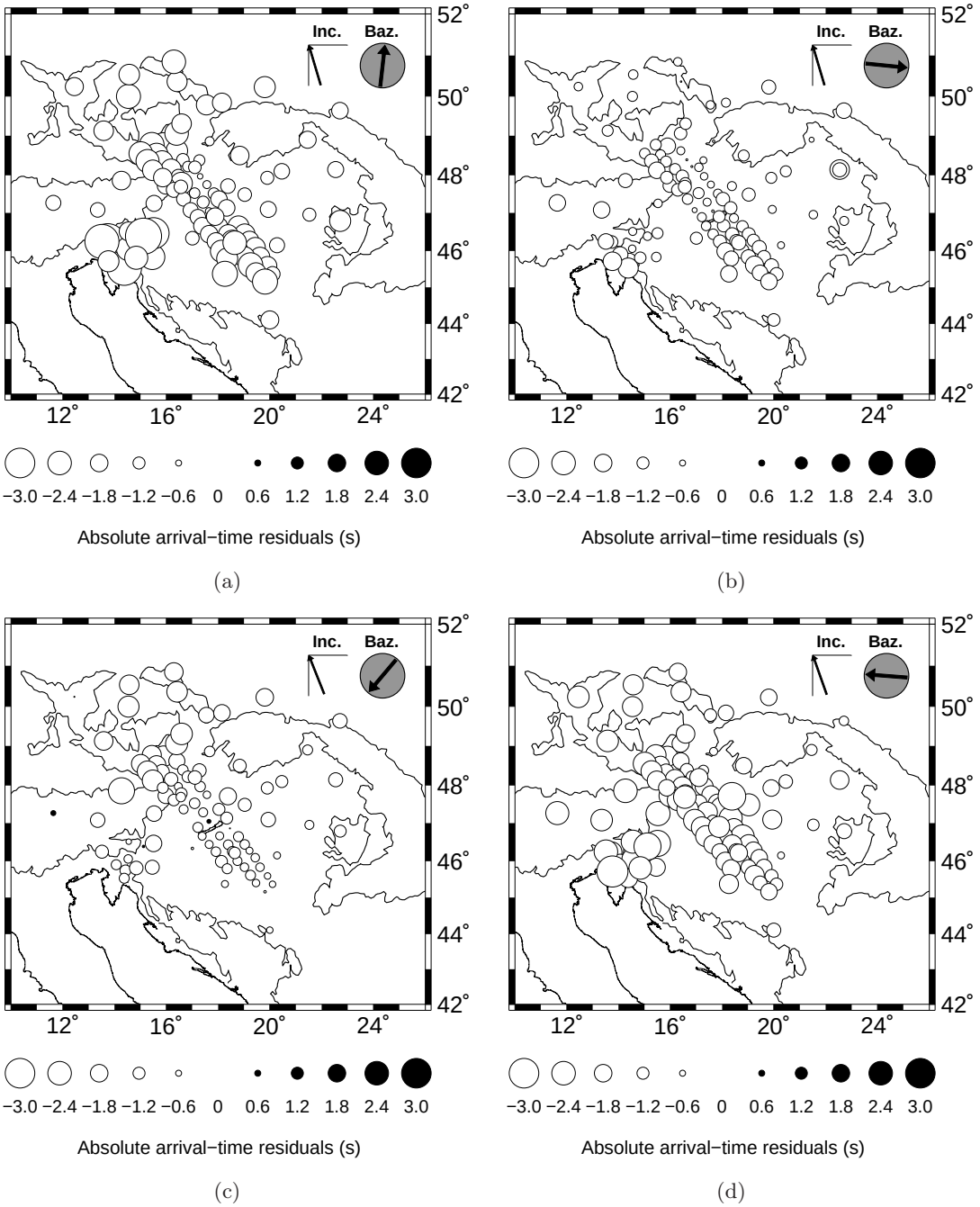

Figure 2.6: Mean absolute arrival-time residuals for P-waves relative to *iasp91* for events in four source regions. 22 events from 0°–10° were used in (a); 30 events from 90°–100° in (b); 7 events from 210°–230° in (c); 22 events from 270°–280° in (d). The average back-azimuth and path inclination are shown.

data provides more control and reduction in error (e.g. Leonard, 2000), but does not eliminate the chance of picking different cycles of energy at different stations, and is time-consuming. To overcome this problem, I used the adaptive stacking procedure of Rawlinson & Kennett (2004), to estimate the initial pick. Prior to the following stages, all traces were bandpass filtered using a zero-phase, two pole Butterworth filter. The corner frequencies were 0.4–2 Hz for the P-waves and 0.04–0.1 Hz for the S-waves.

Adaptive stacking

Adaptive stacking is an automated method for determining residual patterns across a network. For each event, by applying a moveout to traces from a reference Earth model, any remaining misalignment between traces must be due to changes in the velocity structure beneath the network. By stacking the traces and finding the misfit between each trace and the stack, the arrival-time residual is determined.

Traces are approximately aligned by using the time-shifts (t_i^c) from *iasp91*, relative to an arbitrary reference point - station CBP3J was chosen as it is close to the centre of the network. For N stations, a linear stack ($V_l(t)$) is defined for a specified window within the moveout-corrected traces ($u_i(t)$):

$$V_l(t) = \frac{1}{N} \sum_{i=1}^{N} u_i \left(t - t_i^c\right) \tag{2.1}$$

Using a search over a time-shift, τ, the misfit (P) between each moveout-corrected trace and the stack is minimised with an L_3 measure of misfit, defined by:

$$P = \sum_{j=1}^{M} \left| V_l(t_j) - u_i \left(t_j - t_i^c - \tau\right) \right|^3 \tag{2.2}$$

where M is the number of samples in the trace window. The time-lag between each moveout-corrected trace and the stack (τ_i) is added to the moveout correction, to improve the alignment. A new stacked trace is calculated and the procedure is repeated. Iterations continue until the trace alignment is accurate and stable (Figure 2.7). Each event was aligned and visually inspected to ensure there was no cycle skipping; significantly noisy or misaligned traces were removed from the procedure. Rawlinson & Kennett (2004) found using the L_3 measure of misfit the most effective for alignment of teleseismic data with rapid convergence compared with smaller measures of misfit.

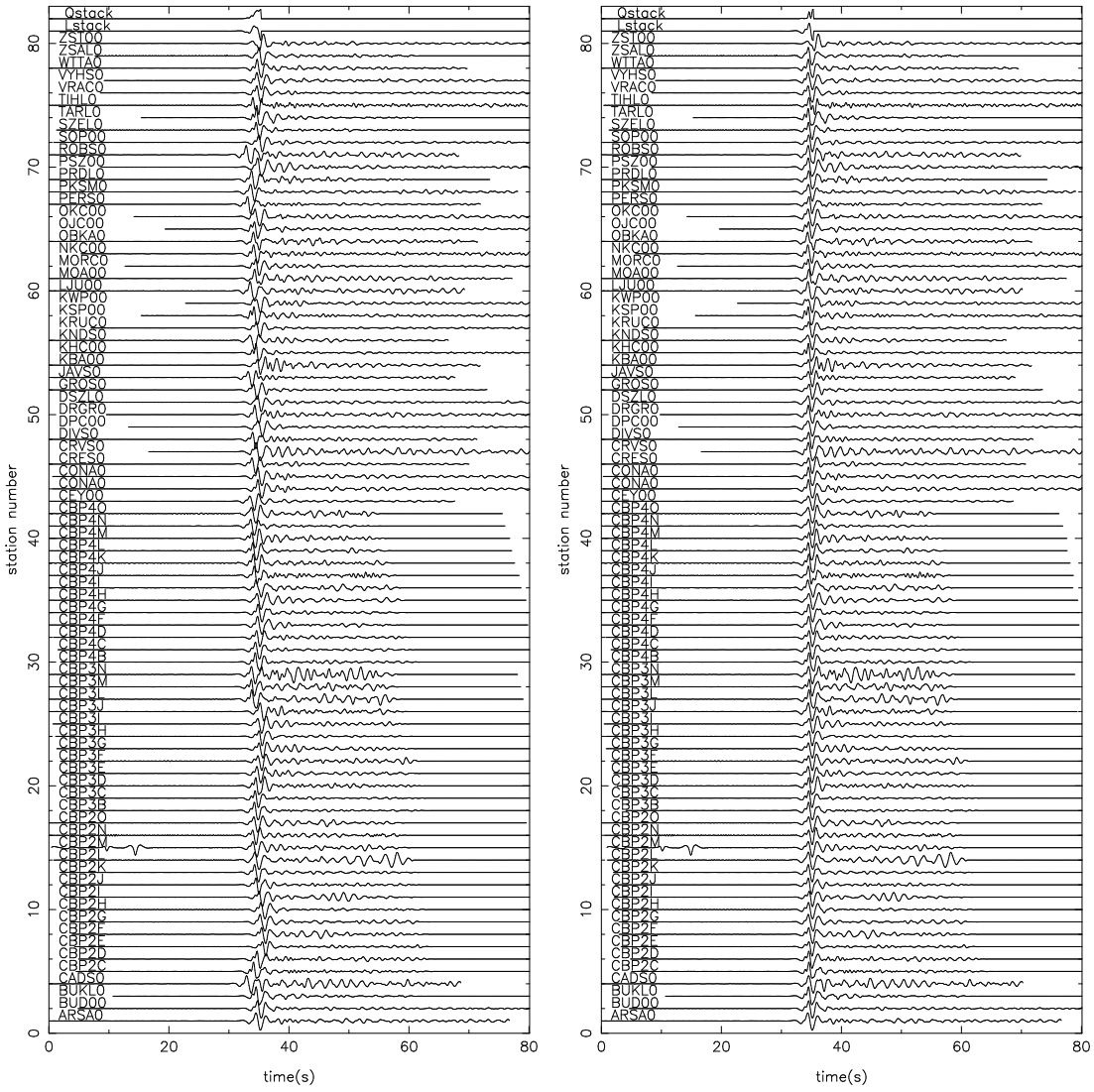

(a) (b)

Figure 2.7: Example of the adaptive stacking procedure for an M_w 6.0 earthquake, at 10:53.11 on 22/06/2006 at $45.4°N$, $149.3°E$, with a depth of 9.5 km. (a) shows the initial alignment after applying a moveout correction from *iasp91*, with the first two traces (Qstack and Lstack), showing the quadratic and linear stack respectively; (b) shows the final solution after 10 iterations, with the updated time-shifts applied to the traces and the final stacks.

After alignment, the stacked trace was manually picked at the first dominant peak or trough (t_{stack}). Using the time-shifts from the adaptive stacking, the pick from each trace was calculated:

$$t_i = t_{stack} - (t_i^c + \tau_i) \tag{2.3}$$

Following this approach, only one manual pick per event is needed to produce the preliminary picks for each trace needed by the MCCC code.

Multi-channel cross-correlation

Within the MCCC, for each pair of stations, i, j, the traces are cross-correlated over a window to produce the delay time between them (Δt_{ij}). Because waveforms are not identical at all stations (correlation coefficient < 1), the delay times are not consistent across the network (i.e. $\Delta t_{12} + \Delta t_{23} \neq \Delta t_{13}$). To produce the relative arrival-times for each station, the least-squares minimisation of the residual is calculated, whilst adding a constraint of a zero mean.

With the relative arrival-times for each station, the relative arrival-time residual (t_{RES_i}) relative to the *iasp91* reference Earth model (Kennett & Engdahl, 1991) is given by:

$$t_{RESi} = (t_i - t_i^{iasp}) - \bar{t}_{event} \tag{2.4}$$

where t_i is the relative arrival-time at each station, t_i^{iasp} is the theoretical *iasp91* arrival-time, with $\bar{t}_{event}$, the mean residual $(t_i - t_i^{iasp})$ for each event.

The parameterisation of the MCCC involves selecting a window over which to perform the cross-correlation. The dominant period of teleseismic P-waves is ~ 1 s; to include at least one cycle of P-wave energy, a window either 3 seconds or 5 seconds long was chosen depending on the dominant period of the event record. All events were processed with both windows. The window, which produced the highest correlation coefficient for an event was chosen for the residuals. The three and five second windows started one second and two seconds respectively, before an initial pick - based on the first dominant peak or trough. Only 36 out of the 225 events used the longer 5 second window. For the S-waves, a 15 and 30 second window were both applied, starting 5 and 10 seconds before the initial pick respectively.

While the adaptive stacking algorithm, can provide the relative arrival-time residuals

required, the MCCC provides an estimate of the data coherency through the correlation coefficient and is most easily incorporated into the inversion procedure of VanDecar et al. (1995). The use of both methods was found to be the quickest and most accurate procedure for producing relative arrival-time residuals for the tomography.

2.6.3 Quality control of the relative arrival-time residuals

Possible sources of error in the relative arrival-time residuals include cycle skipping, timing errors and noisy waveforms. To minimise and remove problematic data, all traces were visually inspected after applying the residual derived time-shifts (Figures 2.8 and 2.9). Cycle skipped arrivals and traces with an average correlation coefficient of less than 0.70 were removed. To assess individual stations, relative residuals were plotted as a function of back-azimuth and distance for individual stations (Figure 2.10). Timing errors in stations were detected with systematic offsets of the residuals in the plots. Data falling outside 2 standard deviations from the median were removed - effectively avoiding the inclusion of anomalous residuals, even from back-azimuths with poor coverage. The remaining residuals were binned in a 10° back-azimuth range in intervals of 1° (e.g. figure 2.11). Data were removed that fell outside 2 deviations within the bins. The MCCC was rerun, resulting in a set of residuals, self-consistent for a particular station (e.g. figure 2.10).

To estimate the measurement error of the relative arrival-time residuals, the residual variation was looked at for earthquakes with hypocentres close to one another. From a cluster of 8 Kuril Islands earthquakes (M_w 5.5 to M_w 7.9), with epicentres within 46 km of each other, the standard deviation of the relative-arrival time residuals are obtained at each of the stations. The average of these standard deviations is ± 0.040 s (with a range from 0.01 s to 0.07 s) for P-waves and ± 0.313 s (with a range from 0.021 s to 0.944 s) for S-waves; these uncertainty estimates are comparable with those from similar tomographic studies elsewhere (e.g Tilmann et al., 2001).

2.6.4 Analysis of the relative arrival-time residuals

The relative arrival-time residuals provide quantitative information on the subsurface structure, which can be extracted by tomographic inversion.

Figure 2.12 shows the 15853 and 8016 relative arrival-time residuals for the P-waves

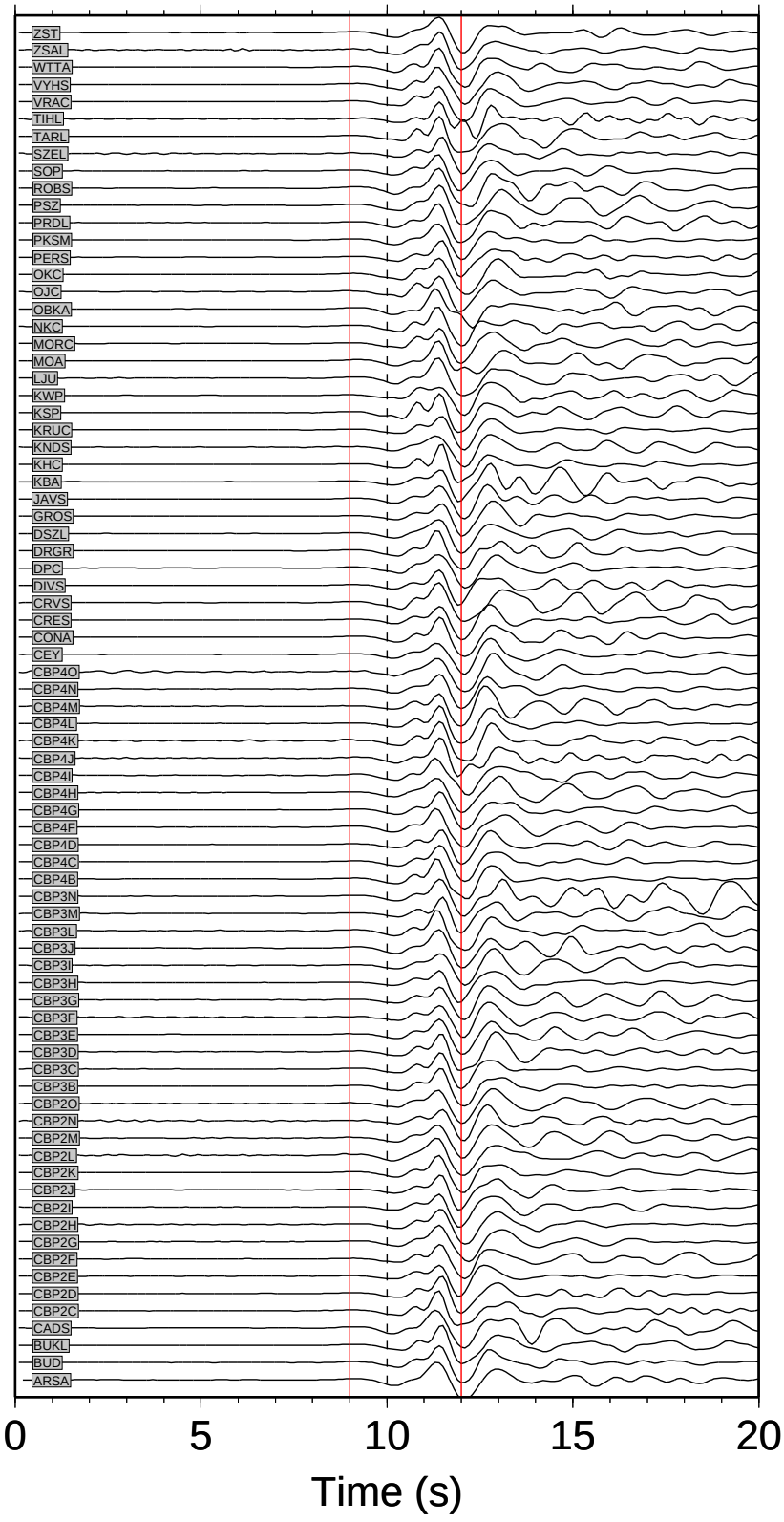

Figure 2.8: Example of the MCCC for P-wave arrivals from a M_w 6.0 earthquake, at 10:53.11 on 22/06/2006 at 45.4°N, 149.3°E, with a depth of 9.5 km. The plot shows the traces aligned around the MCCC derived pick at 10 seconds. The 3 second window around the pick is shown in red.

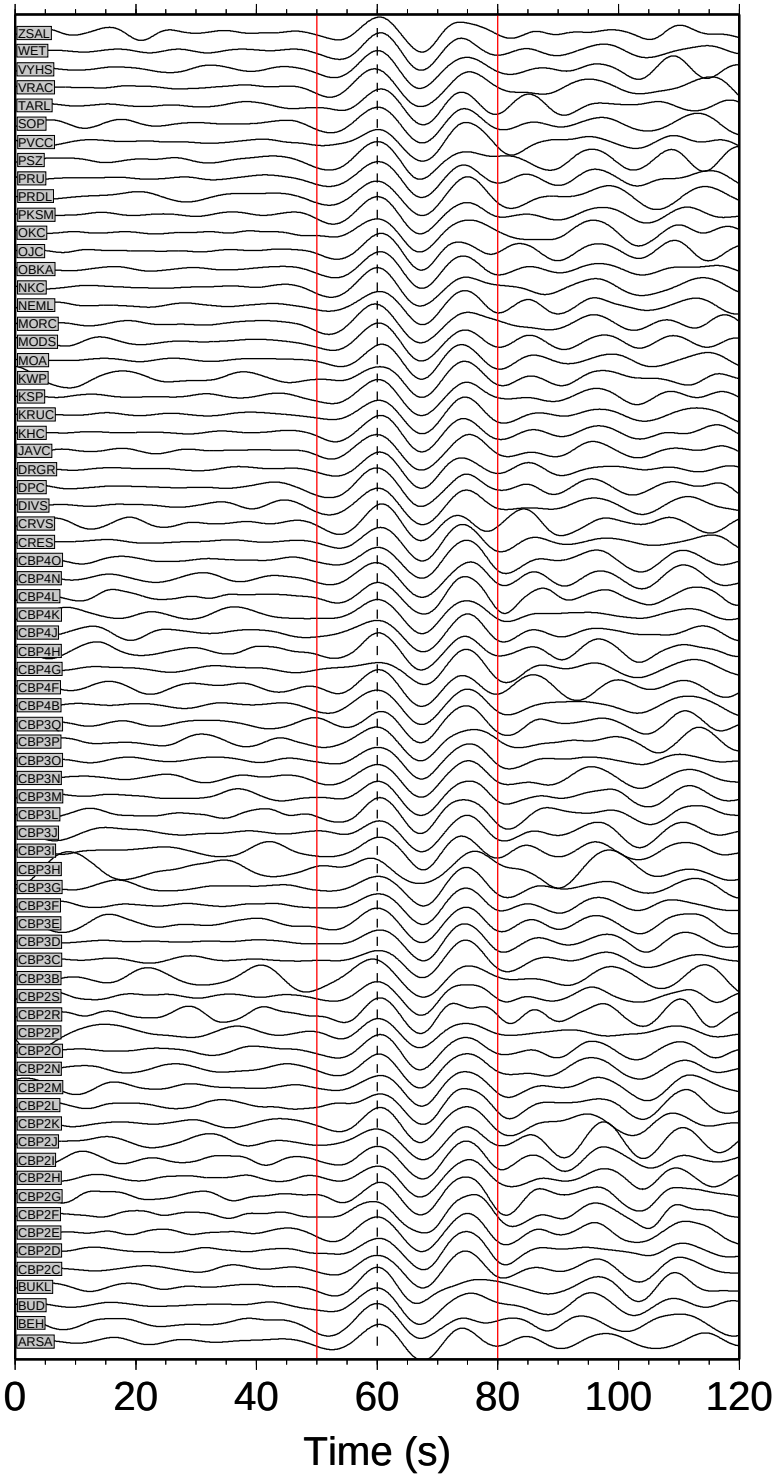

Figure 2.9: Example of the MCCC for S-wave arrivals from a M_w 6.0 earthquake, at 00:26.40 on 20/04/2007 at 25.7°N, 125.1°E, with a depth of 10 km. The plot shows the traces aligned around the MCCC derived pick at 60 seconds. The 30 second window around the pick is shown in red.

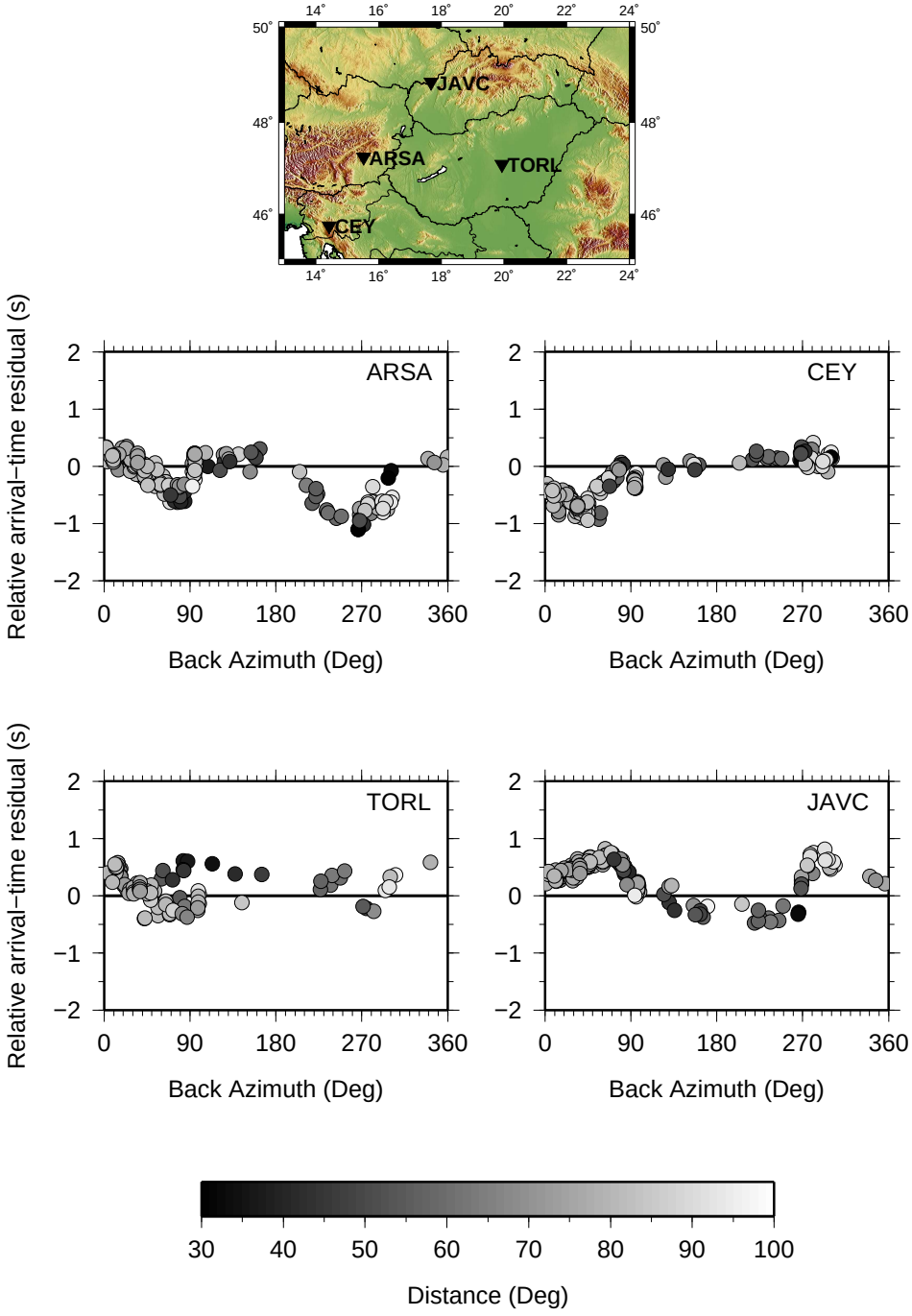

Figure 2.10: Variation of relative arrival-time residuals with back-azimuth for four stations on four different tectonic domains. ARSA, the Eastern Alps; CEY, the Dinarides; TORL, the Tisza-Dacia block in the Pannonian Basin; and JAVC located on the Alcapa block in the Western Carpathians. A constant station term derived from the tomographic inversion has been removed for each station to correct for the effect of crustal variations. A location map is shown for reference.

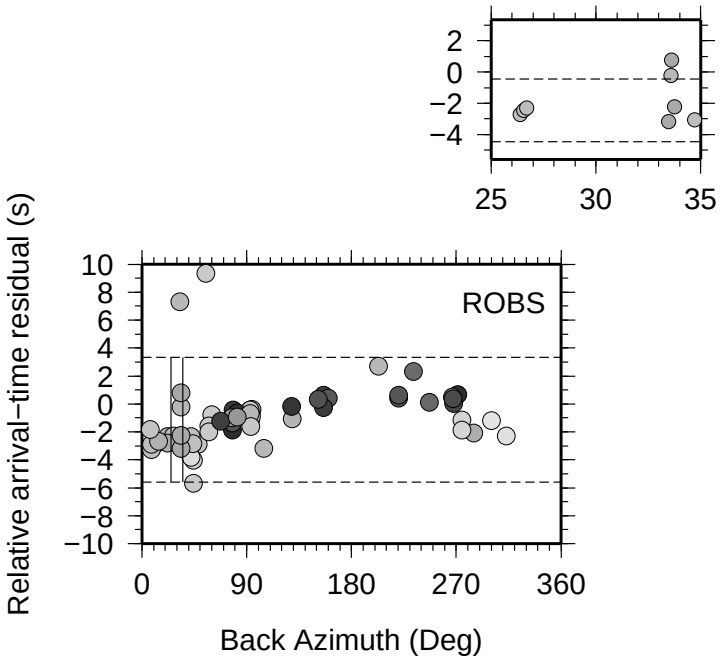

Figure 2.11: Example of the quality control at station ROBS for the S-wave residuals: Poor quality data were removed that fell outside of 2 standard deviations from the median - shown by the horizontal lines. A sliding window 10° wide, every 1° was then applied, with residuals removed that fell outside 2 standard deviations of the window median. The sliding window and zoom is shown between 25°–35°, also showing two standard deviations within the window.

and S-waves respectively. The P-wave residuals range from 1.74 s early beneath CADS to 2.38 s late beneath PERS; whilst the S-waves (not including the likely timing error for PVCC) range from 5.32 s early beneath PERS to 5.50 s late beneath JAVC. The correlation between P-wave and S-wave residuals is shown in figure 2.13 with the least squares regression showing an S-wave relative arrival-time residual 5.37 times greater than the P-wave relative arrival-time residual.

The variation of the relative arrival-time residual with back-azimuth and distance for all stations for both P and S-waves are shown in appendix C. Figure 2.10, shows the P-wave residuals for four stations from four different tectonic domains. For ARSA in the Eastern Alps, we observe early arrivals from the east and west (along strike of the Alps); for CEY in the Dinarides, early arrivals are present from earthquakes in the north to east. In the centre of the basin, TORL shows relatively late arrivals from near events but distant events from the east and west arrive earlier, indicating a possible deep fast structure in this orientation. Conversely, for JAVC, which is on the western most edge of the Carpathians, arrivals from the east and west are delayed, with relatively earlier arrivals from the south.

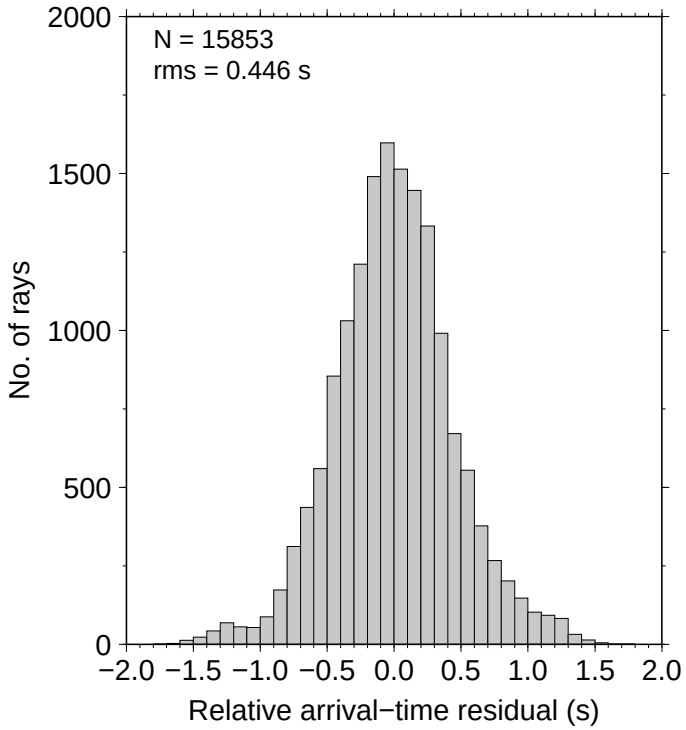

(a)

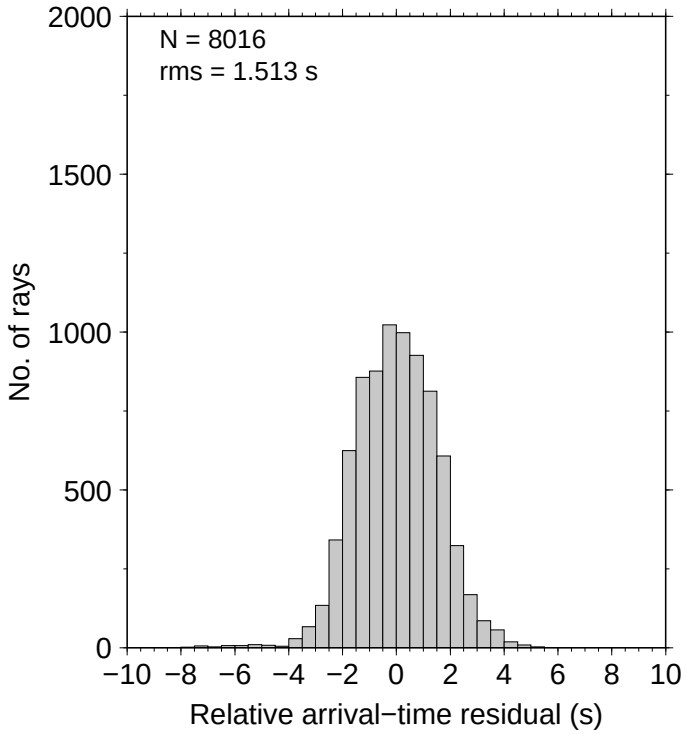

(b)

Figure 2.12: Histograms showing the relative arrival-time residuals produced from the MCCC for: (a) P-waves - binned every 0.1 s; and (b) S-waves binned every 0.5 s.

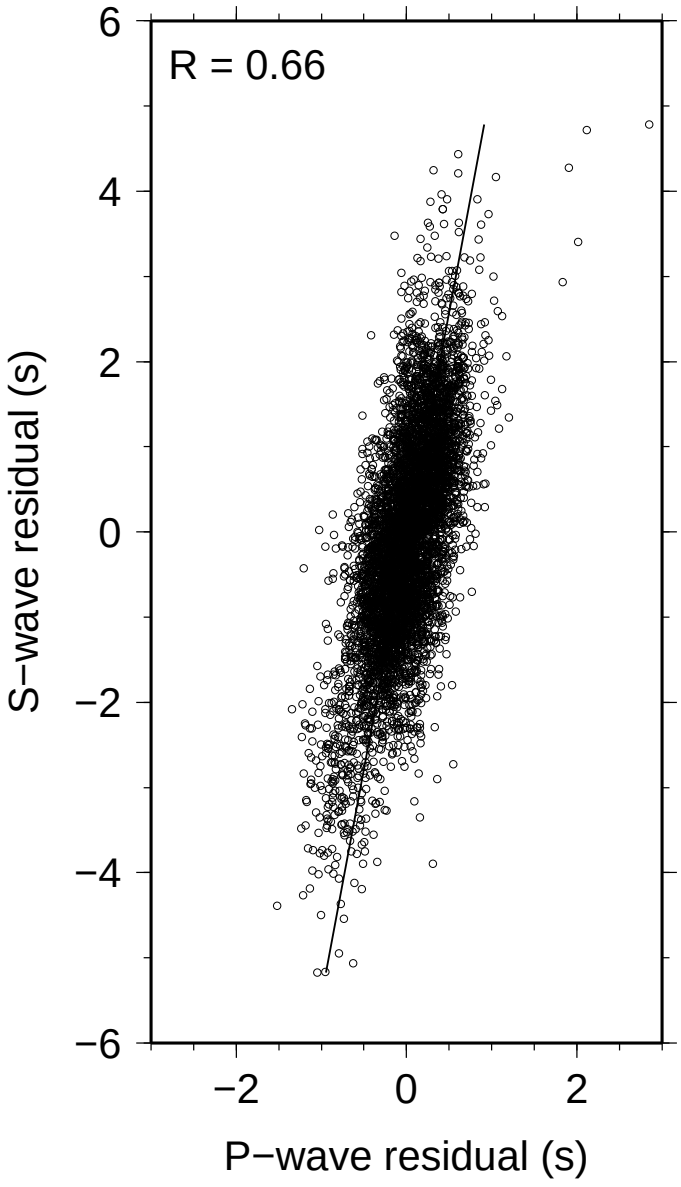

Figure 2.13: Correlation plot of P-wave and S-wave residuals for all common event/station pairs. 5652 residuals are shown from 96 events. The solid line shows the linear regression of the data using least squares and has a gradient of 5.37. The R value shows the correlation coefficient. Station terms derived from tomographic inversion have been removed from the residuals to correct for the effect of crustal variations.

Structure is also revealed by looking at the residual pattern across the entire network for different source regions. Figures 2.14 & 2.15 show residual patterns from four different source regions for the P and S-wave residuals respectively. Station terms determined in the tomographic inversion (section 4.6 & 5.5) have been removed from the residuals to correct for the effect of crustal variations. For events to the north (figure 2.14(a)), we observe P-wave residuals grouped into specific regions; south of the mid-Hungarian shear zone, in the Tisza domain, relatively early arrivals dominate, reflecting a possible deep sourced fast anomaly; late arrivals are observed to the north of the mid-Hungarian shear zone, in the ALCAPA domain, as far north as the Alpine-Carpathian flysch belt, where early arrivals are again observed into the Bohemian block. Early arrivals are also seen in the Dinaride/Slovenian stations, consistent with a high P-wave velocity lithospheric root beneath the Alps. With the events to the east (figure 2.14(b)), the pattern is similar, but the size of the residuals is reduced. For the south-west and western source regions (figures 2.14(c),(d)), the signal across the mid-Hungarian shear zone is reversed, with early arrivals to the north, further evidence of the high velocity lithospheric Alpine root. Late arrivals are observed in the high heat flow (Lenkey et al., 2002) central and southern Pannonian Basin. Qualitatively, similar residual patterns are also seen for the S-waves (figure 2.15); minor differences between P and S-wave residuals are seen in the events from the north (figure 2.15(a)) as relatively late S-wave arrivals are observed south of Lake Balaton and in the south-east of the Pannonian Basin.

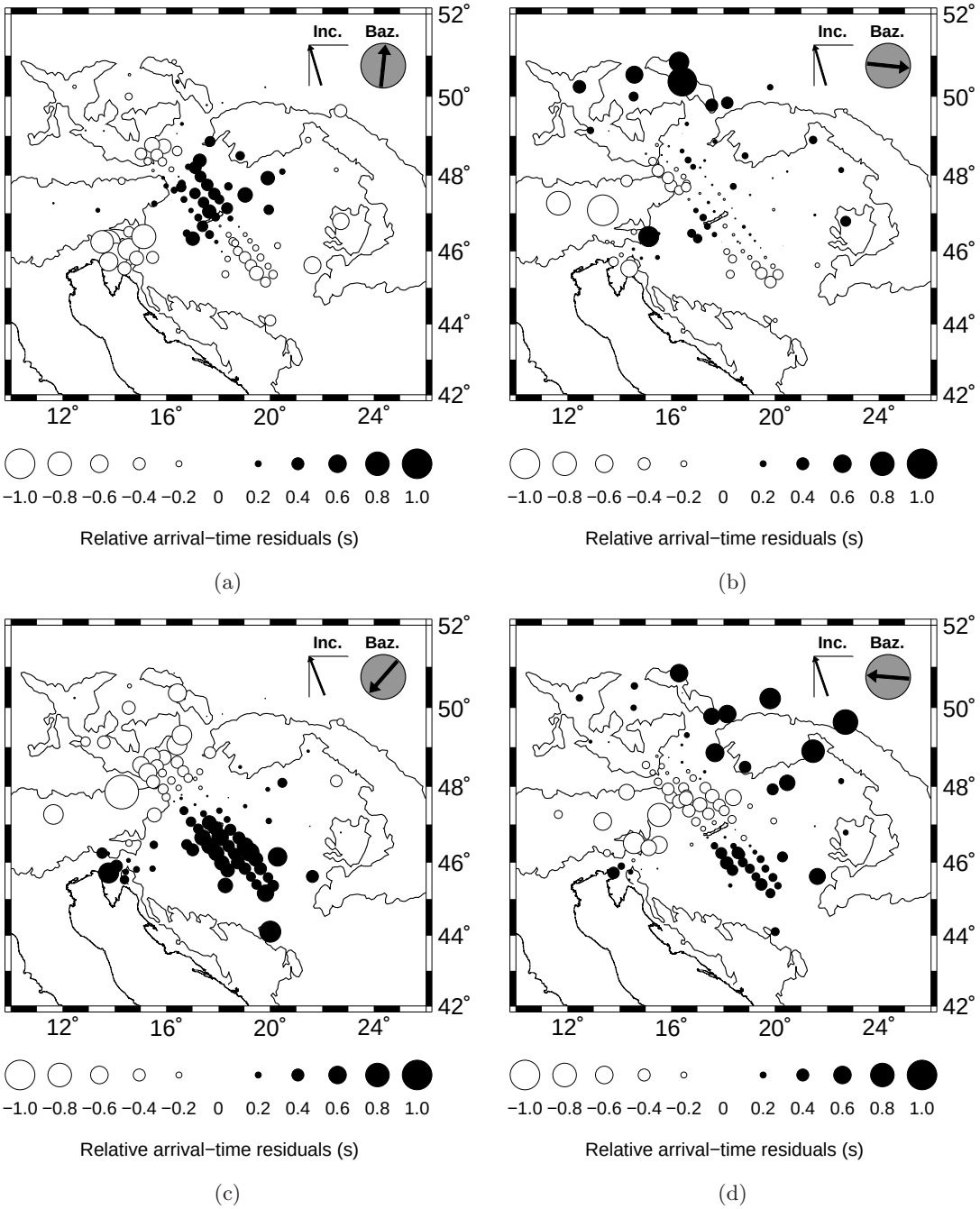

Figure 2.14: Mean relative arrival-time residuals for P-waves for events in four source regions. 22 events from 0°–10° were used in (a); 30 events from 90°–100° in (b); 7 events from 210°–230° in (c); 22 events from 270°–280° in (d). The average back-azimuth and path inclination are shown. Station terms have been removed from the plotted residuals.

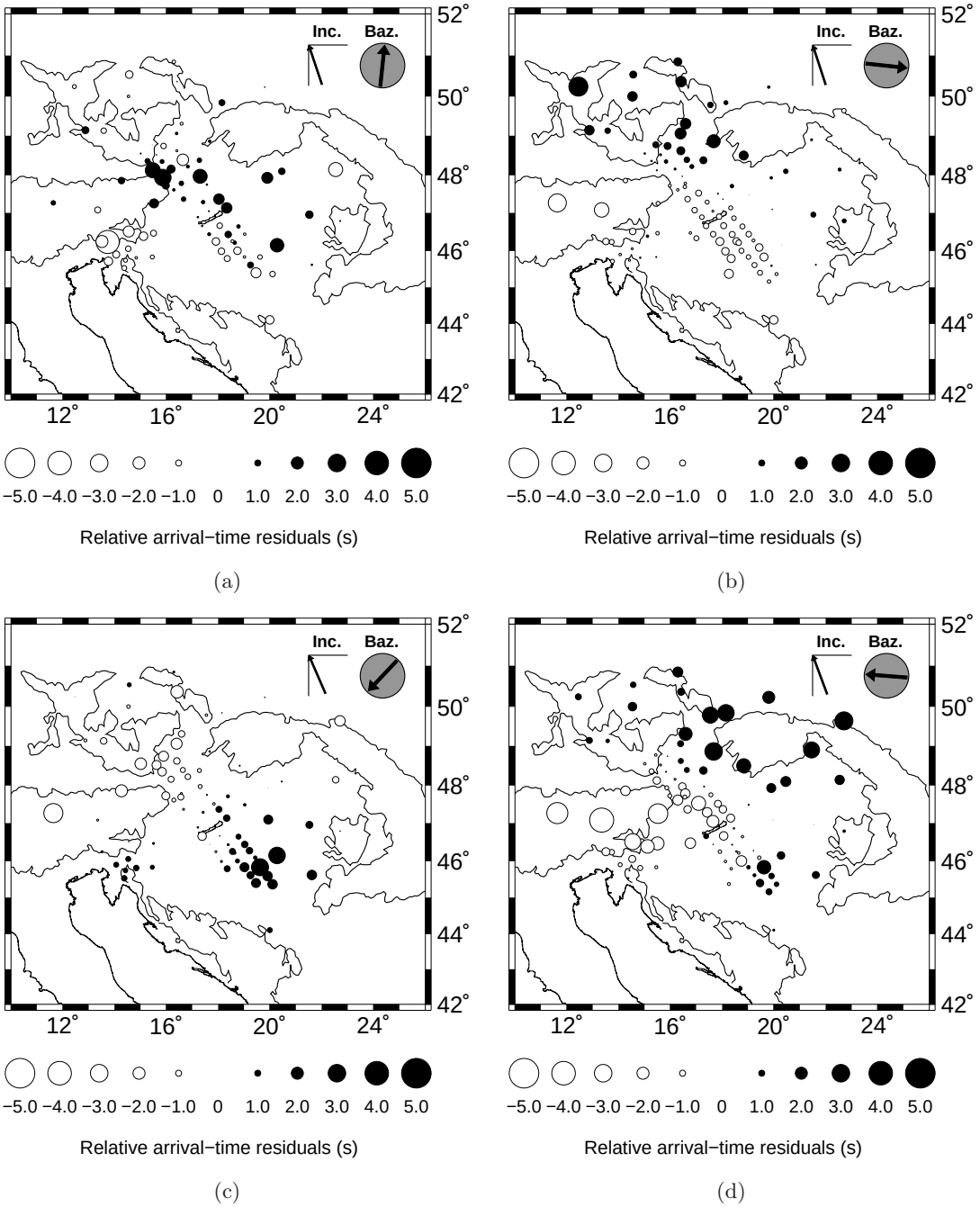

Figure 2.15: Mean relative arrival-time residuals for S-waves recorded from four source regions. 4 events from 0°–10° were used in (a); 24 events from 90°–100° in (b); 3 events from 210°–230° in (c); 6 events from 270°–280° in (d). The average back-azimuth and path inclination are shown. Station terms have been removed from the plotted residuals.

Chapter 3

Seismic tomography

3.1 Overview

In this chapter, I describe the parameterisation, inversion method and resolution tests used in applying relative travel-time tomography to reveal the velocity structure beneath the Carpathian-Pannonian region. The differences in resolution between a linear tomographic inversion and an iterative non-linear inversion are assessed for a simple synthetic case, in order to explain the choice of tomographic inversion algorithm.

3.2 Tomographic technique

Tomography is an imaging technique which reveals the interior of a 'body'. The method requires measuring some property of a signal which passes through the volume to be imaged. In seismic tomography, seismic travel-times, amplitude, attenuation or full waveform inversion can be analysed for either body waves or surface waves to reveal three-dimensional structure. Overviews of the various kinds of seismic tomography can be found in Iyer & Hirahara (1993) and Nolet (1987). Major complications with seismic tomography are that the sources and receivers are distributed unevenly and the ray-paths are non-linear. With earthquakes largely concentrated at plate boundaries, and the receivers located on the Earth's surface, there will be regions within a model which are not well-constrained by data. With unconstrained parameters, the tomographic problem is under-determined, and the solution is non-unique unless regularisation is applied.

Rawlinson & Sambridge (2003) outline the following steps required in seismic tomography:

1. **Model Parameterisation**: The seismic structure of the region being mapped is defined in terms of a set of unknown model parameters. Tomographic methods generally require an initial estimate of model parameter values to be specified.

2. **Forward Calculation**: A procedure is defined for the calculation of model data (e.g. travel-times) given a set of values for the model parameters.

3. **Inversion**: Automated adjustment of the model parameter values with the object of better matching the model data to the observed data, subject to any regularisation that may be imposed.

4. **Analysis of solution robustness**: May be based on estimates of covariance and resolution from linear theory or on the reconstruction of test models using synthetic datasets.

Using travel-time tomography to determine velocity structure from body waves, travel-times are needed for a large number of source-receiver pairs whose ray-paths are characterised by the greatest feasible range of back-azimuth and inclination. For a regional network of stations, we can parameterise a local 3-D volume so that the travel-times along multiple crossing ray-paths can be used to invert for velocity.

3.3 Theory - inverting travel-time data for velocity structure

The travel-time (T) of a seismic wave through an isotropic but inhomogeneous elastic solid can be expressed as the integral:

$$T = \int_{r_0}^{r_1} \frac{d\mathbf{l}}{V(\mathbf{r})} \tag{3.1}$$

where the $d\mathbf{l}$ is the ray-path for a particular segment, $\mathbf{r}$ is the vector function defining the ray-path, V is the velocity, and the integration limits are the start and end of the ray-path.

The relationship between the travel-time and the reciprocal of velocity (slowness, s) along a path is non-linear, since the path depends on the slowness field. Fermat's Principle states that the travel-time of a wave is stationary with respect to small departures in the ray-path. For small slowness perturbations in the model, this allows for a first order

linear relationship between travel-time perturbations and slowness perturbations relative to a reference model. The travel-time perturbation Δt_i is calculated by integrating the slowness perturbations $\Delta s(r)$ along the ray-path L_i^{ref} in the reference model:

$$\Delta t_i = \int_{L_i^{ref}} \Delta s(r) dl_i \tag{3.2}$$

The steeply inclined ray-paths in teleseismic tomography, make the linear assumption more accurate than it is when used with local or regional phases (e.g. local earthquake tomography or wide-angle inversion), as the path will be less affected by the dominant changes in vertical velocity structure (Rawlinson & Sambridge, 2003). However, the linear approximation is only valid if the scale of the inhomogeneity is much larger than the wavelength of the wave (Romanowicz, 1991).

3.3.1 Model parameterisation and inversion procedure

The relative arrival-time residuals were inverted for slowness perturbations using the method of VanDecar et al. (1995), which is based on VanDecar (1991), and has been successfully used in previous regional studies (e.g. Arrowsmith et al., 2005; Bastow et al., 2008; Graeber et al., 2002; Reusch et al., 2010; Rondenay et al., 2000; Sol et al., 2002; Tilmann et al., 2001). The slowness field is parameterised using a set of smoothly-varying cubic splines under tension, relative to a spherically symmetric background model. The splines are locally constrained by a 3D grid of nodes (figure 3.1). In depth, the grid consists of 35 nodes spaced at 25 km intervals between 0-850 km; at each level the grid consists of 60 nodes in latitude, spaced at intervals of 0.25° from 39.75° to 54.5°, and 99 nodes in longitude, from 6° to 30.5° also at intervals of 0.25°. The model is sufficiently large that any heterogeneities outside the imaged region, should not be mapped into internal structure of the final model.

In addition to inverting for slowness, the inversion also simultaneously solves for an arrival-time correction associated with each source and receiver. Source terms are included to account for hypocentral error, as well as ray-path distortions caused by velocity heterogeneities external to the grid. The station terms take into account travel-time anomalies directly beneath each receiver: a lack of crossing rays at shallow depths (less than the station spacing) prevents resolution of vertical structure in the crust and uppermost mantle, whilst variations in crustal thickness, for example, may contribute a

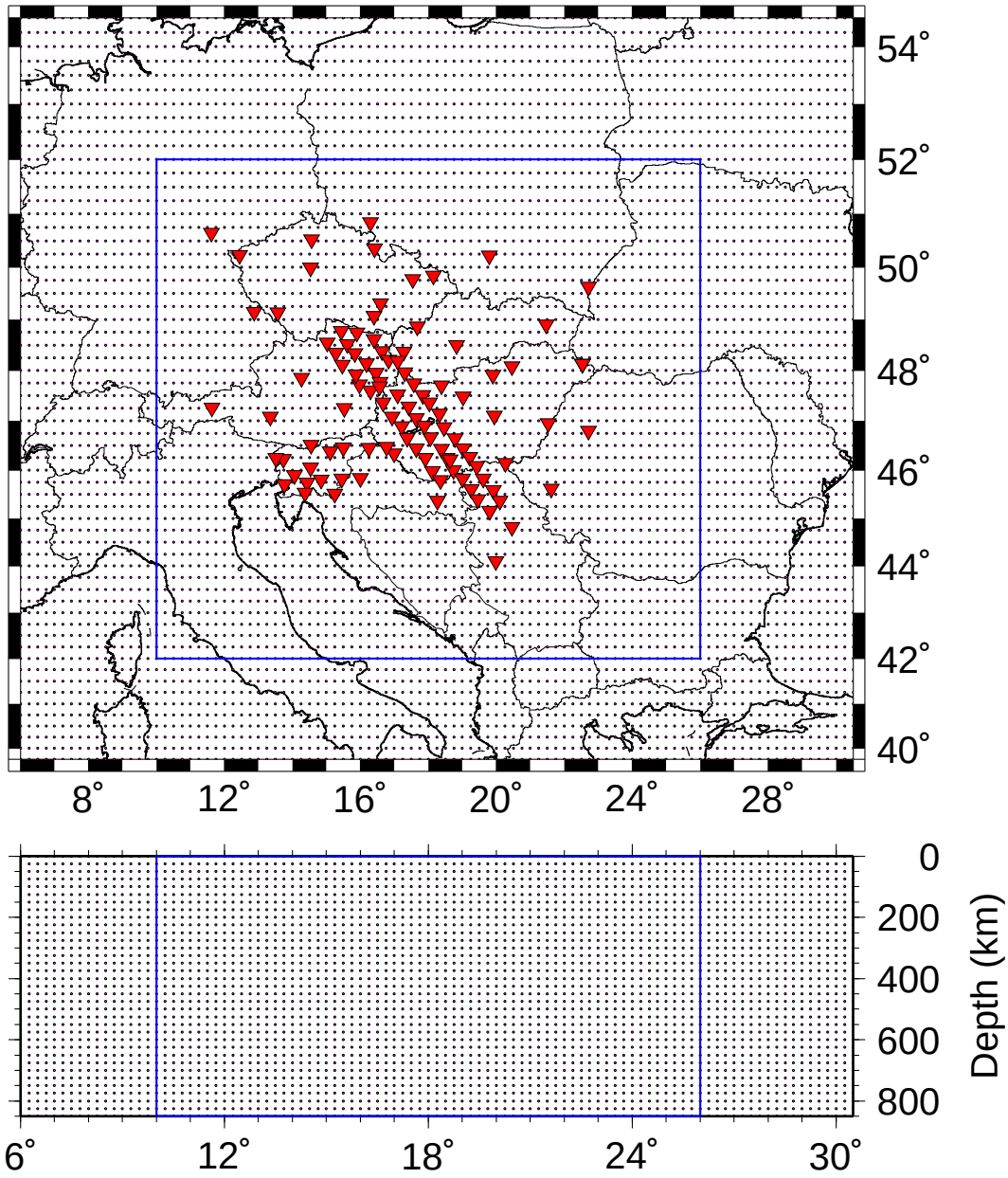

Figure 3.1: Node positions used to define the slowness field. Spherical curvature of the Earth is included in the model but not represented in this diagram. The stations are shown as red inverted triangles. The blue box defines the region used for plotting the final solution model.

consistent early or late arrival signal at a particular station. By using a station delay term, which is approximately the same for any arrival at that station, crustal travel-time variations are not spuriously mapped into the mantle model.

For the model parameterised above, the solution for the travel-time anomaly in equation (3.2) can be discretised for the i^{th} ray as:

$$\Delta t_i = \sum_j p_{ij} \Delta s_j \tag{3.3}$$

where p_{ij} is the Fréchet derivative $\partial t_i / \partial s_j$ through the interpolated model, and Δs_j is the slowness perturbation at the j^{th} node. With the addition of station and source terms (VanDecar, 1991), in matrix form we have to solve

$$\mathbf{WAm} = \mathbf{\Delta t} \tag{3.4}$$

where, $\mathbf{W}$ is a diagonal weighting matrix and,

$$\mathbf{A} = \begin{bmatrix} \mathbf{P} & \mathbf{C} & \mathbf{E} \end{bmatrix} \tag{3.5}$$

and

$$\mathbf{m} = \begin{bmatrix} \mathbf{\Delta s} \\ \mathbf{\Delta c} \\ \mathbf{\Delta e} \end{bmatrix} \tag{3.6}$$

$\mathbf{P}$ contains the derivatives of the travel-times with respect to the model parameters in equation (3.3); $\mathbf{C}$ contains the partial derivatives ($1/cos\ i$ - where i is the angle of incidence) for the station terms; and $\mathbf{E}$ contains the partial derivatives for the hypocentre relocations, with respect to the north, east and vertical directions. The vectors $\mathbf{\Delta s}$, $\mathbf{\Delta c}$, $\mathbf{\Delta e}$ are the slowness, station terms and hypocentre perturbations respectively.

3.3.2 Regularisation - optimal inversion parameters

In addition to solving the set of linear equations in (3.5), the inversion is regularised by using smoothing and flattening parameters to suppress, respectively, the curvature of the model (the Laplacian operator - $\nabla^2 s$) and the spatial gradient of the solution (∇s). Damping constraints may also be added to the station and source terms so that we have the following regularisation equations to solve:

$$\lambda_s \mathbf{S} \mathbf{\Delta s} = 0 \tag{3.7}$$

$$\lambda_f \mathbf{F}\boldsymbol{\Delta}\mathbf{s} = 0 \tag{3.8}$$

$$\lambda_d \mathbf{D_s}\boldsymbol{\Delta}\mathbf{s} = 0 \tag{3.9}$$

$$\lambda_c \mathbf{D_c}\boldsymbol{\Delta}\mathbf{c} = 0 \tag{3.10}$$

$$\lambda_e \mathbf{D_e}\boldsymbol{\Delta}\mathbf{e} = 0 \tag{3.11}$$

where $\mathbf{S}$ and $\mathbf{F}$ are the smoothing and flattening operators; $\mathbf{D_s}$, $\mathbf{D_c}$, and $\mathbf{D_e}$ are the damping operators for the slowness, station term and source term perturbations, with their corresponding weights (λ). Heavy damping of the slowness field ($\mathbf{D_s}$) is applied to the edge nodes of the model to ensure that the anomalous edge effects are avoided.

The inversion is done iteratively, with smoothing applied to the current perturbation model relative to the reference model, rather than the previous iteration's model. The advantage of this method is that noise-generated roughness included in early iterations is suppressed, with improved knowledge of the partial derivatives $\mathbf{P}$. This constraint is achieved by rewriting (3.7)–(3.11) as for example, (3.7) becomes,

$$\lambda \mathbf{S}\boldsymbol{\Delta}\mathbf{s} = -\lambda \mathbf{S}(\sum \boldsymbol{\Delta}\mathbf{s}_{prev}) \tag{3.12}$$

where $\sum \boldsymbol{\Delta}\mathbf{s}_{prev}$ is the total perturbation from the reference model up to and including the previous iteration.

Including the regularisation constraints $\mathbf{G}$ into (3.4), the system of linear equations becomes:

$$\begin{bmatrix} \mathbf{WP} & \mathbf{WC} & \mathbf{WE} \\ \lambda\mathbf{G} & 0 & 0 \end{bmatrix} \begin{bmatrix} \boldsymbol{\Delta}\mathbf{s} \\ \boldsymbol{\Delta}\mathbf{c} \\ \boldsymbol{\Delta}\mathbf{e} \end{bmatrix} = \begin{bmatrix} \mathbf{W}\boldsymbol{\Delta}\mathbf{t} \\ -\lambda\mathbf{G}(\sum \boldsymbol{\Delta}\mathbf{s}_{prev}) \end{bmatrix} \tag{3.13}$$

With 15853 travel-time observations and 208900 model parameters, the total number of equations in (3.13), including the regularisation constraints is 1246130. For this reason, a straight forward least squares solution where $\mathbf{m} = (\mathbf{A}^T\mathbf{A})^{-1}\mathbf{A}^T\mathbf{d}$ is not computationally feasible due to the size of $(\mathbf{A}^T\mathbf{A})^{-1}$. VanDecar (1991) instead, takes advantage of the sparseness of $\mathbf{A}$ by solving the least squares problem using the conjugate gradient method

(Scales, 1987), which reduces the calculations into a series of matrix-vector and vector-vector products, minimizing computer memory requirements.

The data were thoroughly checked for possible errors (section 2.6), but in any case the inversion reduces the effect of outliers on the solution. Residuals greater than 1.5 standard deviations from the mean are progressively down-weighted as the inversion is iterated.

Although the weighting matrix **W** could be set to the reciprocal of the statistical uncertainty in the delay times, the MCCC does not provide reliable uncertainty estimates (e.g. Allen et al., 2002; Tilmann et al., 2001), especially for events with few arrivals. **W** is therefore set to the identity matrix for all subsequent inversions.

3.4 Comparison of linear and non-linear inversions

3.4.1 Overview

Before presenting the results of the linear tomographic inversion using the method of VanDecar et al. (1995), the effect of the linear approximation of (3.2) is tested using synthetic models. Here, I compare results from a synthetic checkerboard test using the linear tomographic inversion of VanDecar et al. (1995) and the iterative non-linear inversion method of Rawlinson et al. (2006). Both methods used identical source-receiver paths for the earthquake distribution in section 2.5.

In linear tomography the ray-paths are determined through the initial reference model, ignoring the path dependence of the rays through the updated slowness field. For iterative non-linear inversions, this potential problem is addressed by repeating the ray-tracing and inversion at each iteration using the updated model to obtain updated ray-paths.

3.4.2 Methods

In the inversion method of Rawlinson et al. (2006), the 3-D velocity model beneath the region is represented by a set of cubic b-splines, controlled by a regular grid of velocity nodes. The iterative non-linear inversion uses a finite difference wave-front tracking scheme known as the Fast Marching Method (FMM) (de Kool et al., 2006) rather than conventional ray-tracing to compute travel-times through the 3-D volume. The finite difference scheme tracks the travel-time of a wave-front along a continuously updating band of grid points at a rate determined by the slowness field, by solving the eikonal

equation,

$$|\nabla_{\mathbf{x}} T| = s(\mathbf{x}) \tag{3.14}$$

where T is the travel-time and s is the slowness at a given point ($\mathbf{x}$).

Compared with the conjugate gradient method, which performs a minimisation in one search direction for each iteration, Rawlinson et al. (2006) use the subspace inversion method of Kennett & Sambridge (1988). The search directions are along multiple basis vectors within a subspace of the model for each iteration. Details of the subspace inversion method are given by Kennett & Sambridge (1988) with overviews of both methods by Rawlinson & Sambridge (2003).

The regularisation applied to the inversion also differs between the methods of VanDecar et al. (1995) and Rawlinson et al. (2006). Rawlinson et al. (2006) optionally allow both a second derivative smoothing operator, but also a damping operator. In comparing the results, the regularisation is initially switched off for both methods. The tradeoff between data fit and model roughness is then compared when second derivative smoothing is applied in both cases.

3.4.3 Comparison parameterisation

Due to the differences in the calculation of the forward travel-times, the model parameterisation used for these tests differs from that described in section 3.3.1. The FMM requires the incoming wave-fronts to impinge on the base of the 3-D model, meaning that the model must be wide enough that no rays hit the side of the model, and shallow enough for rays not to bottom-out, within the model. The parameterisation for both methods is shown in table 3.1.

Direction	Number of nodes	Spacing	Min value	Max value
r (depth)	28	25 km	0 km	675 km
θ (latitude)	106	0.22°	34.90° N	58.00° N
ϕ (longitude)	95	0.33°	3.00° E	34.02° E

Table 3.1: Grid parameters used in both inversions. Grid spacing is isotropic at 47° N, with nodes spaced every 25 km in each direction.

3.4.4 Synthetic model

Synthetic checkerboard models were constructed, with anomalies defined as Gaussian spheres with a maximum width of 45 km. Two synthetic models are used, differing in minor ways, in order to accommodate the differences in the model parameterisation used by the two inversion methods. Rawlinson et al. (2006) calculate perturbations in terms of an absolute change in velocity from the reference model, whereas VanDecar et al. (1995) uses percentage change from the reference model. Thus the anomaly amplitudes have been set equal at 300 km depth (where 0.433 $km\ s^{-1}$ is equal to a 5% change in P-wave velocity). A periodic array of anomalies was used, spaced every 2° in latitude and longitude and 200 km in depth, starting from 100 km. As the anomalies must be centred on grid points, the actual locations of the anomalies vary slightly between the two interpolation schemes (figure 3.2). The synthetic relative arrival-travel residuals calculated using the FMM and ray-tracing separately are shown in figure 3.3.

Due to the restriction on ray-paths in the FMM, the earthquake sample was also reduced from 225 (see section 2.5) to 220 events, reducing the number of ray-paths for which the synthetic travel-times were obtained from 15583 to 15557.

For each inversion test, the synthetic data residuals were computed using the same travel-time computation method employed in that inversion method.

3.4.5 Inversion results

Velocity fields obtained from inversion of the synthetic travel-time data, are shown in figure 3.4. The linear inversion reduces the rms residual to 8.0 x10^{-5} s compared to only 1.7 x10^{-3} s for the iterative non-linear inversion. Almost complete explanation of the synthetic data residuals is therefore obtained by the linearised inversion in the absence of data noise. The combination of the FMM and subspace inversion used in the method of Rawlinson et al. (2006) however, recovers a noisier, more disorted version of the original model, even in the absence of data noise.

To quantify the recovery of the synthetic checkerboard model, the normalised correlation ($corr$) between the synthetic model (M) and solution model (M') is calculated, where

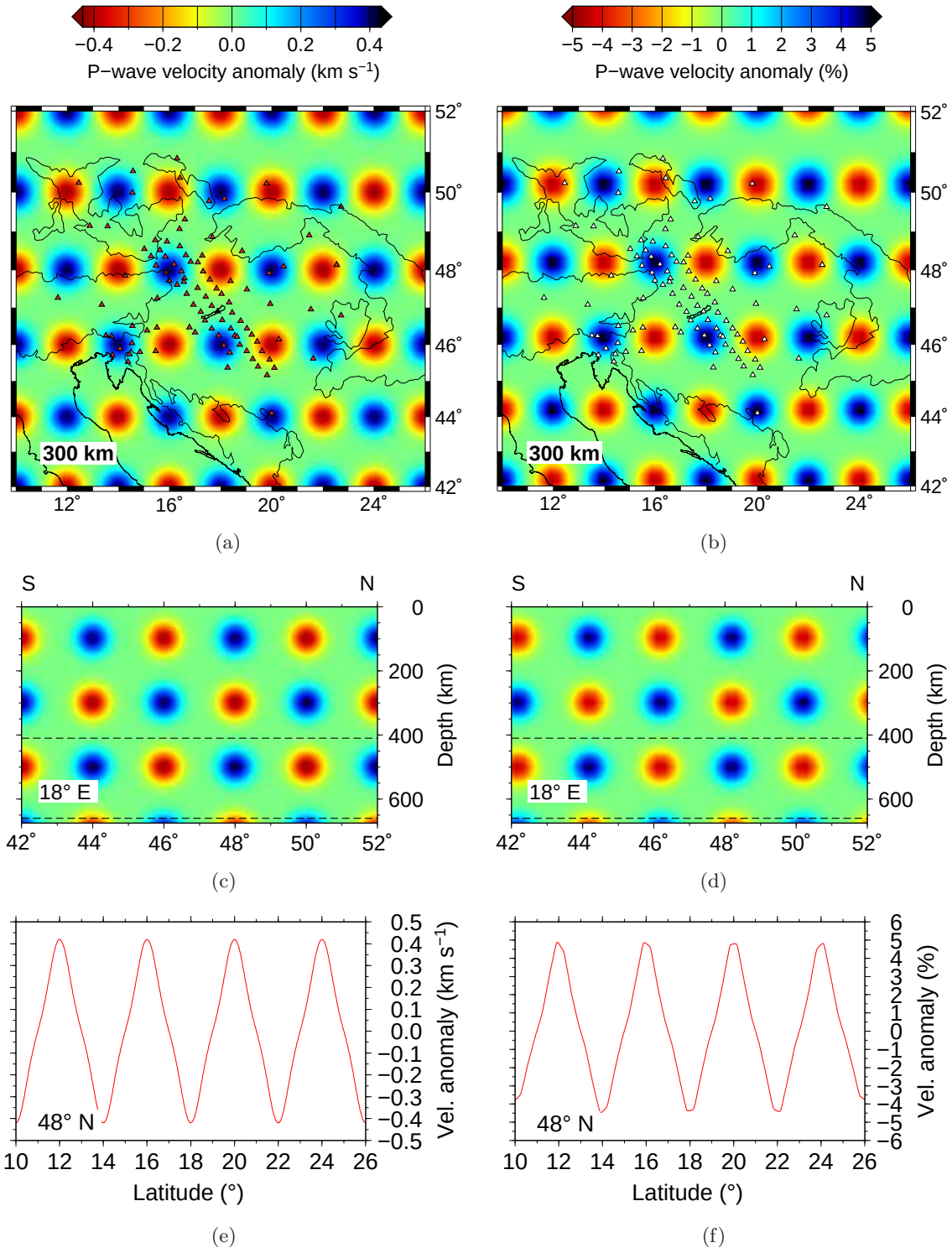

Figure 3.2: Representation of the synthetic input model for each inversion scheme. Figures on the left show input for the Rawlinson model, with that for the VanDecar model on the right: (a) and (b) show a 300 km depth slice; (c) and (d) show a north-south cross-section at 18° E through the model; (e) and (f) shows an east-west velocity profile through the model at 48° N. Dashed lines in the cross-sections show the 410 km and 660 km discontinuities.

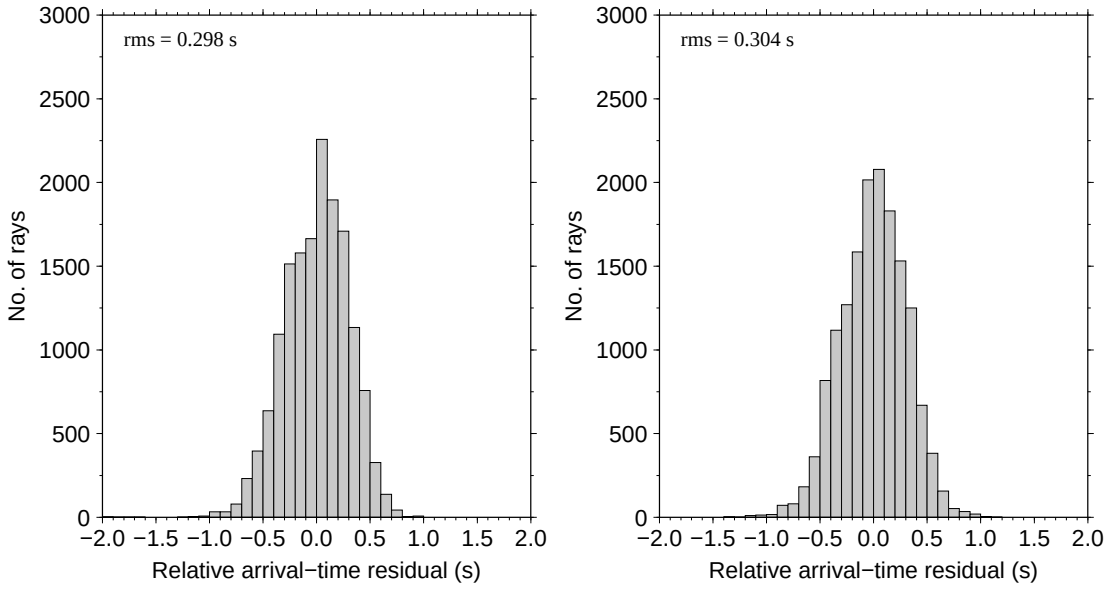

(a) (b)

Figure 3.3: Histograms of the 15557 synthetic travel-times created using (a) the Fast Marching Method for the iterative non-linear Rawlinson inversion and (b) conventional ray-tracing for the linear VanDecar inversion.

$$corr(M, M') = \frac{\sum_j \Delta s_j \Delta s'_j}{\sqrt{\sigma(M)\sigma(M')}}$$
$$\sigma(M) = \sum_j \Delta s_j \Delta s_j, \qquad \sigma(M') = \sum_j \Delta s'_j \Delta s'_j \tag{3.15}$$

The correlation between the input and output models for both inversions are shown in table 3.2. It is clear both from the correlation values and the images of the solution models that the linear inversion has better recovered the synthetic model at all depths. In the linear inversion, the anomalies have less distortion, even at 500 km, compared to increased smearing along ray-paths for the iterative non-linear inversion.

	Correlation	
Depth (km)	Iterative non-linear inversion	Linear inversion
100	0.48	0.62
300	0.61	0.75
500	0.72	0.83

Table 3.2: Table showing the correlation between the synthetic input model and the recovered solution model at three depths for both inversions.

Six iterations were performed for the iterative non-linear inversion with no significant change in the rms residual after the first three iterations (figure 3.5). To test how inversion results were affected by model resolution in the non-linear inversion, tests were performed

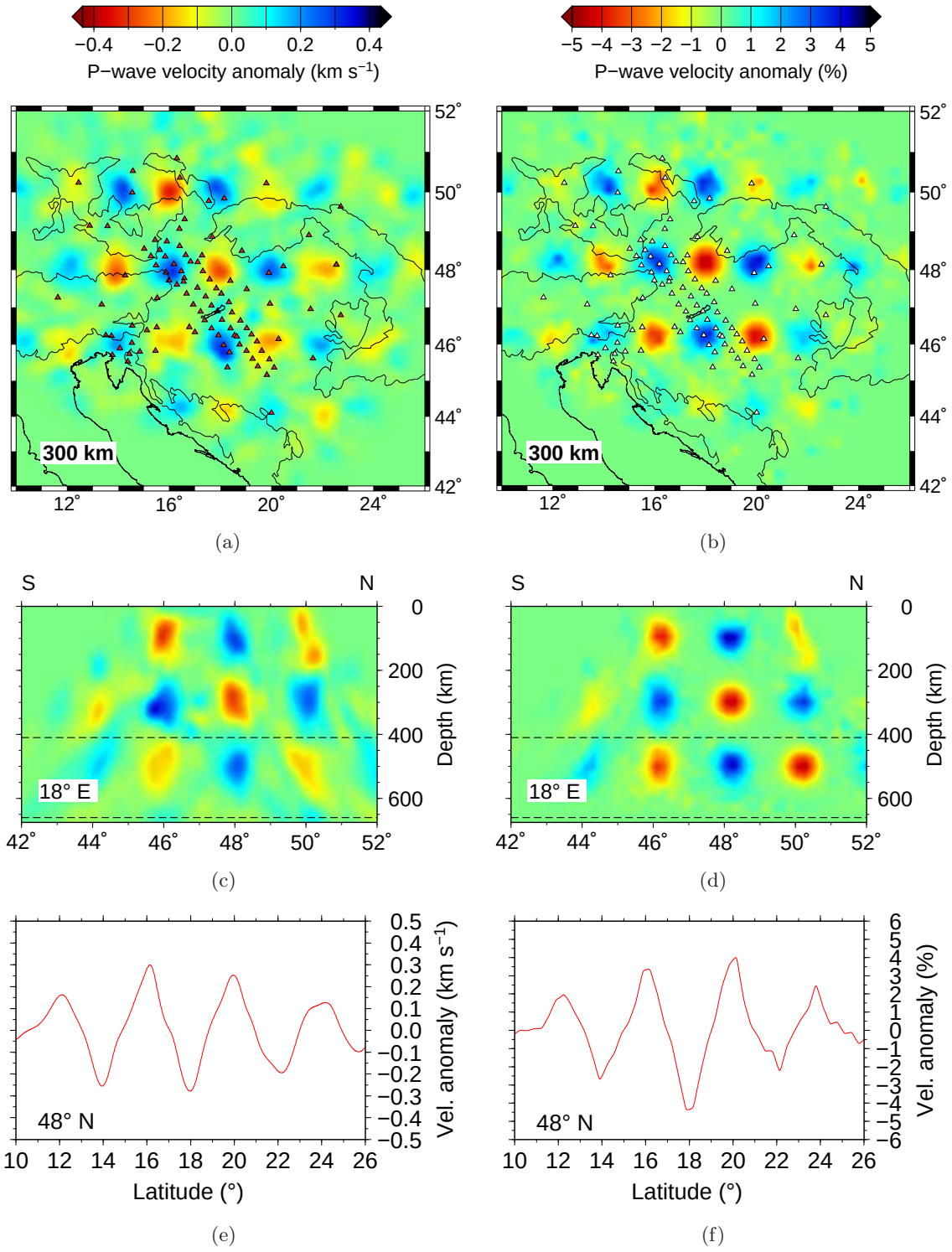

Figure 3.4: Inversion results for each inversion scheme. Figures on the left show the Rawlinson model, with the VanDecar model on the right: (a) and (b) show a 300 km depth slice; (c) and (d) show a north-south cross-section at 18° E through the model; (e) and (f) shows an east-west velocity profile through the 300 km depth slice at 48° N. Dashed lines in the cross-sections show the 410 km and 660 km discontinuities.

using a finer computational grid (based on a dicing factor) for the FMM. The dicing factor describes the contrast in resolution between the model slowness field and the finer grid used in the FMM. For example, with the slowness field parameterised with 28 nodes in depth, a dicing factor of 2 in this direction produces a computational grid of $(28-1)\times 2+1=55$ nodes. The computational grid for the FMM was initially set with a $2\times 2\times 2$ dicing factor (2,193,345 grid nodes). This factor was increased to $3\times 3\times 3$ (7,333,096 grid nodes) and $4\times 4\times 4$ (17,300,153). In addition to being computationally expensive (6 iterations increased from 107 minutes to 439 minutes and 1367 minutes respectively), the resolution of the images showed no significant improvement.

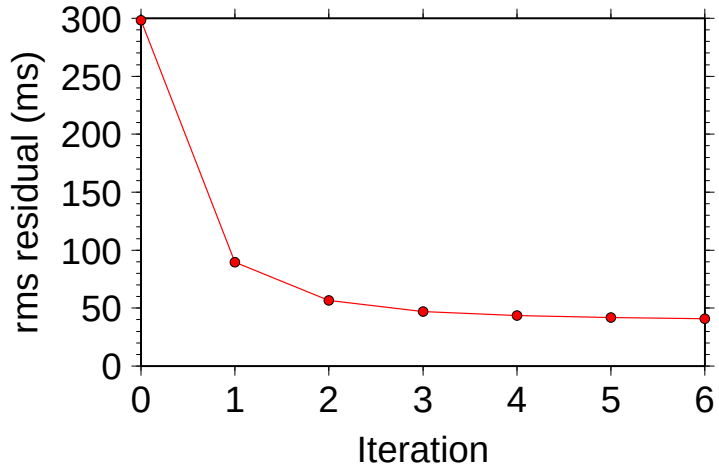

Figure 3.5: Residual reduction from the iterative non-linear inversion.

To assess the effect of regularisation on the inversions, a second derivative smoothing operator ($\nabla^2 s$) was applied at various levels to investigate the tradeoff between model roughness and data fit for each inversion. The final model roughness (M_{rough}) was calculated for each of the interpolated models using the same finite difference approximation of the Laplacian operator, which for a grid with regular spacing is,

$$M_{rough}=\frac{\sum_{i=2}^{N_\phi-1}\sum_{j=2}^{N_\theta-1}\sum_{k=2}^{N_r-1} dp_{ijk}+dt_{ijk}+dr_{ijk}}{(N_\phi-2)(N_\theta-2)(N_r-2)} \tag{3.16}$$

with N the number of interpolated nodes in either the ϕ, θ or r direction and,

$$dp_{ijk}=\frac{s(k,j,i+1)-2s(k,j,i)+s(k,j-1,i)}{((r_k sin\theta)u_\phi)^2} \tag{3.17}$$

$$dt_{ijk}=\frac{s(k,j+1,i)-2s(k,j,i)+s(k,j-1,i)}{(r_k u_\theta)^2} \tag{3.18}$$

$$dr_{ijk} = \frac{s(k+1,j,i) - 2s(k,j,i) + s(k-1,j,i)}{u_r^2} \tag{3.19}$$

where u is the spacing between interpolated nodes in either the ϕ, θ or r direction, s is the percent velocity anomaly for the linear inversion and the absolute velocity anomaly in the iterative non-linear inversion.

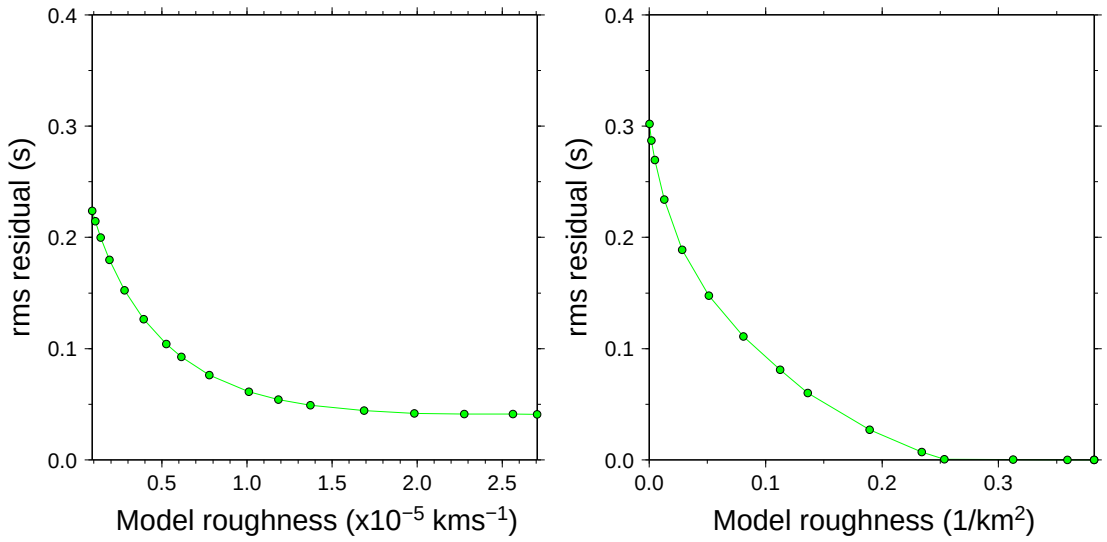

(a) (b)

Figure 3.6: Tradeoff between model roughness and final residual for: (a) the iterative non-linear inversion; and (b) the linear inversion.

The tradeoff between model roughness and data fit for each model is shown in figure 3.6. The tradeoff demonstrates that the linear tomography of VanDecar et al. (1995) is able to fit the synthetic data much better than the non-linear iterative inversion of Rawlinson et al. (2006). Even with moderate regularisation, the linear tomography is still able to produce a smaller final residual, than the iterative non-linear tomography with no regularisation.

3.4.6 Summary

This chapter introduced the seismic tomography method of VanDecar et al. (1995), which is subsequently used to invert the relative arrival-time residuals observed within the Carpathian-Pannonian region.

Using identical source-receiver distributions, the effectiveness of this tomographic method was compared to that of the iterative non-linear method of Rawlinson et al. (2006). In principle, an accurate 3-dimensional wave-front tracking scheme should be capable

of providing better resolved solutions than a method that assumes ray-paths computed through *iasp91*. The non-linear iterative method, however, seems to introduce a relatively greater level of noise in the inverted solution, than the linear inversion. Whether this additional noise is a consequence of using the fast marching method in place of ray-tracing, or using the subspace inversion method in place of a conjugate gradient method is not clear at this time. Based on this comparison, the VanDecar et al. (1995) tomographic code is used in subsequent calculations presented in this thesis.

Chapter 4

Upper-mantle P-wave velocity models

4.1 Overview

In this chapter, I present the results of the inversion of the P-wave relative arrival-time residuals. The robustness of the tomographic model is initially tested with different regularisation, and depth parameterisation. I assess the resolution of the model by using sensitivity tests for a variety of synthetic checkerboard models. The preferred model solution is then presented, before investigating the impact of the station terms on the inversion images.

The tomographic models follow a naming convention, where PCBP indicates a P-wave inversion of observed data. The model PCBPS is the preferred model, where the 'S' indicates station terms have been applied in the inversion. For the sensitivity tests, PCMS is used to indicate a P-wave checkerboard model where station terms have been applied. Dashed lines on the vertical cross-sections show the 410 km and 660 km discontinuities.

In addition to the tomographic images presented in this chapter, a video through the preferred P-wave model (PCBPS) is included on the supplementary CD (see appendix D).

4.2 Effect of regularisation

To compensate for poorly constrained model parameters, the solution is regularised by minimising the spatial gradients of the model - using a smoothing ($\nabla^2 s$) and flattening (∇s) operator (as described in section 3.3.2). The trade-off between fitting the data and

producing a smooth model is determined by the choice of λ_s and λ_f in (3.7) and (3.8).

One method for choosing the optimal regularisation parameters (λ_s, λ_f), is to construct synthetic models such as the checkerboard tests in section 4.4; using the same set of ray-paths used in the observed dataset. The synthetic relative arrival-time residuals can be inverted using a range of regularisation parameters, to assess how well the model is recovered in each case. By adding random noise to the synthetic travel-times, the regularisation parameters required to suppress spurious structure in the recovered model can be estimated. In general, the inversion should not aim to reduce the rms residual below the level of estimated data noise.

A trade-off curve between model roughness and data fit can be constructed by running multiple inversions with various regularisation parameters. Although somewhat *ad hoc* (Gubbins, 2004), a 'knee' in the tradeoff curve can reveal the optimum regularisation parameter, though it is often difficult to define such a point objectively. With only one regularisation constraint, the construction of the tradeoff curve is relatively straightforward. However, with both a smoothing and flattening operator, optimal values for both must be jointly estimated.

One approach for choosing multiple regularisation parameters is to construct multiple tradeoff curves by varying only one regularisation parameter at a time (e.g. Rawlinson et al., 2006). With the first parameter fixed, the second regularisation parameter can be varied, until a model producing a similar data fit is found. The first parameter can then be varied again with the second parameter fixed, to check whether the initial choice was suitable. This process can be iterated until confident that the optimum regularisation parameters have been chosen.

Although computationally time consuming, a more robust method, is to produce a contour map of data misfit on a 2D region defined by the two regularisation parameters.

The following tests were made using the full P-wave CBP inversion. Figure 4.1 shows how the ratio of smoothing to flattening factors (λ_s/λ_f) affects the tradeoff between model roughness and the rms residual. The influence of λ_f on the tradeoff curve is minimal; therefore a constant ratio was used in subsequent inversions. Applying the regularisation operators separately, with the other one set to zero, found smoothing and flattening parameters which seperately produced an identical rms solution residual for $\lambda_s/\lambda_f = 18.67$.

The resulting tradeoff curve obtained by varying both flattening and smoothing parameters in this ratio (table 4.1) is shown in figure 4.2. Three depth slices at 300 km are shown inset where λ_s = 3500, 14000 and 56000. The models show systematic variation along the tradeoff curve: the smoothest model (top left), which has an rms residual of 0.174 s, has probably been over-smoothed and has lost significant structure. The roughest model (bottom right), which has an rms residual of 0.095 s, whilst still close to the 'knee' of the curve has introduced small-scale structure throughout the model, which may be spurious. Although somewhat subjective, I suspect that at least some of this small-scale structure is unrealistic and represents the fitting of noise to the model. The preferred model as indicated by the red point (figure 4.2), provides a compromise; resulting in a smooth model, whilst still containing structure at a scale shown to be resolvable by synthetic tests.

The tradeoff curve is generally consistent with the noise estimate in the data. Estimated at 0.04 s (section 2.6.4), the tradeoff curve shows the reduction flattening off close to this level. The rms residual of the preferred model is ∼3 times greater than the noise estimate, but the inhomogeneous distribution of stations necessitates a cautious choice of regularisation parameters.

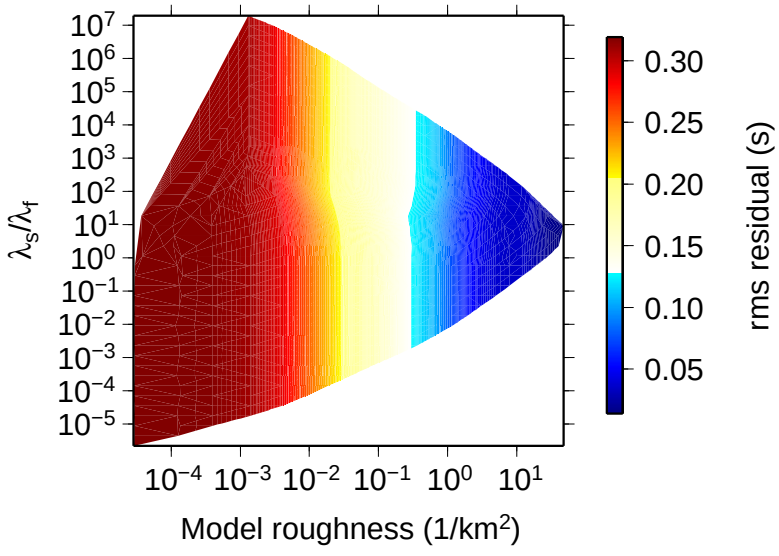

Figure 4.1: Map of rms solution residual as a function of model roughness and the ratio of smoothing (λ_s) to flattening (λ_f) operators.

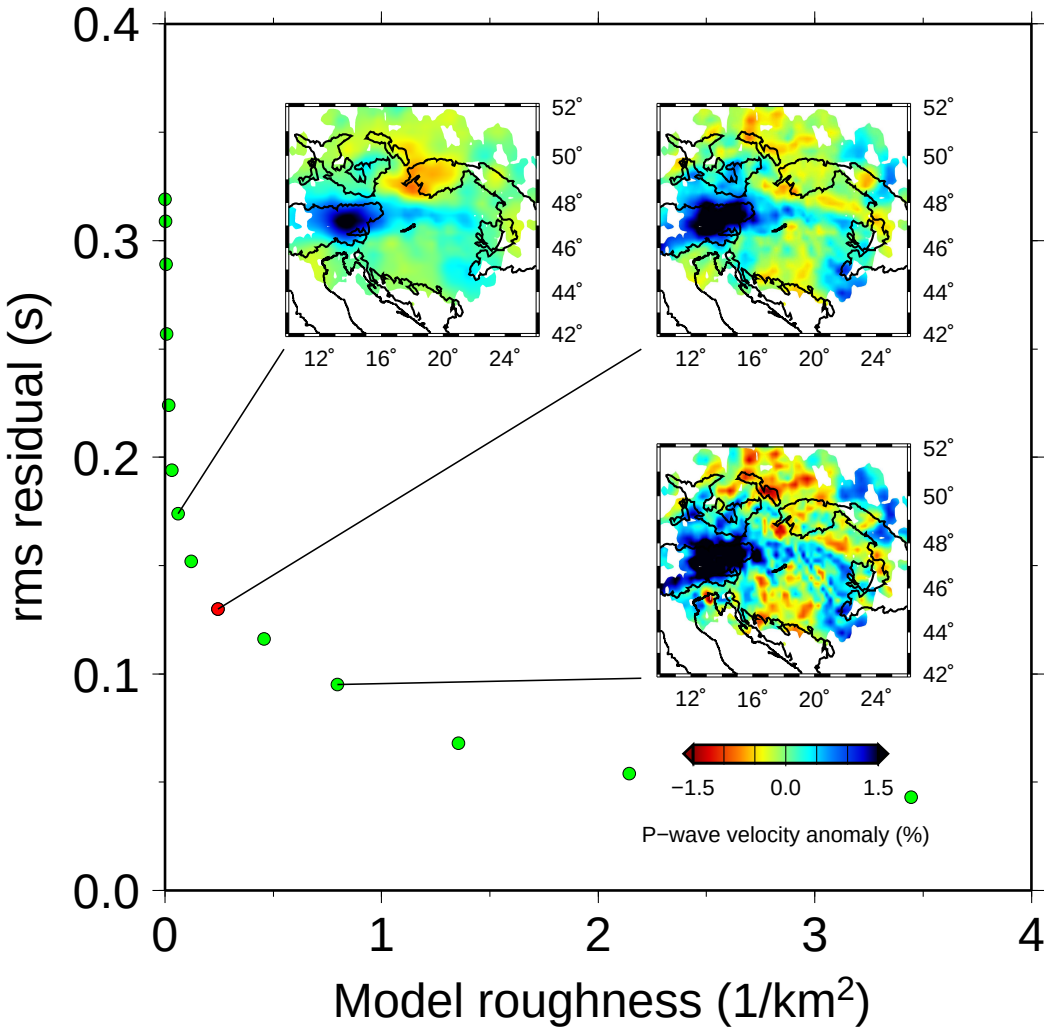

Figure 4.2: Tradeoff between model roughness and rms solution residual. The images show the 300 km depth slice at three different locations on the tradeoff curve. The red point shows the preferred model (PCBPS). The regularisation parameters used are shown in table 4.1.

λ_s	λ_f	rms residual (s)
437.5	23.438	0.043
875	46.875	0.054
1750	93.75	0.068
3500	187	0.095
7000	375	0.116
14000	**750**	**0.130**
28000	1500	0.152
56000	3000	0.174
112000	6000	0.194
224000	12000	0.224
448000	24000	0.257
896000	48000	0.289
1792000	96000	0.309
28672000	1536000	0.319

Table 4.1: Table showing the smoothing and flattening parameters (λ_s and λ_f respectively) and the corresponding rms residual, used in the construction of the tradeoff-curve in figure 4.2. The parameters of the preferred model (PCBPS) are highlighted.

4.3 Effect of model depth

The tomographic model should ideally cover a region where the ray-paths start to diverge from an individual seismic source and thus contribute to differences in relative travel-times. For teleseismic P, the depth at which this occurs is about equal to the network aperture (Evans & Achauer, 1993), although the model depth may be reduced further, commonly to 2/3 the aperture of the network (Bastow, 2005). By imposing a model too shallow, velocity anomalies external to the model region will have contributed to travel-time differences and will be mapped into the model. However, increasing the model to depths where ray-paths have not diverged, can result in reduced amplitude of the anomalies throughout the model and the potential loss of structure (Arrowsmith, 2003). In the case of the CBP network, the stations are also unevenly spaced because of the use of permanent and temporary stations, creating variable resolution within the overall network aperture. The largest distance between any two stations is 888 km between DIVS in Serbia and NKC in the Czech Republic.

Following a similar approach to Hammond (2007), we can investigate the divergence of the ray-paths with depth, in order to choose an optimal depth of model. With increasing depth the Fresnel zone increases in diameter; by calculating the distance between pierce points and estimating the diameter of the Fresnel zones for each station pair per event,

we can quantify the divergence of rays at each depth interval for a given dataset.

The radius (R) of the Fresnel zone for a ray is,

$$R = \left(\frac{\lambda L}{2}\right)^{\frac{1}{2}} \tag{4.1}$$

where λ is the wavelength and L is the raypath length from the receiver to a given depth.

For teleseismic earthquakes, the attenuation over teleseismic distances followed by band-pass filtering produces a near monochromatic signal frequency f, of approximately 1 Hz (Evans & Achauer, 1993). For a particular depth h, $\lambda = V_p/f$, where V_p is obtained from the *iasp91* reference Earth model.

Rather than using a linear ray-path approximation as used by Hammond (2007), the total path length (L_{jk}) for the j^{th} ray is estimated using the ray length in the k^{th} layer of the *iasp91* velocity model, with a layer thickness of d,

$$L_{jk} = \sum_k \frac{d_k}{cos\,\theta_{jk}} \tag{4.2}$$

where

$$sin\,\theta = \frac{pV_p}{r} \tag{4.3}$$

where θ is the incidence angle of the P-wave, p is the ray parameter and r is the Earth's radius.

For a given source and each station pair, the radii of the Fresnel zones at the base of the model are calculated using equation (4.1). The pierce points were found using the TauP toolkit (Crotwell et al., 1999) and the distance (at that depth) between each pair of pierce points calculated. Where the distance between the pierce points is less than the sum of the Fresnel zone radii, the two rays are approximately sampling the same region and are counted in this sample as having not diverged.

The number of rays that have diverged - and thus are sampling different regions before entering the model - was calculated for all station pairs for a model depth up to 1500 km. Figure 4.3 shows that for model depths greater than 500 km, the rays are generally not diverged before entering the solution region. However, this criterion for ray divergence is fairly conservative using as it does the sum of both Fresnel zone radii, as shown by the following test.

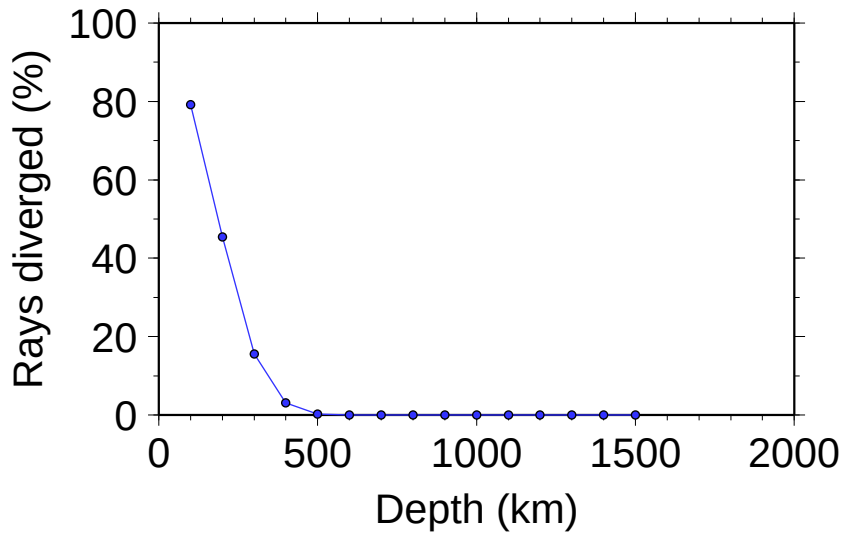

Figure 4.3: Percentage of diverged rays at the base of the model for all 225 P-wave events, as a function of the depth of the model.

To assess whether there are significant changes to the inversion solution with model depths greater than 500 km, inversions were completed for 700 km, 850 km and 1000 km depth models using identical regularisation parameters ($\lambda_s = 14000$, $\lambda_f = 750$). Figure 4.4 shows four depth slices through these three models. The overall structure of the models remains largely unchanged. However, the anomaly amplitudes in the 700 km model are greater towards the base of the model, which suggests that velocity anomalies below 700 km are being mapped into the model above 700 km. This interpretation is supported by the vertical cross-sections (figures 4.5, 4.6).

The 850 km and 1000 km inversion show very little structural differences above about 700 km. The comparison of 850 km and 700 km inversions suggests however, that significant velocity variation below 700 km is mapped up into the MTZ, producing artificially high anomaly amplitudes in those depths. A better fit to the data is also reflected in the final solution residuals, which show a reduction in rms residual from 0.136 s for the 700 km depth model to 0.130 s for the 850 km depth model (figure 4.7). By extending the parameterisation to 1000 km, the MTZ anomalies are reduced in amplitude, as they are distributed over a greater depth interval along the deeper ray-paths. The 850 km parameterisation is therefore preferred in that a greater model depth does not deliver significant structural change and is accompanied by only a small reduction in the final rms residual (0.130 s to 0.128 s - figure 4.7).

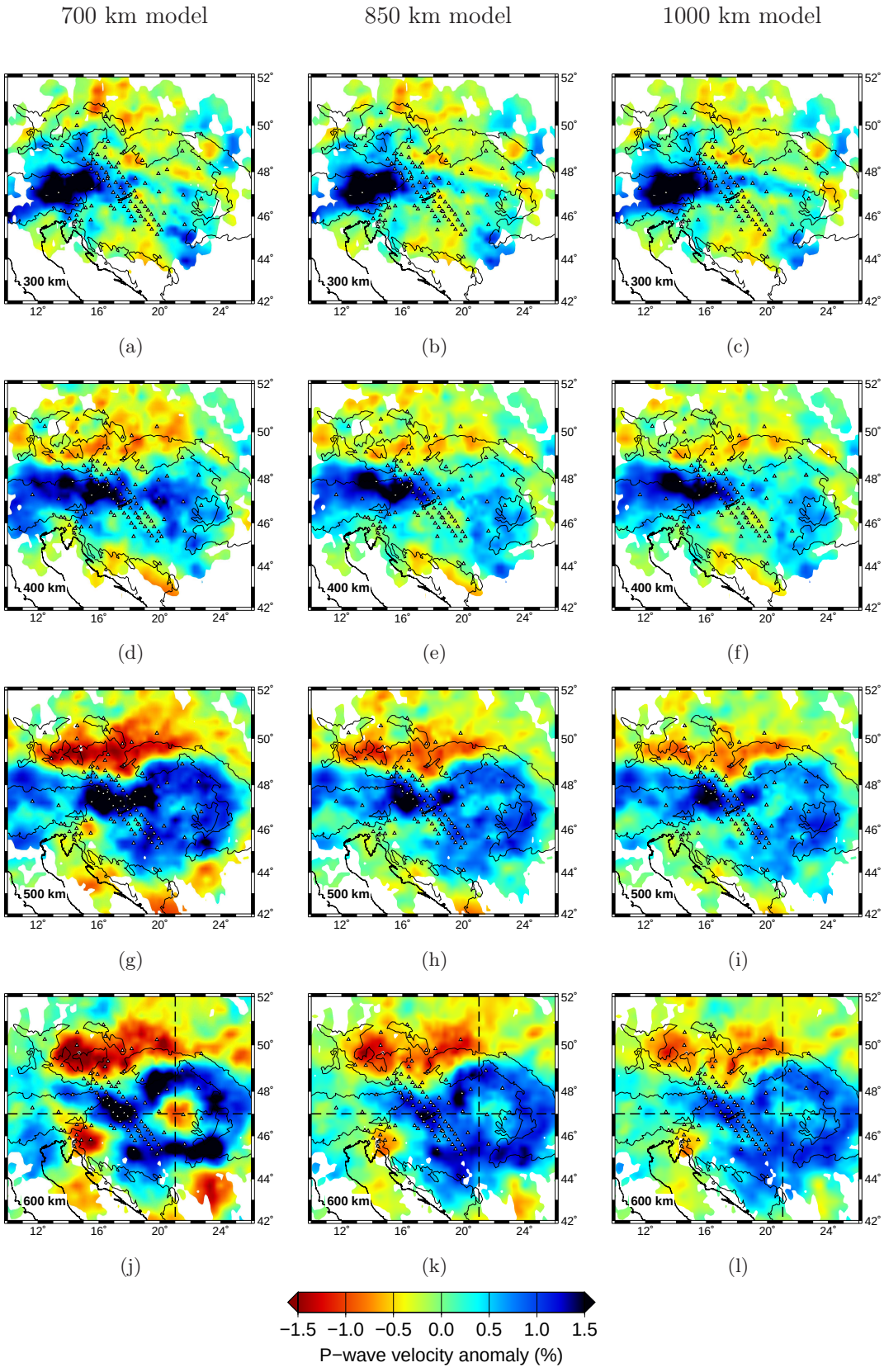

Figure 4.4: Depth slices through models parameterised to 700 km, 850 km and 1000 km depth. Regularisation parameters are identical for each model. Dashed lines in the 600 km depth slices mark the position of the cross-sections shown in figures 4.5 and 4.6. Velocity anomalies are relative to *iasp91*.

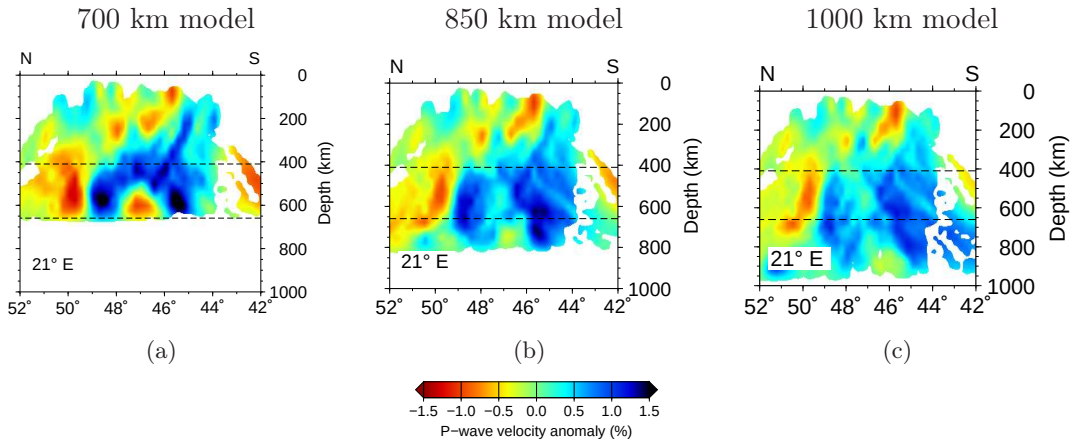

Figure 4.5: North-south cross-sections at 21°E longitude, through models parameterised to 700 km, 850 km and 1000 km depth. The same solution is shown in figure 4.4.

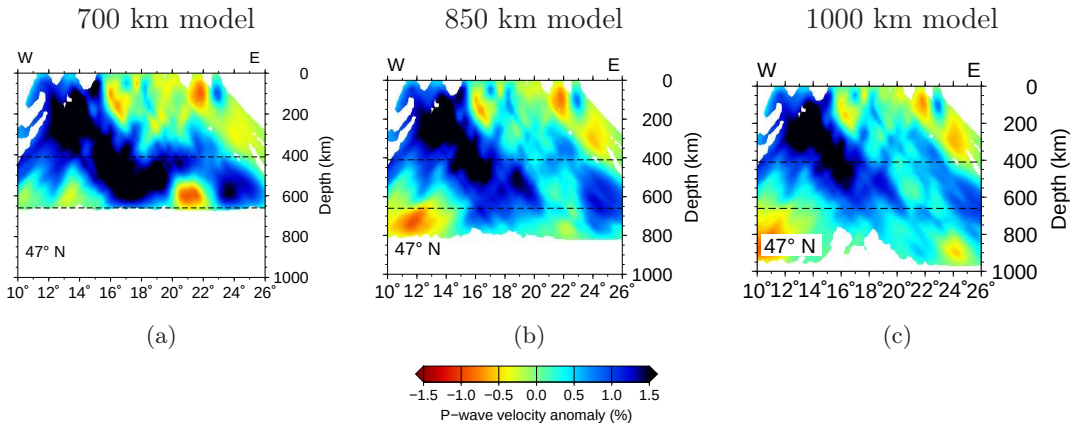

Figure 4.6: East-west cross-sections at 47°N latitude, through models parameterised to 700, 850 and 1000 km depth. The same solution is shown in figure 4.4.

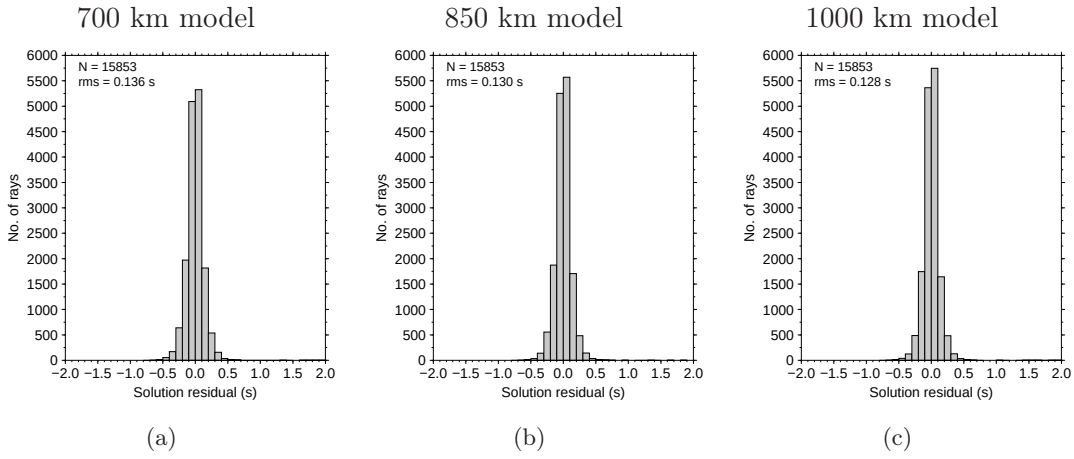

Figure 4.7: Histograms of the final residuals after the inversion procedure for all 3 depth models shown in figures 4.4–4.6. The rms residual is reduced from 0.136 s to 0.130 s to 0.128 s for the 700 km, 850 km and 1000 km models respectively.

4.4 Resolution

Although the relative arrival-time residuals for the inversion were assessed for possible errors, artefacts are still likely within the tomographic images. Poor ray-path coverage leads to inadequate sampling, and regularisation constraints can result in smoothing of the velocity structure, which complicates the interpretation.

The event distribution used in the P-wave tomography is shown as a histogram of back-azimuths and epicentral distances in figure 4.8 (see also figure 2.4(b)). With sampling of most back-azimuths, the lateral resolution of the tomography should be good where the station density is high. However, with the distance range corresponding to angles of incidence from 13.8°–27.5°, and with a modal angle of incidence at 16.6°, the ray-paths are all relatively steep. This limits resolving power in the vertical, and produces smearing of apparent structure along the ray-paths.

Although not taking into account the degree at which ray-paths are crossing, areas with less than 5 rays per 25 km^3 are blanked out in the tomographic images in order to avoid interpreting areas with poor ray coverage.

Resolution has been assessed using synthetic checkerboard tests like those described in section 3.4. Using an input model with known velocity variations, synthetic travel-times are computed using the same set of ray-paths implied by the observed data. By inverting these synthetic data with the same regularisation as the observed data, the accuracy of the inversion method can be judged from the fit between the input and recovered models.

Checkerboard models are limited in their diagnostic value. In synthetic data, phase misidentification and systematic errors, arising for example from variation of crustal structure, or velocity variation outside the solution model, are not present. Because the synthetic data are consistent with the ray-paths in a linearised inversion, the effect of the linearisation is also not accounted for (van der Hilst et al., 1993). However, the checkerboard models still provide a useful indication of spatial variations in resolution for a given data distribution, noting that recovery of small-scale structure does not always ensure that recovery of larger-scale structure will be successful (Lévêque et al., 1993).

The P-wave checkerboard model is constructed by defining slowness anomalies (Δs) at each node using Gaussian spheres,

$$\Delta s = s_a e^{-|\mathbf{x}-\mathbf{x}_o|^2/\sigma_a^2} \tag{4.4}$$

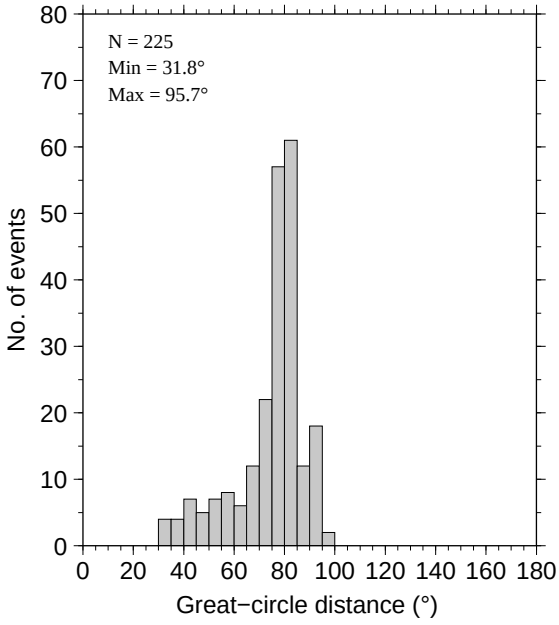

(a)

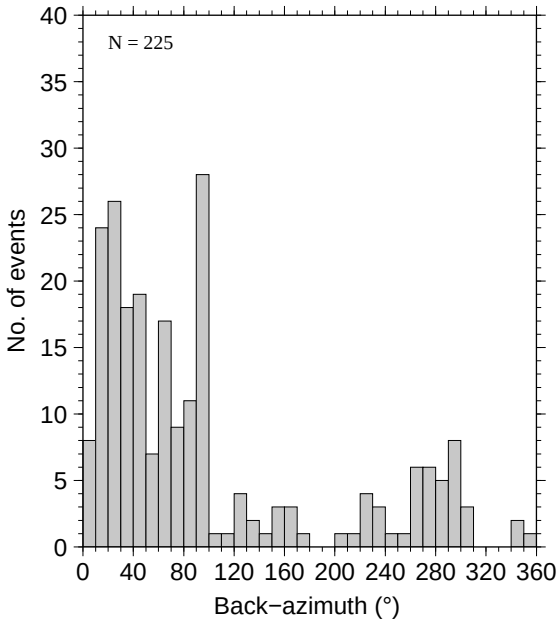

(b)

Figure 4.8: Event distribution for the P-wave tomography relative to a point in the middle of the network, sorted by: (a) great-circle distance; (b) back-azimuth distribution.

where s_a is the maximum slowness anomaly of $\pm 3\%$ from the reference model, $|\mathbf{x} - \mathbf{x}_o|$ is the distance from the maximum anomaly to the node, and σ_a is a scaling factor for the anomaly size. Adjacent anomalies alternate from positive to negative. Due to the slowness anomalies being defined at nodes, the interpolated model differs slightly from the description of (4.4), with possible distortion of the anomalies.

Three different checkerboard models are described here, to assess how well different sized anomalies can be recovered. In checkerboard model 1 (PCMS1) (figures 4.9–4.11), σ_a is 45 km, with anomalies defined every 200 km in depth from 100–700 km; and every 2° in both latitude and longitude from 42°–52° N and 8°–28° E respectively. In the second model (PCMS2) (figures 4.12–4.14), σ_a was increased to 95 km, with anomalies at 100 km, 400 km and 700 km depth, spaced every 4° in longitude and 3° in latitude. For the third model (PCMS3) (figures 4.15–4.16), a mixture of the two length scales are used: the anomaly size and spacing in PCMS1 are used from 100 to 300 km depth, then at 600 km a layer of spherical anomalies are set using the PCMS2 anomaly size spacing.

Synthetic travel-times were computed by ray-tracing through the checkerboard model, assuming an *iasp91* P-wave velocity distribution, and multiplying the Fréchet derivatives by the slowness anomalies (equation (3.3)). To provide a more realistic data measurement, random noise with a Gaussian distribution was added to these travel-times. The standard deviation of the noise was set to the standard error estimated for the P-wave observed data (0.04 s - see section 2.6.4). In inverting the synthetic travel-times, the preferred regularisation parameters ($\lambda_s = 14000$, $\lambda_f = 750$) determined in section 4.2 were applied for all models and station terms were used.

Similar to Tilmann (1999), I calculate the normalised correlation between the synthetic model and the solution model to quantitatively describe how well the inversion has recovered the structure. However, as interpretation involves using the interpolated model, the correlation is calculated between individual 2D images from the interpolated grid, rather than simply correlating the inverted nodes for the whole 3D model. The correlation is defined between the synthetic model (M) and solution model (M') for each figure as,

$$\begin{aligned} corr(M, M') &= \frac{\sum_j r_j \Delta s_j \Delta s'_j}{\sqrt{\sigma(M)\sigma(M')}} \\ \sigma(M) = \textstyle\sum_j r_j \Delta s_j \Delta s_j, &\qquad \sigma(M') = \textstyle\sum_j r_j \Delta s'_j \Delta s'_j \end{aligned} \tag{4.5}$$

where Δs_j and $\Delta s'_j$ are the slowness perturbations in the interpolated model at the j^{th}

interpolation point. r_j is set to either 1 if the ray hit count is above 5 rays per 25 km^3, or 0 if below this threshold (i.e. white areas in the figures).

The input models and inversion solutions for PCMS1, PCMS2 and PCMS3 are shown in figures 4.9–4.16. The correlation between the input and recovered models for each figure is shown in table 4.2.

With regularisation imposed on the inversion, the amplitudes of the recovered anomalies are reduced. The maximum anomaly is reduced from the input amplitude of 3%, by 1.05%, 0.5% and 0.9% for PCMS1, PCMS2 and PCMS3 respectively. The final solution models show a reduction in the rms residual by 83% for PCMS1, 89% for PCMS2 and 87% for PCMS3. The residual reduction corresponds well to the image correlation values given in table 4.2, indicating better resolution of the larger-scale anomalies. For all models there is an increase in correlation with depth, and structure is best resolved to the north-east of the 3-line HST array, where ray coverage is highest. The high correlation values for the north-south cross-sections at 24° E for each model are slightly misleading; the lack of rays above the hit threshold in the upper 150 km means the unresolvable crust and upper-most mantle (from the general lack of *crossing* rays), at this longitude, does not contribute to the correlation value.

In horizontal section (figures 4.9, 4.12, 4.15), each model has recovered the individual anomalies, without major smearing, wherever ray coverage is adequate. In vertical cross-section (figures 4.10, 4.11, 4.13, 4.14, 4.16), smearing (or leakage) of anomalies is evident between some diagonally adjacent anomalies, and is more prominent in the east-west than north-south cross-sections. Despite the leakage, the peaks of the individual anomalies are still interpretable. PCMS3 shows the effect of having anomalies of the same sign beneath each other (figure 4.16). Increased leaking is observed in the anomalies in these vertical sections, but the peak anomalies are again correctly located where ray-coverage is adequate.

Analysis of the residuals in the checkerboard tests also provides confidence in the regularisation choice. The 89% reduction of the rms residual in PCMS2 (figures 4.12–4.14) to 0.039 s was achieved with the same regularisation parameters as described for the preferred model in section 4.2. Adding Gaussian distributed noise with a standard deviation of 0.04 s to the synthetic travel-times, results in a model which is not significantly contaminated by noise when these regularisation parameters are used.

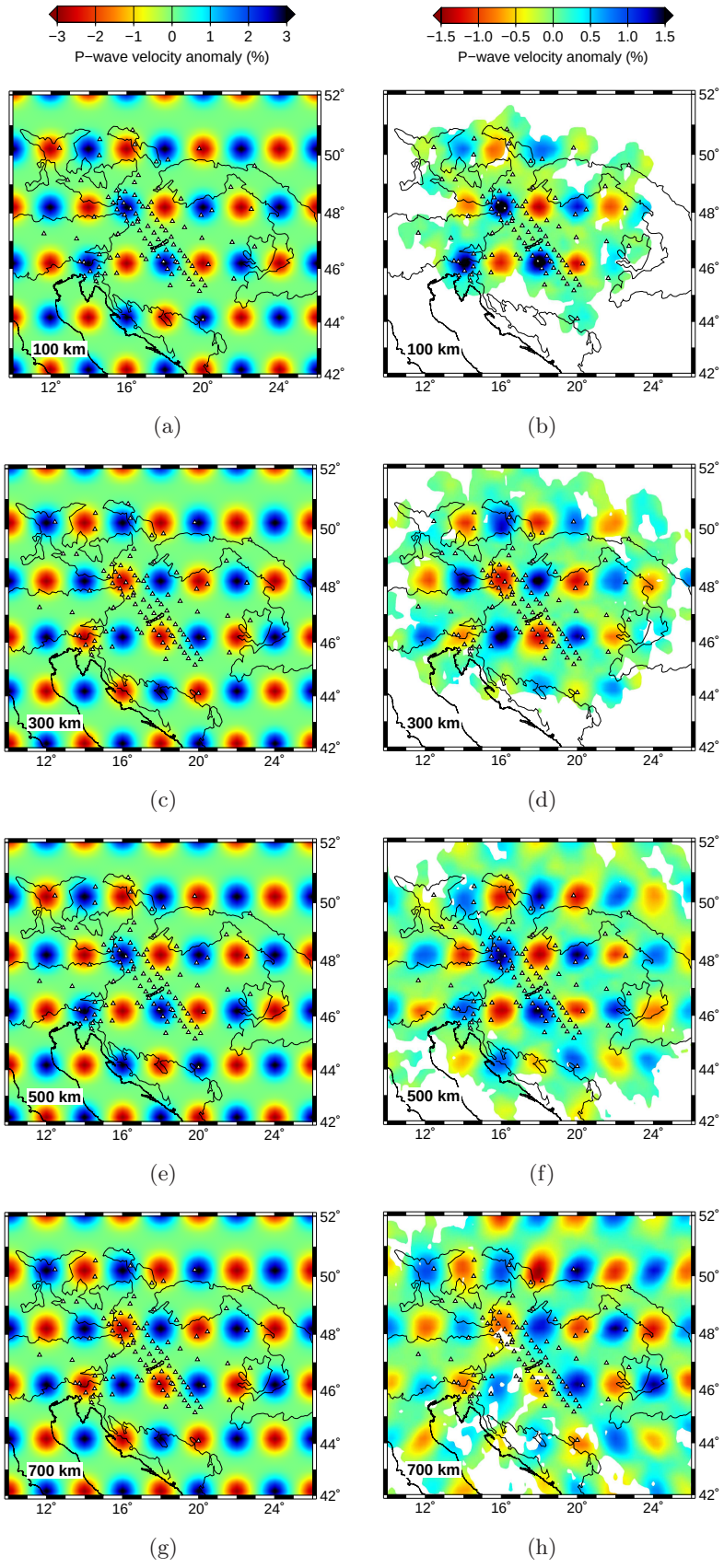

Figure 4.9: PCMS1: Depth slices through the synthetic checkerboard model (left) and the recovered model (right) after inverting the synthetic data, at 100 km, 300 km, 500 km and 700 km depth.

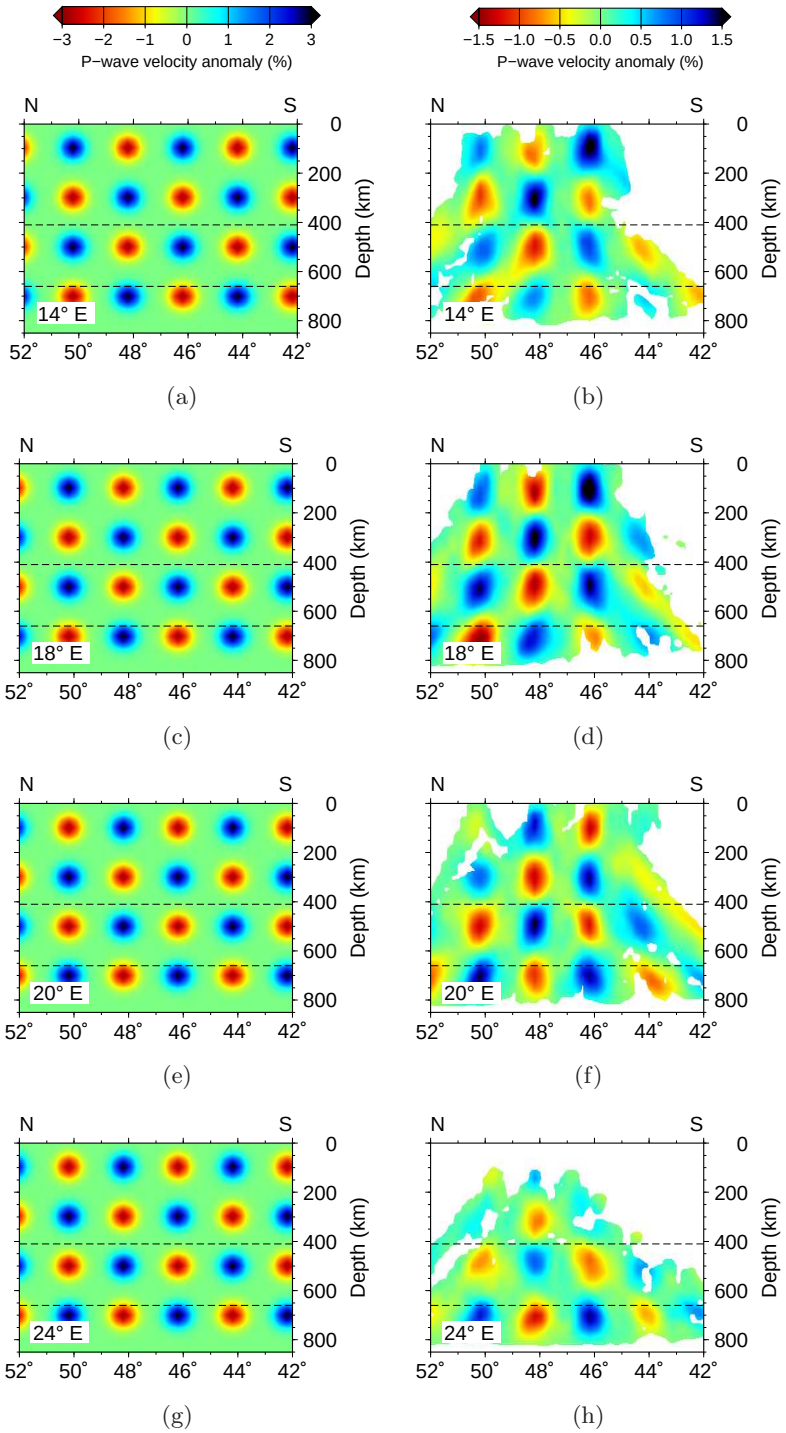

Figure 4.10: PCMS1: North-south cross-sections through the synthetic checkerboard model (left) and the recovered model (right) after inverting the synthetic data, at 14° E, 18° E, 20° E and 24° E.

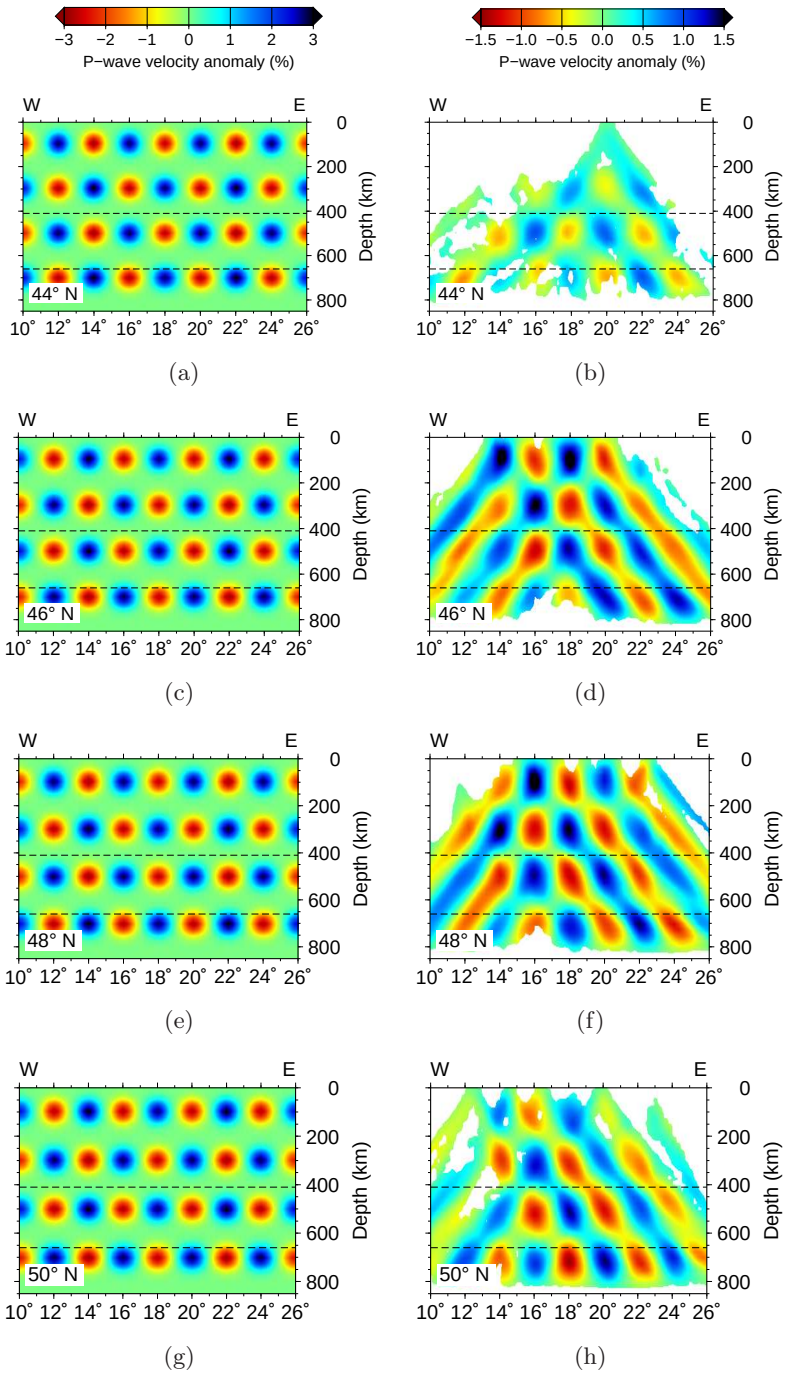

Figure 4.11: PCMS1: East-west cross-sections through the synthetic checkerboard model (left) and the recovered model (right) after inverting the synthetic data, at 44° N, 46° N, 48° N and 50° N.

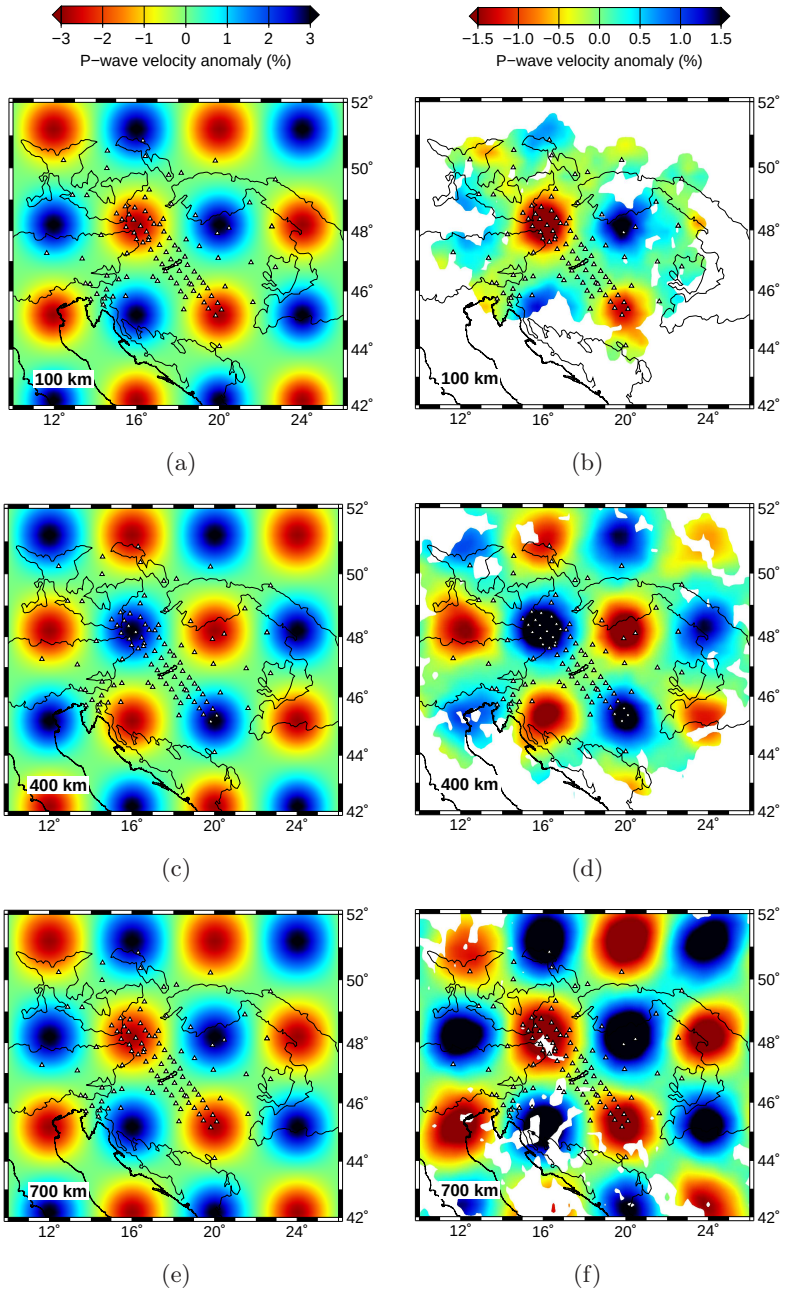

Figure 4.12: PCMS2: Depth slices through the synthetic checkerboard model (left) and the recovered model (right) after inverting the synthetic data, at 100 km, 400 km and 700 km depth.

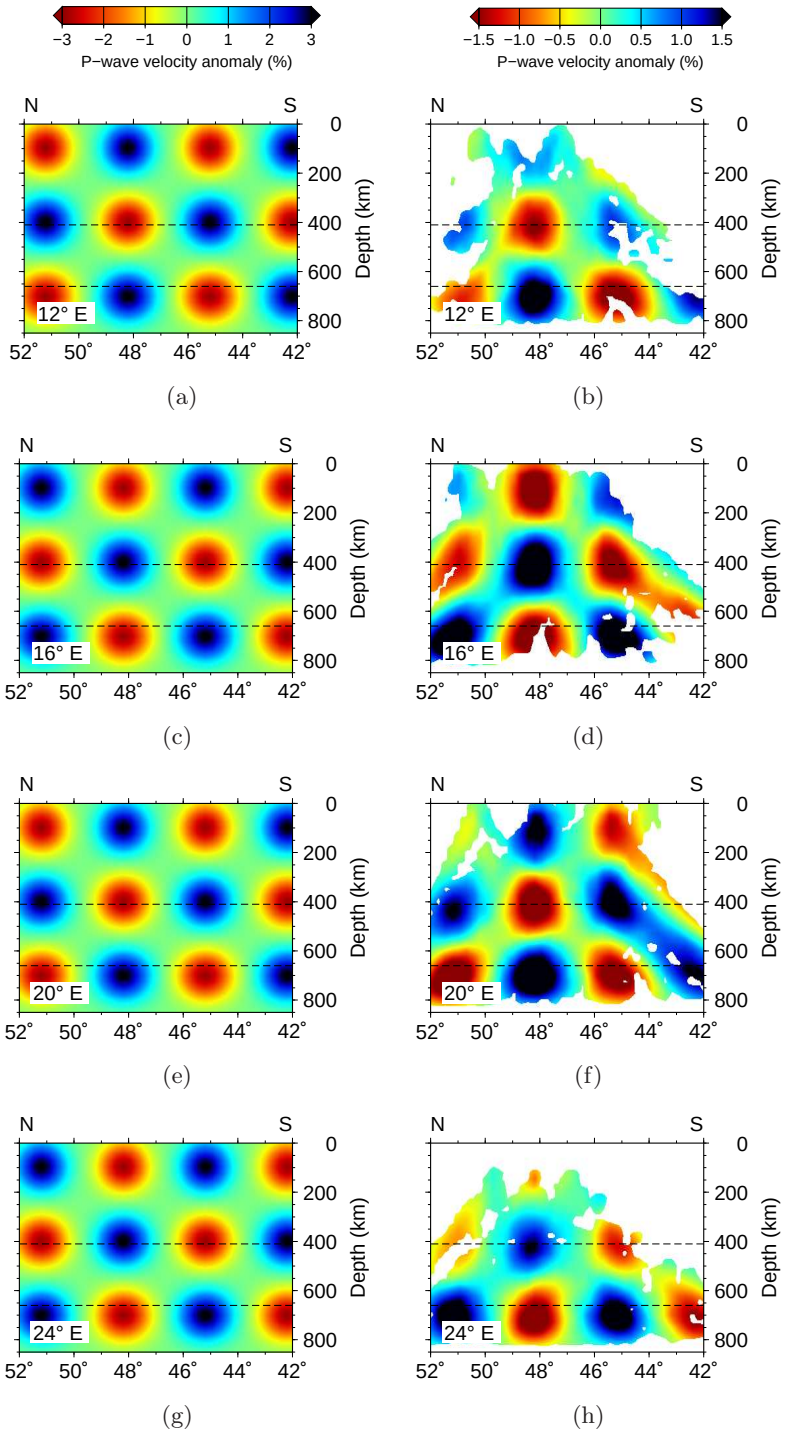

Figure 4.13: PCMS2: North-south cross-sections through the synthetic checkerboard model (left) and the recovered model (right) after inverting the synthetic data, at 12° E, 16° E, 20° E and 24° E.

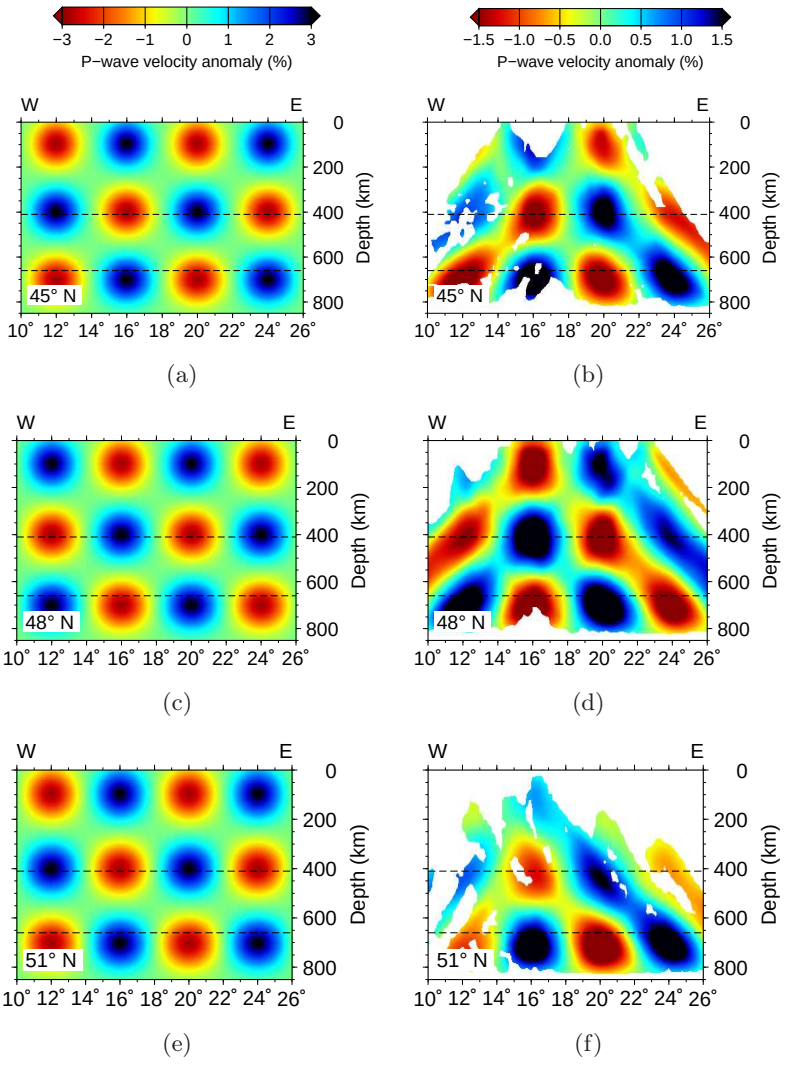

Figure 4.14: PCMS2: East-west cross-sections through the synthetic checkerboard model (left) and the recovered model (right) after inverting the synthetic data, at 45° N, 48° N and 51° N.

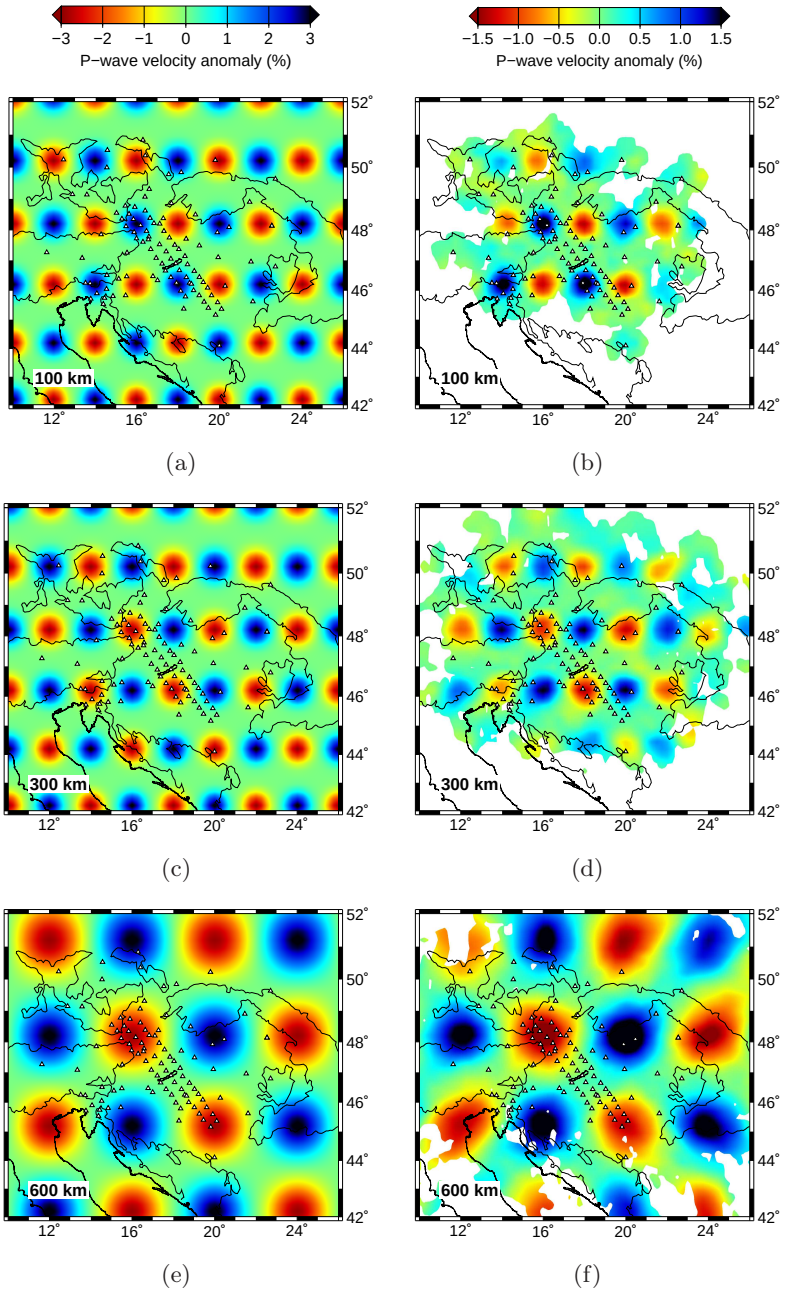

Figure 4.15: PCMS3: Depth slices through the synthetic checkerboard model (left) and the recovered model (right) after inverting the synthetic data, at 100 km, 300 km and 600 km depth.

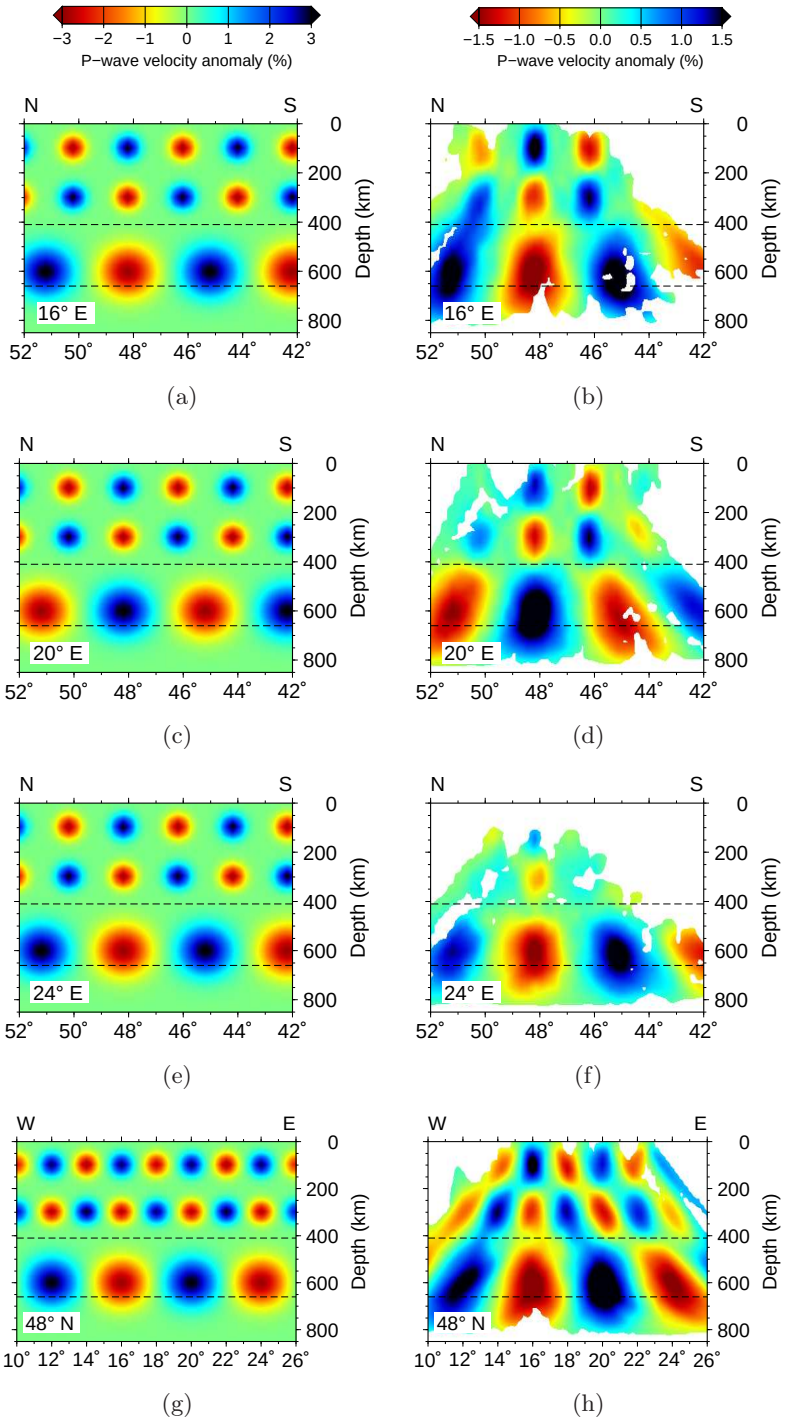

Figure 4.16: PCMS3: Cross-sections through the synthetic checkerboard model (left) and the recovered model (right) after inverting the synthetic data, at 16° N, 20° N, 24° N and 48° E.

Model name	Figures	Plot description	Correlation
PCMS1	4.9(a),(b)	100 km depth	0.87
PCMS1	4.9(c),(d)	300 km depth	0.90
PCMS1	4.9(e),(f)	500 km depth	0.90
PCMS1	4.9(g),(h)	700 km depth	0.91
PCMS1	4.10(a),(b)	N-S at 14° E	0.84
PCMS1	4.10(c),(d)	N-S at 18° E	0.86
PCMS1	4.10(e),(f)	N-S at 20° E	0.84
PCMS1	4.10(g),(h)	N-S at 24° E	0.86
PCMS1	4.11(a),(b)	E-W at 44° N	0.82
PCMS1	4.11(c),(d)	E-W at 46° N	0.80
PCMS1	4.11(e),(f)	E-W at 48° N	0.82
PCMS1	4.11(g),(h)	E-W at 50° N	0.80
PCMS2	4.12(a),(b)	100 km depth	0.89
PCMS2	4.12(c),(d)	400 km depth	0.95
PCMS2	4.12(e),(f)	700 km depth	0.98
PCMS2	4.13(a),(b)	N-S at 12° E	0.94
PCMS2	4.13(c),(d)	N-S at 16° E	0.93
PCMS2	4.13(e),(f)	N-S at 20° E	0.93
PCMS2	4.13(g),(h)	N-S at 24° E	0.95
PCMS2	4.14(a),(b)	E-W at 45° N	0.93
PCMS2	4.14(c),(d)	E-W at 48° N	0.91
PCMS2	4.14(e),(f)	E-W at 51° N	0.89
PCMS3	4.15(a),(b)	100 km depth	0.84
PCMS3	4.15(c),(d)	300 km depth	0.87
PCMS3	4.15(e),(f)	600 km depth	0.97
PCMS3	4.16(a),(b)	N-S at 16° E	0.88
PCMS3	4.16(c),(d)	N-S at 20° E	0.85
PCMS3	4.16(e),(f)	N-S at 24° E	0.90
PCMS3	4.16(g),(h)	E-W at 48° N	0.87

Table 4.2: Table showing the correlation between the synthetic input model and the recovered solution images for the three checkerboard models, PCMS1, PCMS2 and PCMS3. Correlations are shown for each of figures 4.9–4.16.

4.5 P-wave tomography results

The model presented here (PCBPS) is the preferred choice after testing various levels of regularisation, with final smoothing and flattening set at $\lambda_s = 14000$ and $\lambda_f = 750$. The model depth parameterisation, which was investigated in section 4.3 is set to 850 km. The results from the synthetic sensitivity tests in section 4.4 should also be considered; anomalies on a 45 km scale were resolvable but with increased sub-vertical smearing in the east-west direction, and a reduction of the amplitude of the anomalies by at least a factor of about 1.5, although more generally by a factor of about 2 or 3. The inversion of PCBPS was run with station terms to account for unresolvable crustal structure.

The preferred inversion solution shows a final reduction in the rms residual by 71% (from 0.446 s to 0.130 s - figure 4.17). The station terms alone reduce the initial residuals by 18% (from 0.446 s to 0.365 s).

At 75 km depth in this solution (figure 4.18(a)), four localised slow anomalies within the Pannonian Basin are imaged: i) on the northern edge of the Pannonian Basin (48° N, 19.5° E), a low velocity region (-1.66%) overlies the Neogene Central Slovakian volcanics (Kovács et al., 2007); this anomaly appears to be terminated in the south at the mid-Hungarian shear zone; ii) in the eastern Pannonian Basin (47.2° N, 21.8° E), a low velocity anomaly (-0.82%) appears directly beneath the Derecske sub-basin (e.g. Corver et al., 2009); iii) in the south of the Pannonian Basin, close to the Hungarian-Serbian border (46.2° N, 20.0° E) a low velocity anomaly appears directly beneath the deepest and most rapidly subsiding Miocene NW-SE sub-basins of the Pannonian - the Békés and Makó basins. This region also corresponds with anomalously high heat flow up to 130 $mW\ m^{-2}$, relative to the regional average of 90 $mW\ m^{-2}$ (Tari et al., 1999); iv) in the west of the Pannonian Basin a similar low velocity anomaly (-1.05%) is imaged close to the Hungarian-Croatian border (46.6° N, 17.7° E), beneath the Drava depression.

The lithosphere-asthenosphere boundary (LAB) is estimated to be between 45 and 60 km deep (Tari et al., 1999) within the Pannonian Basin, so the 75 km depth slice is just below the LAB. The mantle lithosphere generally in the Pannonian Basin has undergone greater thinning than the crust (Huismans et al., 2002; Royden et al., 1983b) and the anomalies are likely to represent warmer asthenospheric upwellings associated with basin depocentre development. At 200 km (figure 4.18(b)) depth, these slow anomalies have merged and decreased in amplitude to produce a sub-circular low velocity feature, underlying the

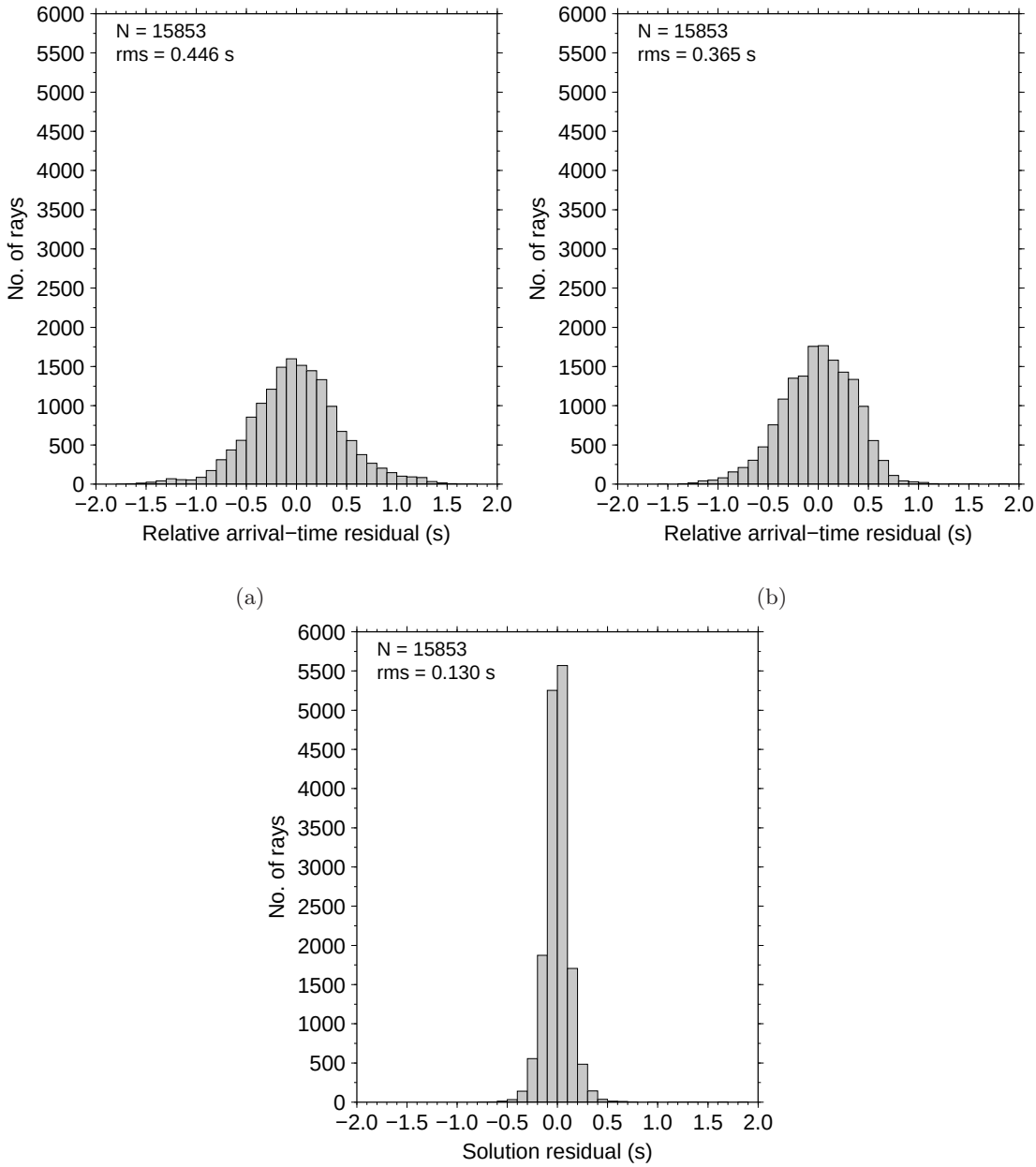

Figure 4.17: Histograms of the (a) initial residuals; (b) initial residuals with the final station terms removed; and (c) the final solution residuals.

surface expression of the Pannonian Basin.

At 75 km depth, high velocity (1.8%) features are imaged beneath the Eastern Alps and are presumably related to the continental convergence and downwelling of colder lithospheric material in the Alpine collision zone. High velocities also extend south into the Dinarides and north into the Bohemian Massif. To the east of the Bohemian Massif, a further slow anomaly (-2%) is imaged. This anomaly is larger in amplitude than those imaged in the Pannonian Basin and may be related to a broad region of slow material in the mantle transition zone below.

The Mid-Hungarian zone (MHZ) is a shear zone (Márton & Fodor, 1995) on which major displacements are inferred, accommodating the rotation of Alcapa and Tisza in the Late Oligocene and early Miocene (Kovács & Szabó, 2008). This lineament is not evident below 75 km, indicating that the MHZ is a purely lithospheric feature. The Alcapa and Tisza blocks appear decoupled at around this level from the mantle structures below.

At 200 km and 300 km depth (figures 4.18(b) & 4.18(c)), the images are dominated by the fast anomaly beneath the Eastern Alps. This high velocity feature has been previously imaged by Lippitsch et al. (2003), who interpreted it in terms of north-east dipping subduction of the Adriatic plate to depths of ∼250 km (differing in polarity from the subduction direction further west). My inversions show that this structure extends further to the east. Although a dip to the north (figure 4.19(b)) of the high velocity anomaly could be interpreted, the structure is near vertical beneath the Eastern Alps. Although a major step in crustal thickness separates the Alpine and Pannonian tectonic domains (Brückl et al., 2007), the fast anomaly is observed to continue into the Pannonian Basin region at 300 km depth (figure 4.18(c)) and into the mantle transition zone (MTZ). Figure 4.19(c), provides a north-south cross-section at 16° E, through the extended Alpine-Pannonian anomaly, showing a vertical fast structure (interpreted as mantle downwelling) extending into the MTZ, connected to the north with another fast anomaly beneath the Bohemian Massif. In figure 4.19(f), continuity with the Eastern Alps structure is shown; the anomaly extends laterally beneath the Pannonian Basin with increasing depth, but with decreased amplitude.

In the MTZ (figures 4.18(e),(f)), there is a sharp contrast (∼ 3.1% at 600 km) between a slow region to the north and the faster sub-Pannonian MTZ region. This boundary, is proximate to the Penninic-Vah-Magura suture zone at the surface (Kovács et al., 2007),

but there is no continuity beneath these surface structure features and the MTZ structure.

Within the MTZ, particularly in the 600 km depth slice, the fastest anomalies approximately follow the outline of the Carpathian mountains enclosing slower material beneath the eastern Pannonian Basin (47° N, 21.5° E), within a doughnut shaped structure. In vertical cross-section, (figures 4.19(d) & (e)), these peak anomalies could be interpreted as separate downwellings which have accumulated in the MTZ. However, the circular shape and continuous nature of the fast anomaly at 600 km suggests that the structures may have spread out laterally from a central location. Interpretation of the apparently slow material within the MTZ 'doughnut' cannot neglect the effect of topography on the 660 km velocity discontinuity. Hetényi et al. (2009) showed that this surface is depressed by up to 40 km beneath the centre of the basin. The problem of interpreting these deep velocity structures is considered further in chapter 7 by using synthetic models.

4.6 Effect of station terms

As outlined in chapter 3, in addition to slowness perturbations, the inversion solves for station terms to account for travel-time anomalies attributable to near-surface structure beneath each receiver, produced in particular by crustal thickness variations. The lack of crossing rays in the crust and uppermost mantle, dictated by the station spacing determines a depth above which velocity variation is indistinguishable from crustal thickness variation. With a mean nearest-neighbour station spacing of 42 km and as great as 131 km, this depth varies in the inversion. Station terms also provide a check on possible time offsets on individual station clocks. Any timing errors, which result in a constant offset for a station will be absorbed into this term.

The station terms produced in the inversion are shown in figure 4.20, with positive correction terms indicating delay. The three largest correction terms are 0.8 s at CBP3J in the middle of the high resolution array; and 0.7 s at both CBP2E and JAVC, between the Eastern Alps and Western Carpathians. Correction terms of this magnitude are unlikely to be due to crustal structure alone.

Considering station CBP3J as an example, the uppermost crustal velocity from *iasp91* is 5.8 $km\ s^{-1}$; incorporating an elevation correction for 528 m (h), would explain a station term of only 0.091 s.

A further adjustment to the station term can be made by including an Airy-type crustal

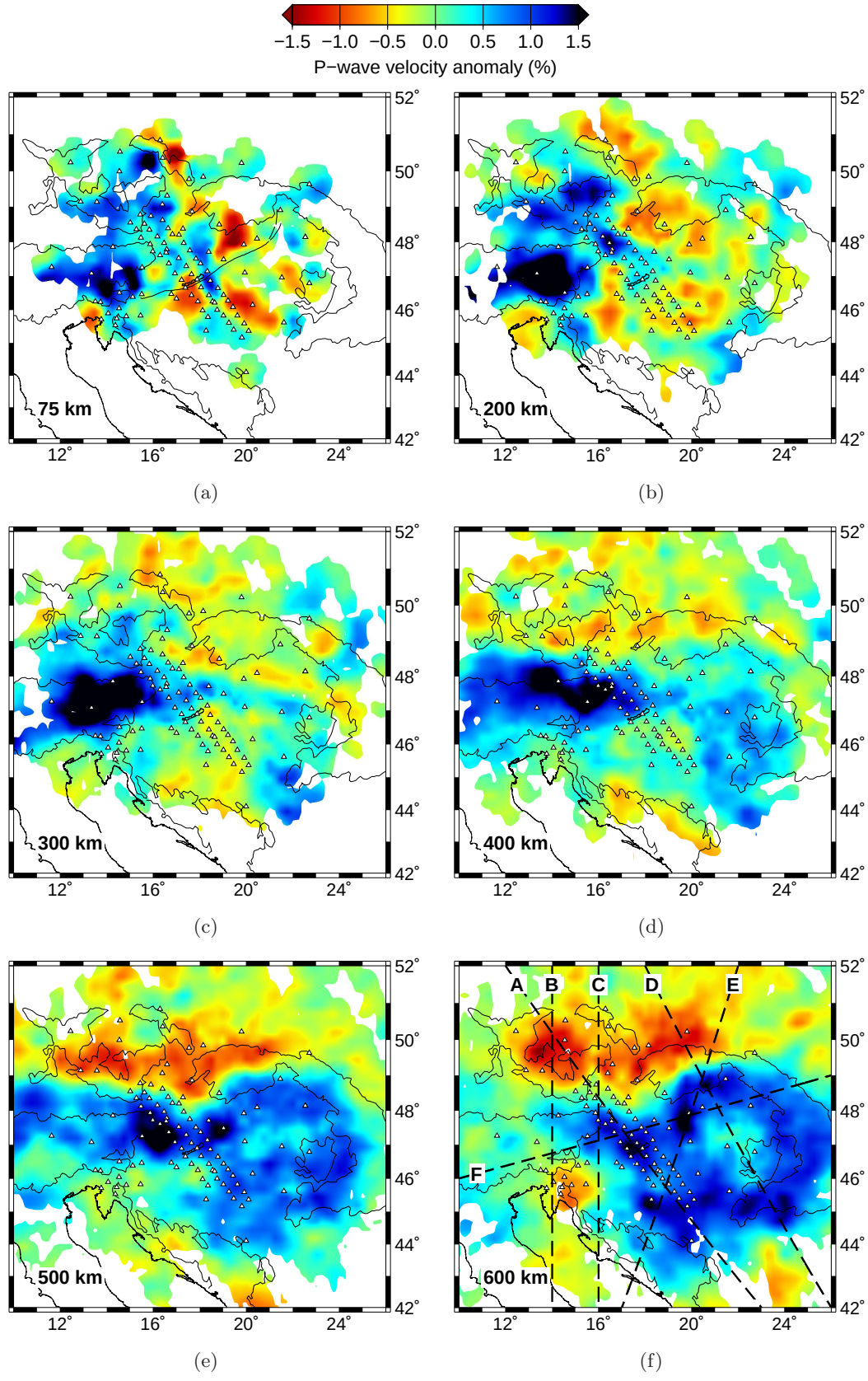

Figure 4.18: PCBPS: Depth slices through the P-wave tomographic model. The locations of stations are shown as triangles. The Mid-Hungarian Line is shown on the 75 km slice. Location of cross-sections are shown in the 600 km slice.

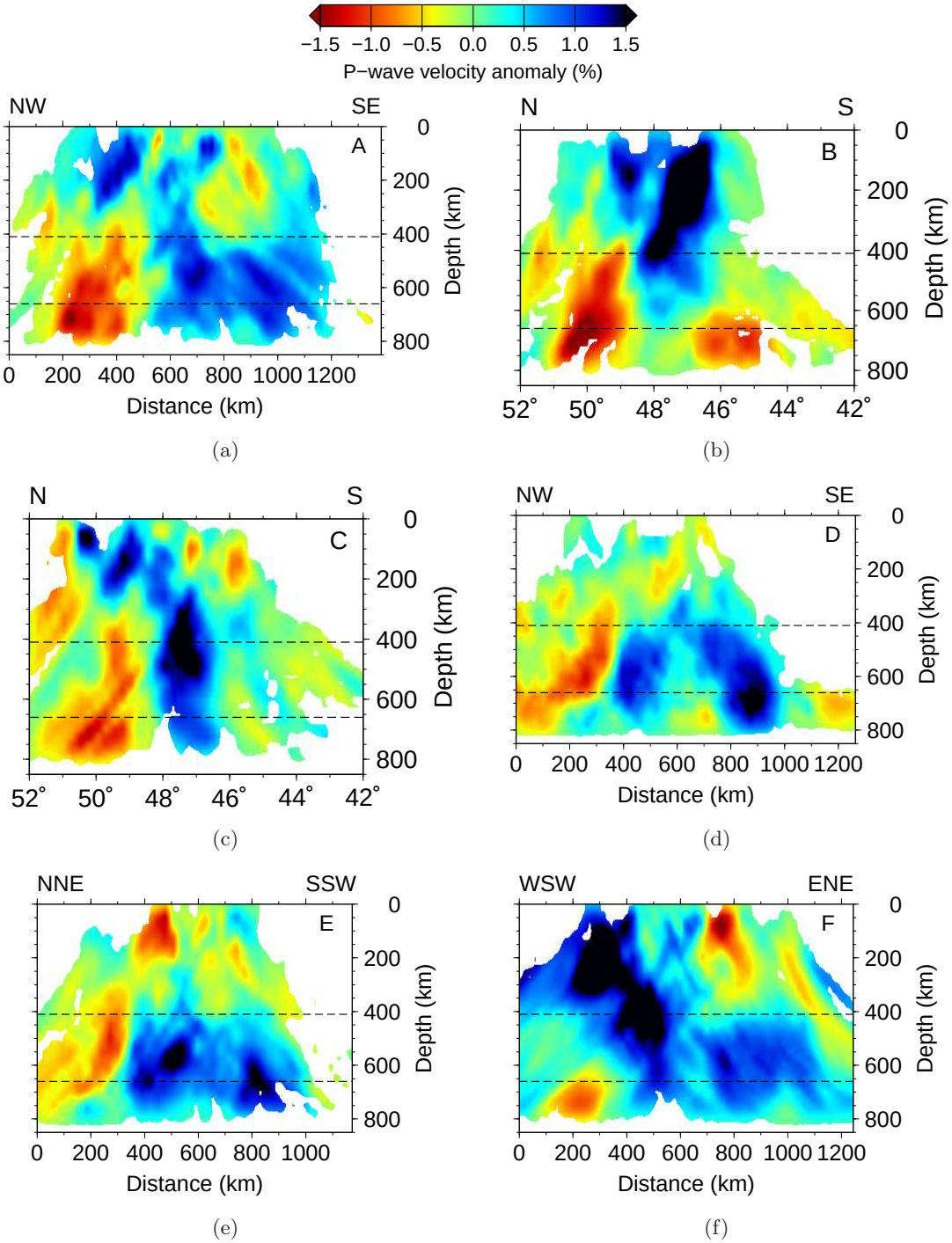

Figure 4.19: PCBPS: Cross-sections through the P-wave tomographic model. Locations of cross-sections are shown in figure 4.18(f).

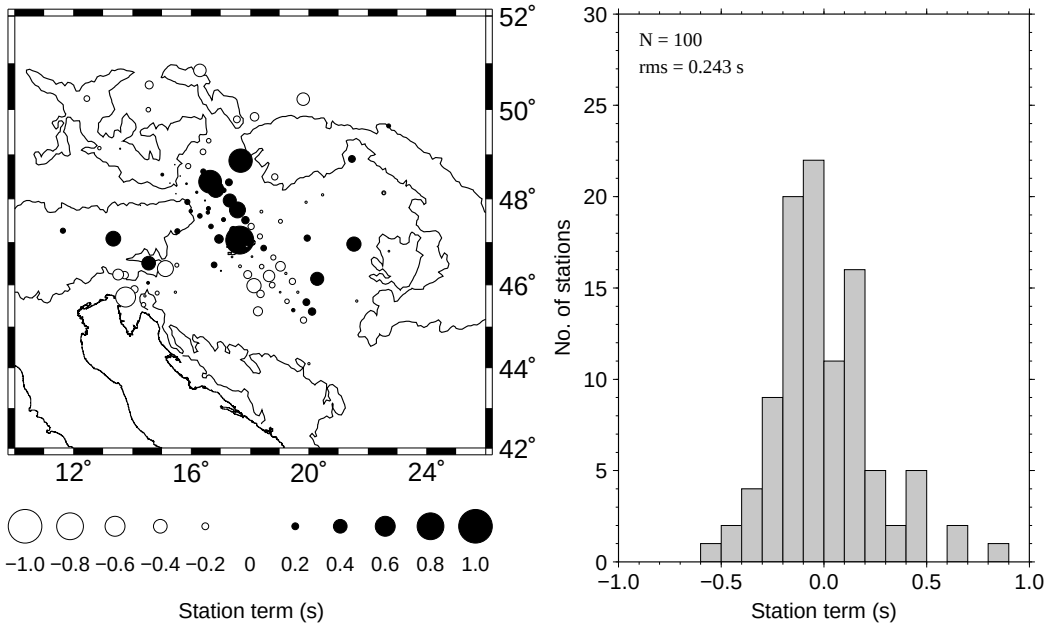

(a) (b)

Figure 4.20: Station terms shown for (a) each station; and (b) as a frequency distribution.

root related to the topography. The additional crustal thickness (the crustal root) attributable to an excess elevation h is:

$$R = \frac{h\rho_c}{\rho_m - \rho_c} \tag{4.6}$$

where, ρ_c is an average crustal density of 2780 $kg\ m^{-3}$, and ρ_m is an average mantle density of 3300 $kg\ m^{-3}$. For station CBP3J, this would produce a crustal root of ~ 2.8 km. Using the lowermost crustal velocity (V_c) of 6.5 km s^{-1} (*iasp91*) in place of a mantle velocity (V_m) of 8.04 km s^{-1} (*iasp91*), the station term is further delayed by,

$$\frac{R}{V_c} - \frac{R}{V_m} = 0.083\ s \tag{4.7}$$

The total station term would still only be 0.174 s. To explain a 0.8 s delay by anomalous crustal thickness, would require a crustal root 27.15 km thick.

Observations of the raw relative arrival-time residuals for the three stations CBP2E, CBP3J and JAVC in appendix C (figures C.2, C.7, C.16), show a constant slow offset of the residuals, not present at neighbouring stations. An alternative explanation is that these large station terms are due to systematic timing errors at these stations.

To assess the effect of a systematic timing error, synthetic data were tested. Using the

noise-free synthetic travel-times for checkerboard model PCMS1 (section 4.4), constant offsets of 1 second were added to the three stations. The resulting station terms after the inversion were 0.91 s for CBP2E, 0.92 s for CBP3J and 0.86 s for JAVC which, accounting for topography, is increased to 0.94 s, 1.01 s and 1.00 s respectively. This test shows that the station terms are able to effectively absorb such a timing error.

To show the overall effect on the tomographic images, inversions were also run without including the station term correction. Figures 4.21 & 4.22 compare images of inversions run with and without station terms. As expected, if a travel-time delay is not incorporated in a station term, then that delay will map into near-surface structure. The images therefore differ most in the upper 150 km. Below this depth, the structures are similar in both inversions. At 75 km (figures 4.21(a),(b))), where the largest differences occur, some features are still apparent though distorted: slow regions beneath the east Pannonian Basin and the Western Carpathians; a fast anomaly running almost north-south through the high resolution array; and similar structure beneath the Bohemian Massif. Major differences are observed beneath the Eastern Alps, and into the Western Carpathians. Without the station terms, neither the crustal root beneath the Alps nor the excess topography is directly accounted for in the inversion and the delay produced by these features is mapped into a spurious slow velocity anomaly in the mantle at 75 km. Station terms are thus essential for resolving and interpreting lithospheric structure.

Not including station terms also increases the final rms residual from 0.130 s to 0.154 s.

4.7 Final solution residuals

The rms data misfit is reduced by 71% (from 0.446 s to 0.130 s - figure 4.17) in the preferred inversion solution. However, it is important to examine the remaining residuals to assess if there is any remaining systematic signal that is not explained by the preferred solution. The remaining residuals were examined for specific stations and for specific events.

For individual stations, the variation in unexplained residuals with back-azimuth and distance was examined. Any misfit is identified as variation from the expected zero mean. By comparing observed data residuals to model predictions, we can infer where the model is inconsistent with the data. Figure 4.23 shows the relative arrival-time residuals for three typical stations. The rms residual misfit for these stations is reduced

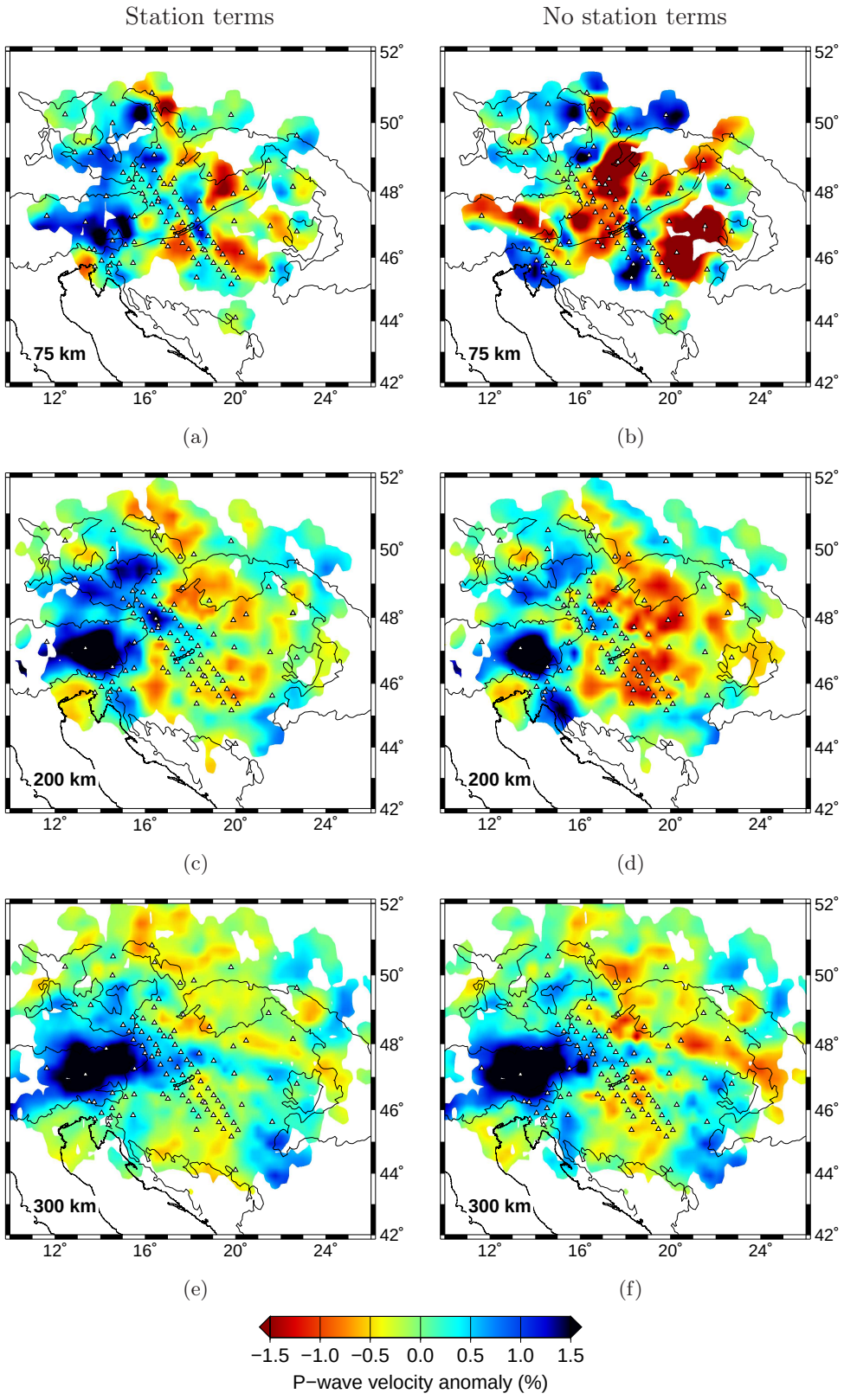

Figure 4.21: Left: PCBPS. Right: PCBP. Comparison of depth slices for inversions with and without station terms.

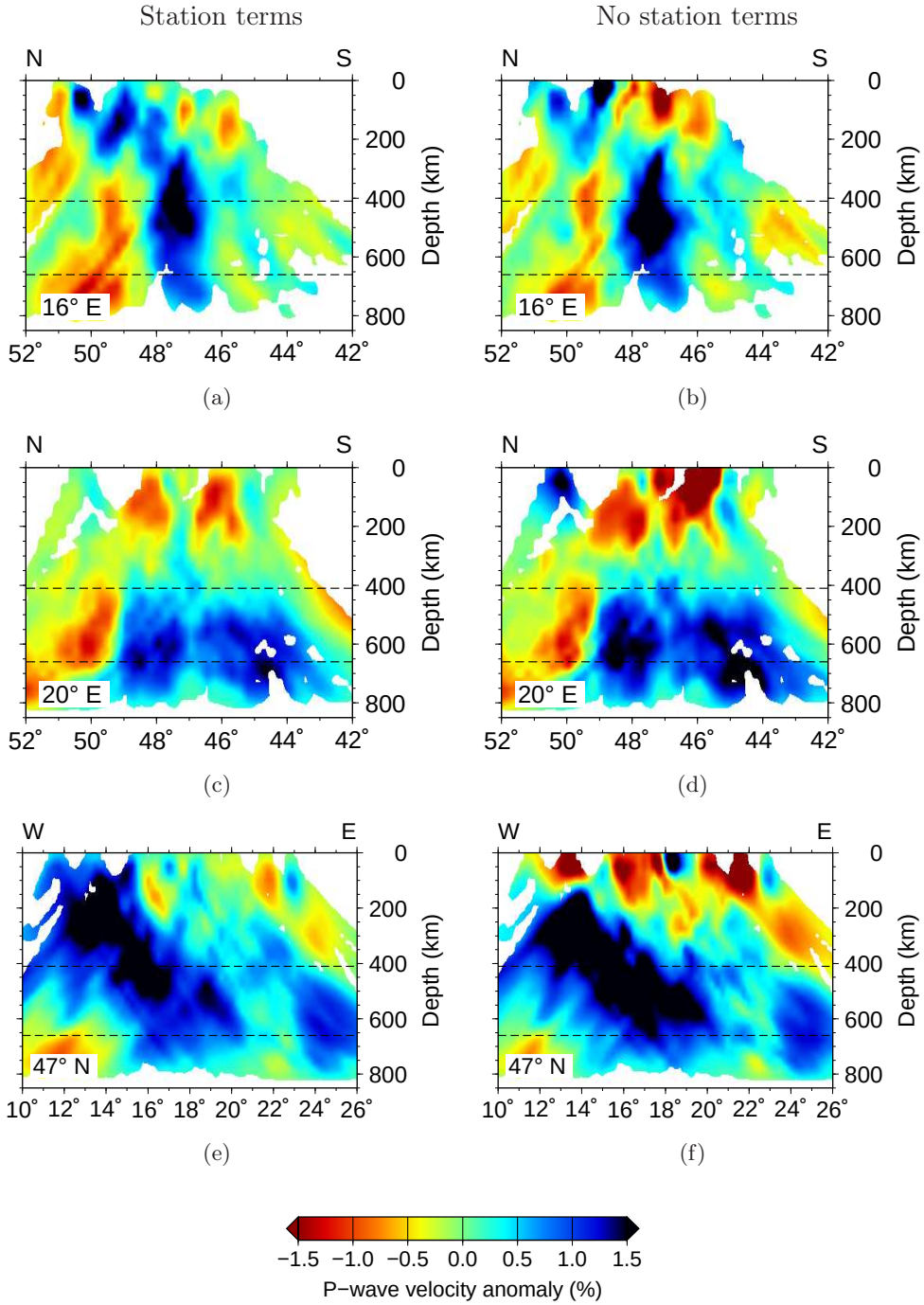

Figure 4.22: Left: PCBPS. Right: PCBP. Comparison of cross-sections for inversions with and without station terms.

to 0.085 s for CBP2D, 0.068 s for CONA and 0.125 s for JAVS. The model arrival-time residuals for these stations fit the data well, satisfying all of the observed signal, leaving no significant systematic signal to be explained.

The mean of all 100 rms station residuals is 0.116 s. Looking at the 10 stations with the worst rms residuals (from 0.170 s to 0.671 s) (figure 4.24), they are all located in different regions, indicating there is no correlation of poor residuals with tectonic domain. Residuals from the three worst stations are shown in figure 4.25, with the largest rms solution residual of 0.671 s, observed at PERS in Slovenia, (figure 4.25(c)). Despite having the second and third largest rms solution residual (0.214 s and 0.205 s), the model arrival-time residuals for stations NKC (figure 4.25(b)) and SZEL (figure 4.25(a)) still satisfy the observed data well, eliminating most of the systematic signal in the observed data, though a relatively large random noise persists. Figure 4.24 highlights this, with PERS as a significant outlier. With clearly defined systematic variation in the observed relative arrival-time residuals for PERS of 4.05 s, large velocity variations are required. The distinctive residual signature, which is not seen at neighbouring stations, is likely to be due to the unique position of this station on the Periadriatic line, the major dextral shear zone (e.g. Ratschbacher et al., 1991) dividing the southern Apulian foreland and the central crystalline zone of the Alps to the north. That an isotropic velocity anomaly is unable to satisfy the strong azimuthal variation in arrival time at this station, suggests that sub-surface anisotropy affects the data recorded at PERS.

Figure 4.26(a) shows the mean solution residuals per event, plotted as a function of back-azimuth and epicentral distance. The rms solution residual is 0.130 s, and with the mean event residuals showing an rms of only 0.017 s, there is little evidence of significant systematic signal correlated with event distance or back-azimuth, confirmed by the unimodal distribution of figure 4.26(b).

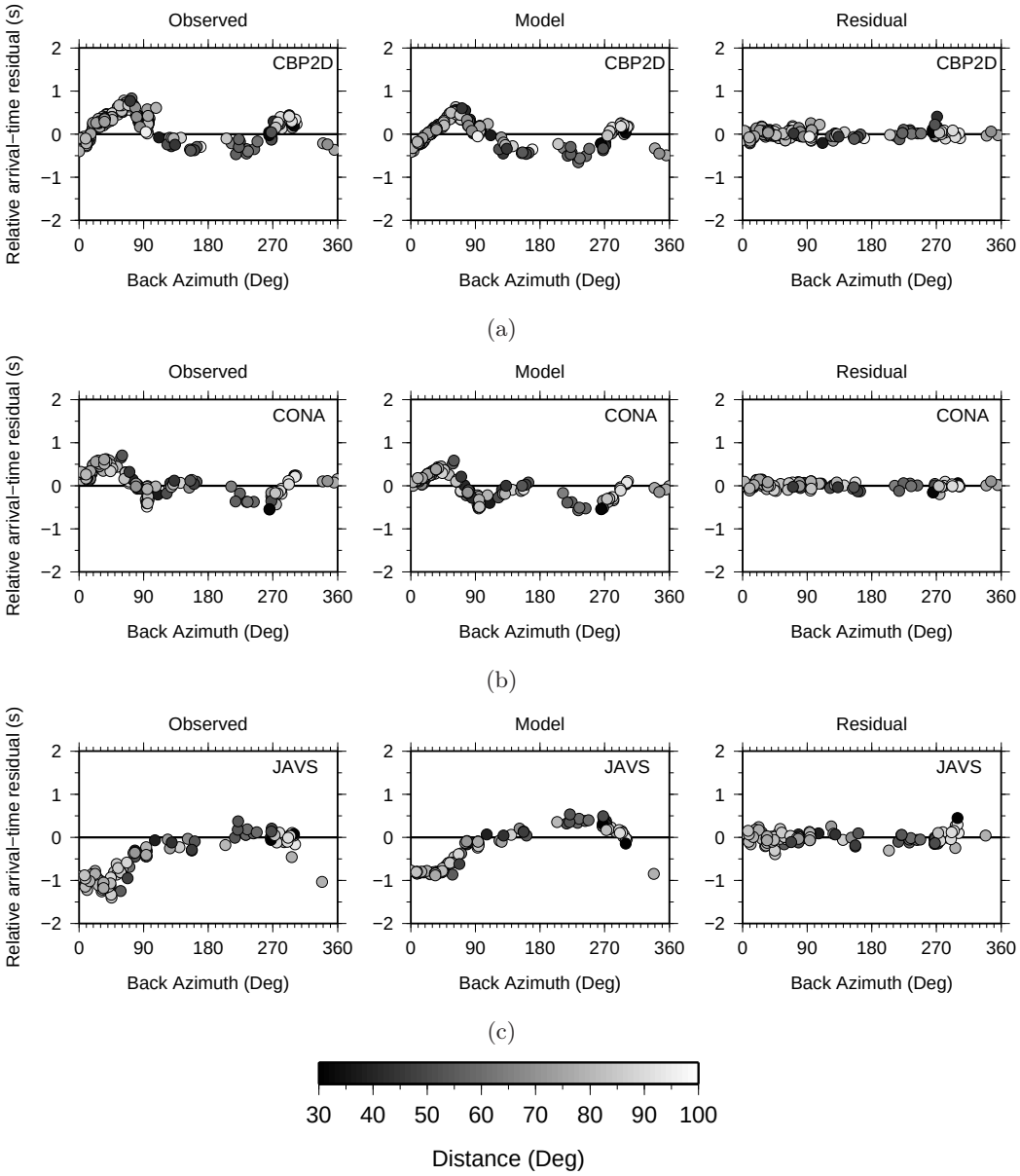

Figure 4.23: Variation of P-wave relative arrival-time residuals with back azimuth for three typical stations: CBP2D (48.62°N, 16.40°E), CONA (47.93°N, 15.86°E) and JAVS (45.89°N, 14.06°E). Left: the observed relative arrival-time residuals; Middle: model prediction for relative arrival-time residuals through the solution model; Right: solution residuals after the inversion.

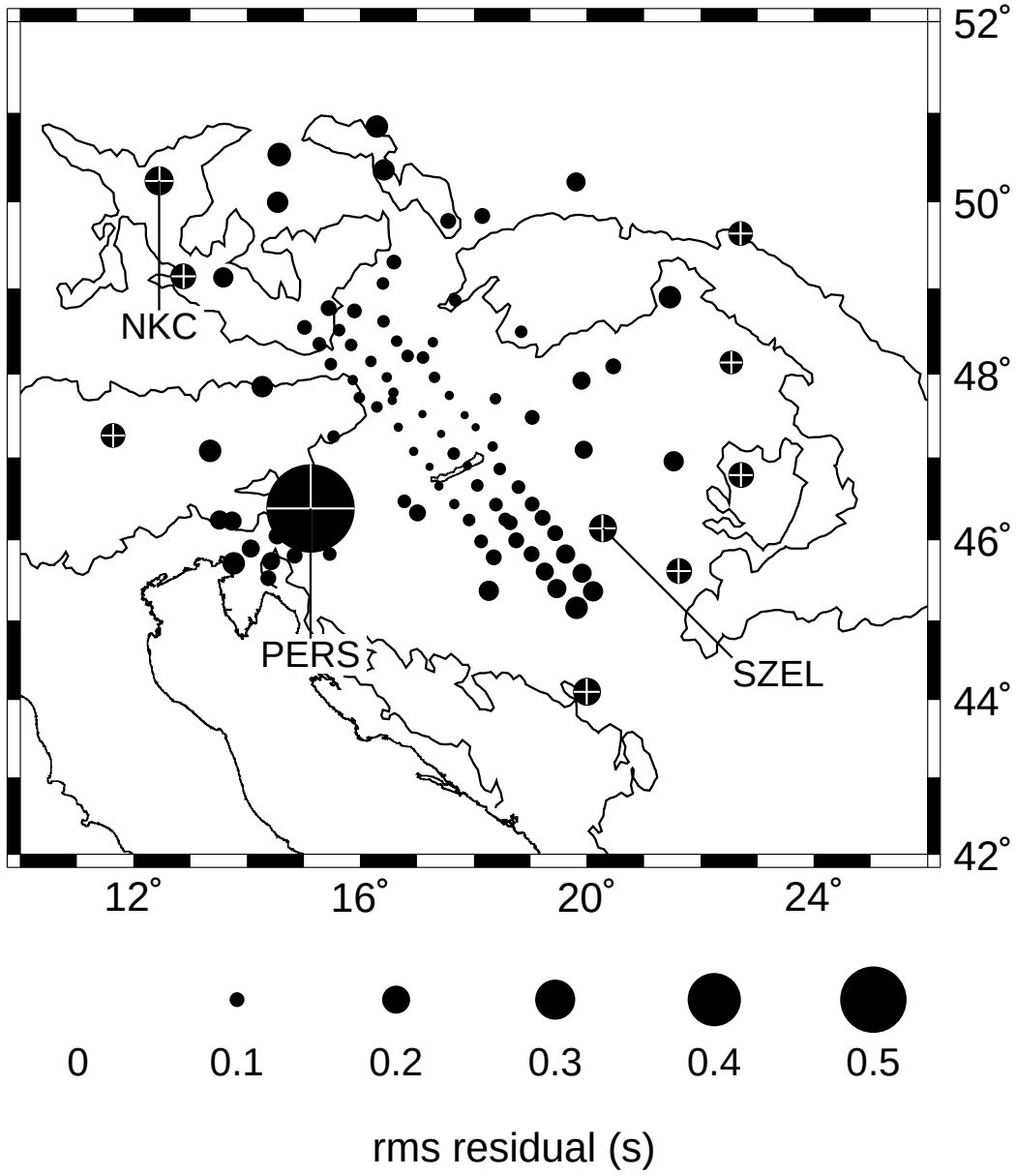

Figure 4.24: Map plot of the rms solution residual at each station. The 10 stations with the largest rms are marked by white crosses. The mean rms solution residual for all stations is 0.116 s. The three stations shown in figure 4.25 are labelled.

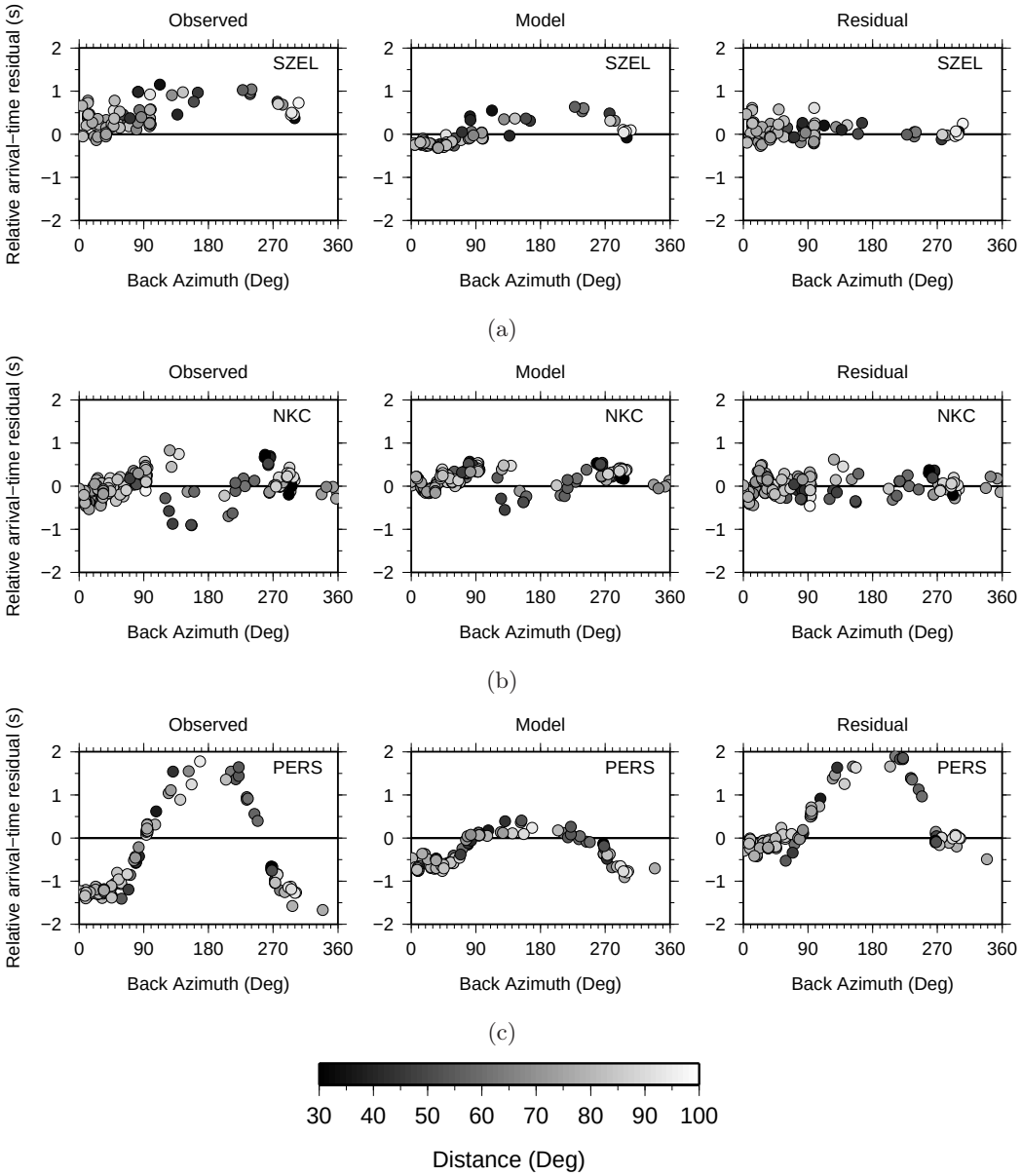

Figure 4.25: Variation of relative arrival-time residuals with back-azimuth for the three stations with the worst fit to the data: SZEL (46.14°N, 20.27°E), NKC (50.23°N, 12.45°E) and PERS (46.38°N, 15.12°E). Left: the observed relative arrival-time residuals; Middle: model prediction for relative arrival-time residuals through the solution model; Right: solution residuals after the inversion.

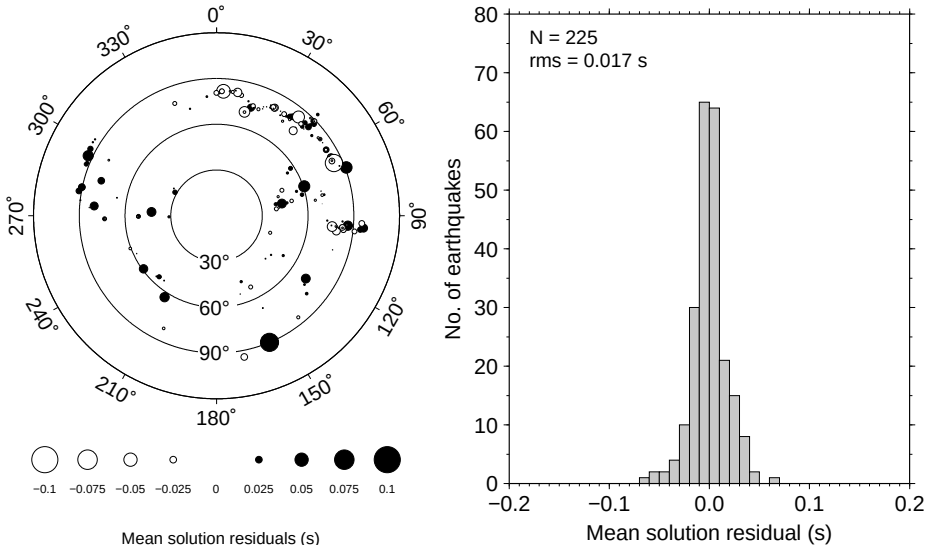

(a) (b)

Figure 4.26: Mean final residuals after the tomographic inversion for each event. In (a) white circles are negative residuals; black circles are positive residuals. Concentric circles show the great circle distance from the centre of the Carpathian-Pannonian region in 30° intervals. Event back-azimuth is shown. In (b) the histogram shows the frequency distribution of the mean solution residuals for each event.

Chapter 5

Upper-mantle S-wave velocity models

5.1 Overview

In this chapter I present the results for the inversion of the S-wave relative arrival-time residuals. All inversions use the same model parameterisation as the P-wave tomography in chapter 4. The regularisation parameters are re-assessed using the tradeoff between rms S-wave arrival-time residual and model roughness. Using S-wave synthetic models like those already described for the P-wave tomography, the resolution is assessed through sensitivity tests. The preferred model solution (SCBPS) is then presented. The effect of station terms on the S-wave inversion is also investigated before analysis of the final solution residuals. Unless otherwise stated the same methods described in chapter 4 are also used in the S-wave analysis.

The tomographic model naming convention follows chapter 4, with SCBPS indicating an S-wave inversion of observed data with station terms included. Dashed lines on the vertical cross-sections show the 410 km and 660 km discontinuities.

In addition to the tomographic images presented in this chapter, a video through the preferred S-wave model (SCBPS) is included on the supplementary CD (see appendix D).

5.2 Effect of regularisation

To investigate the tradeoff between model roughness and rms residual, the regularisation operators were applied separately to find parameters (λ_s and λ_f) which produce an

identical rms solution residual. The S-wave tradeoff curve (figure 5.1) was constructed using the ratio $\lambda_s/\lambda_f = 25.67$. The flattening and smoothing parameters stated in table 5.1 were used to construct this tradeoff curve. The depth slices at 300 km shown on the tradeoff curve were obtained using λ_s = 1232000, 19250 and 4812.5. The three models again show systematic variation along the tradeoff curve, from an rms residual of 0.783 s with the removal of most structure, to a model with an rms residual of 0.511 s which shows high amplitude anomalies and possible spurious structure. The S-wave tradeoff curve has a sharp rise in rms residual, with little effect on model roughness for values above λ_S=77000, indicating most structure is removed above this point on the tradeoff curve. Of note also, is the balance of slow to fast anomalies. The inversion has significantly reduced the distribution of slow anomalies at 300 km with increased smoothing. Further down the tradeoff curve, with less smoothing and a greater reduction in rms residual, the slow anomalies are much more prominent. The preferred model indicated by the red point on the tradeoff curve (λ_s = 19250, λ_f = 750) shows similar structure to the P-wave model, whilst also showing sufficient variation in short wavelength features that the model is not over smoothed.

λ_s	λ_f	rms residual (s)
5046272000	196608000	1.354
2523136000	98304000	1.177
9856000	384000	0.998
2464000	96000	0.853
1232000	48000	0.783
77000	3000	0.685
19250	**750**	**0.624**
9625	375	0.569
4812.5	187.5	0.511
2406.25	93.75	0.443
1203.125	46.875	0.375
601.562	23.438	0.326

Table 5.1: Table showing the smoothing and flattening parameters (λ_s and λ_f respectively) and the corresponding rms residual, used in the construction of the tradeoff-curve in figure 5.1. The parameters of the preferred model (SCBPS) are highlighted.

5.3 Resolution

The event distribution used in the S-wave tomography is shown in figure 5.2. The distribution is similar to that of the P-wave data, with the most significant difference being the

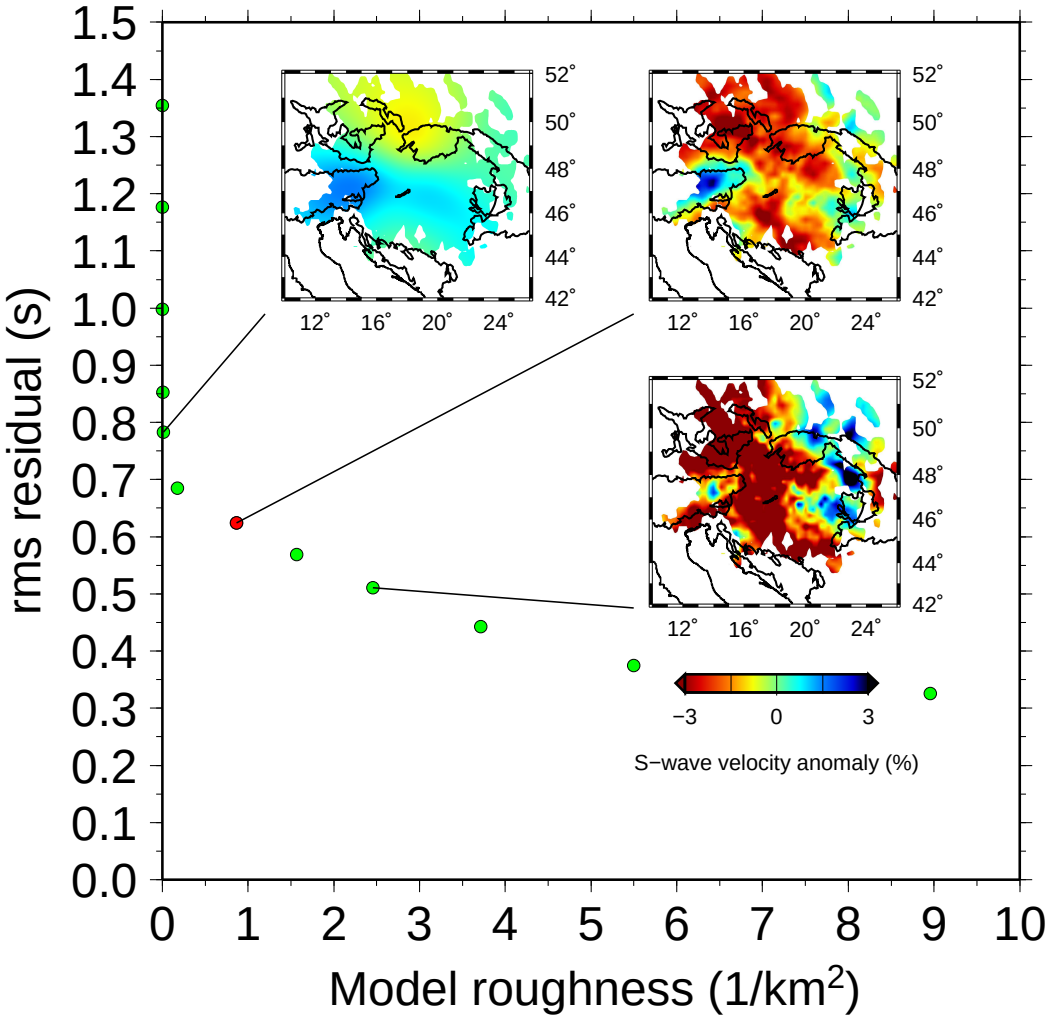

Figure 5.1: Tradeoff between the S-wave model roughness and solution residual. The images show the 300 km depth slice at three different locations on the tradeoff curve. The red point shows the preferred model (SCBPS). The regularisation parameters used are shown in table 5.1

reduction of useful events from the south. We should expect therefore, to see a similar resolving power in the S-waves, despite the reduction in events from 225 to 124. The great circle distance distribution for the S-wave events corresponds to angles of incidence from 14.8°–27.2° with a mode of 18.76°, which is slightly less steep than the P-waves (mode angle of incidence = 16.6°). This increase in incidence angle should improve the resolving power in the vertical direction, as long as there are enough crossing rays.

The sensitivity tests used for the S-wave tomography are applied with a maximum amplitude of ±5% relative to the *iasp91* reference model. Three checkerboard models (SCMS1, SCMS2, SCMS3) were produced with identical locations and radii of anomalies to their P-wave equivalent (PCMS1, PCMS2, PCMS3 - see section 4.4). Synthetic travel-times were computed through the models using the *iasp91* ray-paths and random noise was added with a Gaussian distribution. The standard deviation of the noise was 0.313 s, equal to the estimate of noise in the observed data for the S-waves (see section 2.6.2). The synthetic travel-times were inverted using the preferred regularisation parameters ($\lambda_s = 19250$, $\lambda_f = 750$) determined in section 5.2

The maximum recovered amplitude of the anomalies is reduced from the input amplitude of ±5% by 1.2%, 0.3% and 0.6% for SCMS1, SCMS2 and SCMS3 respectively. The final solution models show a reduction in the rms residual by 71% for SCMS1, 83% for SCMS2 and 76% for SCMS3.

The normalised correlation between synthetic model images and the recovered solution model images are shown in table 5.2. The correlation values correspond well to the rms reduction, with the largest anomalies providing the best resolved inversions. The correlation increases with depth for SCMS3 and is relatively constant for the other two tests. Areas with ray coverage below the hit threshold of 5 rays per 25 km^3 are significantly greater at 700 km in the S-wave data and lateral smearing between anomalies is evident in the 500 km and 700 km depths slice in SCMS1 (figures 5.3(f) and (h)).

The differences in accuracy of the recovered P-wave and S-wave checkerboard models are shown by a cross-plot of the respective correlation values in figure 5.11. The greatest difference is observed between SCMS1 and PCMS1. Contrasting with an increase in correlation with depth for PCMS1, the SCMS1 depth slices show a decrease in resolution from 300–700 km, which is likely due to the reduced number of crossing rays with depth. However, the correlation values for the 100 km depth slices in both SCMS1 and SCMS2

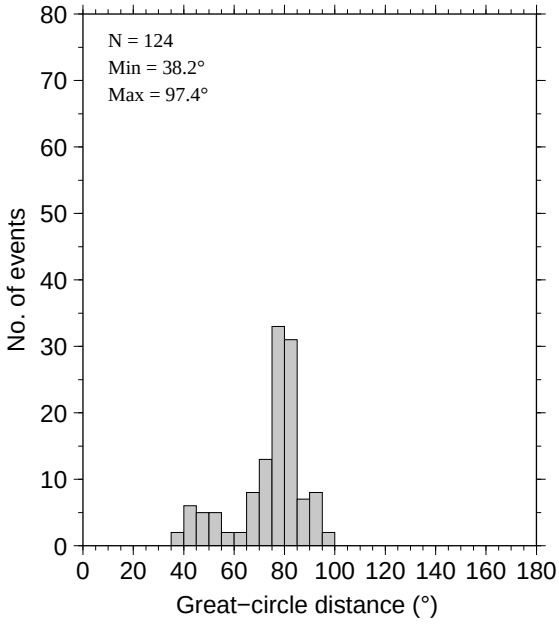

(a)

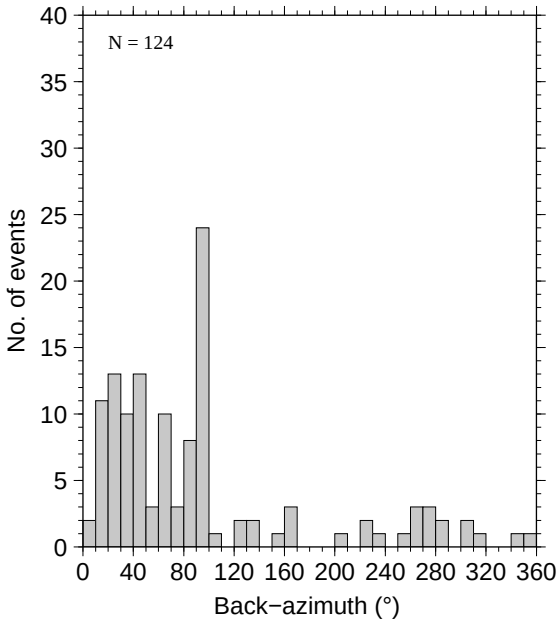

(b)

Figure 5.2: Event distribution for the S-wave tomography relative to a point in the middle of the network, sorted by: (a) great-circle distance; (b) back-azimuth distribution.

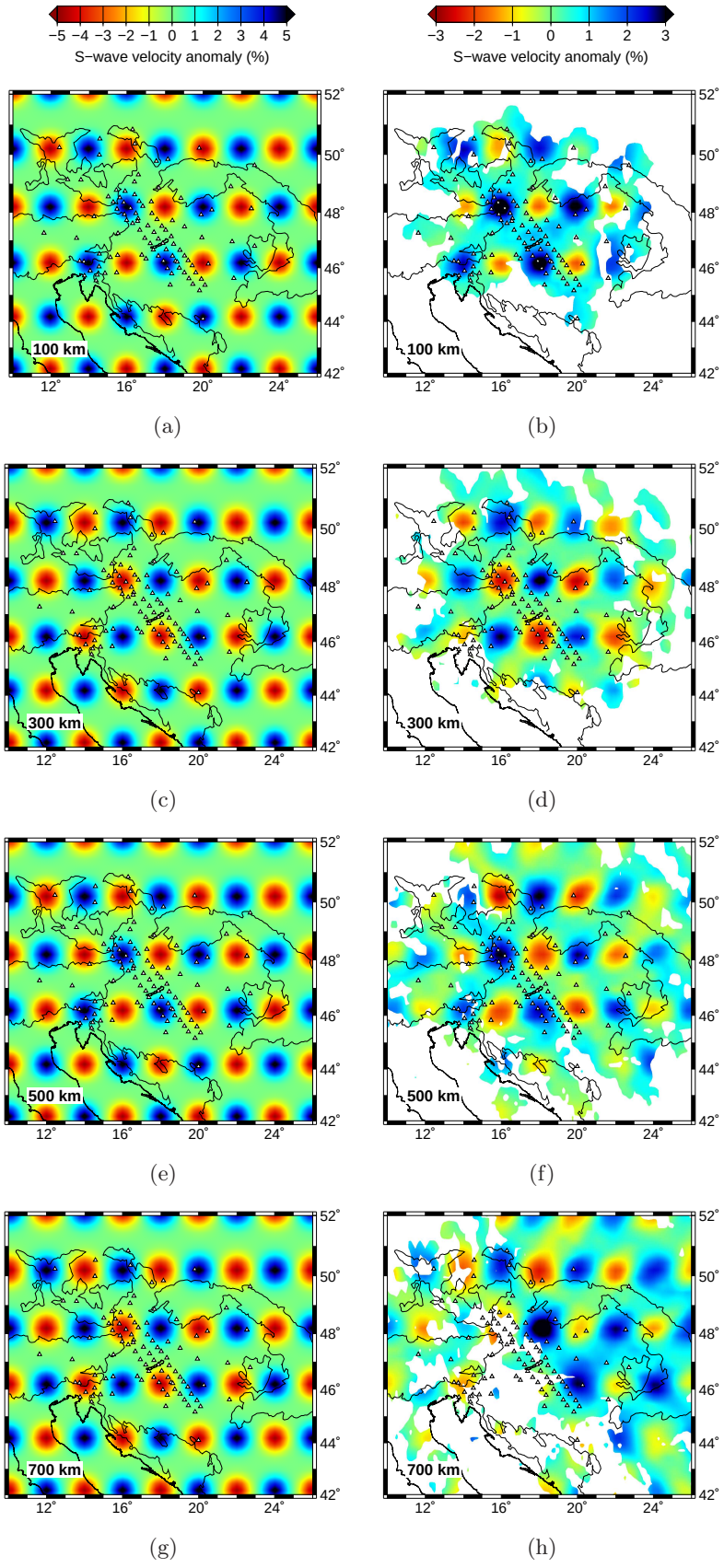

Figure 5.3: SCMS1: Depth slices through the synthetic checkerboard model (left) and the recovered model (right) after inverting the synthetic data, at 100 km, 300 km, 500 km and 700 km depth.

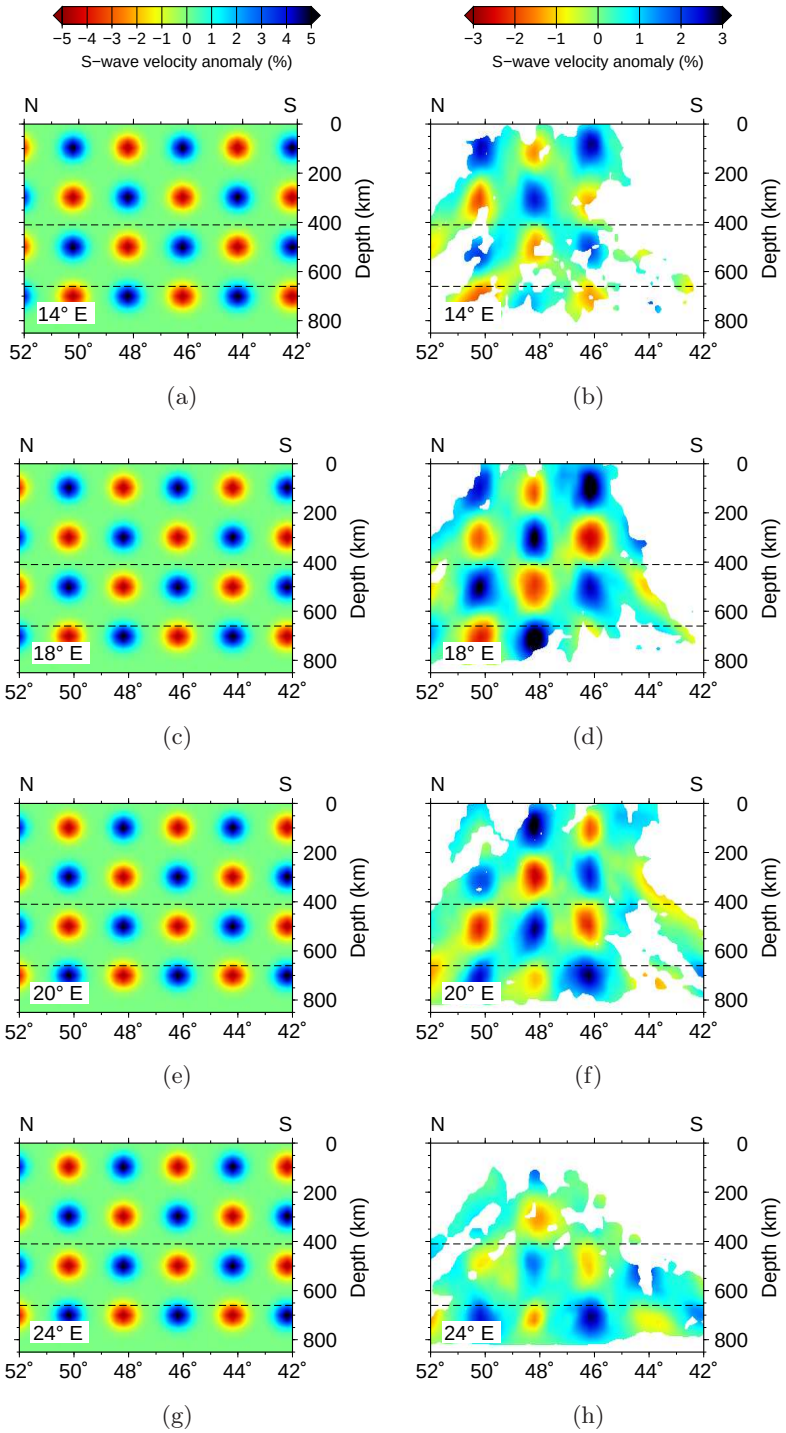

Figure 5.4: SCMS1: North-south cross-sections through the synthetic checkerboard model (left) and the recovered model (right) after inverting the synthetic data, at 14° E, 18° E, 20° E and 24° E.

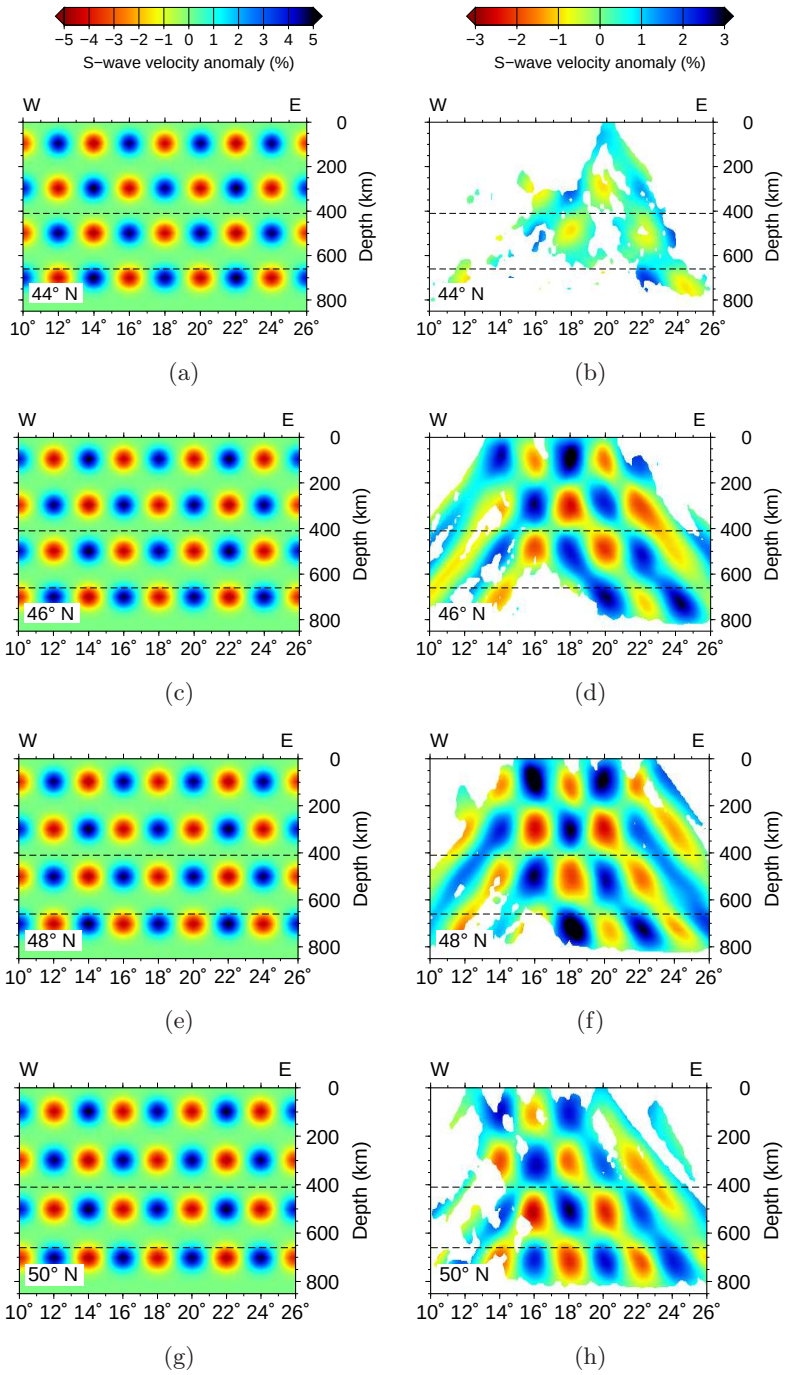

Figure 5.5: SCMS1: East-west cross-sections through the synthetic checkerboard model (left) and the recovered model (right) after inverting the synthetic data, at 44° N, 46° N, 48° N and 50° N.

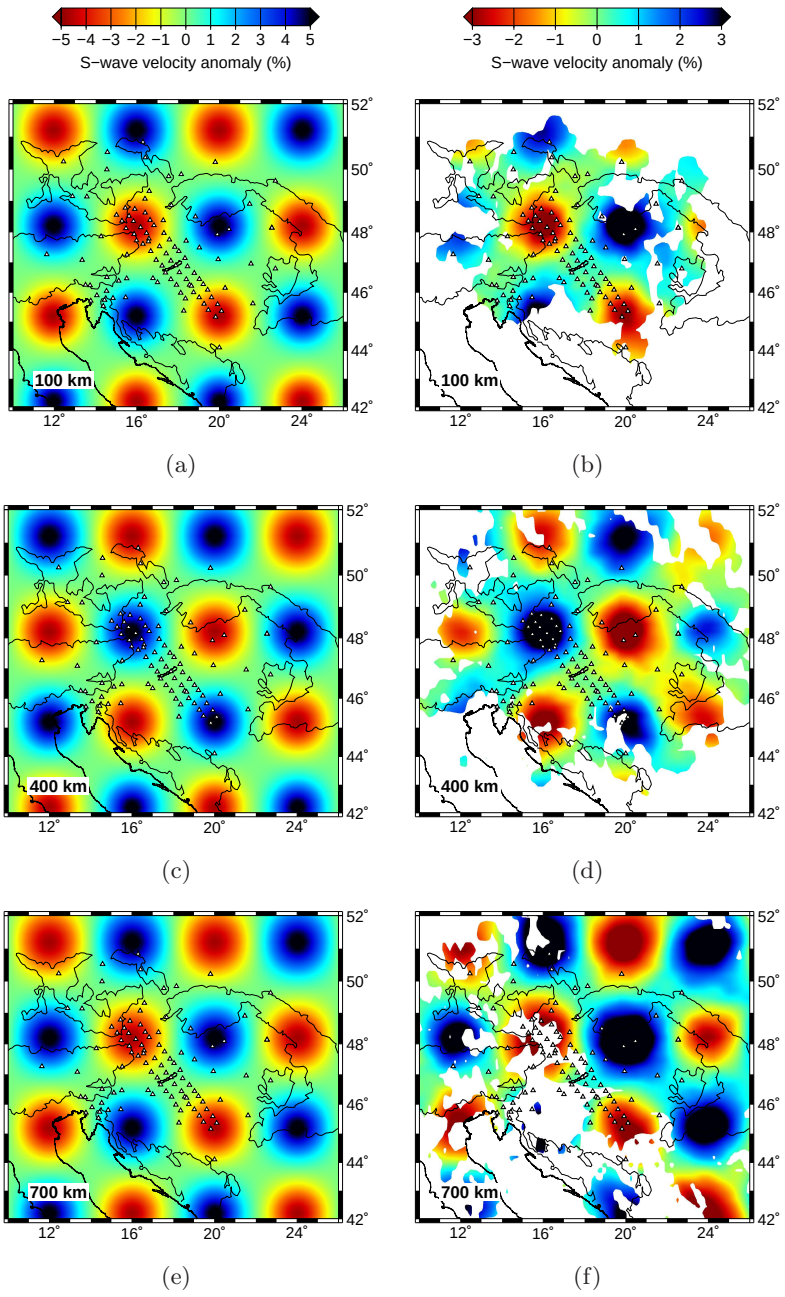

Figure 5.6: SCMS2: Depth slices through the synthetic checkerboard model (left) and the recovered model (right) after inverting the synthetic data, at 100 km, 400 km and 700 km depth.

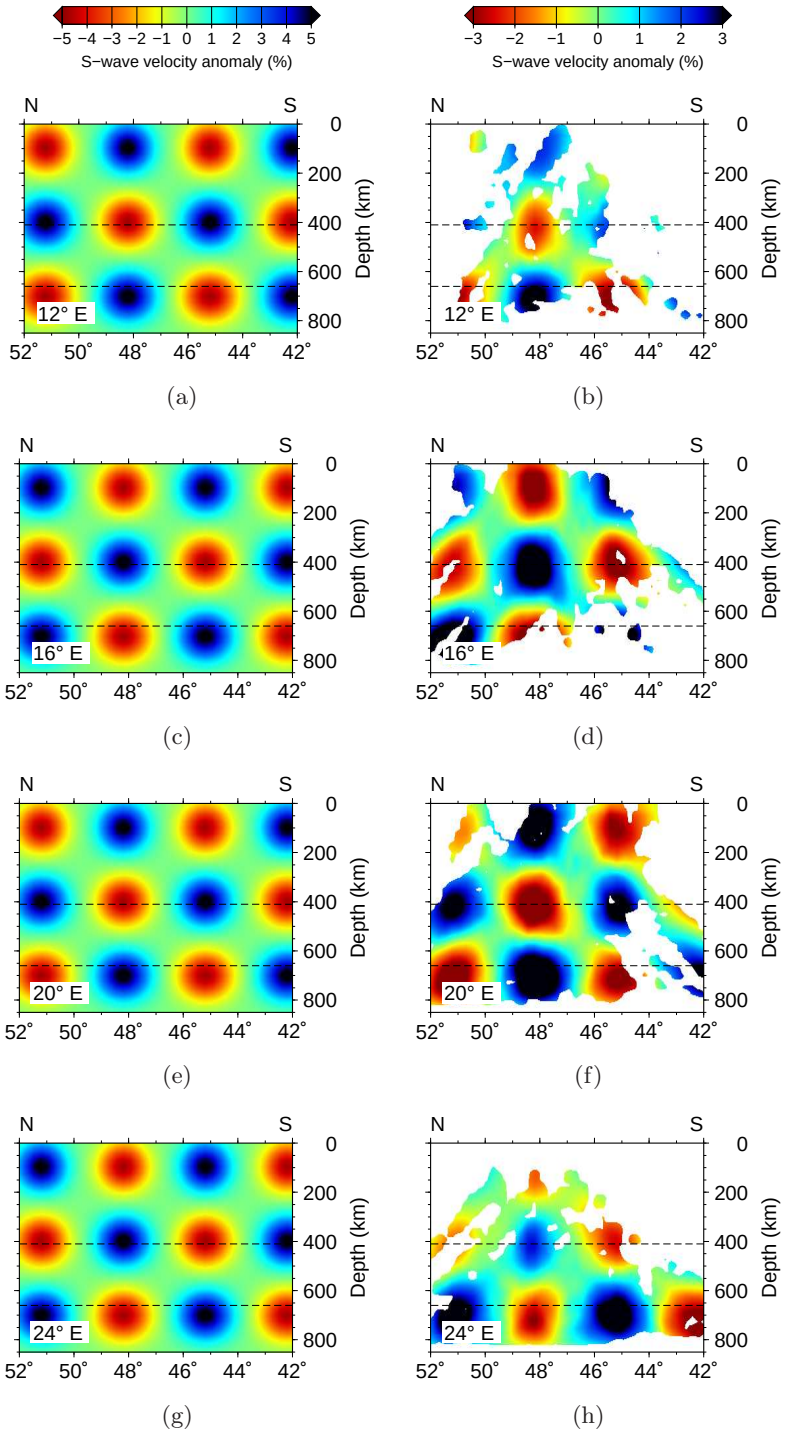

Figure 5.7: SCMS2: North-south cross-sections through the synthetic checkerboard model (left) and the recovered model (right) after inverting the synthetic data, at 12° E, 16° E, 20° E and 24° E.

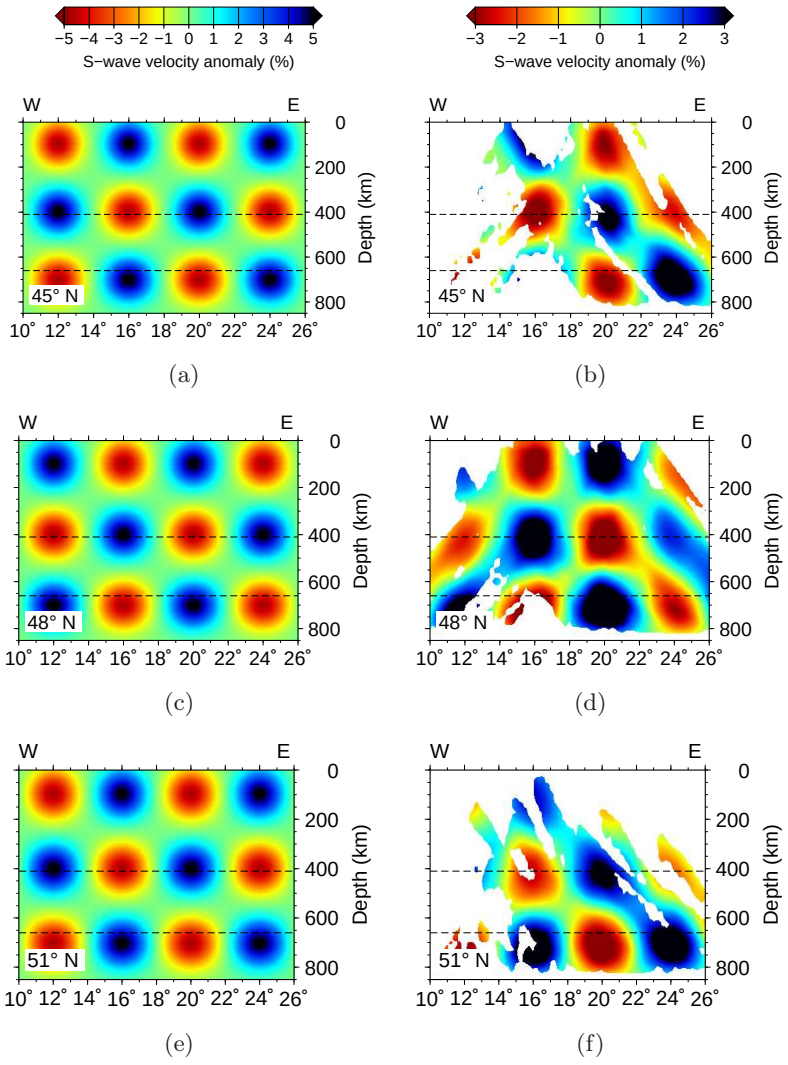

Figure 5.8: SCMS2: East-west cross-sections through the synthetic checkerboard model (left) and the recovered model (right) after inverting the synthetic data, at 45° N, 48° N and 51° N.

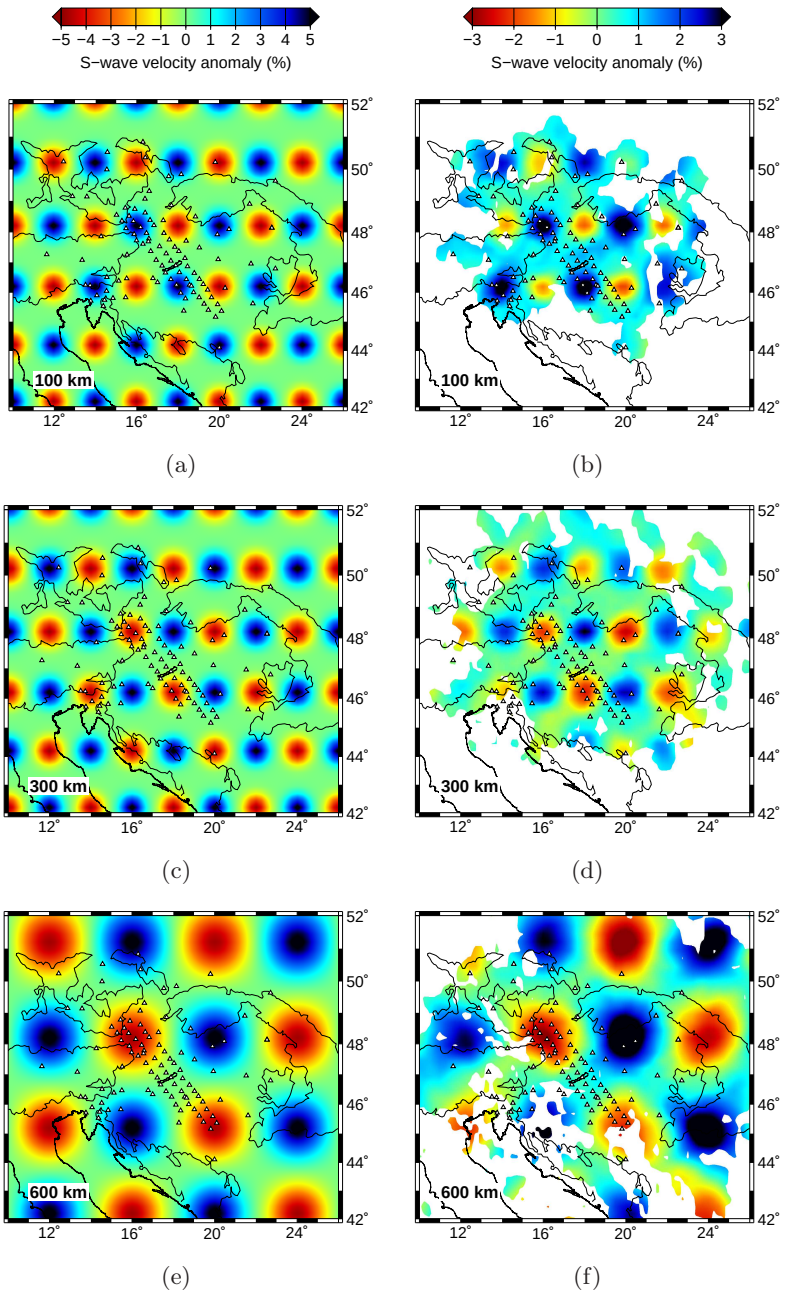

Figure 5.9: SCMS3: Depth slices through the synthetic checkerboard model (left) and the recovered model (right) after inverting the synthetic data, at 100 km, 300 km and 600 km depth.

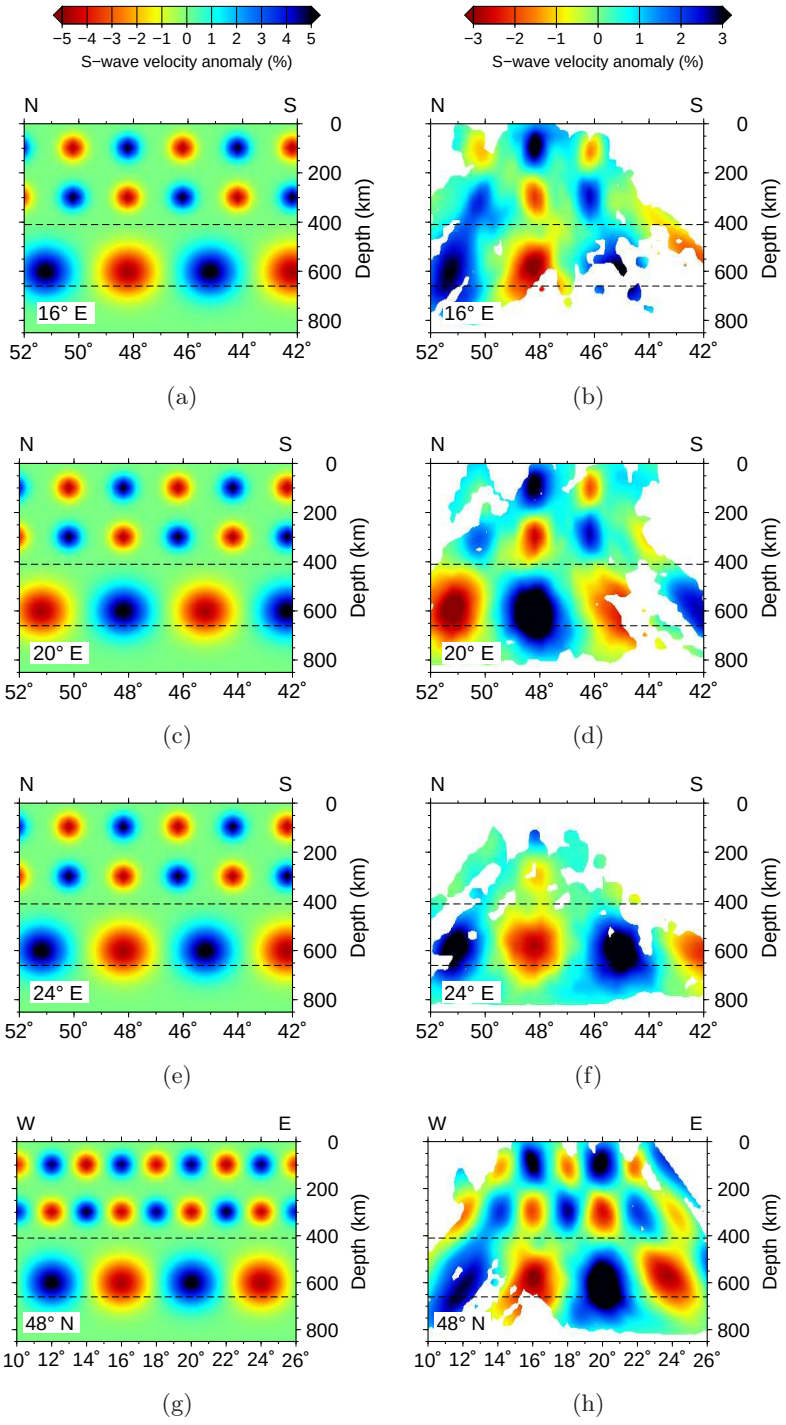

Figure 5.10: SCMS3: Cross-sections through the synthetic checkerboard model (left) and the recovered model (right) after inverting the synthetic data, at 16° N, 20° N, 24° N and 48° E.

Model name	Figures	Plot description	Correlation
SCMS1	5.3(a),(b)	100 km depth	0.75
SCMS1	5.3(c),(d)	300 km depth	0.89
SCMS1	5.3(e),(f)	500 km depth	0.84
SCMS1	5.3(g),(h)	700 km depth	0.77
SCMS1	5.4(a),(b)	N-S at 14° E	0.82
SCMS1	5.4(c),(d)	N-S at 18° E	0.83
SCMS1	5.4(e),(f)	N-S at 20° E	0.78
SCMS1	5.4(g),(h)	N-S at 24° E	0.70
SCMS1	5.5(a),(b)	E-W at 44° N	0.73
SCMS1	5.5(c),(d)	E-W at 46° N	0.77
SCMS1	5.5(e),(f)	E-W at 48° N	0.77
SCMS1	5.5(g),(h)	E-W at 50° N	0.79
SCMS2	5.6(a),(b)	100 km depth	0.94
SCMS2	5.6(c),(d)	400 km depth	0.93
SCMS2	5.6(e),(f)	700 km depth	0.95
SCMS2	5.7(a),(b)	N-S at 12° E	0.95
SCMS2	5.7(c),(d)	N-S at 16° E	0.95
SCMS2	5.7(e),(f)	N-S at 20° E	0.96
SCMS2	5.7(g),(h)	N-S at 24° E	0.93
SCMS2	5.8(a),(b)	E-W at 45° N	0.95
SCMS2	5.8(c),(d)	E-W at 48° N	0.91
SCMS2	5.8(e),(f)	E-W at 51° N	0.94
SCMS3	5.9(a),(b)	100 km depth	0.69
SCMS3	5.9(c),(d)	300 km depth	0.87
SCMS3	5.9(e),(f)	600 km depth	0.95
SCMS3	5.10(a),(b)	N-S at 16° E	0.85
SCMS3	5.10(c),(d)	N-S at 20° E	0.87
SCMS3	5.10(e),(f)	N-S at 24° E	0.90
SCMS3	5.10(g),(h)	E-W at 48° N	0.86

Table 5.2: Table showing the correlation between the synthetic input model and the recovered solution model for the three checkerboard models, SCMS1, SCMS2 and SCMS3. Correlations are shown for each figure from 5.3–5.10.

are significantly lower than their P-wave equivalents, indicating poorer S-wave resolution at shallower depths, compared with the P-wave results.

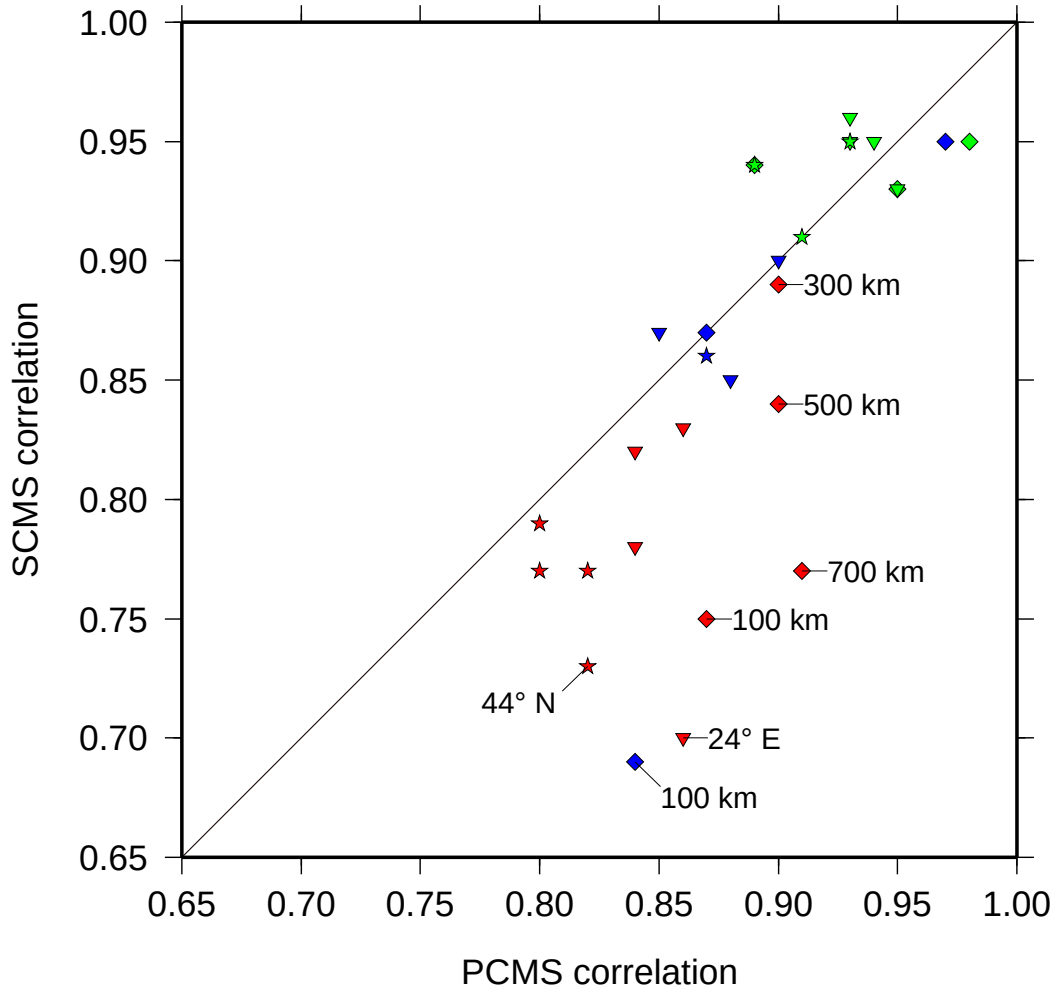

Figure 5.11: Difference in the normalised correlation for the synthetic checkerboard tests for both P-wave models (PCMS - see section 4.4) and S-wave models (SCMS). The colours correspond to each checkerboard model - red: PCMS1 and SCMS1; green: PCMS2 and SCMS2; and blue: PCMS3 and SCMS3. Diamonds show the correlation values for depth slices, inverted triangles show north-south cross-sections, and stars are for east-west cross-sections. Values are shown in tables 4.2 and 5.2. Points referred to in the text are labelled with the plot description.

5.4 S-wave tomography results

The model presented here (SCBPS) is the preferred model after estimating the optimum regularisation parameters in section 5.3 ($\lambda_s = 19250$, $\lambda_f = 750$). The parameterisation is identical to that of the P-wave inversion. The results from the sensitivity tests in section 5.3, showed anomalies on a 45 km scale are resolved within most of the area enclosed by the Carpathian arc, but with less resolution compared to the P-wave images, particularly

at 100 km depth. Anomaly amplitudes were reduced in these sensitivity tests by at least a factor of 1.3 but more generally by a factor of about 2.

The preferred inversion solution shows a final reduction in the rms residual by 59% (from 1.513 s to 0.624 s - figure 5.12). The station terms alone reduce the initial rms residual by 13% (from 1.513 s to 1.317 s).

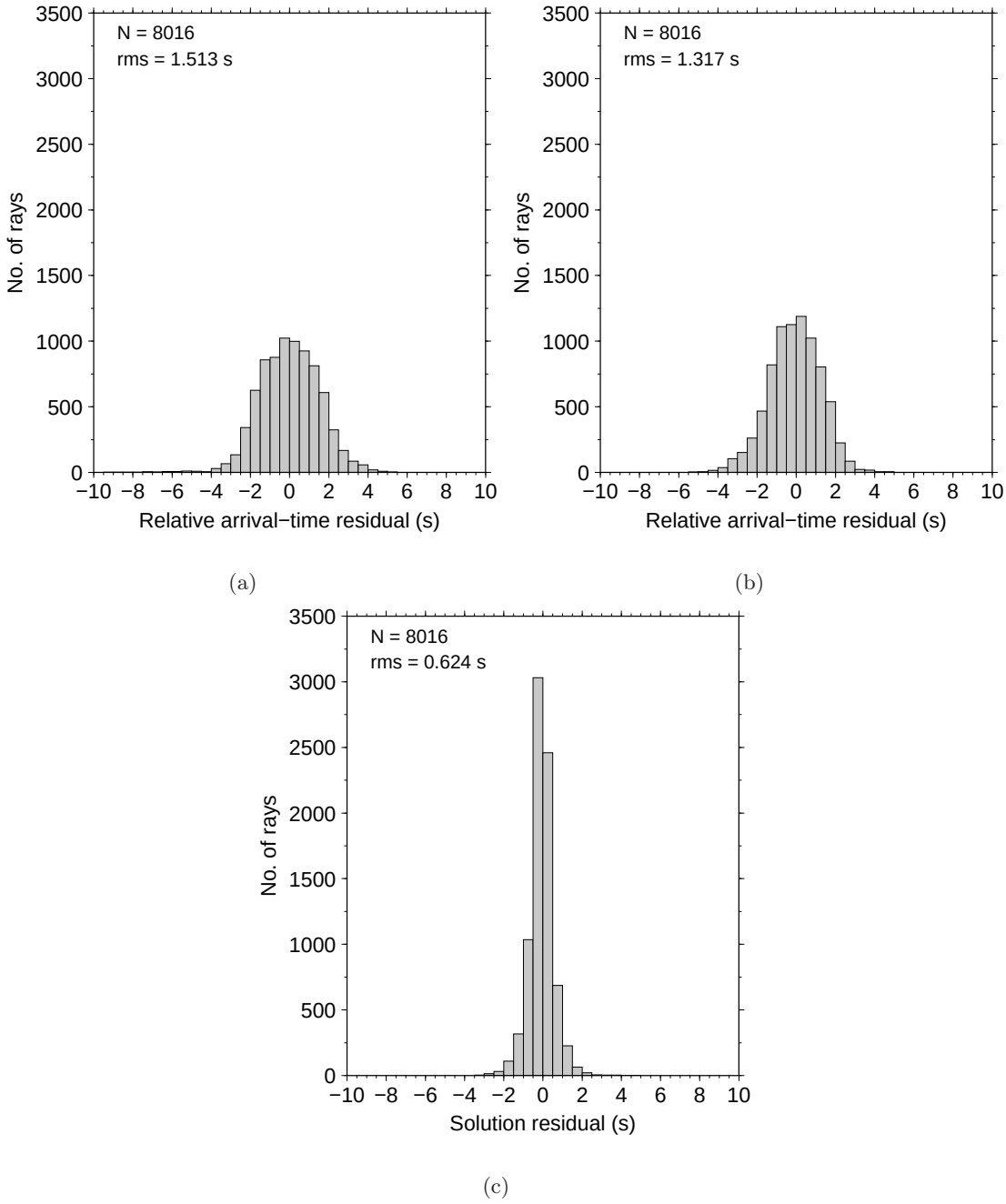

Figure 5.12: Histograms of the (a) initial residuals; (b) initial residuals with the final station terms removed; and (c) the final solution residuals for the preferred S-wave inversion (SCBPS).

At 75 km, the four localised slow anomalies imaged in the P-wave inversion beneath the Pannonian Basin are greater in amplitude and spatial extent in the S-wave image (figure 5.13(a)). Beneath the Békés, Makó and Derecske basins the anomalies have merged, reaching a maximum amplitude of -4.2%. In the south-west of the basin the ray-coverage is not sufficient to interpret any anomaly at this depth, although in the 200 km slice (figure 5.13(b)) with greater ray coverage, slow anomalies are imaged. On the northern edge of the Pannonian Basin, the slow velocity anomaly (-4.02%) underlying the Neogene Central Slovakian volcanics (Kovács et al., 2007) extends further beneath the Western Carpathians than the corresponding P-wave anomaly. This slow anomaly extends laterally into the Vienna basin to the west and northwards beneath the eastern edge of the Bohemian Massif. At 200 km the Bohemian Massif may be bordered to the west by a zone of lower velocities which are associated with possible asthenospheric updoming (Plomerová et al., 2007).

Relatively higher velocities are also imaged at 75 km beneath the Eastern Alps (3.4%) related to the continental collision and downwelling of cold lithospheric material beneath the Alpine collision zone. Similar to the P-wave image, a fast anomaly is observed beneath the Bohemian Massif; however, in the S-wave inversion, this anomaly appears separate from the Alpine anomaly.

A lineament associated with the Mid-Hungarian Line, dividing the Alcapa and Tisza blocks is more apparent in the S-wave images at 75 km; although the degree to which the MHZ controls the location of the slow anomalies on either side of the lineament is uncertain.

At 200 km and 300 km depth (figures 5.13(b), 5.13(c)), the distinctive high velocity anomaly beneath the Eastern Alps reduces from a maximum of 4.6% at 200 km to a maximum of 2.8% at 300 km. In cross-section (figure 5.14(b)), the anomaly beneath the Eastern Alps is limited to the upper 400 km and is a largely vertical downwelling. The anomaly extends eastward with a reduced anomaly of 1.2% (figure 5.14(c)) and into the MTZ beneath the Pannonian Basin (figures 5.14(a) and (f)). The high velocities in figure 5.14(c), do not show any connection to the high velocities beneath the Bohemian Massif, which was imaged in the P-wave tomography. However, sensitivity tests showed poorer resolution of the S-waves at shallow depths preventing clear interpretation in this case. The eastward extension from the Alps and into the MTZ is imaged along strike in figure 5.14(f), which also shows the Alpine anomaly reaching only to 300 km depth. At 500

km and 600 km depth (figures 5.13(e),(f)), the MTZ structure beneath the Pannonian Basin shows S-wave anomalies of up to 2.9% fast. The northern edge of this anomaly again reveals a sharp transition (∼5.1%) to relatively slow material beneath the Western Carpathians and Bohemian Massif. In contrast with the P-wave inversion, these slow anomalies appear to extend upward continuously to lithospheric depths.

5.5 Effect of station terms

With identical station spacing to the P-wave inversion, the effect of station terms with depth should be comparable. However, with fewer rays (8016 cf. 15853), the depth increases for the S-wave inversion but is largely limited to above the MTZ.

The station terms produced in the inversion are shown in figure 5.15. The distribution is largely Gaussian (figure 5.15(b)), except for a single station, PVCC on the Bohemian Massif, showing an anomalous station term of 6.0 s. The observed relative arrival-time residuals for PVCC (figure C.47), show a similar residual pattern to the P-waves (figure C.22) but with a clear systematic offset, which is absorbed by the station term in the inversion.

The effect of the station terms on the tomographic images are shown in figures 5.16–5.17. The rms residual shows a slight decrease from 0.624 s to 0.622 s when not including station terms. With a decrease in crossing rays for the S-wave dataset, the effect of the station terms with depth has increased. The major differences occur in the upper 300 km; below this depth, minor differences appear in the amplitude of the main S-wave anomalies when the station terms are not included in the inversion. Due to the large station term at PVCC, the effects of station terms below the Bohemian Massif extend to much greater depths, with fast velocity anomalies into the MTZ along ray-paths, when the station terms are not included (e.g. figure 5.17(d)).

At 75 km (figure 5.16(a),(b)) however, there are still regions which show similar structure: a slow region beneath the Western Carpathians which also extends up beneath the eastern edge of the Bohemian Massif; a slow region beneath the eastern Pannonian Basin; and a fast velocity anomaly extending along strike of the high resolution array. Similar to the P-wave inversion, without station terms, the crustal root beneath the Alps is not directly accounted for in the inversion, with the delay producing a spurious slow anomaly in the 75 km slice.

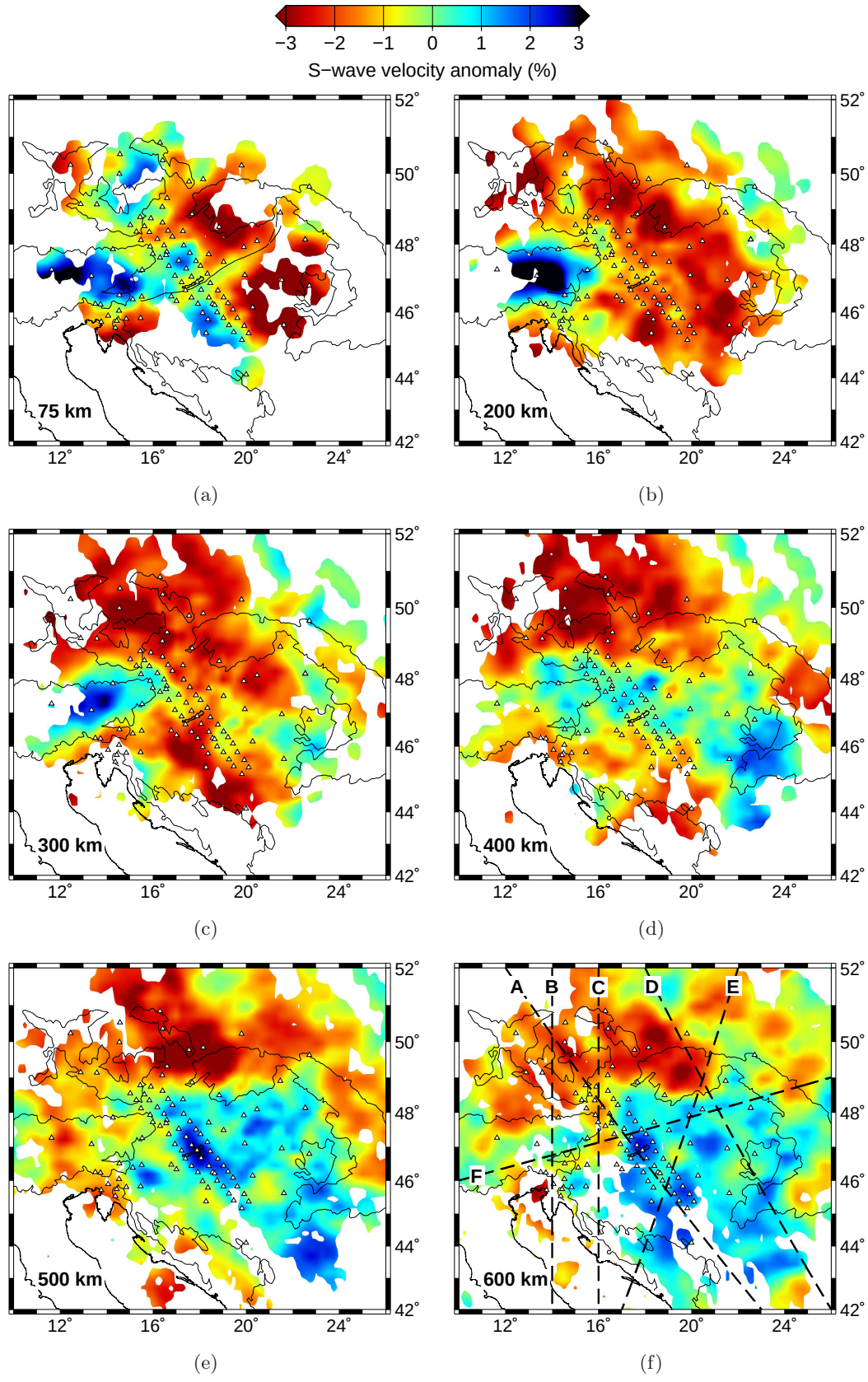

Figure 5.13: SCBPS: Depth slices through the S-wave tomographic model. The locations of stations are shown as triangles. The Mid-Hungarian Line is shown on the 75 km slice. Location of cross-sections are shown in the 600 km slice.

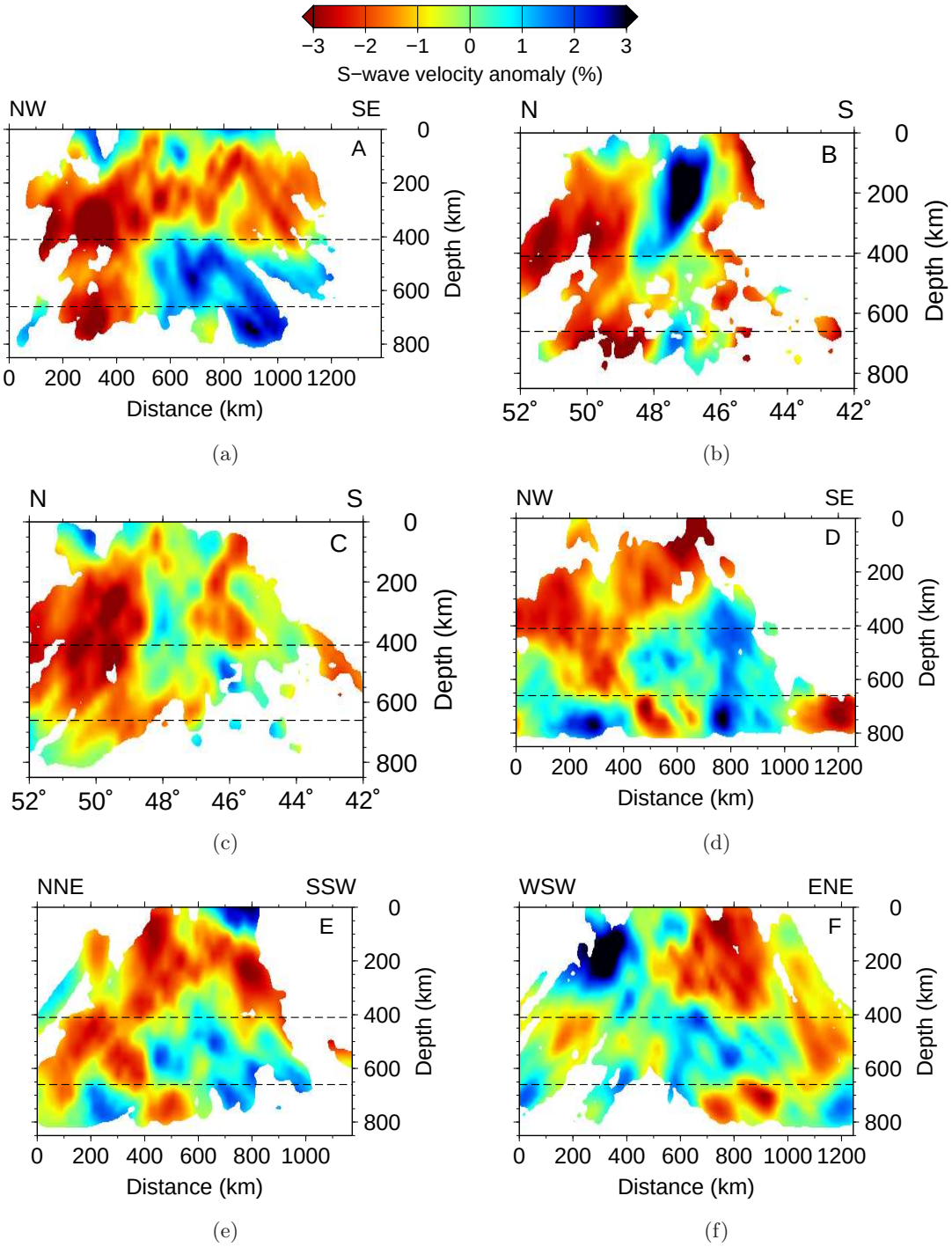

Figure 5.14: SCBPS: Cross-sections through the S-wave tomographic model. Locations of cross-sections are shown in figure 5.13(f).

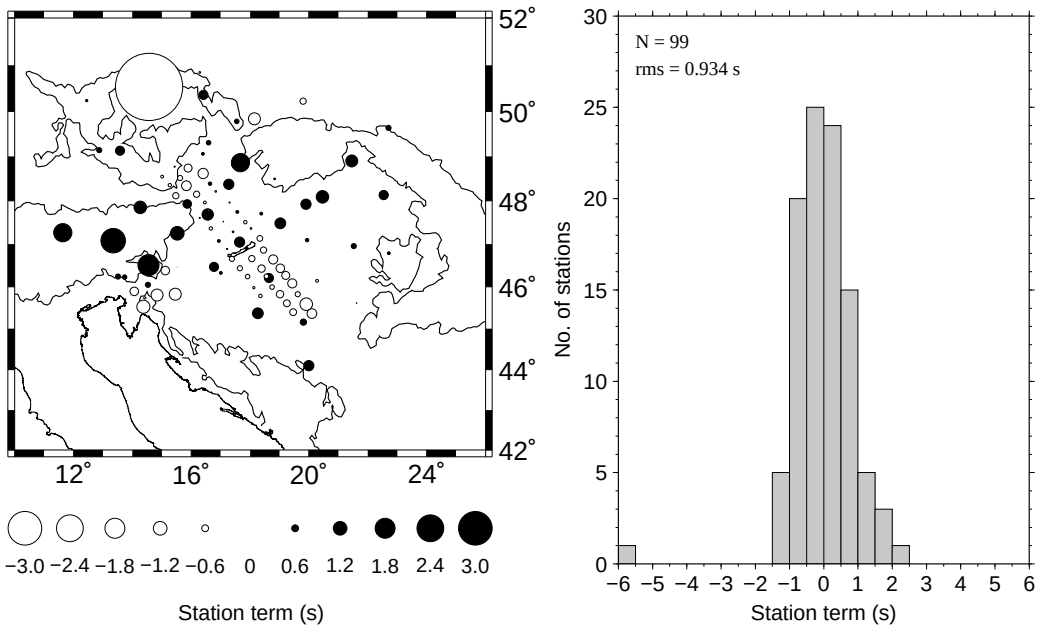

(a) (b)

Figure 5.15: S-wave station terms shown for (a) each station; and (b) as a frequency distribution.

5.6 Final solution residuals

The final S-wave rms residual of 0.624 s (reduced by 59% from 1.513 s - figure 5.12), compares with a 71% reduction for the P-wave tomography. For individual stations the observed, modelled and final station residuals are plotted for three typical stations in figure 5.18. The model evidently explains the data for these stations with no significant systematic misfit remaining. The rms residual at each station and the 10 stations with the largest rms residual are shown in figure 5.19. The map shows there is no regional bias in the distribution of large residuals which could be attributed to strong anisotropy. The mean of all rms station residuals is 0.618 s. Figure 5.20 shows the three stations with the largest rms residual, with station PERS again providing a clear systematic misfit to the data with an rms residual of 1.507 s. Stations CBP3B (figure 5.20(a)) and CBP2Q (figure 5.20(b)) have an rms residual of 1.053 s and 1.135 s respectively, which is caused by the large scatter in the observed data at back-azimuths less than 100° and lack of data at greater back-azimuths.

The mean S-wave solution residuals for each event are shown in figure 5.21. Although there is no bias for any hypocentral location, the histogram (figure 5.21(b)) is skewed towards negative residuals. This indicates that the final model predicts systematically

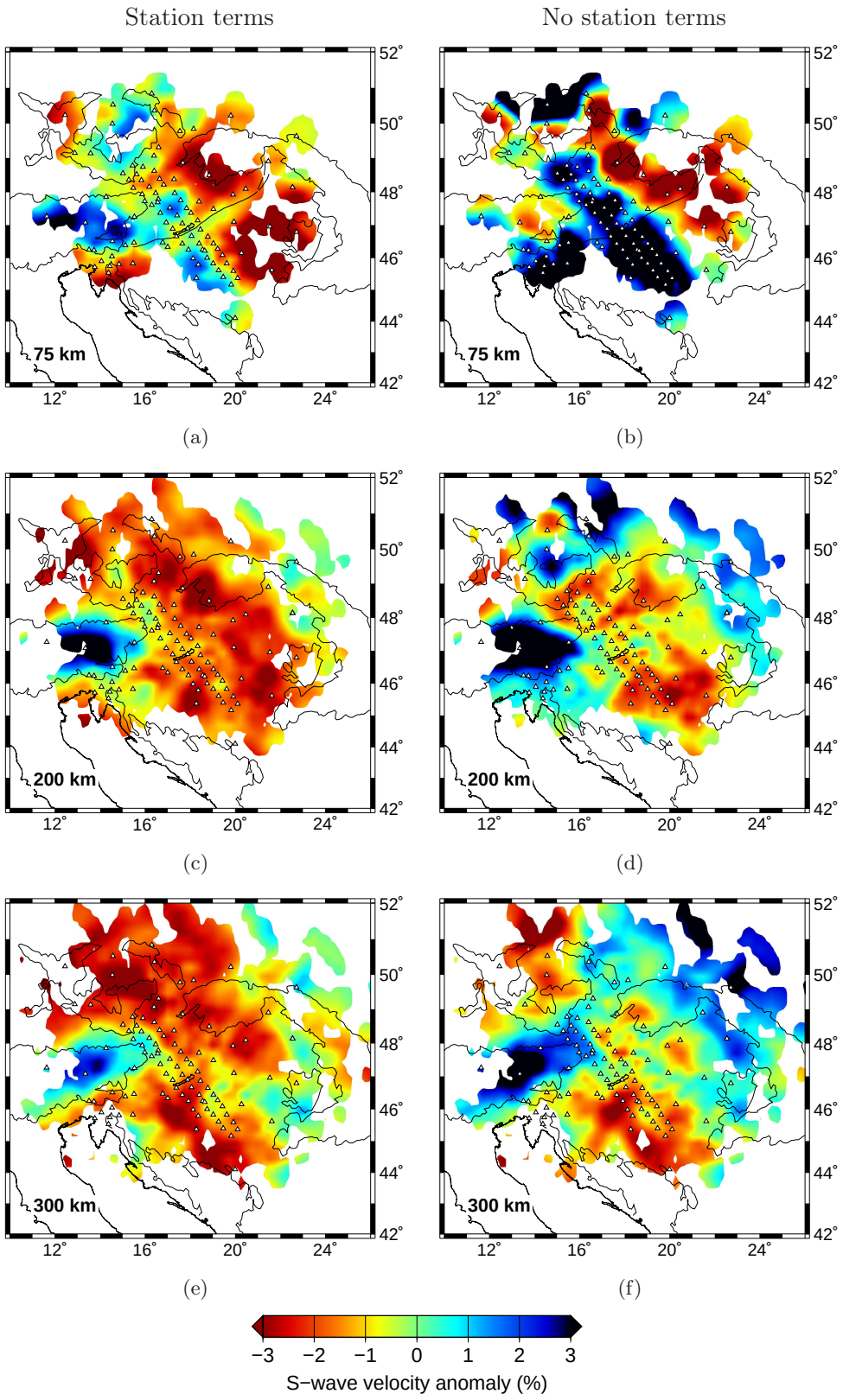

Figure 5.16: Left: SCBPS. Right: SCBP. Comparison of depth slices for inversions with and without station terms.

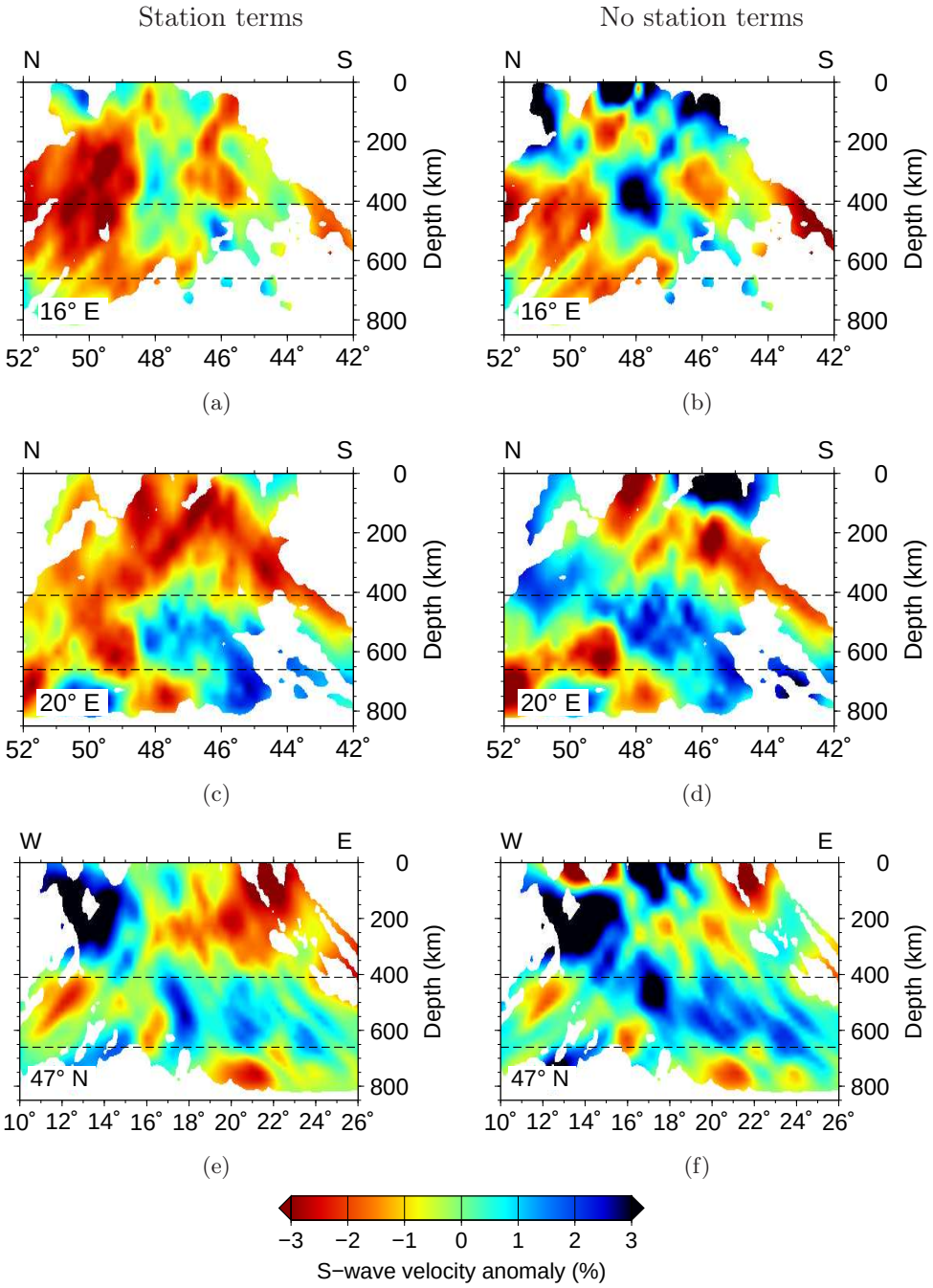

Figure 5.17: Left: SCBPS. Right: SCBP. Comparison of cross-sections for inversions with and without station terms.

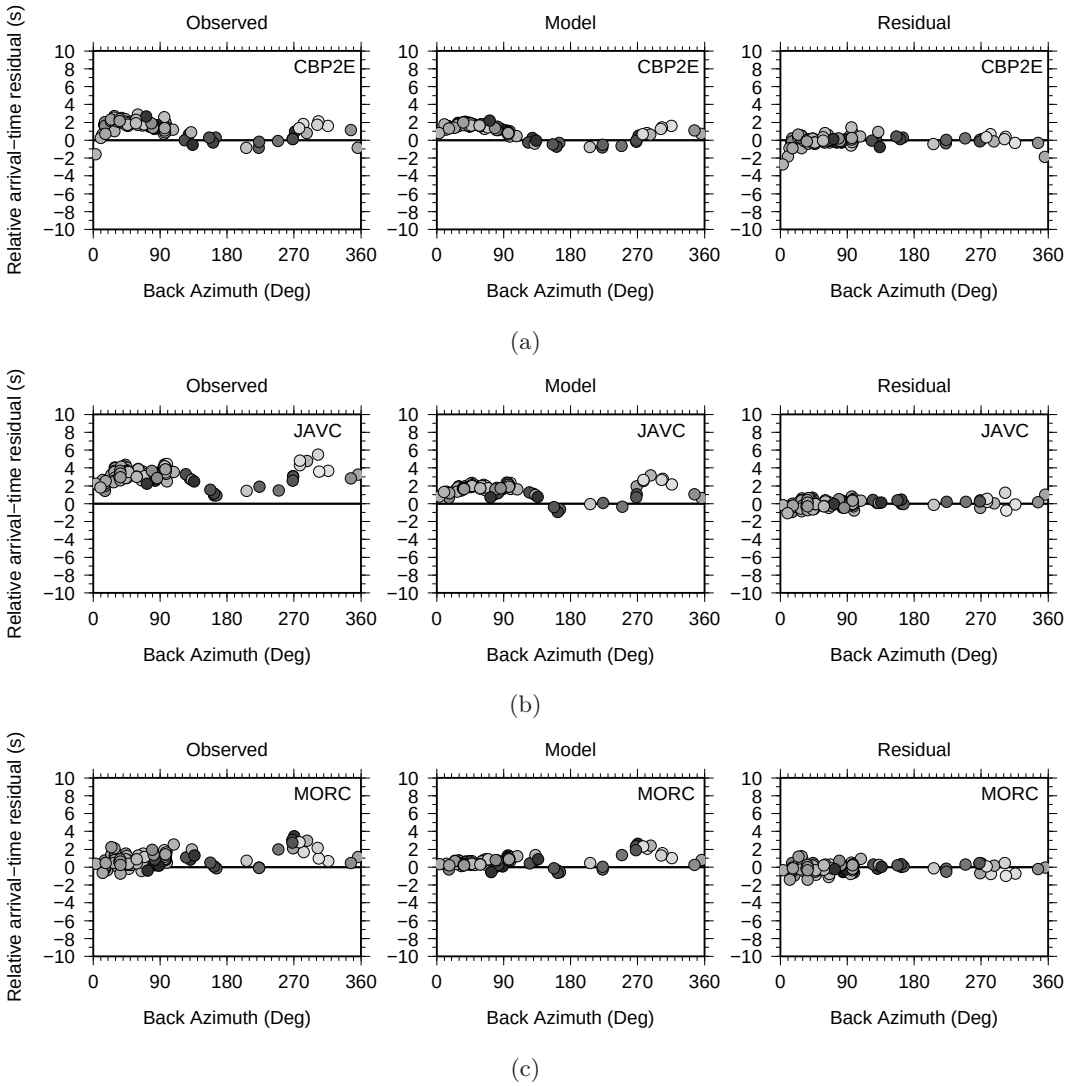

Figure 5.18: Variation of S-wave residuals with back-azimuth for three typical stations: CBP2E (48.38°N, 16.64°E), JAVC (48.86°N, 17.67°E) and MORC (49.78°N, 17.54°E). Left: the observed relative arrival-time residuals; Middle: model prediction for the relative arrival-time residual through the solution model; Right: Solution residuals after the inversion.

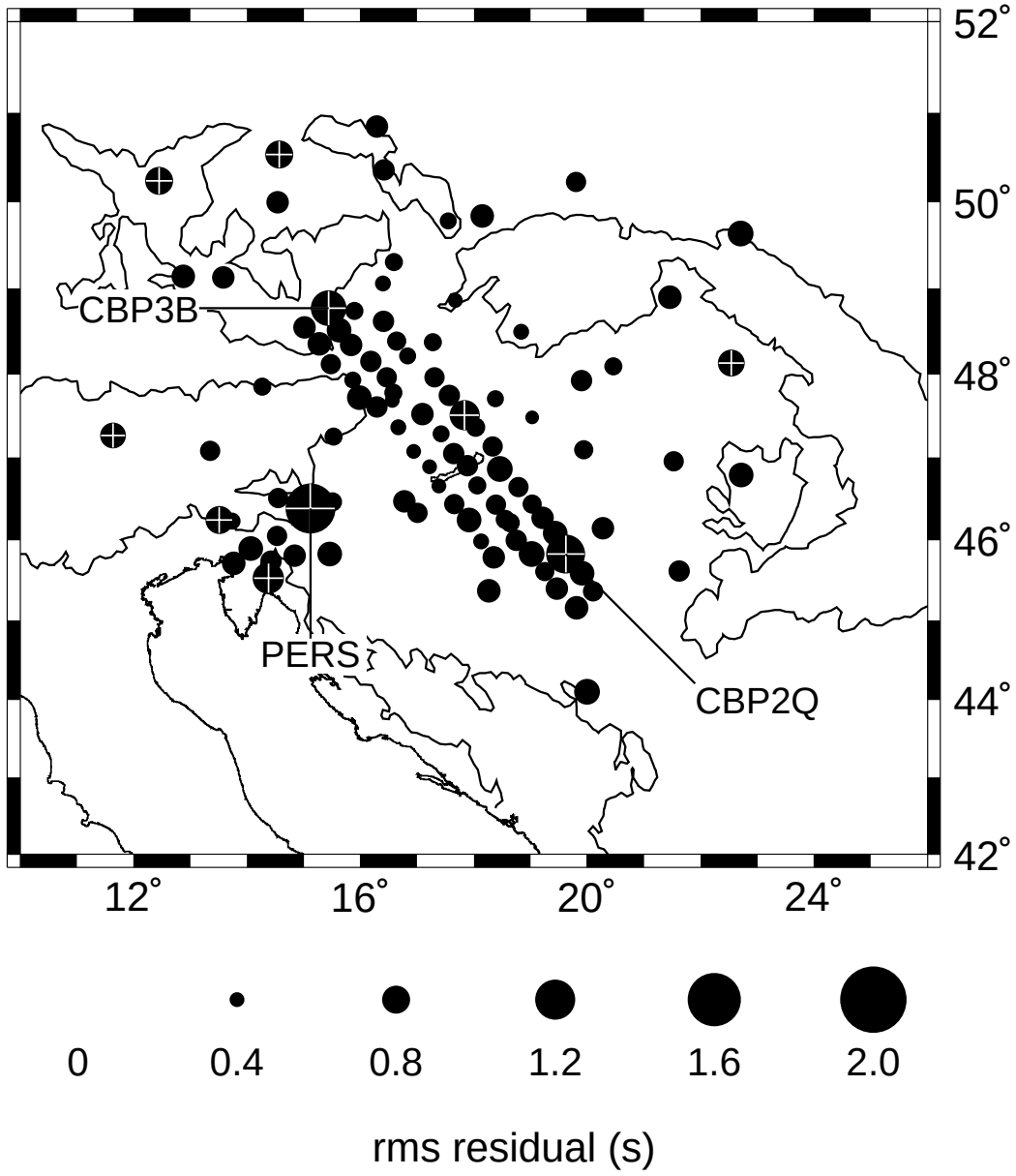

Figure 5.19: Map plot of the rms solution residual at each station. The 10 stations with the largest rms are marked by white crosses. The mean rms solution residual for all stations is 0.618 s. The three stations shown in figure 5.20 are labelled.

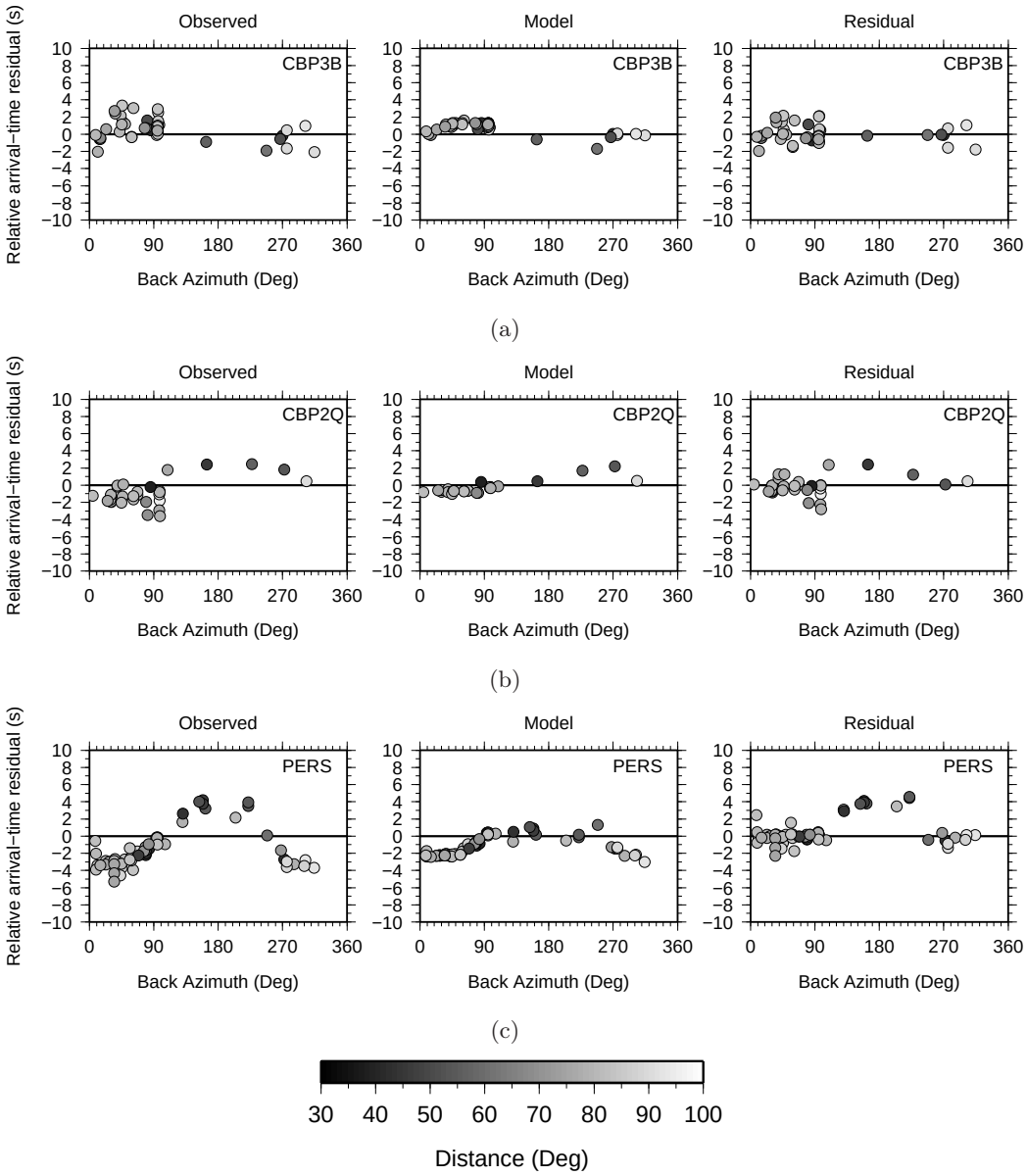

Figure 5.20: Variation of relative arrival-time residuals with back-azimuth for the three stations with the worst fit to the data: CBP3B (48.77°N, 15.44°E), CBP2Q (45.82°N, 19.62°E) and PERS (46.38°N, 15.12°E). Left: the observed relative arrival-time residuals; Middle: final model prediction for relative arrival-time residuals; Right: solution residuals after the inversion.

late arrival-times compared to the observed data, though the delay is small compared to the rms misfit.

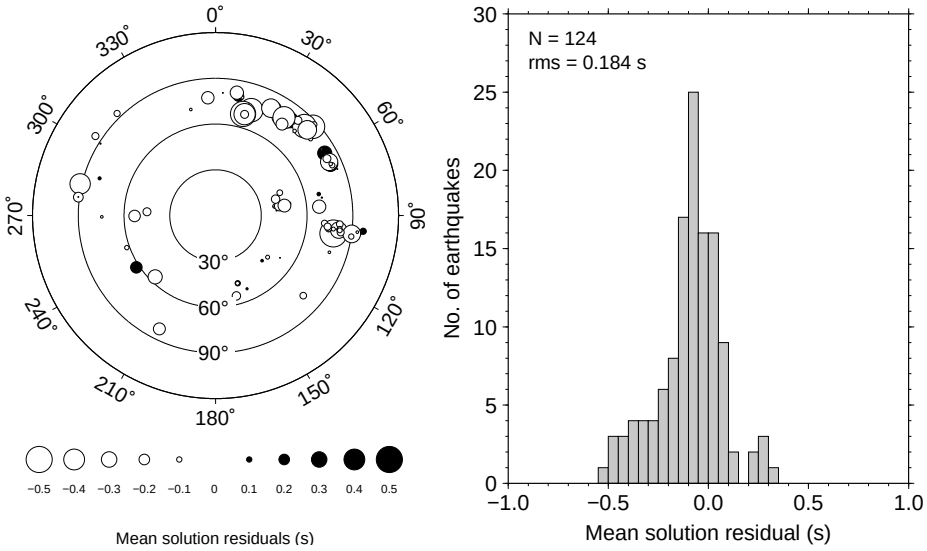

(a) (b)

Figure 5.21: Mean final residuals after the tomographic inversion for each event. In (a) white circles are negative residuals; black circles are positive residuals. Concentric circles show the great circle distance from the centre of the Carpathian-Pannonian region in 30° intervals. Event back-azimuth is shown. In (b) the histogram shows the frequency distribution of the mean solution residuals for each event.

Chapter 6

Deterministic crustal corrections

6.1 Overview

In this chapter, I assess the effect of using an *a priori* deterministic crustal correction on the P-wave relative arrival-time residuals. The correction times are obtained from a variety of sources including wide-angle seismic reflection, seismic refraction data and receiver functions, and comprise the best crustal velocity data available for the region. The results of inverting the corrected data are compared to the inversion of uncorrected data, both with and without station terms included in the inversion procedure. The naming convention for the tomographic models follows the previous chapters, with the addition of CC indicating the deterministic crustal correction was applied to the relative arrival-time residuals prior to the inversion.

6.2 Motivation

The results presented in chapter 4 have all been inverted for slowness perturbations, source terms (earthquake relocations) and station terms. The station terms absorb time corrections beneath each receiver to reduce the effect of the heterogeneous and unresolvable crust. As shown in section 4.6, by including station terms, short wavelength crustal features are prevented from being mapped into the long wavelength mantle model. Any further systematic errors associated with a station are also absorbed into this term. Completely neglecting the effect of the crust can lead to large errors introduced into the tomographic model. For example, Koulakov et al. (2009) cites the change in sign of the velocity anomaly seen beneath the south-eastern Carpathians between the tomographic models of Piromallo & Morelli (2003) and Martin et al. (2006). A similar effect was

shown in my results beneath the Eastern Alps in comparing the effect of station terms on the inversion (section 4.6).

A number of regional tomographic studies (e.g. Koulakov et al. (2009); Martin et al. (2005); Waldhauser et al. (2002)) instead of using station terms, apply deterministic crustal corrections to the travel-time residuals using *a priori* knowledge of crustal velocity structure from previous geophysical studies. Waldhauser et al. (2002) shows that for these inversions, if crustal anomalies are not corrected for, they are erroneously mapped into the upper-mantle, causing systematic errors in the inverted mantle structure. Their corrections are applied on an event-station basis, with Waldhauser et al. (2002) stating that static travel-time corrections (station terms) are inadequate due to large azimuth and distance-dependent residual variations. However, in studies only using teleseismic data, waves will traverse the crust near-vertically. For the P-wave data in the present study, the mean epicentral distance is 74.8°, which corresponds to an angle of incidence at the base of the Moho (at 35 km) of 24.8°. For two events with epicentral distances of 74.8°, the maximum distance between piercing points (i.e. for a 180° difference in back-azimuth), at the Moho is 24.3 km. With the radius of the Fresnel zone approximately 25.4 km at this depth, a large residual variation at a station, would reflect mantle structure rather than crustal heterogeneity.

The use of station terms however, does ignore prior knowledge that we have about the Earth. Nolet (2008) warns that with a velocity anomaly under a station - e.g. from a deep craton or mantle plume - there is a danger that the heterogeneity will always result in a late or early arrival, which will be absorbed into the station term and could be interpreted as a crustal correction.

With a large amount of data available for the European crust, I can assess both the robustness of the station terms and the validity of applying a deterministic crustal correction using the *a priori* data. I compare the tomographic inversions which use the deterministic crustal corrections, with the inversions for which the station corrections have been calculated during the inversion process (i.e. station terms).

6.3 Crustal model

Choosing a suitable crustal model to use for the Carpathian-Pannonian region is not straightforward. Multiple Moho maps exist for Europe which vary in resolution, and

display large discrepancies. For example, Tesauro et al. (2008) finds differences of up to 15 km between the Moho depths of CRUST5.1 (Mooney et al., 1998), CRUST2.0 (Bassin et al., 2000) and SVEKALAPKO (Kozlovskaya et al., 2004).

The EuCRUST-07 model (Tesauro et al., 2008) provides a high resolution (15' x 15' grid) 3-D crustal velocity model for Europe, which has been successfully used in previous tomographic studies (e.g. Koulakov et al., 2009) as a reference model for crustal corrections. However, despite the excellent resolution of the model, the datasets included from the Carpathian-Pannonian region are relatively sparse and the model relies heavily on interpolation. With seismic refraction and wide-angle reflection projects such as CELEBRATION 2000 and ALP 2002 (Guterch et al., 2003), the crustal velocity in the Carpathian region is now better constrained than in the EuCRUST-07 model. The Moho depth map of Grad et al. (2009), includes these data in their compilation to produce a European Moho depth map (figure 6.1).

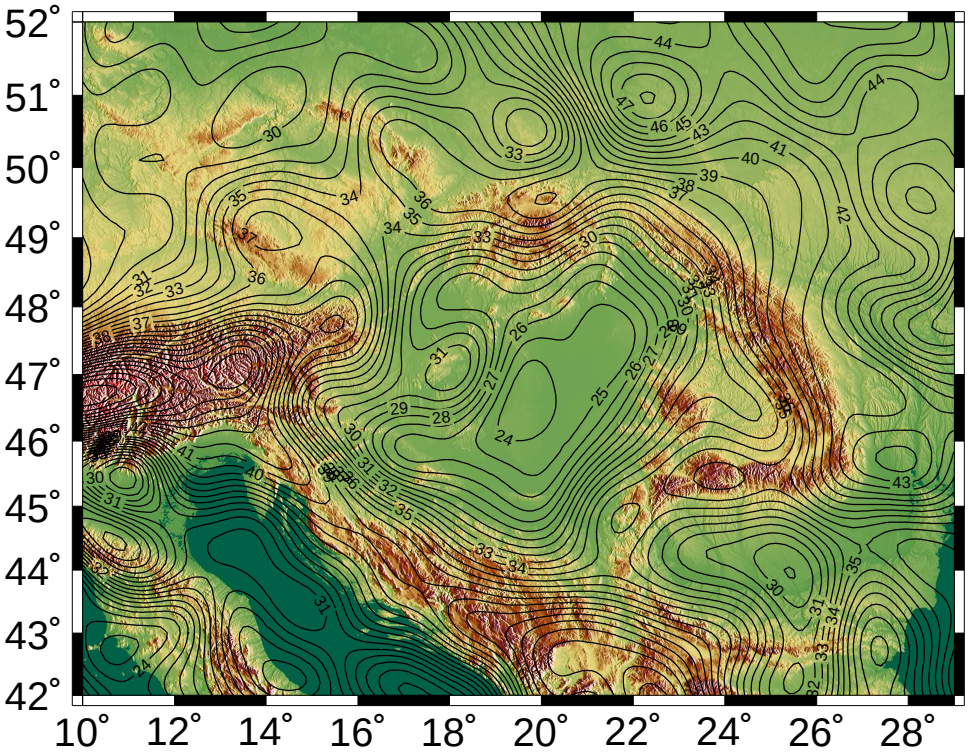

Figure 6.1: Contour map of the Moho in the Carpathian-Pannonian region using data from Grad et al. (2009).

I therefore used the Moho depth map of Grad et al. (2009) to obtain a crustal thickness at every station. To obtain crustal velocities beneath the stations, I have used velocity models obtained from seismic reflection and refraction lines from regional 3D tomography, and from receiver function studies.

Average P-wave crustal velocities are obtained for 58 of the 100 stations using the 3D model of Behm et al. (2007b). Local 3D tomography by Kovács (2009) for eastern and western Hungary has also provided crustal velocities for a further 28 stations. The crustal velocities beneath the remaining 15 stations are obtained from the BM3A velocity model of Geissler et al. (2008) and from the crustal velocities of Crotwell & Owens (2005).

In calculating the crustal correction time (t_{corr}), a datum of 32.2 km equal to the mean Moho thickness is used. The travel-time is calculated from receiver to the Moho defined by Grad et al. (2009), through this new crustal velocity model beneath each station for each ray-path. The *iasp91* travel-time from the Moho to the datum is added to produce a uniform correction depth. The crustal correction is then defined as the difference between this travel-time and the *iasp91* time to the datum.

In addition to the crust, the effect of topography is also accounted for by removing the travel-time from the surface to each station elevation for the *iasp91* ray-paths (i.e. vertical ray-paths are not assumed). The correction becomes,

$$t_{corr} = t^{D}_{iasp91} - \left(t^{M}_{mod} + t^{MD}_{iasp91}\right) - t_{topo} \tag{6.1}$$

where (t^{D}_{iasp91}) is the *iasp91* time to the datum, t^{M}_{mod} is the new crustal model time to the Moho, t^{MD}_{iasp91} is the time from the Moho to the datum, and t_{topo} is the travel-time associated with the topography. Figure 6.2 shows a representation of the travel-times used in (6.1).

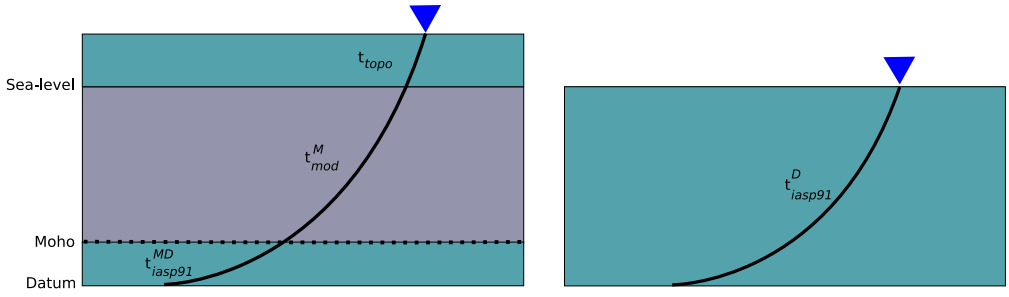

Figure 6.2: Cartoon showing the travel-times for the deterministic crustal correction in (6.1). The blue shaded region represents the *iasp91* model and the grey shaded region represents the new velocity model beneath each station.

The average crustal velocity and Moho thickness for each station are shown in table 6.1, with the velocity contoured in figure 6.3. As the correction is dependent on ray geometry, the 15583 crustal correction times are provided in the supplementary CD (see appendix D).

Table 6.1: Table showing the crustal thickness, and average crustal velocity used to compute the deterministic crustal correction for each station. Data references are: 1. Eastern Alps and western Pannonian Basin - Behm et al. (2007b); 2. Pannonian Basin - Kovács (2009); 3. European wide receiver functions - Geissler et al. (2008); 4. Earthscope receiver functions - Crotwell & Owens (2005).

Station	Moho Depth (km) (Grad et al., 2009)	Mean Vp (kms^{-1})	Reference
ARSA	37.471	6.377	1
BEH	28.957	5.944	1
BUD	27.710	6.061	2
BUKL	26.306	6.313	2
BZS	31.800	6.210	3
CADS	43.124	6.517	1
CBP2C	36.255	6.398	1
CBP2D	34.913	6.271	1
CBP2E	34.084	6.138	1
CBP2F	32.786	6.032	1
CBP2G	29.261	6.016	1
CBP2H	28.784	6.000	1
CBP2I	30.121	6.113	1
CBP2J	31.242	6.180	1
CBP2K	31.503	6.444	2
CBP2L	30.007	6.234	2
CBP2M	26.432	6.438	2
CBP2N	24.334	6.435	2
CBP2O	23.714	5.984	2
CBP2P	23.836	5.771	2
CBP2Q	24.354	5.937	2
CBP2R	24.778	5.937	2
CBP2S	25.600	5.937	2
CBP3B	36.895	6.412	1
CBP3C	37.497	6.416	1
CBP3D	37.962	6.415	1
CBP3E	37.460	6.271	1
CBP3F	35.647	6.257	1
CBP3G	34.407	6.205	1
CBP3H	30.234	5.999	1
CBP3I	30.284	5.987	1
CBP3J	31.360	6.107	1
CBP3L	30.236	6.107	1
CBP3M	27.203	6.385	2
CBP3N	25.511	6.392	2
CBP3O	24.672	5.902	2
CBP3P	24.691	5.804	2
CBP3Q	25.132	6.006	2
CBP3R	25.445	6.198	2
CBP4B	36.922	6.371	1
CBP4C	37.767	6.406	1
CBP4D	39.109	6.428	1
CBP4F	39.001	6.384	1
CBP4G	36.565	6.347	1
CBP4H	32.678	6.189	1
CBP4I	31.022	6.056	1
CBP4J	30.641	6.094	1
CBP4K	30.000	6.053	1
CBP4L	28.647	6.014	1

Table 6.1: Continued.

Station	Moho Depth (km) (Grad et al., 2009)	Mean Vp (kms^{-1})	Reference
CBP4M	27.084	5.987	1
CBP4N	25.715	6.147	2
CBP4O	25.597	6.052	2
CEY	42.273	6.454	1
CONA	39.454	6.386	1
CRES	34.947	6.171	1
CRVS	28.769	6.260	3
DIVS	33.277	6.264	4
DPC	35.767	6.180	3
DRGR	30.560	6.100	4
DSZL	29.399	6.169	2
FGSL	25.934	6.276	4
GROS	31.216	6.148	1
JAVC	32.497	6.224	1
JAVS	42.713	6.547	1
KBA	47.890	6.433	1
KHC	37.059	6.354	1
KNDS	41.836	6.460	1
KRUC	34.168	6.384	1
KSP	34.307	6.240	3
KWP	36.554	6.530	4
LJU	40.199	6.378	1
MOA	39.649	6.285	1
MODS	30.449	6.036	1
MORC	36.401	6.375	1
NEML	27.633	5.936	1
NKC	30.656	6.210	3
OBKA	37.277	6.344	1
OJC	32.615	6.300	3
OKC	36.523	6.300	3
PERS	32.917	6.217	1
PKSM	25.100	6.326	2
PRDL	27.457	6.141	1
PRU	32.580	6.209	1
PSZ	26.537	5.753	2
PVCC	30.260	6.210	3
ROBS	43.392	6.478	1
SOP	34.429	6.215	1
SZEL	24.226	5.814	2
TARL	28.016	5.627	2
TIHL	31.629	6.177	1
TORL	23.791	5.545	2
TRI	41.674	6.456	1
TRPA	28.007	5.627	2
VISS	39.991	6.353	1
VRAC	34.092	6.382	1
VYHS	28.401	6.240	3
WET	34.100	6.510	3
WTTA	44.864	6.770	3
ZSAL	24.827	5.495	2
ZST	30.872	6.015	1

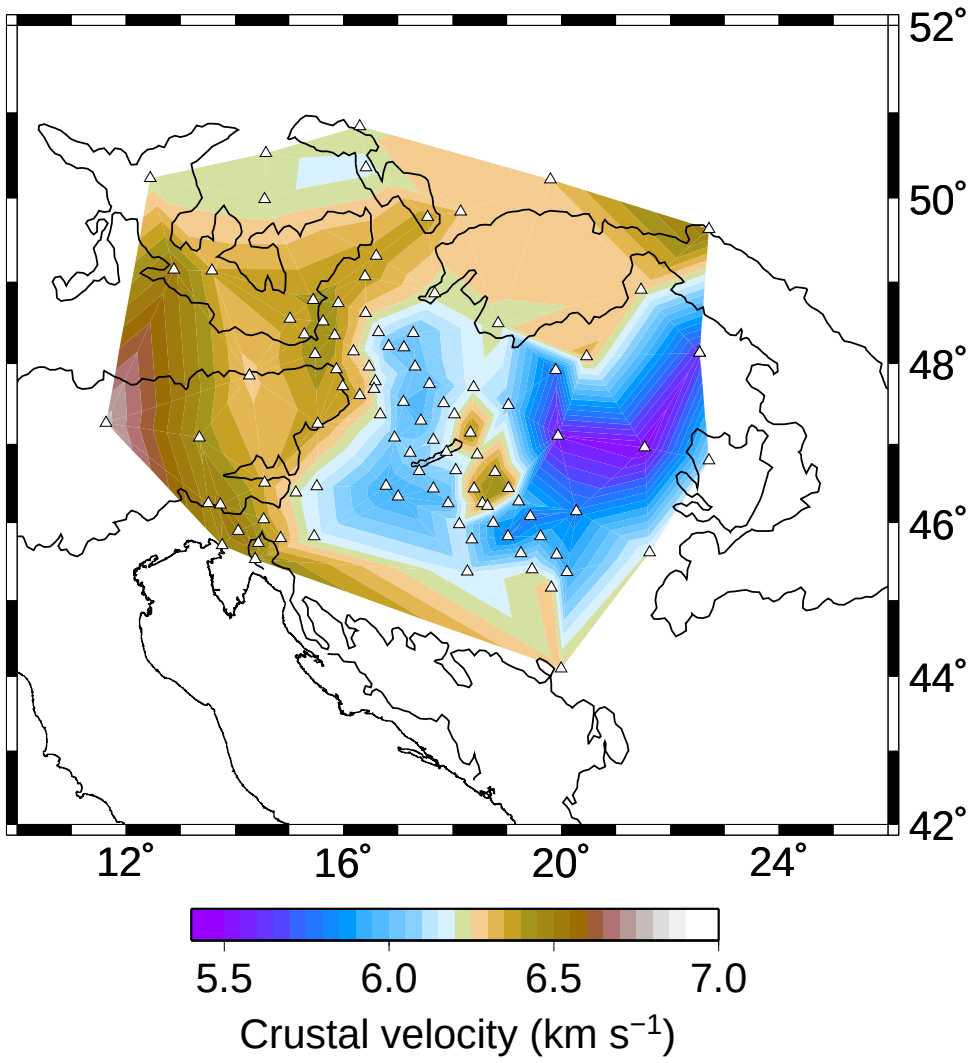

Figure 6.3: Contour map of the average P-wave crustal velocity beneath each station used for the deterministic crustal correction. The velocities are shown in table 6.1.

6.4 Results

The results for the deterministic crustal correction are split into two sections. Firstly, I present models which have not included a station term parameter in the inversion and compare results both with (model PCBPCC) and without (model PCBP) the deterministic crustal correction. Secondly, I include the station term in the inversion and assess the effect of the deterministic crustal correction (models PCBPS and PCBPSCC). A direct comparison between applying only a deterministic crustal correction (PCBPCC) and only including a station term is shown in the summary.

6.4.1 Inversions without station terms

In this section I compare images from the results of two inversions (models PCBP and PCBPCC) - with and without deterministic crustal corrections applied to the residuals. Figure 6.4 shows histograms of the relative arrival-time residuals and the solution residuals. The effect of the crustal correction on the relative arrival-time residuals has reduced the rms residual from 0.446 s to 0.438 s. The remaining residuals after the inversion also show an increased reduction, with a decrease in rms residual by 3.2% (from 0.154 s to 0.149 s) after applying the deterministic crustal correction.

The inversion models are shown in figures 6.5 and 6.6. For the depth slices shown (figure 6.5), the effect of the crustal correction is limited largely to the upper 75 km, with only minor changes in the amplitude of the anomaly at depths of 200 km and greater. At 75 km significant differences in structure are produced, but some similarities remain; in the eastern Pannonian Basin for example, the crustal correction has produced a larger, more discrete anomaly beneath the Makó/Békés, and Derecske basins. The crustal correction has the largest impact on the anomaly beneath the Eastern Alps. Without the correction, the inversion is mapping the late travel-times associated with the excess topography into slow anomalies. For example, for station KBA in the Eastern Alps, the topography correction (t_{topo} in (6.1)) is in the range of 0.305 s to 0.335 s, compared with the correction time not including t_{topo} (i.e. $t^{D}_{iasp91} - (t^{M}_{mod} + t^{MD}_{iasp91})$ from (6.1)), which is in the range of -0.038 s to -0.113 s. The crustal correction has little effect below 100–150 km depth (figure 6.6). The positive increase in velocity anomaly in the eastern Pannonian Basin has also decreased the smearing seen to the east of the model (figure 6.6(g)–6.6(i)).

6.4.2 Inversions with station terms

Including station terms in the inversions should ideally account for all unresolved crustal variations. Here, I present the results from inversions which include a station term in the inversion both with (model PCBPSCC) and without (model PCBPS) the deterministic crustal correction. The histograms of the residuals in figure 6.7 show an almost identical solution rms residual (0.130 s and 0.131 s). The station terms show a decrease in their rms from 0.243 s to 0.229 s (figure 6.8), indicating the deterministic crustal correction is reducing but not eliminating the need for the station term.

With an almost identical solution rms residual, the inversion results appear almost iden-

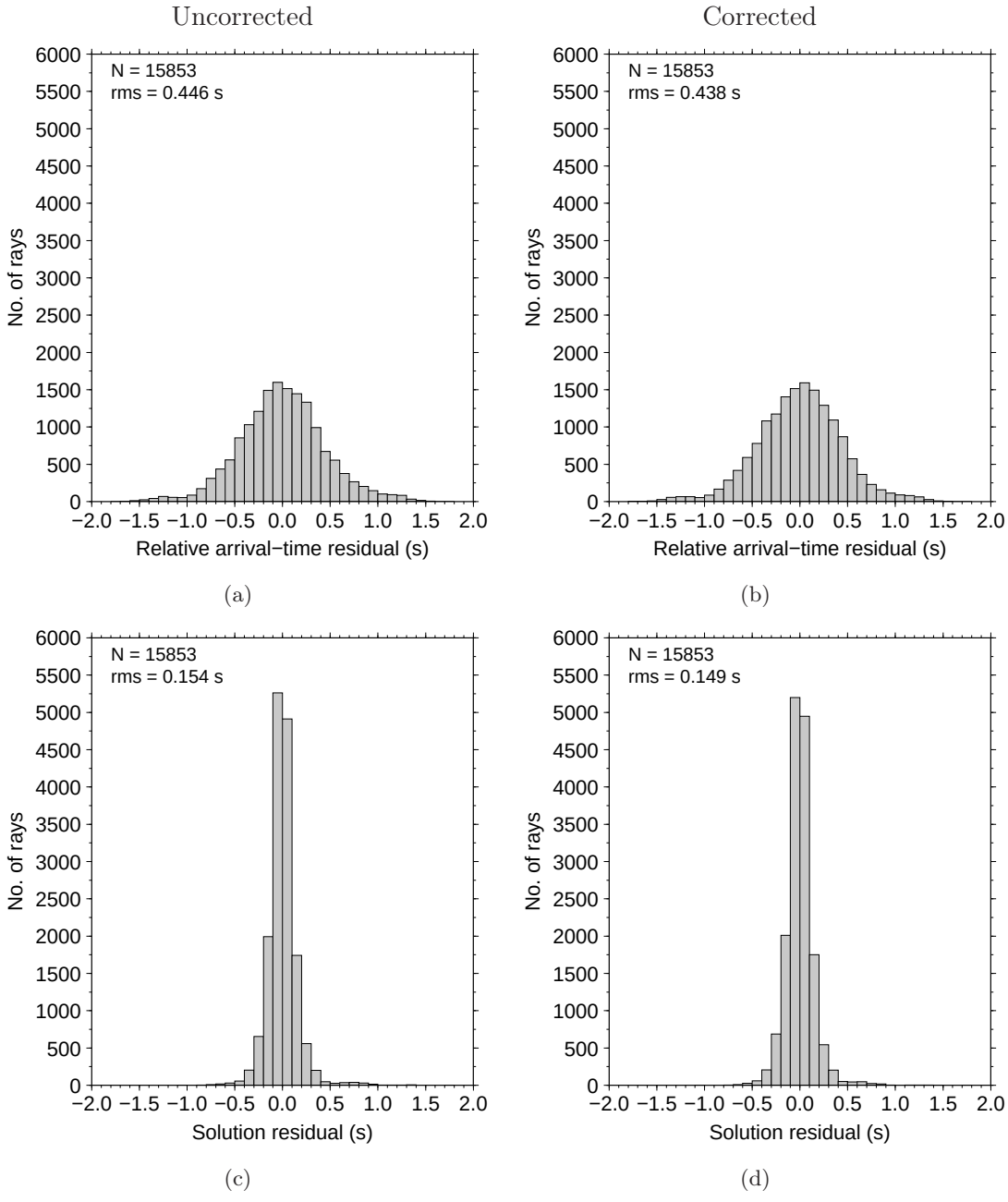

Figure 6.4: Histograms of the initial relative arrival-time residuals ((a),(b)) and the solution residuals after the inversion ((c),(d)) for the uncorrected (PCBP) and crustal corrected (PCBPCC) data, without station terms.

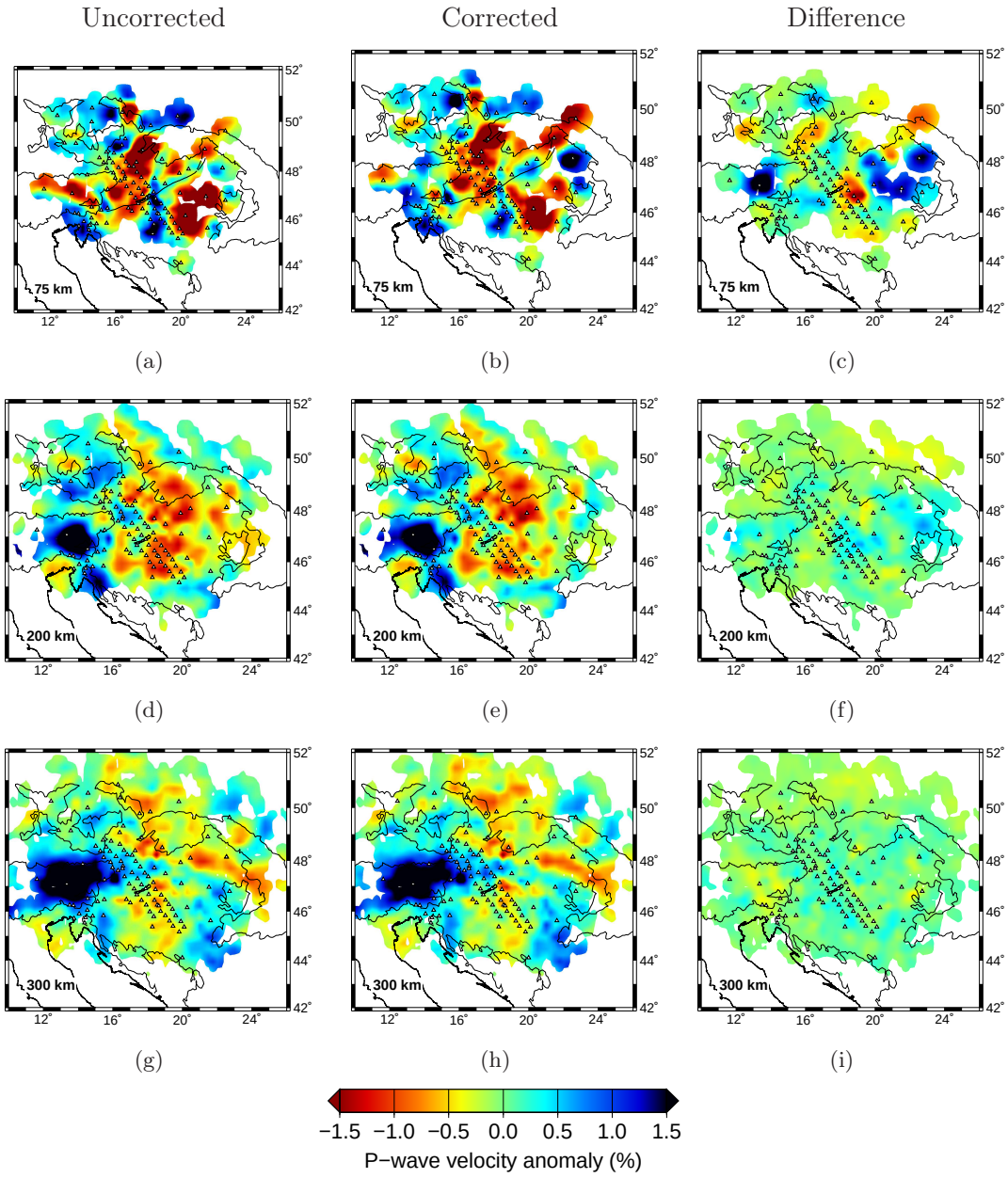

Figure 6.5: Left: model PCBP; Middle: model PCBPCC. Comparison of depth slices for inversions with and without the deterministic crustal correction, with no station terms included. The column on the right is the difference between the corrected and uncorrected models.

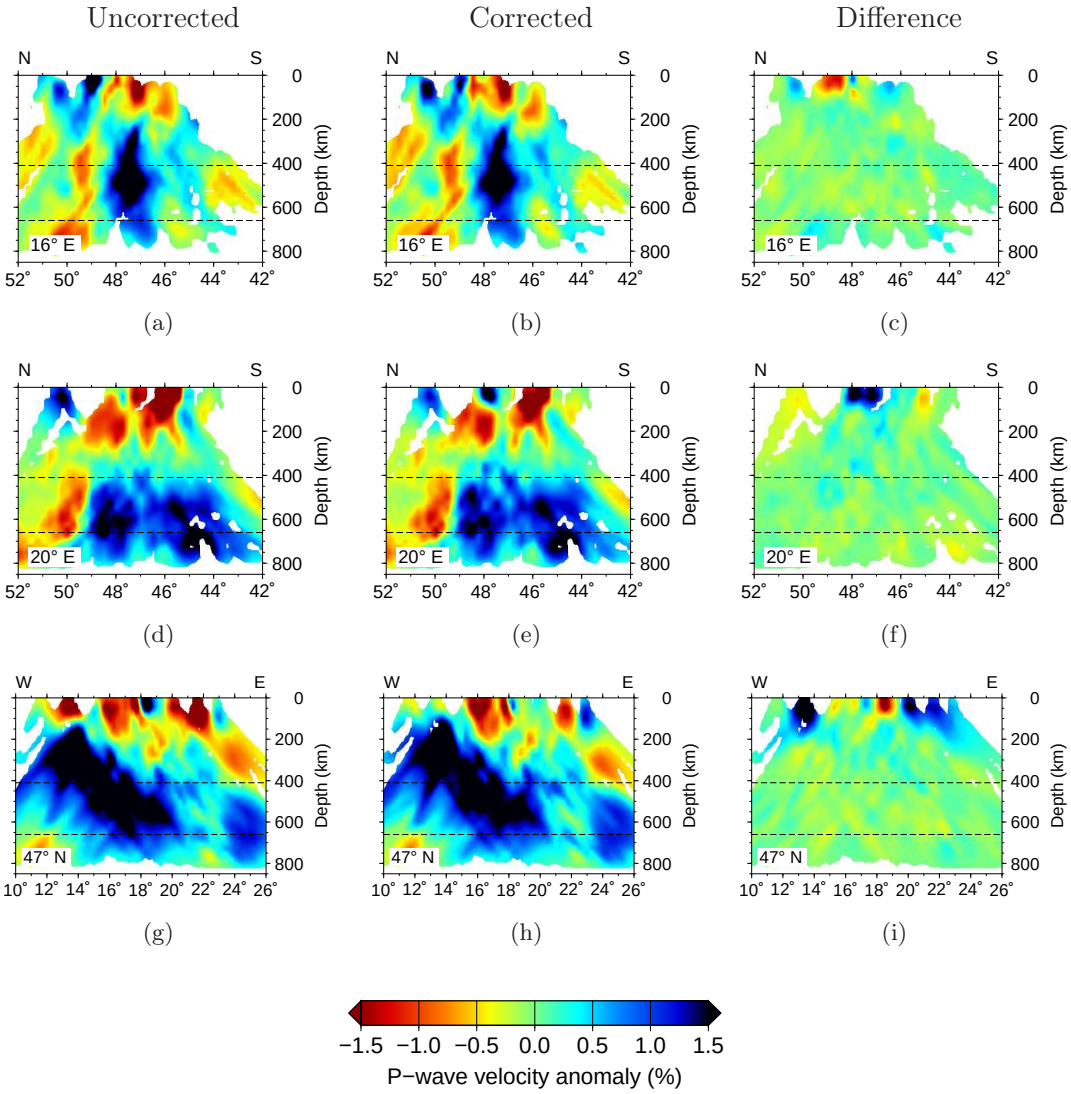

Figure 6.6: Left: model PCBP; Middle: model PCBPCC. Comparison of cross-sections for inversions with and without the deterministic crustal correction, and no station terms. The column on the right is the difference between the corrected and uncorrected models.

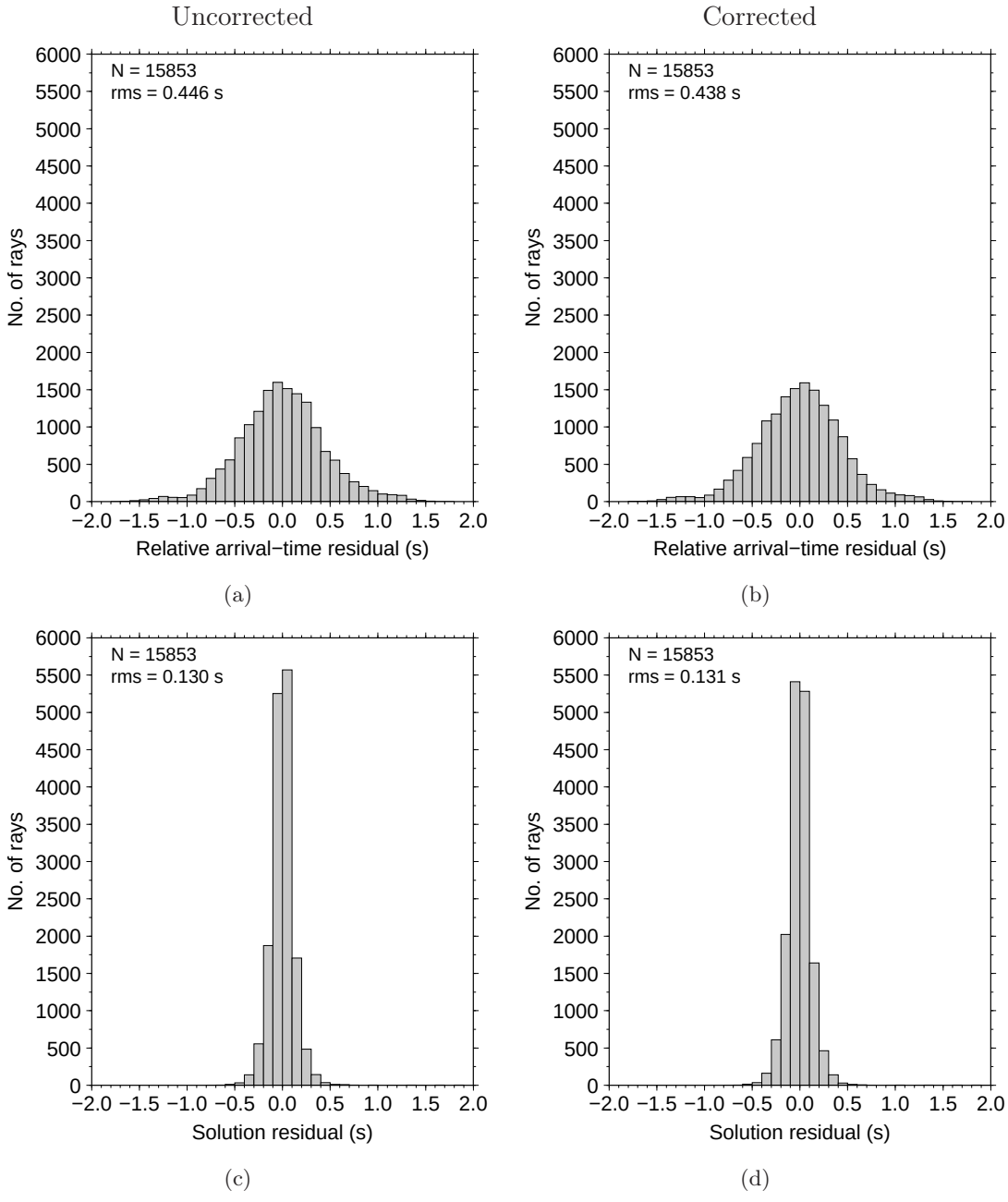

Figure 6.7: Histograms of the initial relative arrival-time residuals ((a),(b)) and the solution residuals after the inversion ((c),(d)) for the uncorrected (PCBPSCC) and crustal corrected (PCBPSCC) data with the station terms applied.

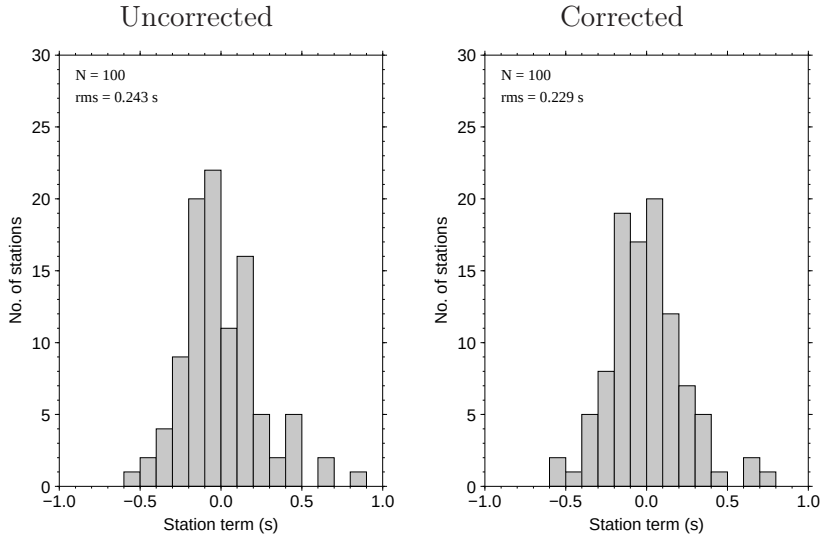

Figure 6.8: The station terms shown before (a) and after (b) the deterministic crustal correction is applied to the raw P-wave residuals. The histograms show a reduction in the rms station term from 0.243 s to 0.229 s with the correction applied.

tical. In both depth (figure 6.9) and cross-section (figure 6.10) there is no discernible difference between the models, as the station term is absorbing any remaining offsets not accounted for by the crustal correction.

6.5 Summary

With station spacing limiting resolution at shallow levels, accounting for crustal variations is essential to avoid spurious structure in the tomographic inversion. My results have shown that applying a deterministic crustal correction to the relative arrival-time residuals prior to the inversion improves the fit to the data, shown by a reduction in the rms residual (0.154 s to 0.149 s). This is reflected in changes to the tomographic models (PCBPCC and PCBP) to depths of up to 150 km.

When a station term is included in the tomographic inversion (model PCBPSCC), a deterministic correction further improves the fit to the data (rms residual of 0.131 s). However, solely including a station term whilst not applying a deterministic crustal correction (model PCBPS) produces a near identical fit to the data (rms residual of 0.130 s) as the station term is effectively able to absorb the total crustal variations accounted for in the deterministic correction. This is reflected in the increased rms station term of 0.243 s when the deterministic correction is not applied, compared to 0.229 s with the *a*

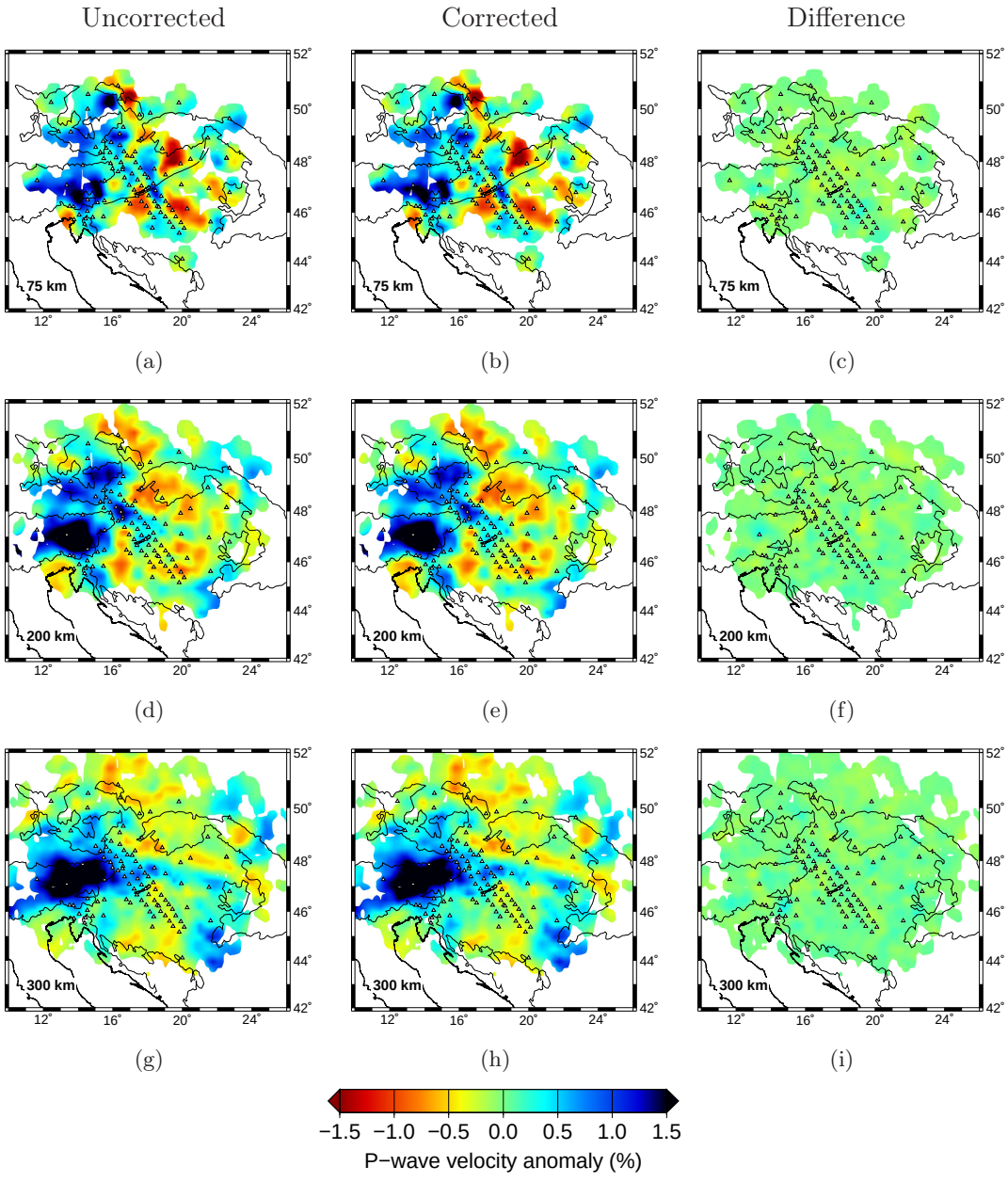

Figure 6.9: Left: model PCBPS; Middle: model PCBPSCC. Comparison of depth slices for inversions with and without the deterministic crustal correction, with station terms used in each case.

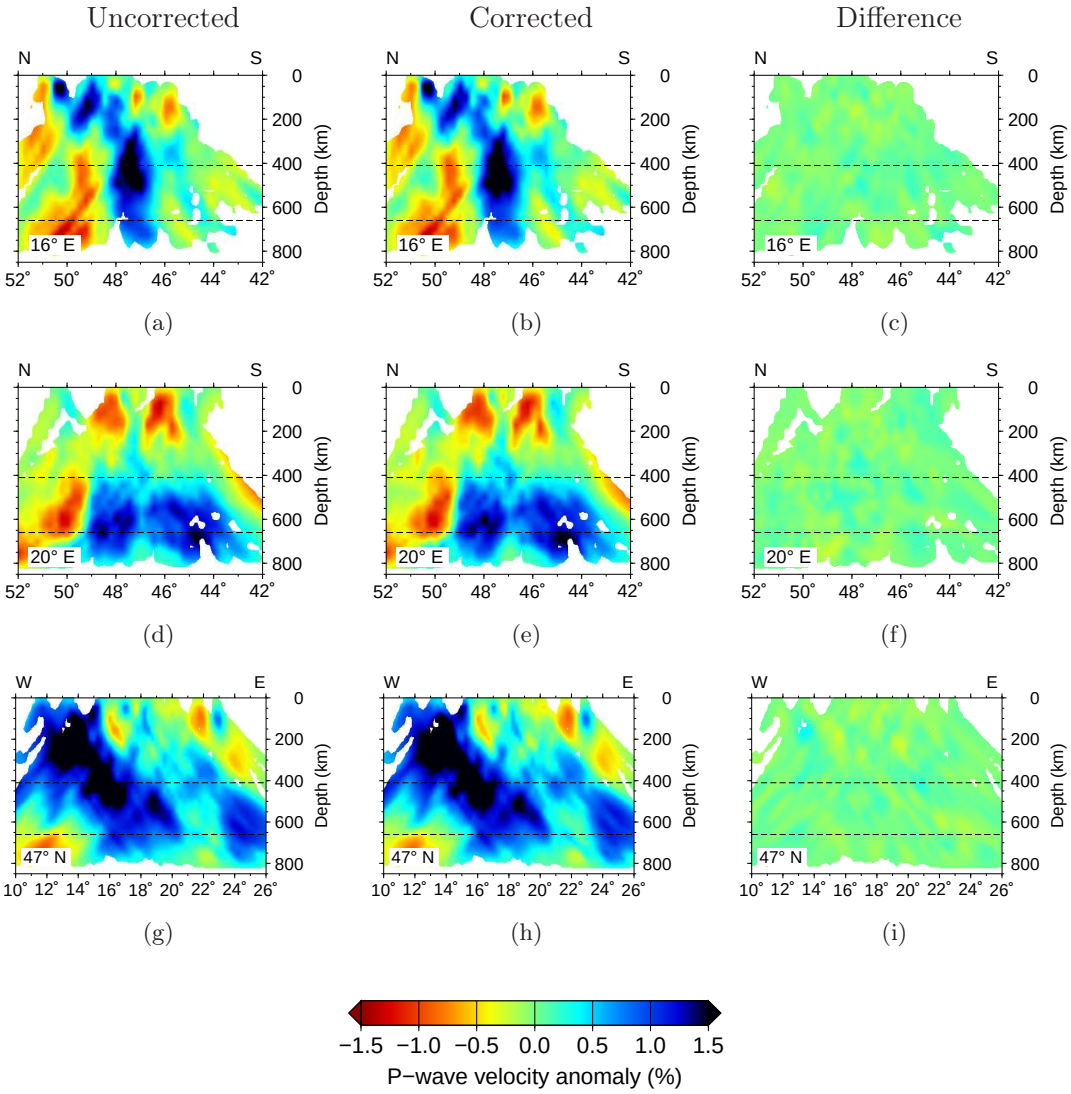

Figure 6.10: Left: model PCBPS; Middle: model PCBPSCC. Comparison of cross-sections for inversions with and without the deterministic crustal correction, with station terms used in each case.

priori correction. A direct comparison between models PCBPS and PCBPCC is shown in figure 6.11; the inclusion of station terms produces significant differences in the upper 150 km of the inversion solution.

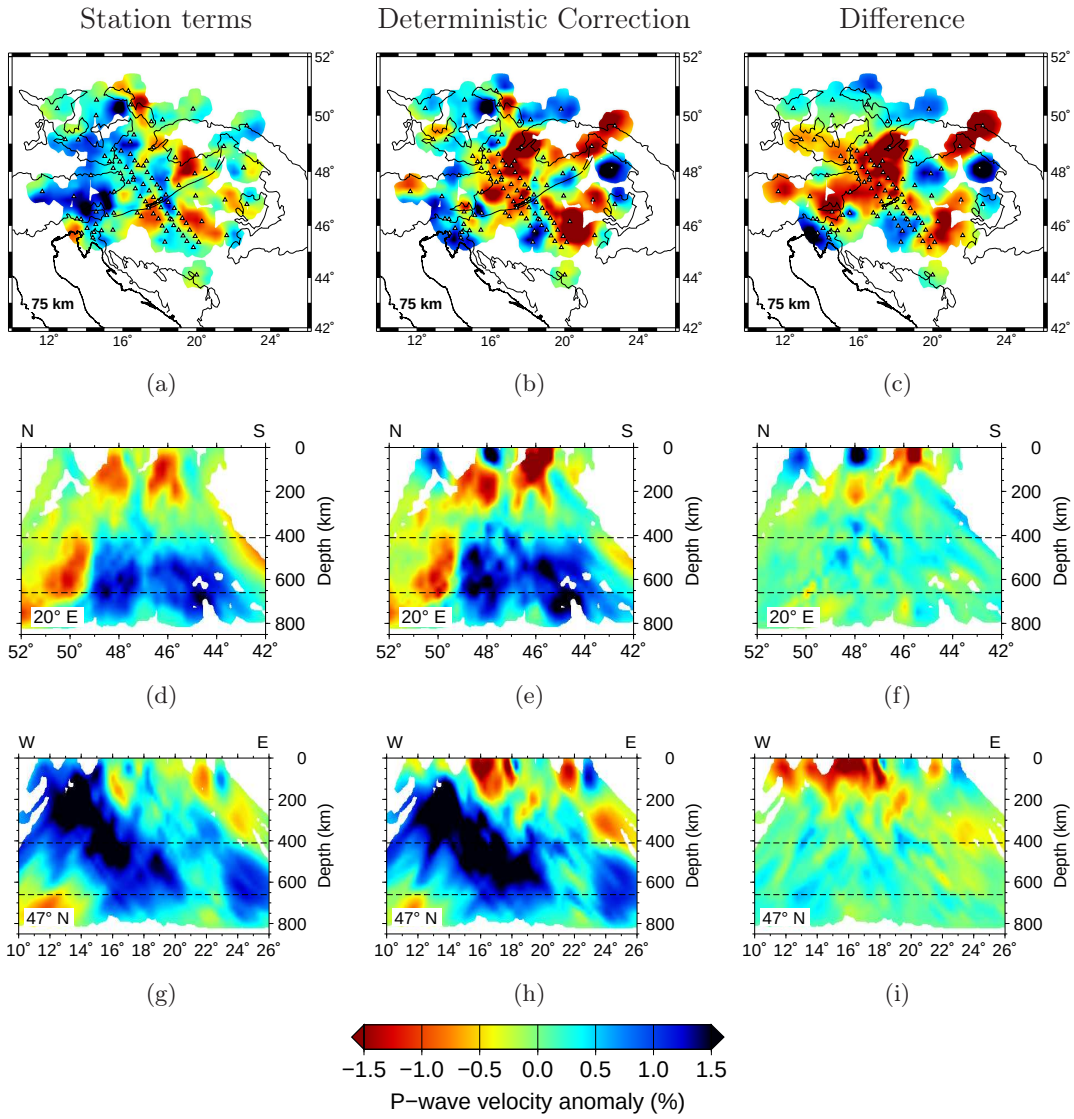

Figure 6.11: Left: model PCBPS; Middle: model PCBPCC. Comparison of depth slices and cross-sections for inversions with a station term and with a deterministic crustal correction but no station term.

The improved inversion achieved by including a station term compared to solely using the deterministic crustal correction is likely due to structure in the uppermost mantle also being unresolved. Comparing the mean deterministic crustal correction at each station with the corresponding station term (figure 6.12) shows the greater range in correction times for the station terms, which can accommodate the improved fit to the data in the inversion. With the minimum station spacing as much as 131 km, the depth at which

rays are unresolved is clearly going to extend beyond the crust and shows the necessity of a station term in the inversion.

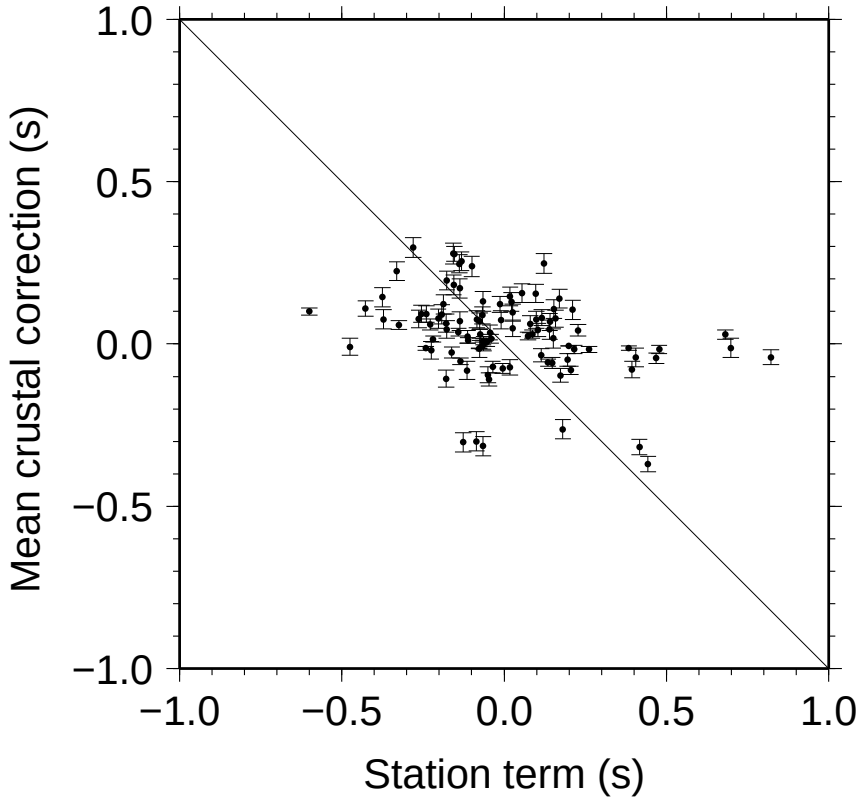

Figure 6.12: Comparison of the mean deterministic crustal correction at each station with the tomographic inversion derived station terms. A positive station term equates with a negative deterministic crustal correction. Error bars show 1 standard deviation for the deterministic crustal corrections.

Chapter 7

Discussion

7.1 Overview

In this chapter, the main features observed in the higher resolution P-wave tomographic model in chapter 4 are tested against a simple synthetic block model (PSBMS), to help characterise the observed anomalies and ensure that artefacts of the inversion are not being interpreted. The P and S-wave anomalies are then discussed and interpreted in terms of their geologic and geodynamic origin and compared with previous seismological studies. The effect of topography on the 660 km discontinuity is discussed and its impact on the inversion is assessed using competing synthetic models. Finally, implications for the interpretation on tectonic models of the Carpathian-Pannonian system are discussed.

7.2 Synthetic model resolution test

To assess the reliability of the interpretation of the preferred final P-wave model, the inversion procedure is applied to a simple synthetic block model (PSBMS) with structures similar to those observed in the solution model. The synthetic model is designed to include the following features in the upper-mantle: i) four localised slow anomalies (-3%) around the Pannonian Basin from 50–100 km depth; ii) a fast tabular vertical structure (+3%) beneath the Alps from 50–350 km, which extends out beneath the Pannonian Basin from 300–410 km; iii) an anomalously fast (+2%) mantle transition zone (410–660 km) roughly underlying the Pannonian Basin. The exact anomaly locations are shown in table 7.1. These structures are implemented as tabular blocks so that heterogeneity introduced by the inversion procedure is readily available. The synthetic travel-times are computed using the same method used for the checkerboard sensitivity tests (section 4.4)

and Gaussian distributed noise with a standard deviation of 0.04 s is added.

Anomaly (%)	Latitude (°)	Longitude (°)	Depth (km)
3	47.5–48.5	19.0–20.0	50–100
3	45.5–46.0	17.0–18.0	50–100
3	45.5–46.0	19.0–20.0	50–100
3	46.2–47.2	21.5–22.5	50–100
3	46.5–47.5	9.0–15.0	50–350
3	46.5–47.5	15.0–17.0	300–410
2	46.5–47.5	15.0–17.0	410–660
2	45.0–49.0	20.5–25.0	410–660
2	45.5–48.5	18.5–20.5	410–660
2	45.0–48.0	17.0–18.5	410–660

Table 7.1: Table showing the anomalies used in the simple synthetic model, PSBMS, shown in figure 7.1.

The input model for PSBMS and the images recovered from inverting the synthetic travel-times are shown in figure 7.1. The corresponding inverted images from the final solution model are shown for comparison in figures 7.1(k)–(o).

In the 75 km depth slice (figure 7.1(f)), the four slow anomalies are clearly imaged, although their amplitude is decreased by a factor of about 2. The anomaly associated with the Békés and Makó basins in the south-east Pannonian Basin (45.5°N–46.0°N, 19°E-20°E and 50–100 km depth), has similar volume to the synthetic model but has less volume than the corresponding anomaly in the PCBPS model solution. The shallow slow anomalies have almost doubled in their depth extent in the PSBMS inversion (figure 7.1(j)) but still do not extend as deep as the corresponding anomalies implied by the observed data (figure 7.1(o)). The slow anomalies in PSBMS are also associated with surrounding fast halos; an artefact of the inversion, which may account for the similar fast anomalies observed in the PCBPS model at 75 km beneath the Pannonian Basin (figure 7.1(k)). The fast Alpine block beneath the Eastern Alps and western Pannonian Basin is also generally well represented in the inversion images where ray coverage is adequate, with only minimal vertical smearing up to 50 km. In the central Alps, recovery of the fast anomaly is prevented here by lack of ray coverage at lithospheric depths.

It is also important to note features at 75 km in the PCBPS model (figure 7.1(k)), which are not accounted for in the inversion of the PSBMS model. For example, the inversion of the observed data shows slow material extending beneath the Vienna basin from the western edge of the Carpathians. On the eastern edge of the Bohemian Massif the slowest

anomaly (-2%) at 75 km is imaged and contrasts with a fast anomaly (maximum of 1.8%) occurring beneath the Bohemian Massif. The absence of these anomalies in the inversion of the synthetic data, suggests that they represent real structure, rather than an artefact of the inversion.

At 300 km (figure 7.1(g)), the Alpine anomaly is recovered well due to the good ray coverage to the west. However, compared to the structure evident in the inversion of the observed data (model PCBPS - figure 7.1(l)), the linear nature of the synthetic anomaly appears an oversimplification. Rather, consistent with previous tomographic images from the Alps (e.g. Lippitsch et al., 2003), this fast structure appears as localised fast anomalies, relative to the elongate structure of the Alps as a whole.

The fast mantle transition zone is adequately recovered in the PSBMS model (figure 7.1(h)), though vertical smearing increases its apparent depth extent by up to 100 km, both to shallower and deeper levels (figure 7.1(i)). Although the synthetic model does not image the 'doughnut'-like structure at 600 km depth, somewhat faster velocities are inferred around the edge of the fast MTZ structure (figure 7.1(h)). Thus, some of the variation within the real solution (figure 7.1(m)), could be an artefact of the inversion, demonstrating the need for caution to be applied in interpretation.

Minor low velocity shadows to the north of the fast anomaly in the MTZ are present in the inverted synthetic image, but comparison with the steep velocity gradients in the real solution shows that the localised transition from fast material beneath the Pannonian Basin to slow beneath the Western Carpathians must be present in the MTZ. In summary, the accuracy with which the synthetic model is recovered provides confidence that the P-wave images for the MTZ are well resolved.

7.3 Seismic structure of the Carpathian-Pannonian region

7.3.1 Slow anomalies of the upper-mantle

Whilst there is better spatial resolution in the P-wave inversion from the increased ray-coverage, both the P and S-wave inversions should be considered together for a more complete interpretation of seismic structure in the Carpathian-Pannonian region. Figure 7.2 shows the correlation between P and S-wave anomalies from six depth slices with a similar moderate linear correlation at each depth. With differences in resolution and

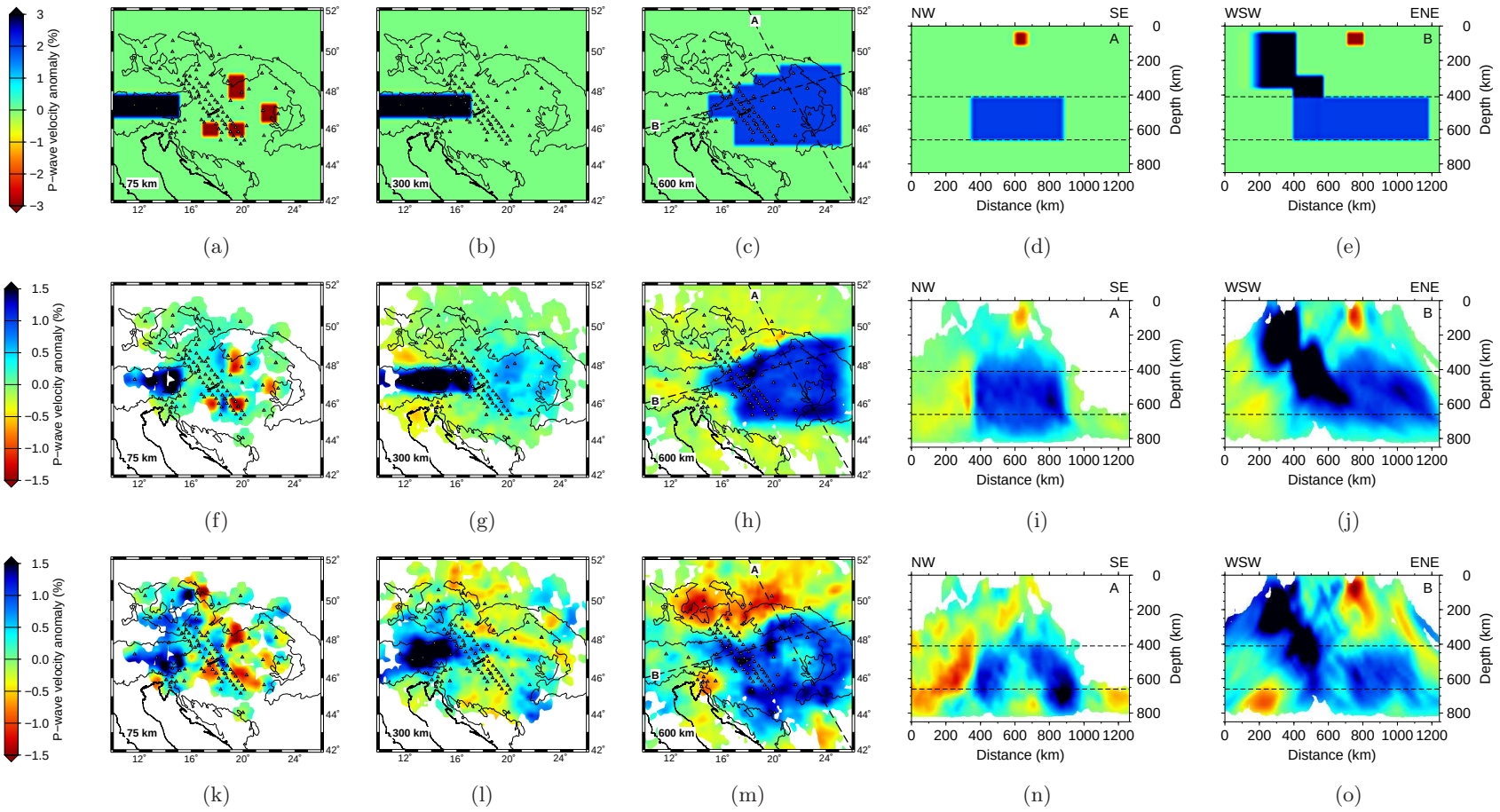

Figure 7.1: Top (a)–(e): PSBMS - synthetic model of a simplified structure inspired by the results of the data inversion. The anomaly locations are listed in table 7.1 and describe: four localised slow anomalies from 50–100 km depth; a fast vertical structure beneath the Alps from 50–350 km, which extends beneath the Pannonian Basin from 300-410 km; and an anomalously fast MTZ from 410–660 km. Middle (f)–(j): Recovered structure after the inversion of the synthetic travel-times from the above model. Bottom (k)–(o): corresponding sections from the preferred solution model. Locations of the cross-sections are shown in the 600 km depth slice.

regularisation between the P and S-wave inversions, and by using relative arrival-time residuals, direct interpretation of V_p/V_s or $\delta V_p/\delta V_s$ is not possible. However, the differences observed in the amplitudes of the P and S-wave anomalies are probably due to the nature of the anomaly. Goes et al. (2000) suggest that velocity perturbations in the European upper-mantle are most likely due to temperature changes. Compositional variations only have a secondary effect on seismic velocity (e.g. Goes et al., 2000; Jackson et al., 1998), and are typically of the order of ±1% for P-waves (Cammarano et al., 2003). For fluid to play a significant role Nakajima et al. (2001) show that in regions of low velocity, a low V_p/V_s is needed, whilst for thermal anomalies Goes et al. (2000) show that for a 100°C increase in temperature, reductions of 0.5–2% in V_p and 0.7–4.5% in V_s are predicted. In the synthetic tests, the recovered anomalies are typically reduced in amplitude by a factor of about 2. The inferred actual maximum amplitudes of the anomalies of about 3% and 5% (for P and S-waves respectively) imply that the slow anomalies are likely to be primarily thermal features.

The shallowest depth slice I interpret is 75 km, which for the Pannonian Basin is just below the lithosphere-asthenosphere boundary, estimated at 45–60 km depth (Tari et al., 1999). With the numerous controlled source refraction and wide-angle reflection seismic experiments throughout the region, the depth to the basement is reasonably well-known and the sedimentary sub-basins can be identified through the present-day sediment thickness maps. In figure 7.3, a compilation of sediment thicknesses from Behm (2006); Laske & Masters (1997) and Kilényi et al. (1991), show the main sedimentary basins in the Pannonian Basin.

The localised slow anomalies observed in the 75 km P-wave section (figure 7.3(c)), which extend roughly from 50–150 km, largely correspond with local extensional depocentres seen in figure 7.3(b). In the east of the Pannonian Basin a slow anomaly (-1.28%) appears beneath the Makó and Békés sub-basins (figure 7.3(b)), which are related to the failed Tisza rift (Tari et al., 1999), with a further anomaly (-0.82%) beneath the Derecske sub-basin (e.g. Corver et al., 2009) in the north-east of the Pannonian Basin. In the S-wave images, these slow anomalies have merged (figure 7.3(d)) and have significantly larger amplitudes (up to -4.2%). With better spatial resolution in the P-wave inversion, the lateral velocities are presumably better resolved. However, with the high amplitude slow anomalies extending to 200 km depth for the S-wave inversion, a regional thermal anomaly is also probable, accounting for the apparent change in the P and S-wave anomalies. In

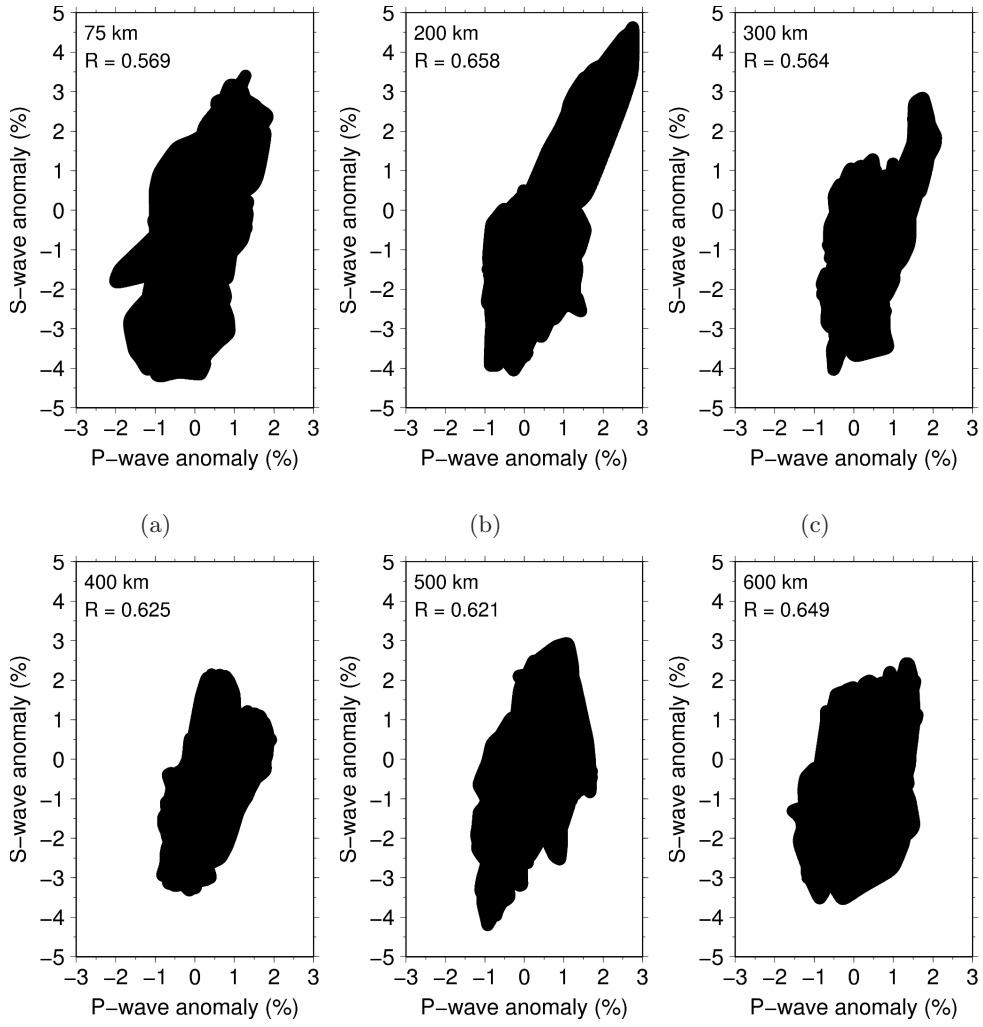

Figure 7.2: Correlation of the P-wave and S-wave anomalies from the PCBPS model and the SCBPS model respectively, for 6 depth slices. Anomalies are plotted for the interpolated nodes where both models are over the hit count of 5 rays per 25 km^3. R value shows the correlation coefficient.

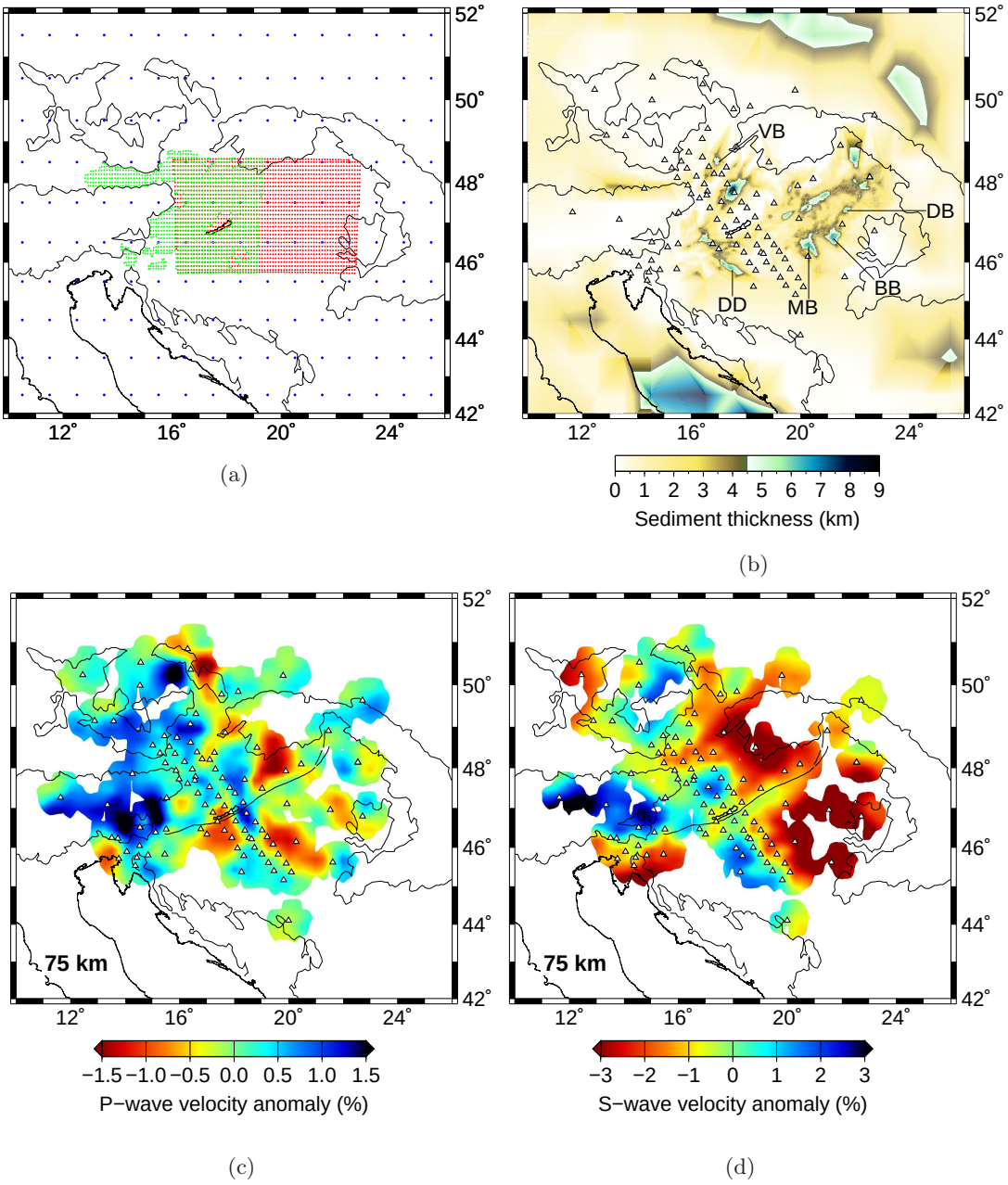

Figure 7.3: Correlation of low velocity anomalies with extensional depocentres. (a) Data points used in the construction of the sediment thickness map in (b). Blue points are thicknesses from the 1°x1° global sediment thickness model of Laske & Masters (1997); green points show thicknesses from Behm (2006); and red points are sediment thicknesses from Kilényi et al. (1991). The sub-basins referred to in the text are labelled: VB - Vienna Basin; DD - Drava depression; MB - Makó basin; BB - Békés basin; DB - Derecske basin. (c) P-wave velocity anomaly at 75 km; (d) S-wave velocity anomaly at 75 km.

the west of the Pannonian Basin, a slow anomaly in the P-wave inversion is also imaged beneath the Drava depression and extends northwards towards Lake Balaton. In the equivalent S-wave image, ray coverage is below the hit threshold and no significant slow anomaly is imaged. These low velocity anomalies also correlate with anomalously high heat flow ($> 100\ mW\ m^{-2}$; e.g. Lenkey et al. (2002); Tari et al. (1999)) (figure 7.4).

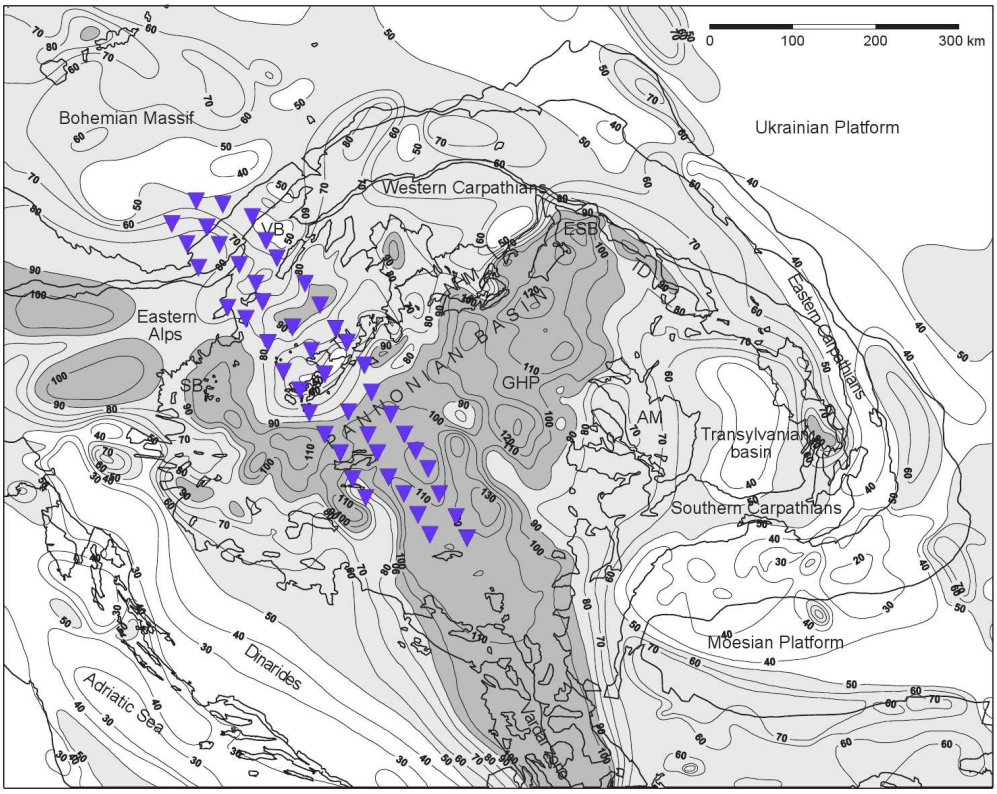

Figure 7.4: Heat flow of the Pannonian-Carpathian region corrected for Neogene sedimentation. After Lenkey et al. (2002). The blue triangles show the approximate location of the CBP HST array.

Beneath the surface boundary between the Western Carpathians and northern Pannonian Basin a slow anomaly (-1.66%) in the P-wave inversion is imaged, which does not directly correspond to any sub-basin in figure 7.3(b). However, the Neogene Central Slovakian Volcanic field (e.g. Kovács & Szabó, 2008) is directly above the anomaly, where calc-alkaline volcanism occurred from ∼20–11 Ma with large volumes of acidic and intermediate rocks, and alkalic basaltic volcanism ∼11–0.5 Ma (Seghedi et al., 2004). In the S-wave images (figure 7.3(d)) the corresponding anomaly is again much higher amplitude (-4.04%) and broader, linking up with the anomalies observed beneath the Vienna basin and on the eastern edge of the Bohemian Massif.

By using station terms and testing independent deterministic crustal corrections (see

chapter 6), the influence of crustal variations on the inversion solution at 75 km has been effectively removed. The mantle lithosphere has undergone greater thinning than the crust of the Pannonian Basin (Huismans et al., 2002; Royden et al., 1983b) and these slow anomalies could represent localised mantle upwellings associated with rift depocentres and Neogene volcanism. In the S-wave tomographic study of Chang et al. (2010) along the Tethyan margin, extensive low velocity anomalies are imaged down to ∼200 km beneath the Pannonian Basin. They suggest this anomaly extends to the north-east, linking up with a low velocity structure beneath the East-European platform at 400–500 km depth, which has previously been interpreted as hydrated mantle by Nolet & Zielhuis (1994). The higher resolution S-wave images from this study (figures 5.13–5.14), broadly concur with this interpretation, with the slow anomalies at 75 km depth linked to the low velocity anomalies within the MTZ, beneath the Western Carpathians and Bohemian Massif. The P-wave inversion does show low velocity anomalies from the north of the Pannonian Basin at 75 km extending down into the MTZ (figure 4.18). However, the amplitude of these anomalies in the 200–400 km depth range (e.g. figure 7.5(b)) is much lower than the corresponding S-wave anomalies.

In addition to the plume beneath the Massif Central, Granet et al. (1995) suggested that possible diapiric mantle upwellings may occur beneath the Rhenish Massif, Bohemian Massif and the Pannonian Basin, based on the distribution of volcanic fields and zones of Variscan basement uplift. Plomerová et al. (2007) target the Eger Rift in the western Bohemian Massif as part of the eastern limb of the European Cenozoic Rift System. They image a broad low velocity zone down to 250 km beneath the Eger Rift, interpreting this zone either as a thermal upwelling of the lithosphere-asthenosphere boundary or as the result of a deep seated mantle plume. The inversion solution from this study has limited resolution in the western Bohemian Massif but slow anomalies, particularly in the S-wave images are consistent with their results. East of the Bohemian Massif, a small localised slow anomaly is present in both P (figure 7.5(a)) and S-wave images, and extends both into the MTZ and to the east and west. Cross-sections through this anomaly in the P-wave inversion (figure 7.5) show the anomaly (-2.0%) extending down to a broad region of slow material below the 410 km discontinuity. This slow structure can also be seen in the tomography images of Plomerová et al. (2007). Although the major volcanism in the Bohemian Massif is along the Eger Rift to the west, this localised slow anomaly is proximate to the location of the smaller Boskovice Graben where smaller volcanic fields are present (e.g. Ulrych et al., 1999). Although caution should be used in comparing

relative velocity anomalies, for the 'baby-plumes' imaged beneath the French Massif Central (Granet et al., 1995) and the Eifel volcanic fields in Germany (Ritter et al., 2001), the velocity anomalies are comparable at -2 to -2.5% for the Massif Central and -2% for the Eifel plume. With the lower amplitudes of the eastern Bohemian Massif anomaly reduced between depths of 200–400 km in the P-wave images (figure 7.5(b)), the anomaly may represent the dying phase of a plume upwelling.

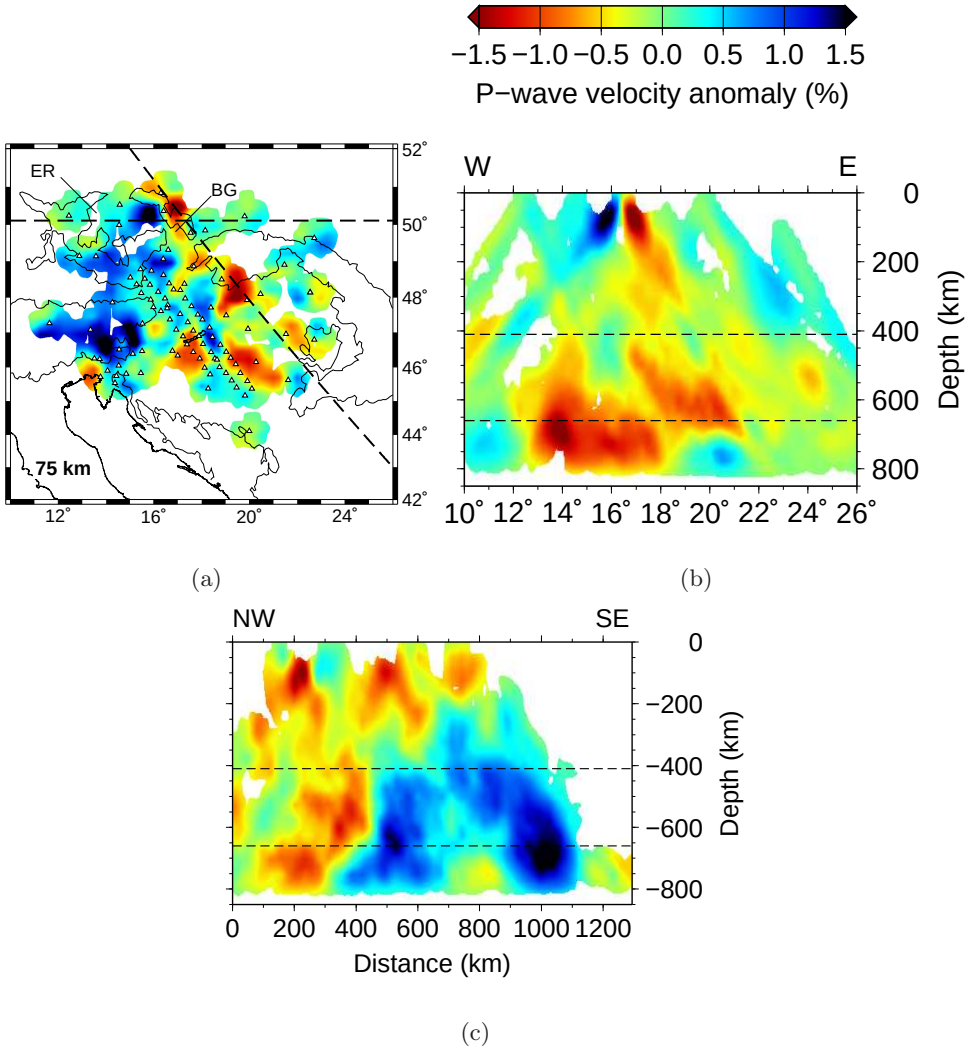

Figure 7.5: Two cross-sections through the P-wave tomographic model showing the slow anomaly to the east of the Bohemian Massif. Cross-section locations are shown in (a). The labels show the approximate location of the Eger Rift (ER) and the Boskovice Graben (BG), referred to in the text

7.3.2 Cold downwellings and the mantle transition zone

Fast seismic velocities are indicative of cold, higher density material, often associated with mantle downwelling. The fast anomaly imaged beneath the Eastern Alps has previously

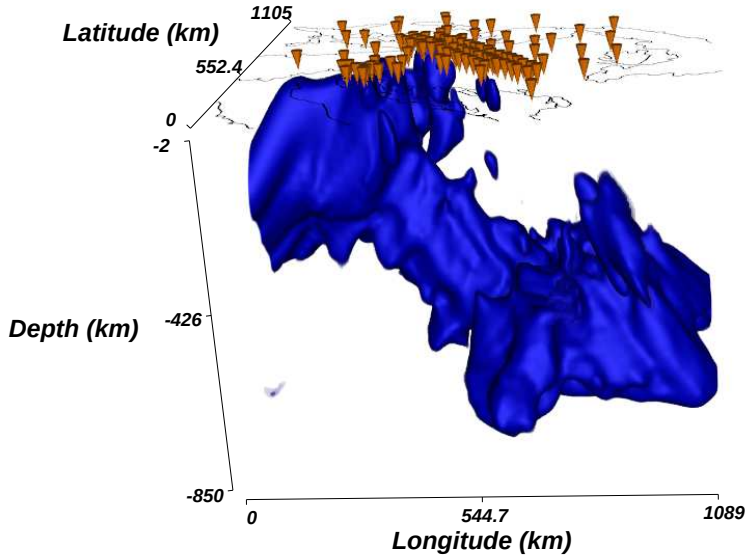

(a)

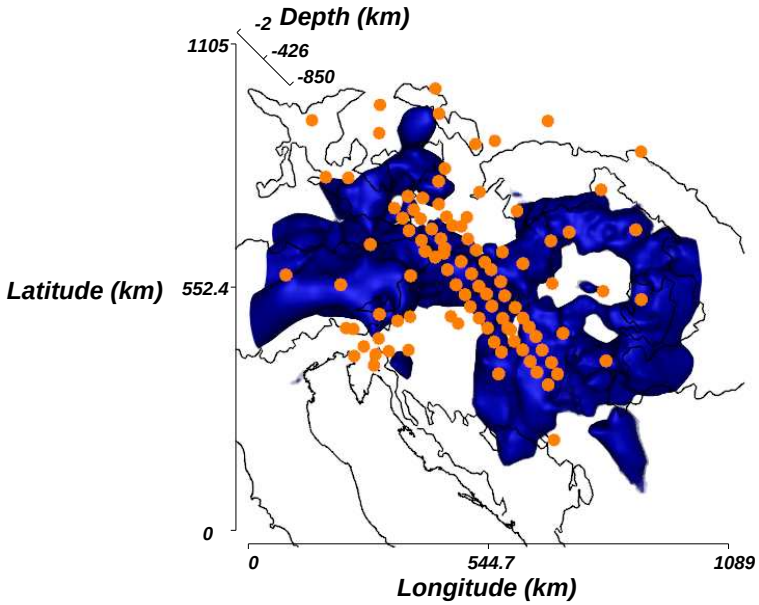

(b)

Figure 7.6: 3D rendering of the P-wave tomographic model with an isocontour at 0.8% anomaly, highlighting anomalously fast mantle beneath the Carpathian-Pannonian region. (a) view looking north showing the link between the East Alpine structure and the fast material in the MTZ beneath the Pannonian Basin; (b) view from above showing the extent of the fast material and the 'doughnut'-like structure beneath the Pannonian Basin. The model is converted into Cartesian coordinates for ease of plotting, with the origin at 10°E and 42°N.

been observed using seismic tomography by Lippitsch et al. (2003). They interpreted this anomaly near 15° E as having a near-surface north-easterly dip, differing in polarity from the subduction direction further west along the Alps. Evidence of north- or south-dipping near-surface structure is equivocal in my images (figure 4.19(b)). The solution shows, however, that this fast Alpine anomaly extends further east beyond the region investigated by Lippitsch et al. (2003). Below about 200km, a near vertical fast anomaly is imaged (figures 4.19(c) and (f), and figures 5.14(c) and (f)), which I interpret as a cold mantle downwelling, continuous with, but extending further east and deeper than the East Alpine anomaly. Recent work by Mitterbauer & Brückl (in preparation), based on the ALPASS dataset, also shows a near vertical seismically fast structure beneath the Eastern Alps, extending down to about 400 km.

This sub-vertical fast structure extends eastward and down into a more extensive high velocity anomaly in the MTZ beneath the Pannonian Basin. The high velocity MTZ in this region has previously been imaged using seismic tomography (e.g. Koulakov et al., 2009; Piromallo & Morelli, 2003; Wortel & Spakman, 2000), but the large number of stations deployed in the CBP network shows this feature in new detail. Of particular interest is the relationship between the Alpine and Pannonian high velocity anomalies, probably best seen in figure 4.19(f) and figure 5.14(f). The Pannonian anomaly appears joined to the East Alpine anomaly at mid upper-mantle depths but above 300 km, it loses coherence and strength. Although this image may be affected by sub-vertical smearing in the E-W direction, the continuity of the structure between Alpine and Pannonian fast anomalies appears to be robust, based on the synthetic test shown in figure 7.1. 3D rendering of the tomographic model (figure 7.6(a)) provides a different perspective, showing the continuity of the Alpine and Pannonian fast anomalies.

This continuity of the Pannonian fast anomaly with the East Alpine fast anomaly, which is clearly linked to shallow structures in the Alpine orogenic zone, suggests a similar origin for the fast material: downwelling beneath a surface convergent zone. The interpretation that emerges from the images is that a continuous collision zone extended from the Alps through present day western and central Hungary. With the shallow fast anomaly observed directly beneath the Alps relating to the present day Alpine collision, the deep fast anomaly beneath the Pannonian Basin is a relict of a pre-extensional Pannonian collision zone that reached eastward from the present-day Alps. The apparent reduction of anomaly amplitude (e.g. figures 4.19(c) and (f), and figures 5.14(c) and (f)) with depth

and the increased lateral extent (figure 4.18(f)) may reflect the structure's older origin and gradual re-equilibration with the mantle. When extension began in the Pannonian, the fast material detached from the lithosphere, and indeed the Pannonian Basin extension may have been triggered by the detachment of the cold slab produced by prior Pannonian convergence.

The northern boundary of the fast material in the mantle transition zone shows a sharp and well resolved contrast with slow material beneath the Western Carpathians and Bohemian Massif. As discussed in section 7.3.1, there is evidence that this structure is linked to the localised slow anomalies observed at 75 km depth (figure 7.3). With strong evidence that downwelling occurred beneath the Pannonian to create a fast MTZ region, this boundary may represent relatively warm upper-mantle which has been displaced northwards by the colder material when it descended into the MTZ from the Alpine-Pannonian convergent zone since the Cretaceous.

7.4 Topography on the 660 km discontinuity

In the lower part of the MTZ beneath the eastern Pannonian Basin, the circular high velocity region surrounds a lower velocity zone producing a hole or 'doughnut' structure (imaged in figure 4.18(f)). In vertical section (figures 4.19(d) and 5.14(d)), the lower velocity region appears to extend beneath the 660 km discontinuity and to be enclosed above and around by a dome of fast material. In the large-scale tomographic images of the region (Koulakov et al., 2009; Piromallo & Morelli, 2003; Wortel & Spakman, 2000), these apparently lower velocities can also be seen, albeit at lower resolution. The structure is also clearly seen as a 'hole' in the 3D rendering of the solution (figure 7.6(b)). To interpret this structure as a hot, low velocity mantle upwelling surrounded by cold, downwelling material would be to neglect, however, the effect of topography on the 660 km discontinuity. Hetényi et al. (2009), using receiver functions and a similar teleseismic dataset as used in this study, showed deepening of the 660 km discontinuity by up to 40 km beneath the eastern Pannonian Basin approximately beneath the centre of the 'doughnut' structure, compared to an almost flat 410 km discontinuity. This observation, is also consistent with the interpretation of a continuous continental collision zone which extended eastwards from the Alps, resulting in downwelling beneath the region.

The thickening of the MTZ caused by deepening of the '660' discontinuity however, needs

to be addressed in terms of its effect on the tomography. To take this into account, I consider the low velocity region in the centre of the 'doughnut' with two alternative adjustments to the synthetic block model (PSBMS) in figure 7.1. In figure 7.7(b) part of the high velocity material is removed in the range 410–660 km to represent a lower velocity core in the MTZ. This model is designed to represent possible downwelling around the edge of the Pannonian Basin, in contrast to a central downwelling, which has spread laterally with depth. In figure 7.7(d) I consider a locally deepened '660' discontinuity. The inversion model is defined relative to the *iasp91* reference Earth model, where P-wave velocity increases from 10.20 km s^{-1} to 10.79 km s^{-1} across the 660 km discontinuity. In figure 7.7(d) I address the effect of a 40 km depression of the '660' discontinuity as found by Hetényi et al. (2009) by using a thin rectangular patch with velocity reduced by 3% from 660–700 km.

Comparison with the inversion of the observed data in model PCBPS (figures 7.7(i) and (j)) shows the low velocity core in the inversion of model 1 (figures 7.7(e) and (f)), is much higher in amplitude, suggesting this is not a realistic model. In reality, downwelling around the perimeter of the Pannonian Basin would produce some 'infilling' of fast material in such a hole, which would reduce the amplitude of the central slow anomaly. However, the second model when compared with PCBPS, clearly provides a reasonable explanation of the doughnut structure, consistent with the previous observations of a depressed '660' and the physical model of fast material downwelling beneath the centre of the basin. Depression of the 660 km discontinuity is not necessarily inconsistent with upper-mantle descending through this phase transition, but given the relatively high viscosity of lower mantle and the relatively recent history of convergence and detachment, the cold downwelling may have caused a depression of the '660' without actually transferring material across it.

7.5 Implications for tectonic models of the Carpathian-Pannonian system

The interpretation of a continuous continental collision zone (section 7.3) extending eastward from the Alps across the present-day Pannonian Basin has important implications for tectonic models of the Carpathian-Pannonian region. The detachment of mantle lithosphere and its relation to extension has been previously modelled in other contexts by Davies & von Blanckenburg (1995); Göğüş & Pysklywec (2008); Schott & Schmeling

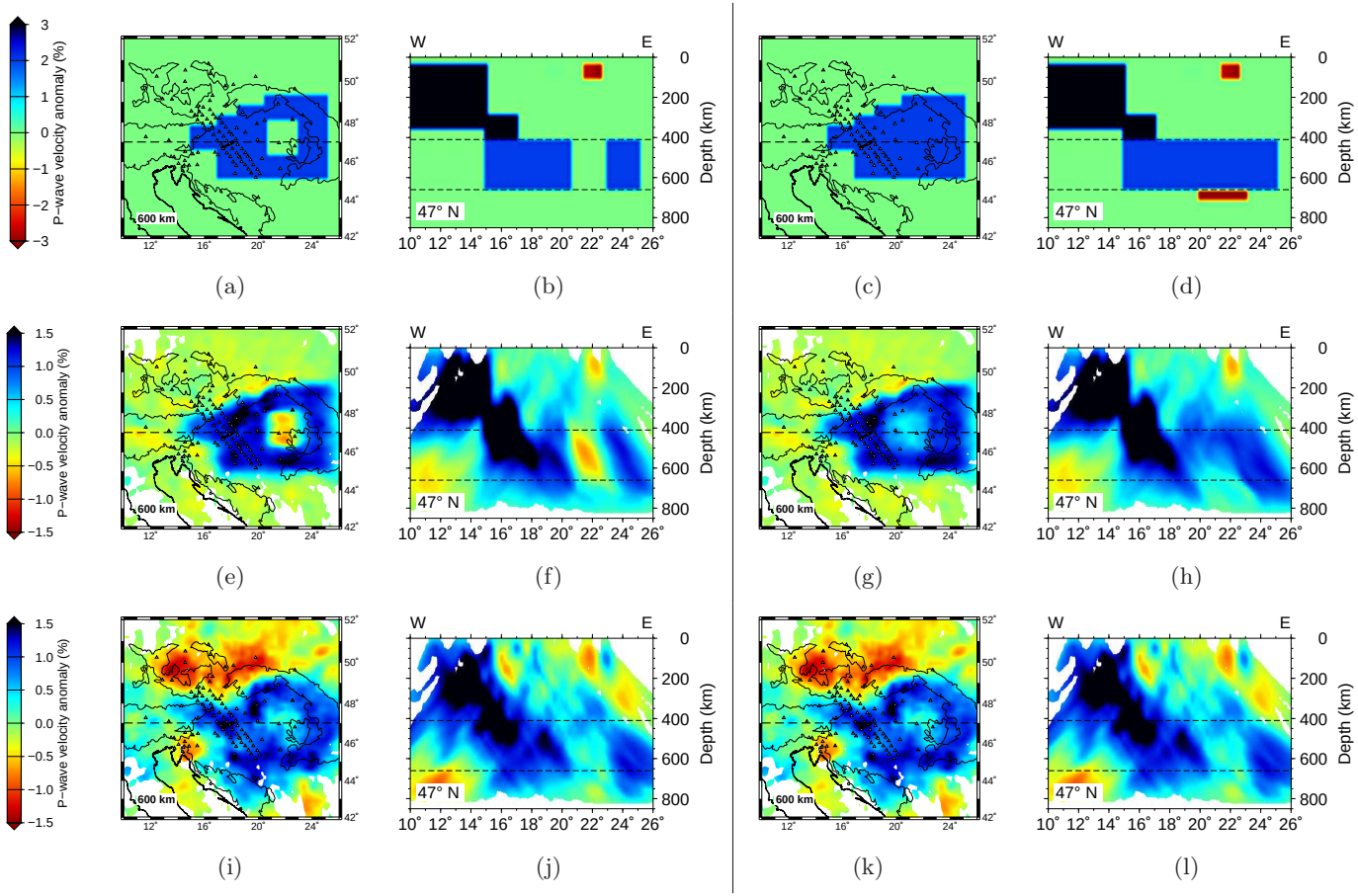

Figure 7.7: Two synthetic models to explain the low velocity core in the fast velocity MTZ beneath the Pannonian Basin. In model 1 ((a) & (b)), the core of MTZ fast anomaly has been removed; in model 2 ((c) & (d)), a slow velocity thin layer representing a local depression of the 660 km discontinuity is placed directly beneath the MTZ. The inversion of synthetic travel-times for model 1 are shown in (e) & (f) and for model 2 in (g) & (h). The results are compared with the corresponding images from the actual P-wave inversion solution (PCBPS) in (i) to (l).

(1998) and Marotta et al. (1999). In the development of a gravitational instability of mantle lithosphere synchronous uplift occurs directly above the instability (e.g. Houseman & Gemmer, 2007). With detachment of the gravitational instability, Schott & Schmeling (1998) and Marotta et al. (1999) show how the cold lithospheric root is replaced by hot upwelling asthenosphere, which provides a large input of heat into the crust. This type of mechanism is consistent with the seismological observations of fast velocity anomalies in the MTZ and low velocity anomalies at the base of the lithosphere.

With the continued convergence of Adria into Europe since the Cretaceous, the Carpathians, which had formed along this suture, were forced eastwards by the extrusion and rotation of the Alcapa and Tisza-Dacia tectonic blocks in the Eocene (Csontos & Nagymarosy, 1998; Csontos et al., 1992). With detachment of the mantle lithosphere suggested by the present tomographic study, the resulting asthenospheric upwelling may have provided the driving force for extension in the Pannonian Basin. Using numerical models, Lorinczi & Houseman (2010) showed that internal buoyancy forces provided by thickened crust or by asthenospheric uplift are needed to drive the observed extension. With crustal shortening in the outer Carpathians ending from the middle to Late Miocene (Royden et al., 1983a), gravitational collapse from the over-thickened and elevated zones of the orogen (e.g. Horváth & Berckhemer, 1982; Pichon & Angelier, 1979; Platt & Vissers, 1989) may also have contributed to the extension. The interpretation showing the role of detachment of continental lithosphere accompanied by eastward extrusion and basin formation is shown in figure 7.8.

Previous tectonic models have largely focused on extension in the Pannonian Basin driven by roll back of a slab subducting beneath the Carpathian margin (e.g. Horváth, 1993; Royden et al., 1982; Wortel & Spakman, 2000). These models propose that fast material within the mantle transition zone is remnant oceanic lithosphere subducted along the Carpathian margin. However, if the fast material within the MTZ represents ponding of previously subducted oceanic lithosphere, water stored in the slab would result in a hydrated MTZ. Cao & Levander (2010) show that the 410 km phase transition from olivine to wadsleyite is strongly affected by hydration and can be elevated from 10–30 km with the presence of water (Hirschmann et al., 2005; Smyth & Frost, 2002). Hetényi et al. (2009) have shown that despite topography on the '660', the 410 km discontinuity is almost flat, indicating water has not played a significant role here.

In the slab roll-back model of Wortel & Spakman (2000), they suggest a gradual steep-

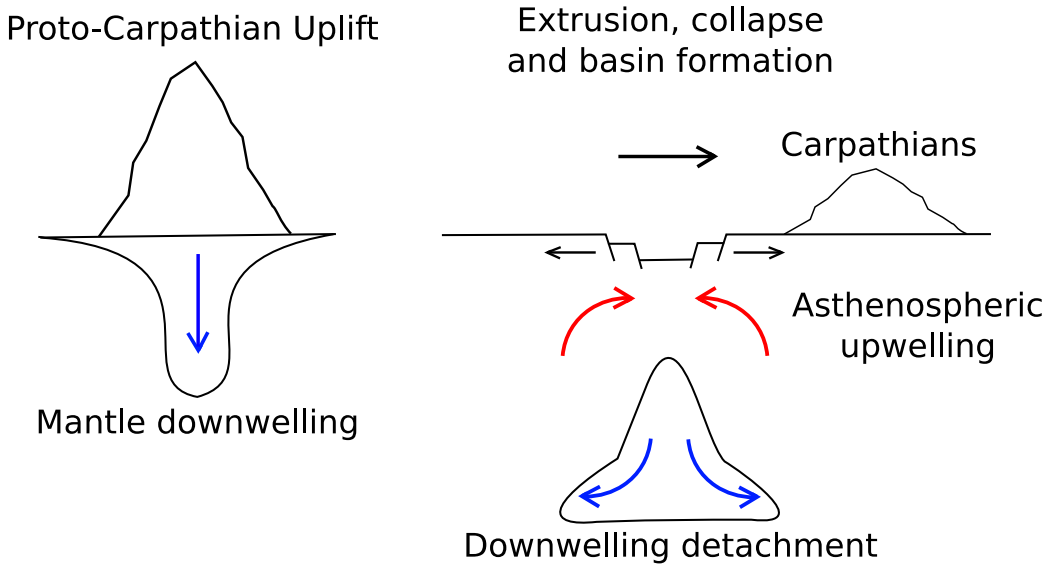

Figure 7.8: Cartoon showing the development of the Pannonian Basin. Left: uplift of the Carpathian mountains, which was continuous with the Eastern Alps, and the development of a lithospheric downwelling. Right: Detachment of the lithospheric downwelling resulting in hot asthenospheric upwelling. Upwelling accompanied by eastward extrusion and orogenic collapse of the Carpathians, led to extension in the Pannonian.

ening of subduction beneath the outer Carpathians, followed by an eastward migration of slab detachment along the Carpathian margin towards the Vrancea region, which is interpreted as the last remnant of oceanic lithosphere to remain attached. However, the Vrancea region in the SE Carpathians has also been explained in terms of a gravitational instability (Lorinczi & Houseman, 2009), which successfully explains the spatial variation of strain-rates calculated from seismicity as well as the uplift in the region (e.g. Sanders et al., 1999). Moreover, subduction along the entire Western Carpathians has now been questioned by various authors (Grad et al., 2006; Szafián & Horváth, 2006; Szafián et al., 1997; 1999; Tomek, 1993). The tomographic images presented in this study, also show no evidence of recent subduction along this margin.

Remnants of Tethyan oceanic lithosphere have previously been included in reconstructions of the Alpine-Carpathian palaeogeography (e.g. Kovács, 1984). More recently, based on both the Paleogene to early Miocene volcanic suites (Kovács et al., 2007) and the Late Permian and Triassic sedimentary facies, multiple oceans have been proposed, including the Meliata, Vardar, Pindos and Pieniny oceans with various subduction histories predating the uplift of the Carpathians (Channell & Kozur, 1997). The multiple subducted oceanic lithospheric slabs that these interpretations suggest, may well be ponding in the MTZ and contribute to the fast anomaly observed, but the continuity of the structure

with the Alpine collision zone suggests an alternative interpretation that continental lithosphere has contributed to the downwelling fast material in the transition zone, beneath the Pannonian Basin.

Chapter 8

Conclusions

Using a 16-month deployment of 56 temporary broadband stations in the CBP (Carpathian Basins Project) network, supplemented by data from another 44 permanent stations, P-wave and S-wave tomographic images have revealed the velocity structure of the mantle beneath the Pannonian-Carpathian region with a resolution that has not previously been available.

The images reveal slow anomalies in the upper 200 km, which are likely to be primarily thermal features, and are consistent with the thermal history of volcanism and the location of extensional depocentres. The location of these anomalies shows where active mantle upwelling has taken place, which may have provided a significant driving force for extension in the Pannonian Basin. Although these slow anomalies could be interpreted as terminating close to the Mid-Hungarian shear zone, there is no distinct velocity signature related to this zone, which separates the Alcapa and Tisza-Dacia blocks, indicating that it is a lithospheric or crustal structure.

The tomographic solution for the upper-mantle is dominated by fast anomalies arising from near-vertical lithospheric downwelling produced by the continuing convergence of Adria and Europe. Fast material produced by downwelling of lithosphere beneath the Eastern Alps dominates the model in the upper 300 km. This fast anomaly extends eastward from the Alps beneath the Pannonian Basin, where it is attenuated above 300 km depth but clearly defined in the mantle transition zone. Beneath the Pannonian Basin this fast material is detached from the lithosphere and is interpreted as relict downwelling of continental lithosphere from a convergent zone which pre-dated the Pannonian extension and was laterally contiguous with the Eastern Alps.

The fast material in the mantle transition zone beneath the entire Pannonian Basin region is terminated to the north by a relatively sharp transition to slower material beneath the Bohemian Massif and the Western Carpathians. There is evidence of this slow material being linked to shallower slow anomalies and it is interpreted as hot mantle material, which has been displaced by the cold downwelling beneath the Pannonian Basin. The transition from fast to slow anomalies, marks the northern boundary of the fast material, which has been spreading outward beneath the basin since the downwelling began in the Cretaceous.

Towards the base of the mantle transition zone, the fast material is disposed in a doughnut shaped structure around the Carpathian arc, surrounding apparently slower material beneath the central Pannonian Basin. This feature is inferred to be the consequence of a large mass of cold dense material depressing the 660 km seismic discontinuity beneath the cold downwelling structure throughout the mantle transition zone and is an artefact of the tomography.

Vertical cross-sections through the Western Carpathians, show no evidence of recent subduction or lithospheric foundering, mechanisms which have been previously suggested as possible causes for the lithospheric extension of the Pannonian Basin. Rather, the downwelling and detachment of the continental lithosphere, which is continuous with the Alpine collision zone, resulted in hot asthenospheric mantle flow into the uppermost mantle and potentially helped to drive the extension of the Pannonian Basin.

8.1 Future research

This thesis focused on the P and S-wave velocity structure beneath the Carpathian-Pannonian region. With data now available throughout the Pannonian region, efforts are needed to link the structure observed in this study to the surrounding regions, which were unresolvable. For example, deployment of seismometers in the Eastern Carpathians, would enable imaging of the eastern extent of the fast mantle transition zone and would answer questions on the possible existence of recent subduction along the Eastern Carpathian margin. Similarly the distinct arcuate shape of the Carpathians raises questions about the southern margin of the Carpathians and its relationship with the Moesian Platform, which could be investigated with the deployment of additional seismometers.

Although images have been produced for P and S wave tomography, constraints on the

nature of the anomalies would be improved with knowledge of V_p/V_s. A joint inversion of P and S would allow a direct comparison between anomalies. Furthermore, with surface wave tomography, the absolute shear-wave velocity structure of the region could be constrained. This would provide a good context for the relative velocity anomalies of this study, in addition to improving the vertical resolution unavailable with body-wave tomography.

The distribution of the seismological stations also provides an opportunity to study phase conversions in the region. Receiver functions have been used to study the 410 km and 660 km seismic discontinuities by Hetényi et al. (2009). With the HST array perpendicular to the Mid-Hungarian Line, the Moho could be imaged across the Alcapa and Tisza-Dacia blocks and compared with the previous seismic refraction lines which have crossed the structure. Similarly, S-P conversions from the lithosphere-asthenosphere boundary could be investigated to comment on the boundary, particularly in relation to the lithospheric detachment interpreted in this study beneath the Pannonian Basin. A drawback of trying to study receiver functions in Carpathian-Pannonian region however, is the thick sediment, which produces multiple reverberations in the crust and possibly mask the crustal structure.

With an interpretation of the velocity anomalies established, this provides a basis for numerical modelling of the geodynamics. The modelling could incorporate a continuous collision zone with the Eastern Alps, accompanied by cold mantle downwelling and subsequent lithospheric detachment beneath the present day Pannonian Basin. Modelling of resulting mantle flow and subsequent extension in such a geodynamic model would provide a strong argument for downwelling providing the driving force for extension.

Appendix A

Data quality control

This appendix lists the procedures involved in the deployment and servicing of the Guralp CMG-6TD seismometers. Figure A.1 shows the procedures used in the deployment of the seismometers. Figure A.2 shows the procedures for the service run. Accuracy and continuity of the GPS was checked for each site as shown in figure A.3. GPS continuity plots are included for each station on the supplementary CD - see appendix D. The continuity of the data is shown in A.4.

SEIS-UK 6TD DEPLOYMENT SHEET

Date (dd/mm/yyyy)		Arrival time	
Project		Site code	
Site name		Weather	
Personnel			

Use external GPS for these figures (WG584 referencing system)

Latitude			Longitude		
UTM Zone		Coordinates		Altitude	
GMT time			Julian Day		

Distance to Road		Road type	
Distance to power cables		Distance to trees	
Distance to buildings		Land use	
Deployment method And soil description			

Sensor serial No					
			Mag N		Grid N (plus Declination)
Size of flash memory		Alignment		or	
GPS serial Number		Number of solar panels, type and barcodes			
Sensor depth (top)					
Battery voltage before connection		Battery type			
Battery voltage after all connections made		Regulator number			

In Shout

Baud rate is 19200 (*port0)*	y/n		GPS cycle				
Device levelled	y/n		Z	N	E		
Legs locked	y/n		Masses				
SOH	Z N E mass		Temp		Autocentre @ 90%		
Taps (enter all -circle all recording)	Tap0:	Tap2:	Tap3:	Tap4:			
Streams:Velocity offset	Z_		N_		E_		

In ptelnet:

Show flash: last write chip 1			Date of last flush		
Show flash: last write chip 2					
Mode?			*OK-1*(firmware Version)		

In Shout (note: it is essential that you see offset and drift)

GPS Lat		GPS Long		GPS sync time	
Offset and drift values seen					

				Draw detailed location sketch overleaf. Add any other comments and/or sources of unusual potential seismic noise as well as contact details for the landowner.
Bag around battery	y/n	All connections made	y/n	
Breakout Box in bag	y/n	Cables secured and sketched	y/n	
All connections made	y/n	Deployment Sheet Complete	y/n	
Photo taken	y/n	Departure time (local and GMT)		

Figure A.1: Deployment sheet used for the Guralp CMG-6TD seismometers used in the HST array.

SEIS-UK 6TD SERVICING SHEET

DATE (DD/MM/YYYY): _____ LOCAL TIME:_____

Project _____ Site Name _____ Site Code_____

Servicing team members_____

External Battery Voltage_____V GPS Serial No._____

Sensor Type 40TD / 3TD / 6TD Sensor Serial No._____

In Ptelnet

Last GPS Sync Time - *fix*? _____

If no lock; restart the GPS with: *ok-1, close, ok-1, 1 hr-cycle*

Connect the Lacie with the firewire connection and connect power – ready when LED green

Lacie No: _____ *dir*: Diskfree (MB)
_____

Flush: Last Flush _____

Flush Successful? Y / N Approx. Time Taken: _____

dir: Last dump: Serial No. _____ Start: _____ End: _____

Diskfree (MB) _____

Calculated approximate download volume (MB) _____

Remove power from Lacie disk now to prevent battery wastage.

In Shout:

Mass Positions: M8(Z)_____ M9(E)_____ MA(N)_____

*Streams:*Velocity Offsets: Z0 _____ N0 _____ E0 _____

GPS details (1-hr-cycle)
_____

GPS lock? Y / N 1D / 2D / 3D ? Offset? Y / N Drift? Y / N

Offset/Drift Reasonable? Y / N
It is essential that an offset and drift are observed – if they are not then the GPS may not be functioning correctly. You may have to wait a few minutes to observe these numbers.

Cables Damaged ? Security / Fencing ?
Solar Panels Clean ? Water Penetration ?
Battery Levels / terminals ?

Further Comments:

Figure A.2: Servicing sheet used for the Guralp CMG-6TD seismometers in the HST array. The documents shows the procedures involved in checking the working status at each site.

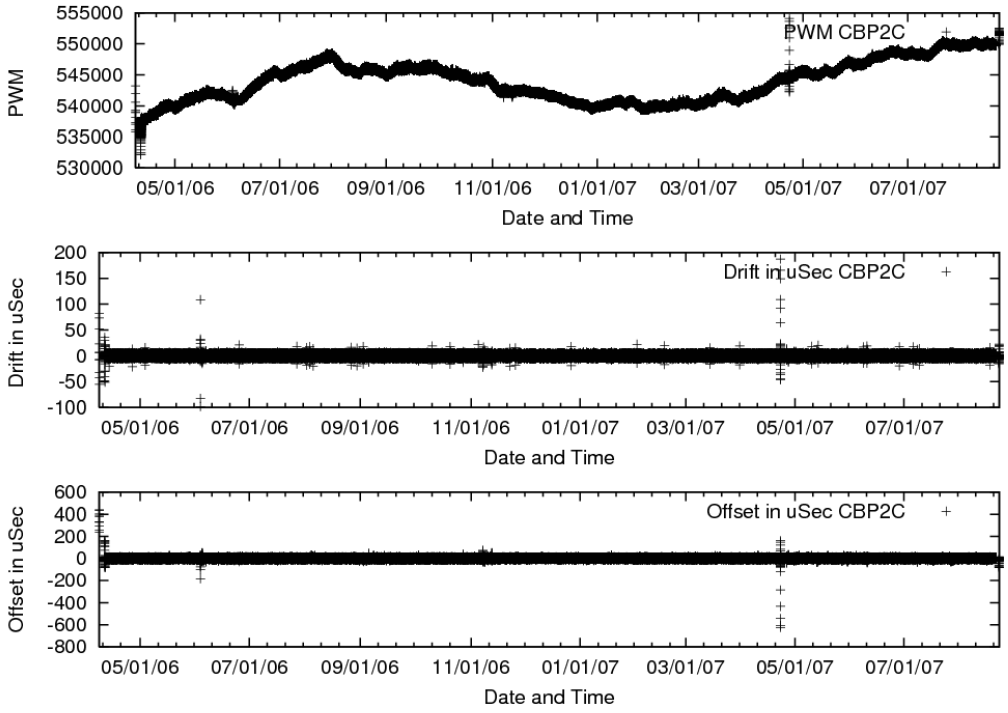

Figure A.3: GPS continuity plot, showing pulse-width modulation, drift and offset at a single station, CBP2C. The GPS continuity plots for all Guralp CMG-6TD stations are included in the supplementary CD listed in appendix D.

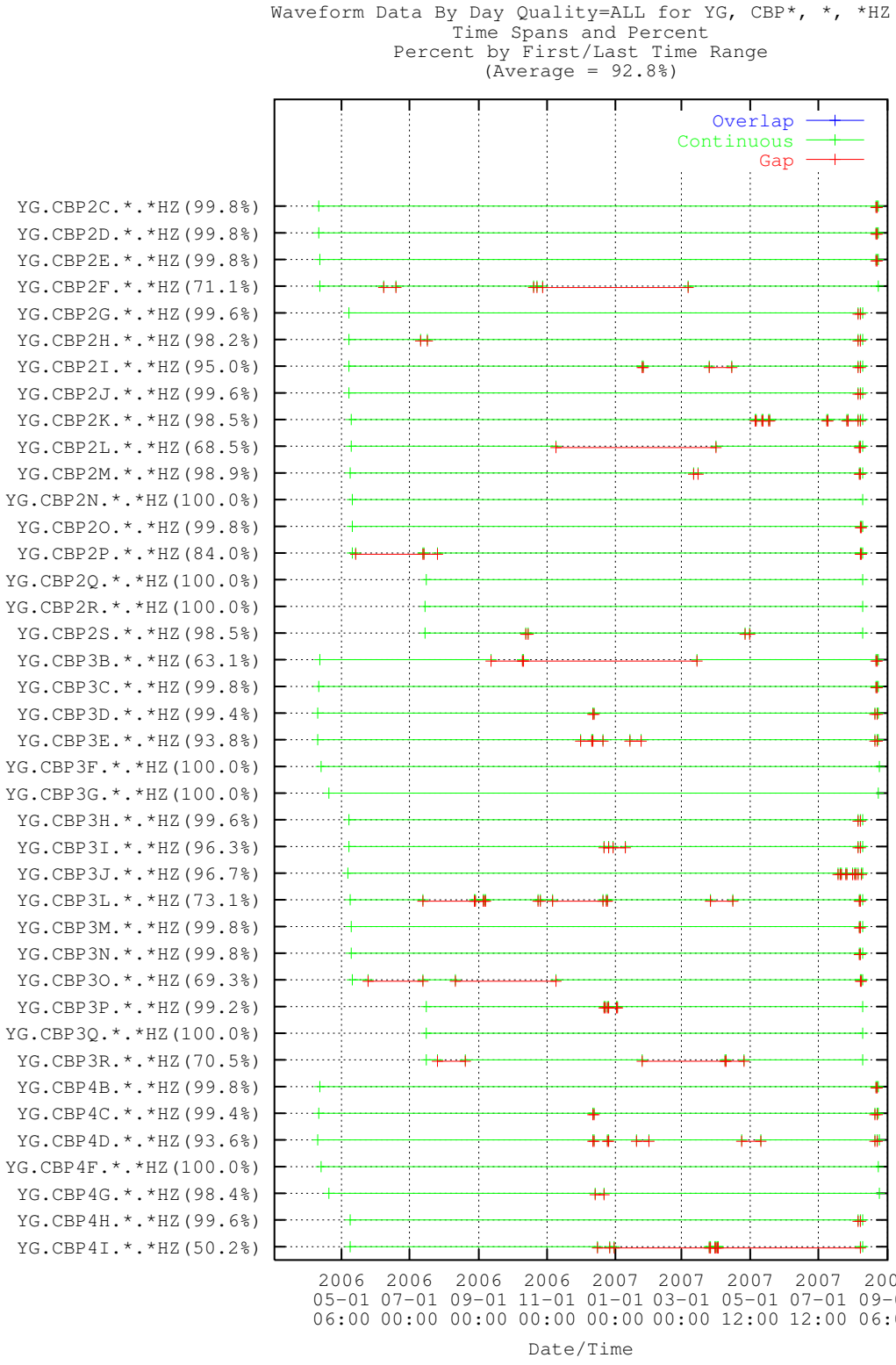

Figure A.4: Continuity of data for each of the Guralp CMG-6TD stations in the HST array.

Appendix B

Teleseismic events

This appendix lists the hypocentral information for the events used in the teleseismic tomography. The event catalogue was retrieved from IRIS using JWEED. The final inventory used the Bulletin of the International Seismological Centre (ISC) catalogue, which is published two years after an event.

Table B.1: Hypocentral information for events used in the P and S-wave tomography.

Year	Month	Day	Time	Latitude (°)	Longitude (°)	Depth (km)	M_w	Phase
2006	04	12	01:06:58.70	56.240	164.250	24.0	6.05	P, S
2006	04	14	09:27:40.10	35.460	89.740	17.7	5.61	P
2006	04	15	22:40:00.00	22.700	121.400	65.0	6.20	S
2006	04	15	22:40:54.10	22.870	121.400	21.7	5.90	P
2006	04	16	11:48:00.00	30.200	139.000	440.0	5.70	S
2006	04	16	11:48:56.99	30.242	138.565	431.6	5.70	P
2006	04	19	20:36:43.50	2.880	93.280	0.0	6.00	P, S
2006	04	19	21:05:43.00	31.610	90.670	23.2	5.69	P
2006	04	20	17:50:00.00	34.900	139.200	8.0	5.60	S
2006	04	20	17:50:40.50	34.920	139.200	12.0	5.59	P
2006	04	20	23:25:02.20	60.890	167.050	12.0	7.59	P, S
2006	04	21	04:32:43.80	60.500	165.980	23.4	6.13	P, S
2006	04	21	11:14:15.30	61.270	167.640	14.8	6.04	P
2006	04	22	07:21:58.00	61.140	167.410	17.5	5.51	P, S
2006	04	25	18:26:17.10	1.780	96.770	12.0	6.33	P, S
2006	04	29	16:58:04.50	60.620	167.530	0.0	6.80	P, S
2006	04	30	00:43:10.60	44.560	102.440	12.0	5.71	P
2006	05	01	07:47:59.90	8.110	-82.880	12.0	5.91	P, S
2006	05	01	09:13:32.00	8.130	-82.880	12.0	5.55	P
2006	05	08	09:16:57.90	-5.240	102.080	39.2	5.87	P, S
2006	05	09	11:02:22.20	60.770	165.970	12.0	5.70	P, S
2006	05	10	02:42:51.00	52.210	-169.190	29.7	6.42	P
2006	05	11	17:22:54.10	23.310	94.300	33.7	5.56	P
2006	05	13	03:11:42.90	5.330	94.300	43.1	5.66	P
2006	05	16	15:28:24.60	0.160	97.100	0.0	6.90	P, S
2006	05	18	23:04:45.00	54.550	164.040	25.6	5.71	P
2006	05	22	11:12:00.40	60.860	165.810	12.0	6.62	P, S
2006	05	22	13:08:01.70	54.190	158.870	198.0	6.20	P
2006	05	28	09:00:12.40	19.320	120.940	35.0	5.66	P
2006	06	05	06:27:07.40	1.130	-27.950	0.0	6.00	P
2006	06	05	06:34:31.80	1.070	-28.020	26.0	5.69	P

Table B.1: Hypocentral information for events used in the P and S-wave tomography.

Year	Month	Day	Time	Latitude (°)	Longitude (°)	Depth (km)	M_w	Phase
2006	06	09	23:17:27.90	-47.180	32.370	17.2	5.77	P
2006	06	11	20:01:00.00	33.200	131.400	130.0	6.40	S
2006	06	11	20:01:26.30	33.150	131.340	144.5	6.36	P
2006	06	14	04:18:42.50	51.960	177.070	13.3	6.48	P, S
2006	06	14	04:46:42.40	51.970	177.130	15.4	5.96	P
2006	06	15	06:49:48.80	45.370	97.490	21.8	5.79	P
2006	06	16	17:10:00.00	40.400	143.800	14.0	5.50	P, S
2006	06	16	20:19:21.40	40.380	143.960	15.0	5.50	P
2006	06	18	18:28:02.20	32.970	-39.750	12.0	5.97	P, S
2006	06	20	10:02:04.02	51.339	-130.899	10.0	5.80	P
2006	06	21	12:34:52.70	6.830	92.460	12.0	6.03	P, S
2006	06	22	10:53:00.00	44.800	149.500	101.0	6.10	P
2006	06	27	02:39:35.30	52.190	176.180	18.2	6.24	P
2006	06	27	13:03:12.10	14.950	-94.530	12.0	5.82	P
2006	06	27	18:07:22.70	6.310	92.570	12.0	6.27	P, S
2006	06	28	21:02:09.20	26.770	55.810	12.0	5.81	P
2006	07	01	19:34:39.60	50.980	-179.240	21.3	5.51	P
2006	07	02	03:53:56.50	52.010	177.030	19.0	5.72	P
2006	07	02	16:58:00.90	50.980	-179.320	20.9	5.54	P
2006	07	02	17:20:25.80	50.930	-179.320	21.0	5.59	P
2006	07	06	03:57:53.50	39.220	71.700	12.9	5.77	P, S
2006	07	08	20:40:01.00	51.040	-179.120	28.0	6.61	P, S
2006	07	10	07:21:37.90	-11.540	-13.390	12.0	5.53	P
2006	07	12	14:44:46.00	-8.740	67.720	20.7	5.71	P
2006	07	17	08:19:23.50	-9.240	107.360	0.0	7.70	S
2006	07	17	15:45:59.80	-9.570	108.290	12.0	6.12	S
2006	07	19	09:53:07.20	33.060	96.270	24.6	5.52	P
2006	07	19	10:57:36.90	-7.180	105.210	46.3	6.15	P, S
2006	07	27	11:16:40.40	1.660	97.010	15.0	6.29	P, S
2006	07	28	07:40:00.00	24.100	122.600	41.0	5.90	P, S
2006	07	29	00:11:51.30	37.360	68.560	12.0	5.57	P
2006	07	29	19:53:41.90	23.740	-63.830	0.0	5.60	P
2006	07	30	01:20:59.20	26.870	-111.360	22.9	5.91	S
2006	07	30	01:28:14.69	1.463	97.182	30.0	5.60	P
2006	08	04	13:41:40.80	10.002	-70.642	8.8	5.50	P
2006	08	06	14:26:19.30	37.570	74.670	24.0	5.60	P, S
2006	08	06	18:16:40.20	26.230	144.130	19.2	5.86	P
2006	08	11	14:30:40.70	18.500	-101.060	57.8	6.01	P, S
2006	08	11	20:54:10.20	2.460	96.390	0.0	6.20	S
2006	08	11	20:54:14.40	2.100	96.180	20.6	6.17	P
2006	08	12	18:39:00.00	28.700	130.200	44.0	5.50	P
2006	08	15	12:26:17.40	51.090	179.250	21.8	5.66	P
2006	08	16	18:39:00.40	-28.850	61.540	12.0	5.89	P
2006	08	17	11:11:35.50	55.490	162.260	65.9	5.72	P
2006	08	17	15:20:35.50	46.540	141.770	18.1	5.65	P
2006	08	19	05:41:28.50	16.260	-97.270	26.6	5.57	P
2006	08	20	03:01:02.40	49.580	156.870	35.6	5.99	P
2006	08	21	22:20:00.00	33.700	136.000	440.0	5.50	P
2006	08	24	21:50:36.70	50.920	158.170	50.2	6.46	P, S
2006	08	26	23:40:39.50	51.200	-179.420	21.6	5.70	P
2006	08	26	23:46:18.50	51.090	-179.470	34.0	5.75	P
2006	08	31	22:58:25.80	28.600	130.330	30.5	5.52	P
2006	09	01	12:04:22.20	53.880	-166.160	75.7	5.89	P
2006	09	10	14:56:08.20	26.320	-86.840	29.6	5.87	P
2006	09	11	18:12:22.30	35.620	78.090	18.9	5.50	P, S
2006	09	13	13:25:00.00	46.400	146.700	380.0	5.50	P
2006	09	16	02:22:50.60	41.330	135.710	382.2	5.87	P, S
2006	09	18	03:45:58.90	51.490	-173.870	19.8	5.76	P

Table B.1: Hypocentral information for events used in the P and S-wave tomography.

Year	Month	Day	Time	Latitude (°)	Longitude (°)	Depth (km)	M_w	Phase
2006	09	24	22:56:21.70	-17.590	41.780	12.0	5.56	P
2006	09	28	01:36:00.00	46.500	154.000	17.0	5.90	S
2006	09	28	01:36:48.00	46.520	153.440	0.0	5.80	P
2006	09	29	13:08:24.80	10.797	-61.300	54.1	6.10	P, S
2006	09	29	18:23:03.40	10.781	-61.323	25.6	5.50	P
2006	09	30	12:47:22.90	7.440	-34.640	12.0	5.53	P
2006	09	30	17:50:00.00	46.300	153.900	17.0	6.40	S
2006	09	30	17:50:23.00	46.290	153.450	12.8	6.57	P, S
2006	09	30	17:56:16.10	46.180	153.370	19.1	5.97	P
2006	10	01	09:05:00.00	46.400	153.600	8.0	6.40	S
2006	10	09	10:01:00.00	20.700	120.500	11.0	6.20	S
2006	10	09	11:08:28.10	20.710	119.980	12.0	5.88	P
2006	10	10	23:58:00.00	37.200	143.100	11.0	5.60	P, S
2006	10	10	23:58:04.20	37.200	143.040	19.1	5.66	P
2006	10	11	06:43:53.80	20.710	119.940	12.0	5.72	P
2006	10	12	14:46:30.90	23.880	122.540	35.2	5.76	P
2006	10	13	13:47:00.00	46.300	153.600	11.0	5.80	S
2006	10	20	17:27:03.20	13.520	121.520	16.9	5.84	P
2006	10	20	22:09:27.40	13.520	121.570	15.3	5.58	P
2006	10	21	18:23:21.00	13.490	121.520	15.0	5.91	P
2006	10	23	21:17:00.00	29.200	140.400	5.0	6.40	P, S
2006	10	29	08:31:44.60	29.430	140.290	12.0	5.64	P
2006	11	08	14:56:52.20	47.160	154.430	17.9	5.62	P
2006	11	12	21:27:42.40	48.170	154.750	48.4	5.94	P
2006	11	15	11:14:17.80	46.710	154.330	13.5	8.30	P, S
2006	11	15	11:15:00.00	46.600	153.600	8.0	7.80	P
2006	11	15	11:40:55.10	46.470	154.830	23.3	6.69	P
2006	11	15	21:22:00.00	47.200	154.600	20.0	6.00	P, S
2006	11	16	06:20:20.80	46.400	154.680	12.0	5.96	P
2006	11	17	18:03:12.30	28.370	130.220	30.5	6.17	P
2006	11	18	13:55:21.10	4.580	94.570	36.4	5.94	P, S
2006	11	18	13:57:53.80	4.600	94.670	23.0	5.88	P
2006	11	22	11:15:00.00	44.000	146.800	92.0	5.60	P
2006	11	23	20:04:46.60	47.520	154.620	27.9	5.51	P
2006	11	24	15:34:00.00	46.600	154.400	5.0	5.70	P
2006	11	25	12:10:22.00	53.350	-163.790	19.5	5.54	P
2006	11	29	15:38:44.50	53.740	-35.260	12.0	5.62	P
2006	12	01	03:58:21.80	3.460	99.050	208.4	6.33	P, S
2006	12	03	08:19:51.30	-0.380	-19.760	23.2	5.59	P
2006	12	03	20:52:15.90	13.900	-91.770	46.7	5.98	P
2006	12	07	19:10:00.00	46.500	154.100	11.0	6.40	S
2006	12	07	19:10:21.90	46.240	154.440	15.4	6.37	P
2006	12	09	14:48:00.00	46.900	147.500	420.0	5.70	P, S
2006	12	10	15:28:00.00	29.700	130.700	38.0	5.80	P
2006	12	15	16:59:02.40	46.350	153.290	19.8	5.56	P
2006	12	17	21:10:21.90	4.580	94.890	54.4	5.77	P
2006	12	17	21:39:17.50	0.570	99.830	18.2	5.81	P
2006	12	22	19:50:44.60	10.700	92.110	22.0	6.18	P, S
2006	12	25	20:01:00.40	42.170	76.060	18.8	5.84	P, S
2006	12	26	12:26:00.00	21.600	120.800	17.0	6.90	P, S
2006	12	26	12:26:21.10	21.810	120.520	19.6	6.99	P, S
2006	12	26	12:34:00.00	21.800	120.700	5.0	6.60	P
2006	12	26	12:34:13.80	22.020	120.400	32.8	6.91	P
2006	12	26	15:19:45.20	48.190	155.170	37.7	6.01	P
2006	12	27	02:30:00.00	22.000	120.600	44.0	5.60	P
2006	12	30	08:30:49.80	13.670	51.440	16.0	6.62	P, S
2007	01	05	16:52:22.40	55.370	-155.890	22.1	5.79	P, S
2007	01	08	12:48:38.60	8.110	92.490	0.0	6.10	P, S

Table B.1: Hypocentral information for events used in the P and S-wave tomography.

Year	Month	Day	Time	Latitude (°)	Longitude (°)	Depth (km)	M_w	Phase
2007	01	08	17:21:47.00	39.820	70.320	0.0	6.00	P, S
2007	01	09	15:49:35.00	59.470	-137.180	16.4	5.73	P, S
2007	01	13	04:23:00.00	46.900	155.100	11.0	8.00	S
2007	01	13	04:23:21.20	46.170	154.800	12.0	8.11	P, S
2007	01	13	17:37:06.30	47.030	156.390	28.0	5.99	P, S
2007	01	15	18:17:59.20	34.940	138.810	169.8	5.89	P, S
2007	01	17	23:18:50.10	10.210	58.590	22.9	6.22	P, S
2007	01	18	15:27:18.30	-6.020	101.180	14.9	5.60	S
2007	01	25	10:59:00.00	22.700	122.100	17.0	5.90	P
2007	01	31	20:31:34.80	-8.140	107.250	72.2	5.52	P
2007	02	04	20:56:57.40	19.550	-78.470	0.0	6.20	P, S
2007	02	14	19:50:00.80	0.330	97.220	12.0	5.71	P, S
2007	02	17	00:02:00.00	41.700	143.700	29.0	6.00	S
2007	02	17	00:02:56.80	41.650	143.970	38.2	5.99	P, S
2007	02	18	21:37:44.80	5.920	-82.560	17.7	5.65	P
2007	02	19	02:33:44.40	1.720	30.650	28.5	5.61	P, S
2007	03	01	23:11:52.10	26.540	-44.570	12.0	5.98	P, S
2007	03	04	11:26:12.00	33.750	-38.550	14.1	5.58	P
2007	03	06	03:49:38.10	-0.390	100.430	0.0	6.30	P, S
2007	03	06	05:49:26.90	-0.510	100.470	21.9	6.29	P, S
2007	03	07	10:53:37.60	1.800	97.740	49.0	5.90	P, S
2007	03	08	05:03:30.50	30.000	140.230	0.0	6.10	P
2007	03	09	03:22:00.00	43.000	134.300	580.0	6.10	S
2007	03	09	03:22:39.10	43.220	133.520	0.0	6.20	P
2007	03	09	07:27:31.20	-11.580	66.320	12.0	5.68	P
2007	03	10	21:12:58.50	55.070	162.570	44.8	5.83	P
2007	03	11	07:09:26.40	43.970	148.180	58.0	5.70	P
2007	03	12	18:59:25.20	46.820	152.090	136.3	5.59	P
2007	03	17	22:43:09.60	4.610	-78.530	13.1	6.01	P, S
2007	03	18	01:25:00.00	42.100	144.300	29.0	5.60	S
2007	03	18	01:25:24.10	42.000	144.290	41.7	5.55	P
2007	03	18	02:11:05.50	4.690	-78.530	12.0	6.23	P, S
2007	03	22	06:10:43.10	-3.350	86.760	33.0	5.91	P, S
2007	03	25	00:41:57.80	37.280	136.610	12.0	6.68	P, S
2007	03	28	21:17:08.10	-6.290	29.570	0.0	5.80	P, S
2007	03	30	09:05:00.00	44.000	146.300	101.0	5.60	P, S
2007	04	01	02:51:00.00	32.400	137.900	400.0	5.70	P, S
2007	04	03	03:35:07.28	36.451	70.688	222.1	6.20	P, S
2007	04	04	19:58:03.80	-17.230	66.790	10.0	5.80	P, S
2007	04	04	21:40:00.00	31.000	142.000	5.0	5.60	P, S
2007	04	05	03:56:48.50	37.391	-24.680	12.0	6.30	P
2007	04	07	05:20:49.60	-39.800	46.190	18.8	5.76	P
2007	04	07	07:09:22.20	37.281	-24.679	8.6	6.10	P
2007	04	07	09:51:51.60	2.740	95.480	12.0	6.11	P, S
2007	04	09	10:18:04.58	48.304	154.695	36.0	5.70	P
2007	04	13	05:42:23.00	17.370	-100.140	42.7	5.96	P
2007	04	15	04:12:30.19	47.002	153.435	34.9	5.50	P
2007	04	18	15:07:31.60	42.670	141.960	125.6	5.51	P
2007	04	20	00:26:00.00	25.800	125.100	5.0	6.10	S
2007	04	20	00:26:40.60	25.722	125.093	10.0	6.00	P, S
2007	04	20	01:45:00.00	25.700	125.100	5.0	6.10	S
2007	04	20	01:45:56.10	25.570	125.100	12.0	6.26	P, S
2007	04	20	02:23:34.00	25.600	125.070	14.3	5.96	P
2007	04	20	19:37:57.20	27.510	128.430	0.0	5.70	P
2007	04	27	08:02:49.70	5.090	94.430	49.2	5.90	P, S
2007	04	29	12:41:56.90	52.040	-179.920	0.0	6.50	P, S
2007	05	04	12:06:51.40	-1.440	-14.840	0.0	6.00	P
2007	05	05	08:51:39.10	34.330	81.970	23.9	6.06	P, S

Table B.1: Hypocentral information for events used in the P and S-wave tomography.

Year	Month	Day	Time	Latitude (°)	Longitude (°)	Depth (km)	M_w	Phase
2007	05	06	18:27:20.90	17.430	120.140	38.2	5.52	P, S
2007	05	14	09:31:43.10	1.255	97.248	30.0	5.50	P, S
2007	05	16	08:56:16.50	20.520	100.890	12.6	6.29	P, S
2007	05	18	15:59:58.53	41.597	141.991	58.3	5.50	P
2007	05	23	04:41:44.90	52.345	-31.811	14.9	5.70	P
2007	05	23	19:09:15.10	21.980	-96.310	24.0	5.65	S
2007	05	30	20:22:12.66	52.137	157.293	116.0	6.40	P, S
2007	06	02	21:34:57.80	23.020	101.130	12.0	6.10	P, S
2007	06	13	19:29:40.20	13.430	-91.220	31.6	6.68	P
2007	06	15	18:49:53.40	1.750	30.710	24.2	5.85	P, S
2007	06	23	08:17:19.89	21.473	99.779	22.0	5.60	P
2007	07	01	04:12:00.00	43.500	144.900	140.0	5.80	P, S
2007	07	03	08:26:00.80	0.810	-30.040	17.0	6.32	P, S
2007	07	06	01:09:19.00	16.350	-93.990	113.0	6.00	P
2007	07	13	21:54:43.10	51.560	-175.960	49.8	5.97	P
2007	07	15	13:08:00.80	52.300	-167.900	14.7	6.09	P, S
2007	07	15	13:26:15.20	52.290	-167.920	15.3	5.88	P
2007	07	16	01:13:00.00	37.500	138.600	8.0	6.60	S
2007	07	16	01:13:22.40	37.500	138.470	12.0	6.63	P
2007	07	16	06:37:40.40	37.560	138.550	18.4	5.75	P
2007	07	16	14:17:00.00	36.900	135.100	380.0	6.80	S
2007	07	16	14:17:37.30	36.840	135.030	374.9	6.82	P
2007	07	16	22:58:23.60	7.192	-72.158	5.0	5.50	P
2007	07	17	14:10:42.50	-2.720	35.930	12.0	5.87	P, S
2007	07	20	10:06:52.00	42.930	82.380	25.3	5.57	P, S
2007	07	23	22:30:08.40	14.360	-91.350	112.5	5.53	P
2007	07	25	23:37:31.50	7.060	92.520	12.0	5.98	P, S
2007	07	29	04:54:36.70	53.570	169.650	37.0	5.87	P, S
2007	07	30	22:42:05.60	19.060	95.770	12.0	5.60	P, S
2007	07	31	15:07:00.00	27.300	126.800	5.0	5.90	S
2007	07	31	22:55:31.10	0.040	-17.860	21.8	6.18	P, S
2007	08	01	08:15:00.00	34.000	136.800	400.0	5.50	S
2007	08	01	08:16:00.18	33.905	136.613	370.5	5.50	P
2007	08	02	02:37:00.00	47.200	141.700	5.0	6.10	S
2007	08	02	02:37:42.38	47.116	141.798	5.0	6.20	P
2007	08	02	03:21:42.80	51.100	-179.730	31.9	6.74	P
2007	08	02	05:22:00.00	47.000	141.700	5.0	5.70	P
2007	08	02	06:23:11.50	50.920	-179.870	28.4	5.61	P
2007	08	02	10:37:31.59	46.626	141.771	10.0	5.50	P, S
2007	08	02	13:37:29.20	12.620	47.510	16.3	5.69	P, S
2007	08	07	00:02:00.00	27.600	126.500	5.0	6.00	S
2007	08	08	17:04:57.80	-6.030	107.580	304.8	7.54	P
2007	08	09	17:25:05.18	25.918	-45.001	10.0	5.60	P, S
2007	08	13	22:23:04.50	-31.070	-13.370	12.0	5.55	P, S
2007	08	14	04:13:34.45	46.877	141.746	10.0	5.50	P, S
2007	08	15	20:22:11.10	50.280	-177.690	12.0	6.47	P, S
2007	08	20	12:37:06.70	-0.020	-18.140	20.8	5.75	P, S
2007	08	20	22:42:27.40	8.068	-39.255	9.7	6.50	P, S

Appendix C

Residual analysis

This appendix complements the content of chapter 2 and presents the relative arrival-time residuals at each station. The results are the raw data obtained from the MCCC, which are used in the tomography in chapters 4 and 5. The statistical information on the histograms show the number of data (N), mean ($\bar{x}$), median ($\tilde{\mathrm{x}}$) and standard deviation (σ).

C.1 P-wave relative arrival-time residuals

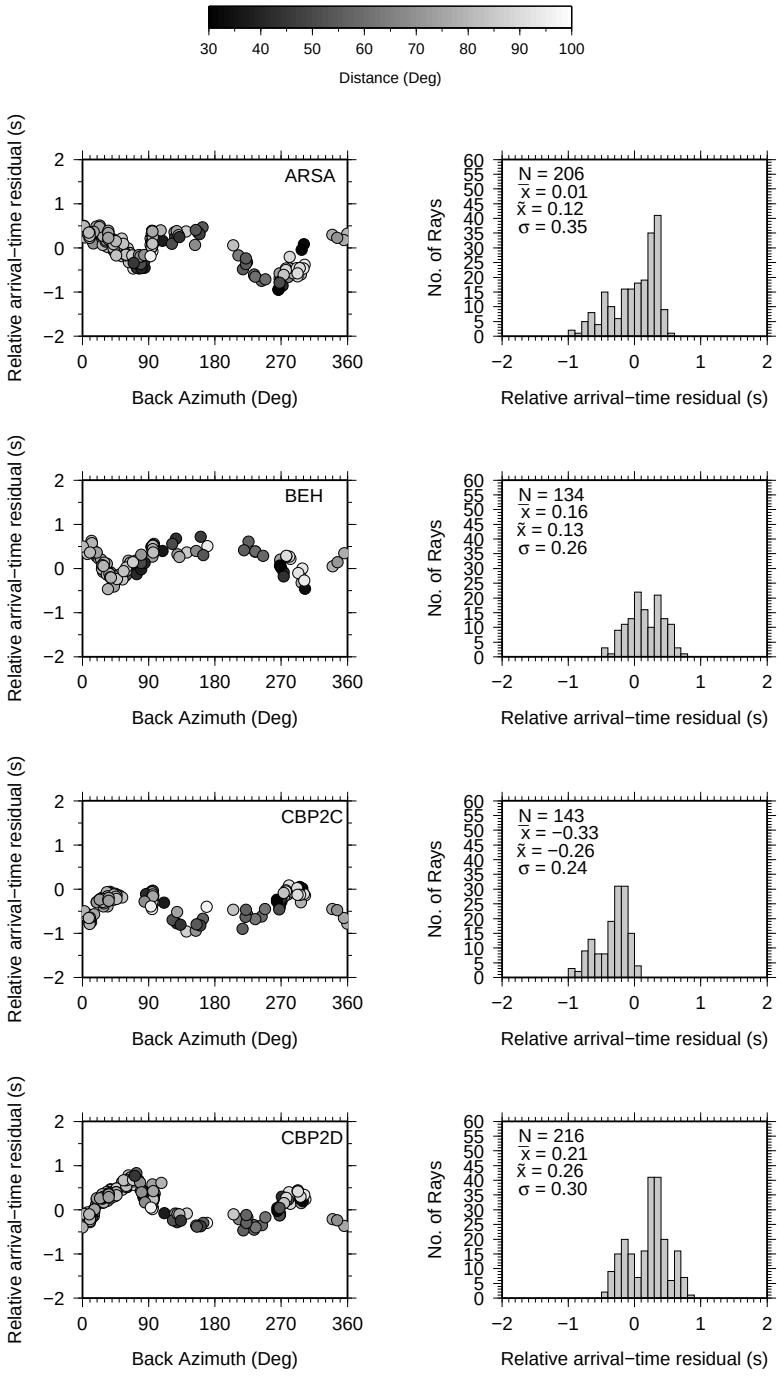

Figure C.1: P-wave relative arrival-time residuals for stations ARSA, BEH, CBP2C and CBP2D

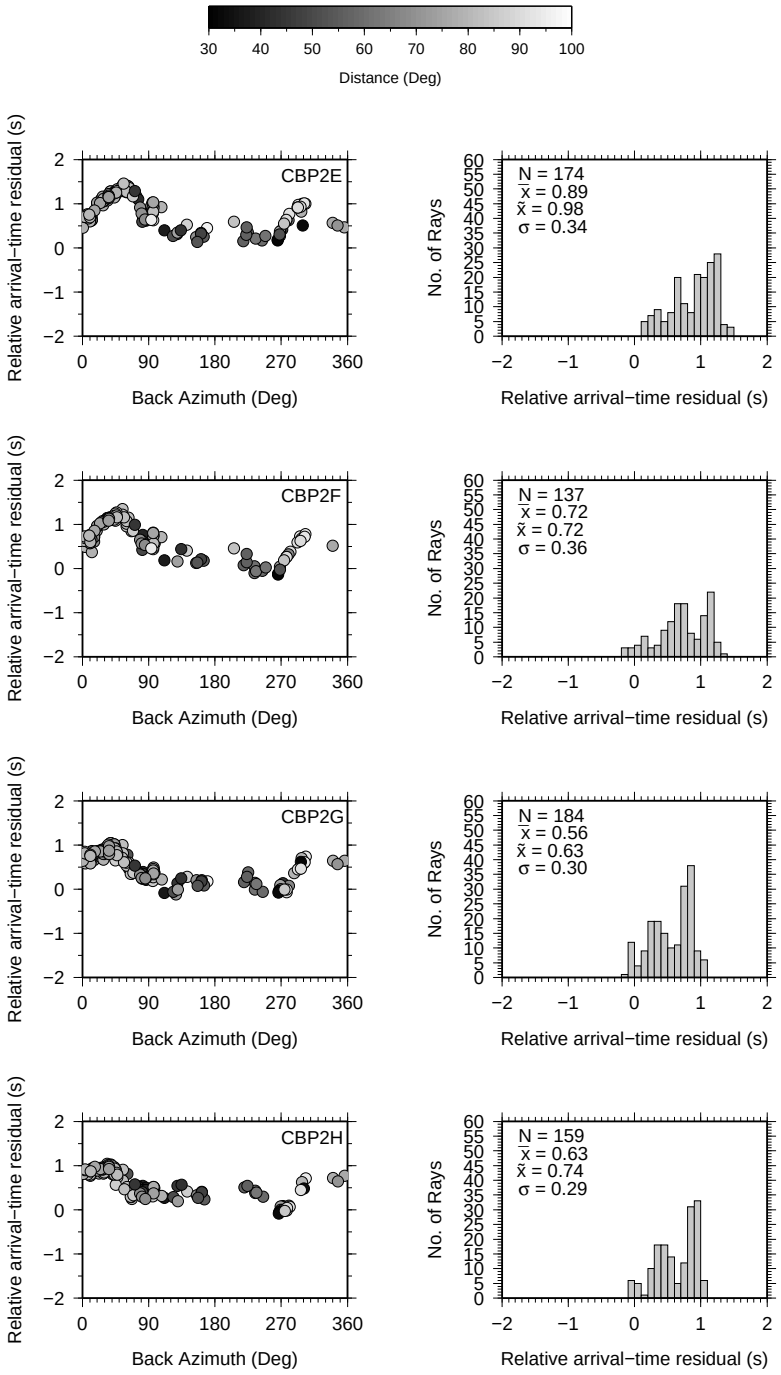

Figure C.2: P-wave relative arrival-time residuals for stations CBP2E, CBP2F, CBP2G and CBP2H

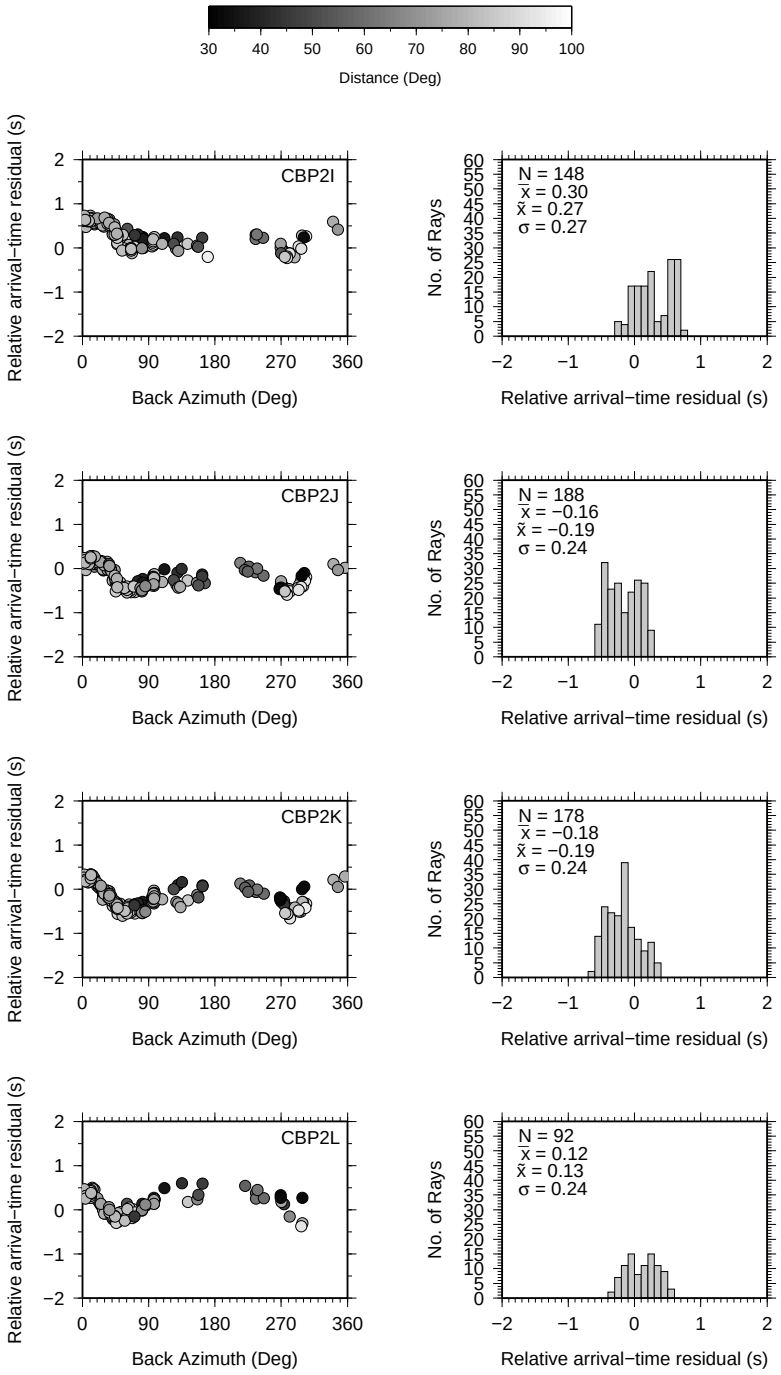

Figure C.3: P-wave relative arrival-time residuals for stations CBP2I, CBP2J, CBP2K and CBP2L

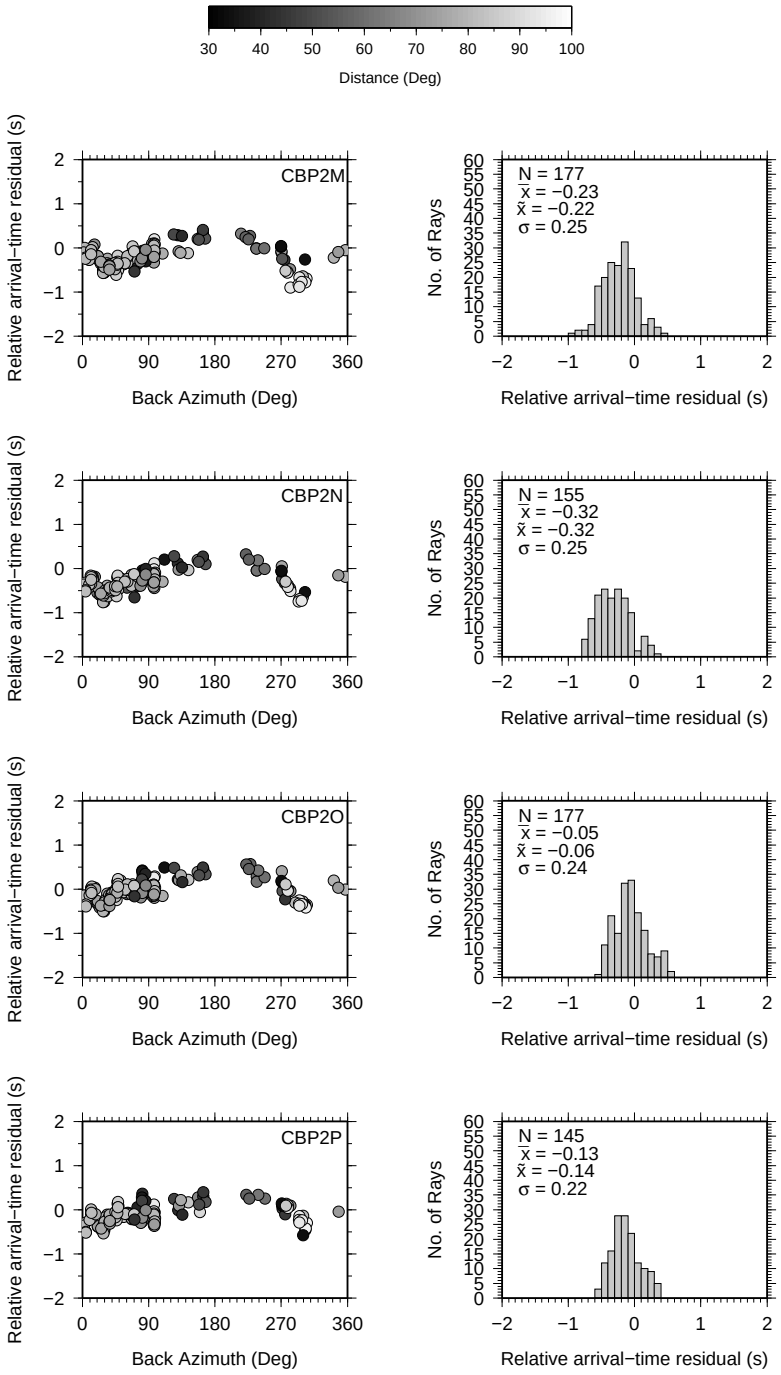

Figure C.4: P-wave relative arrival-time residuals for stations CBP2M, CBP2N, CBP2O and CBP2P

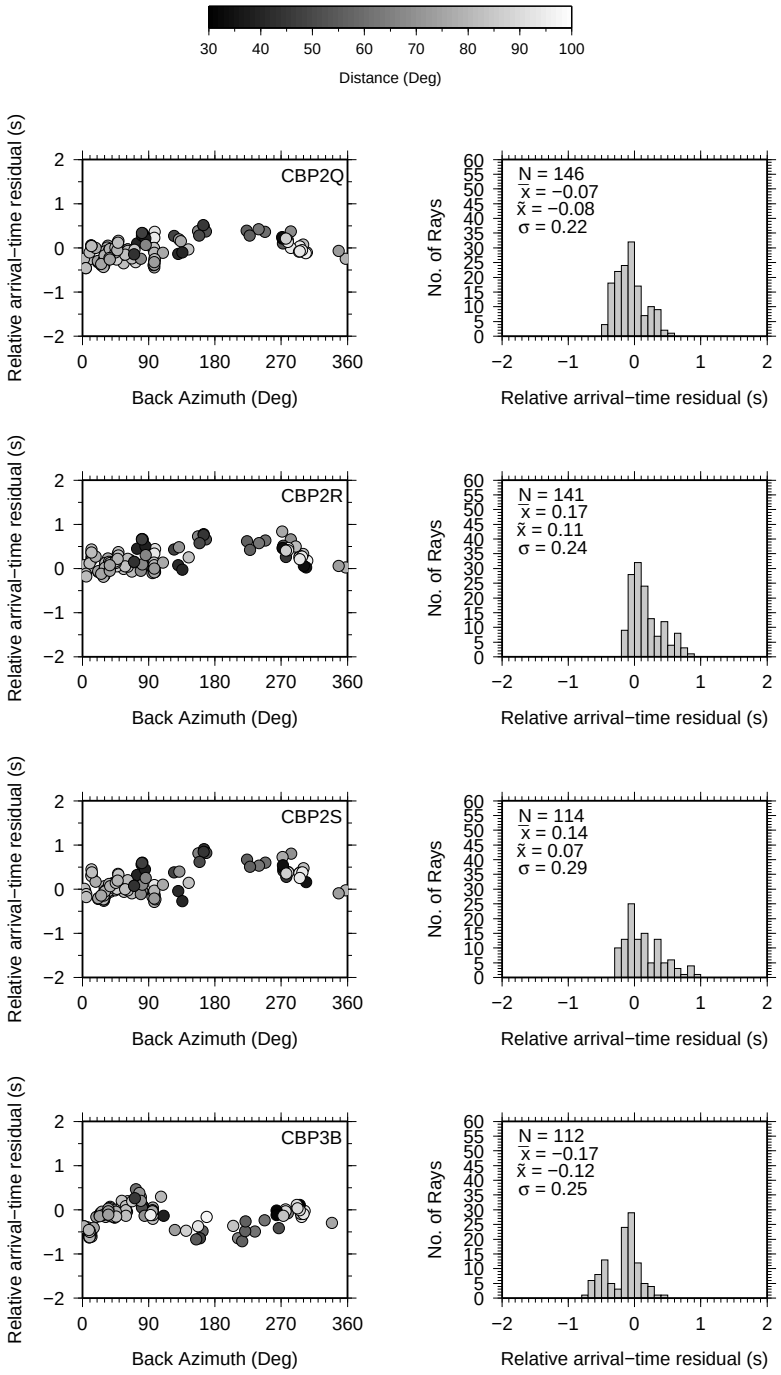

Figure C.5: P-wave relative arrival-time residuals for stations CBP2Q, CBP2R, CBP2S and CBP3B

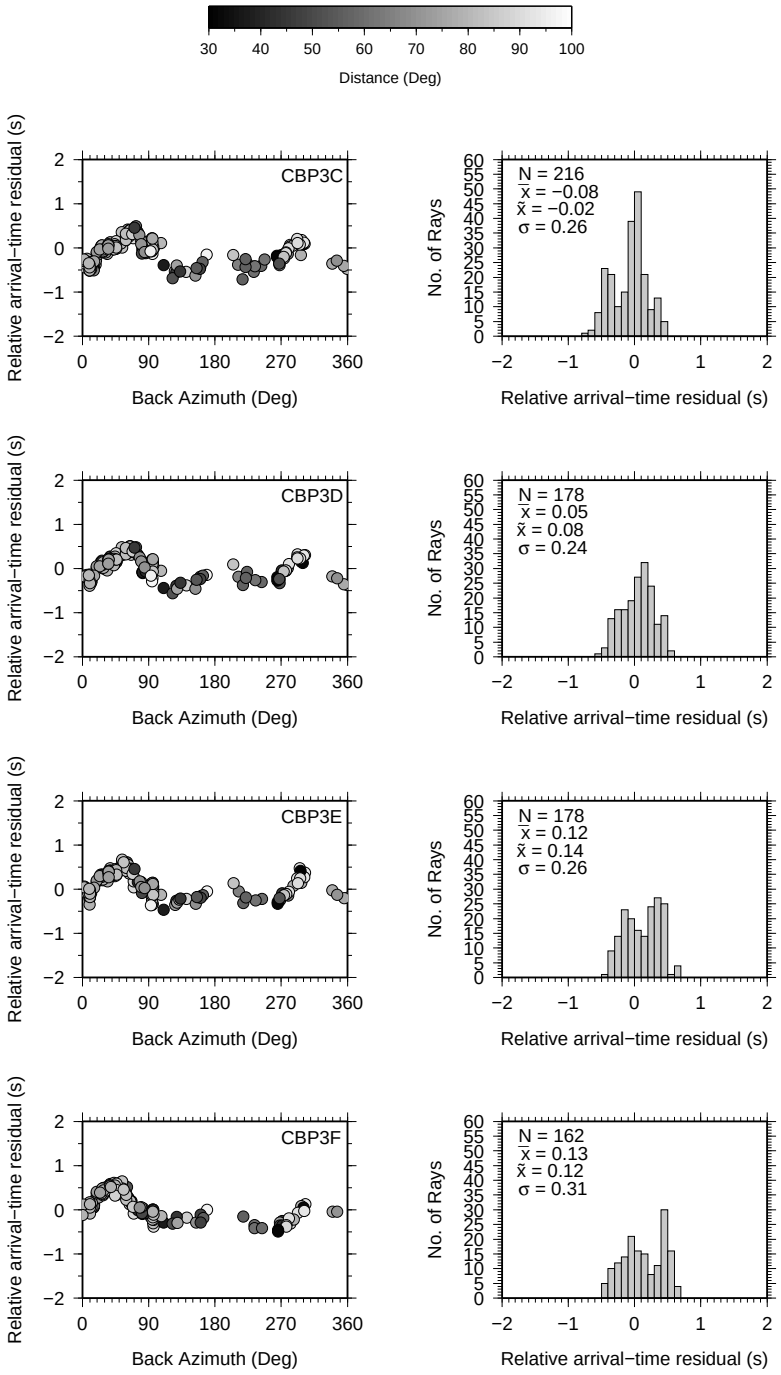

Figure C.6: P-wave relative arrival-time residuals for stations CBP3C, CBP3D, CBP3E and CBP3F

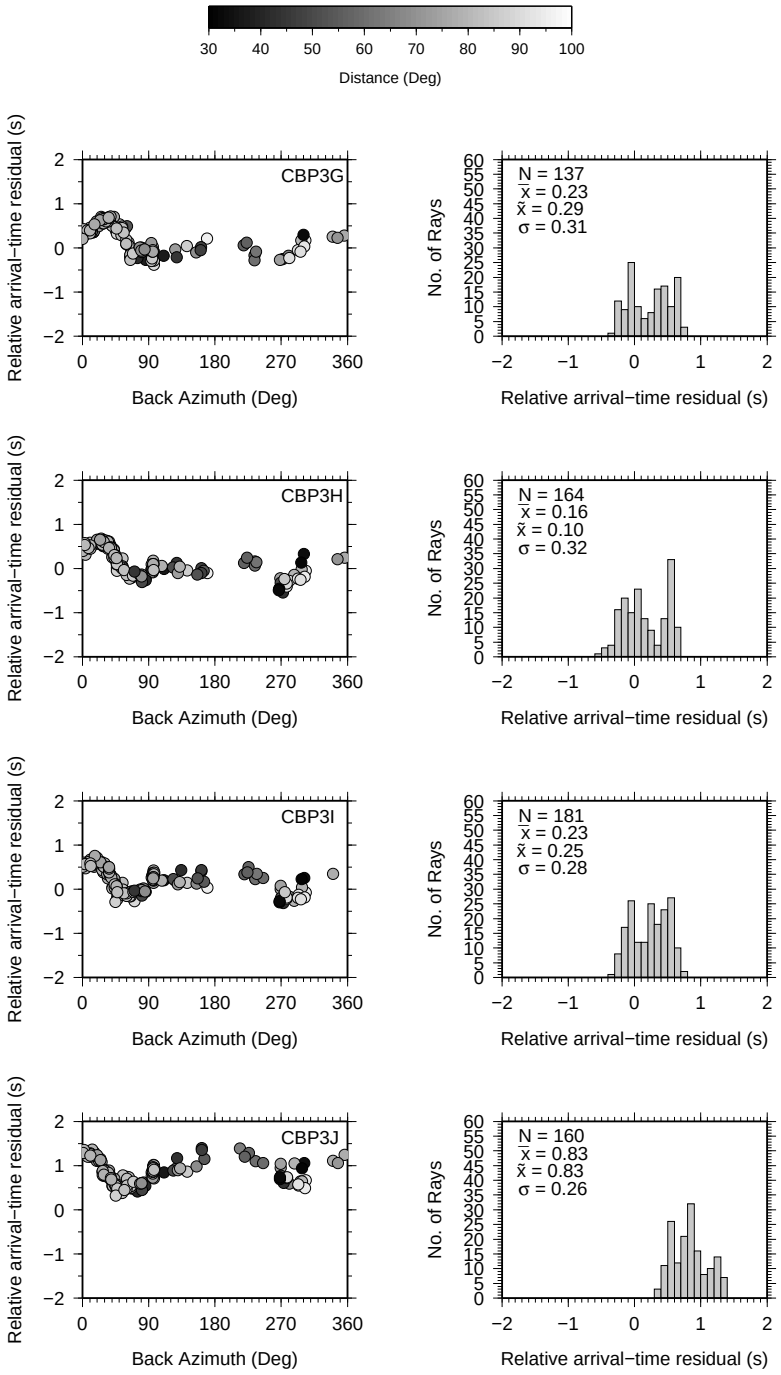

Figure C.7: P-wave relative arrival-time residuals for stations CBP3G, CBP3H, CBP3I and CBP3J

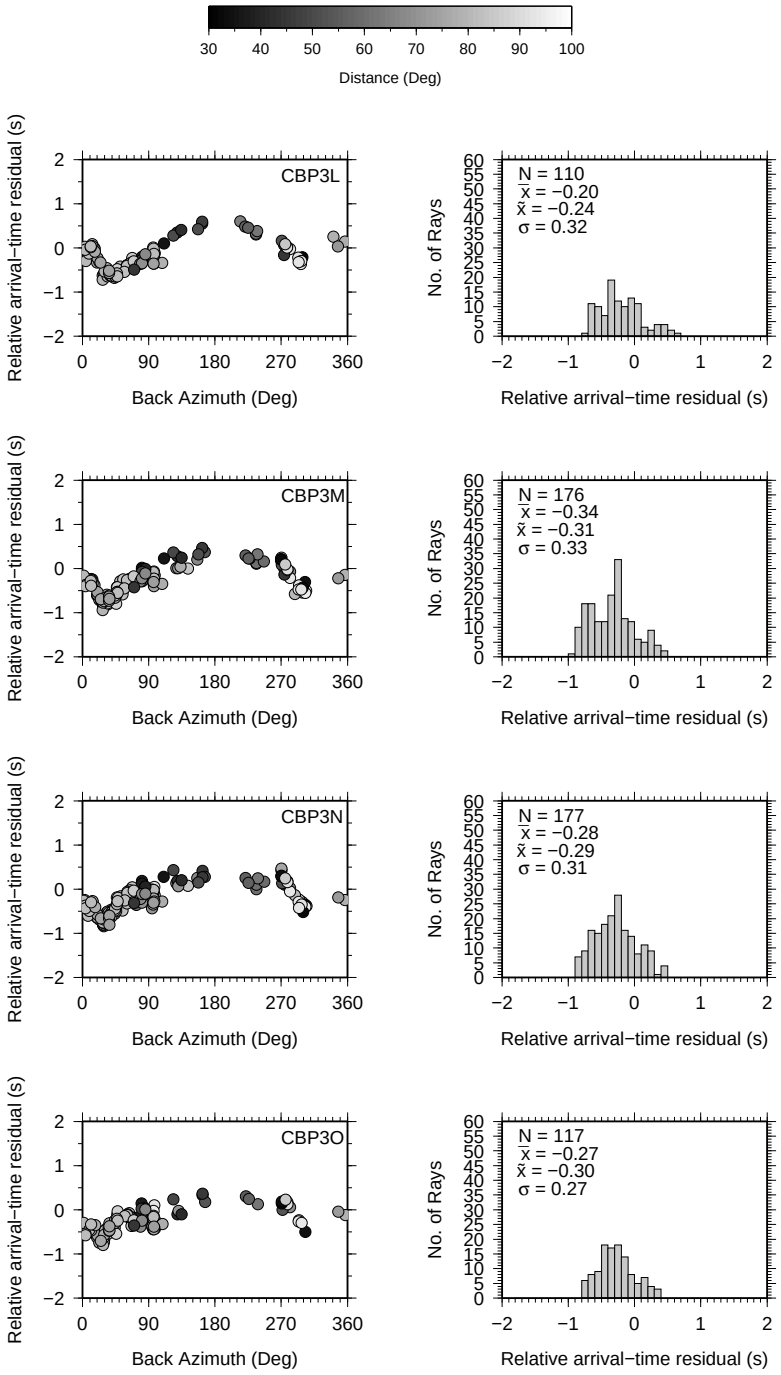

Figure C.8: P-wave relative arrival-time residuals for stations CBP3L, CBP3M, CBP3N and CBP3O

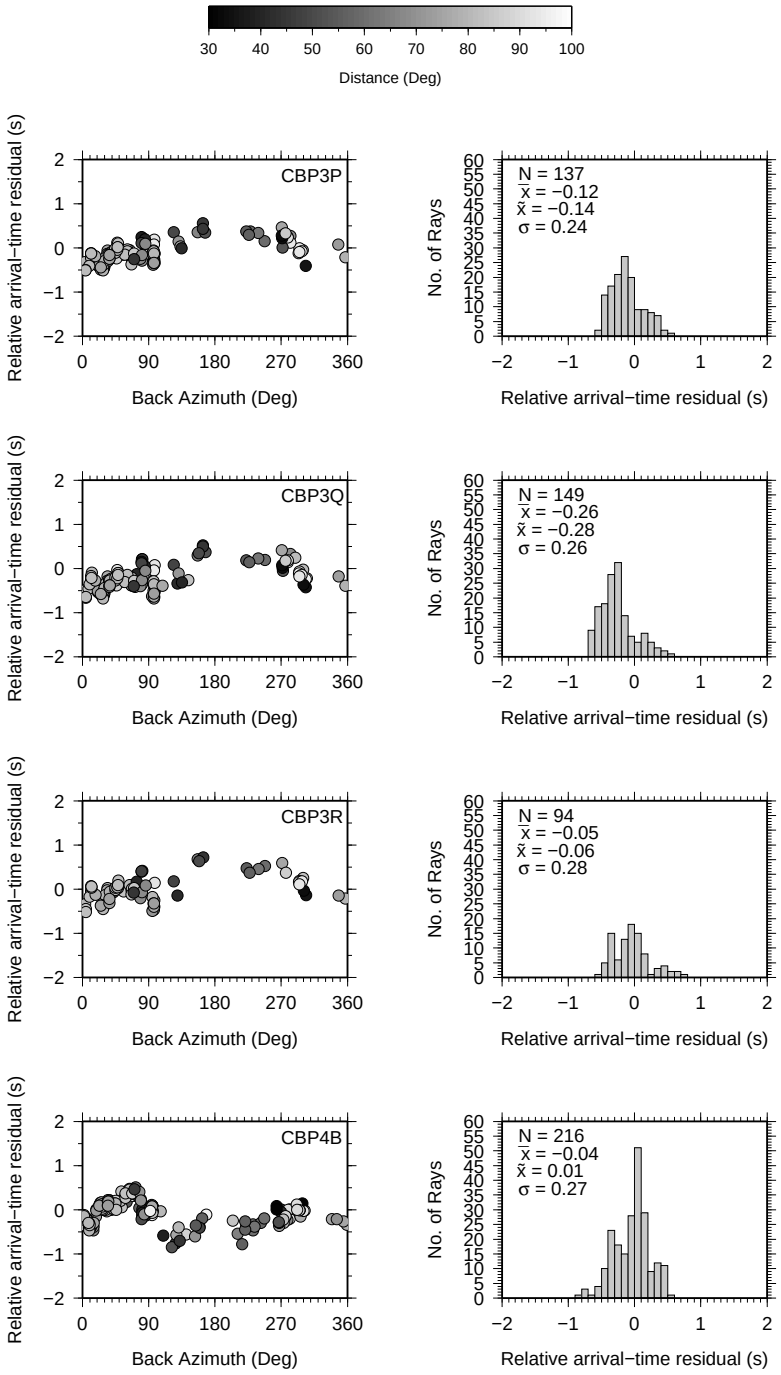

Figure C.9: P-wave relative arrival-time residuals for stations CBP3P, CBP3Q, CBP3R and CBP4B

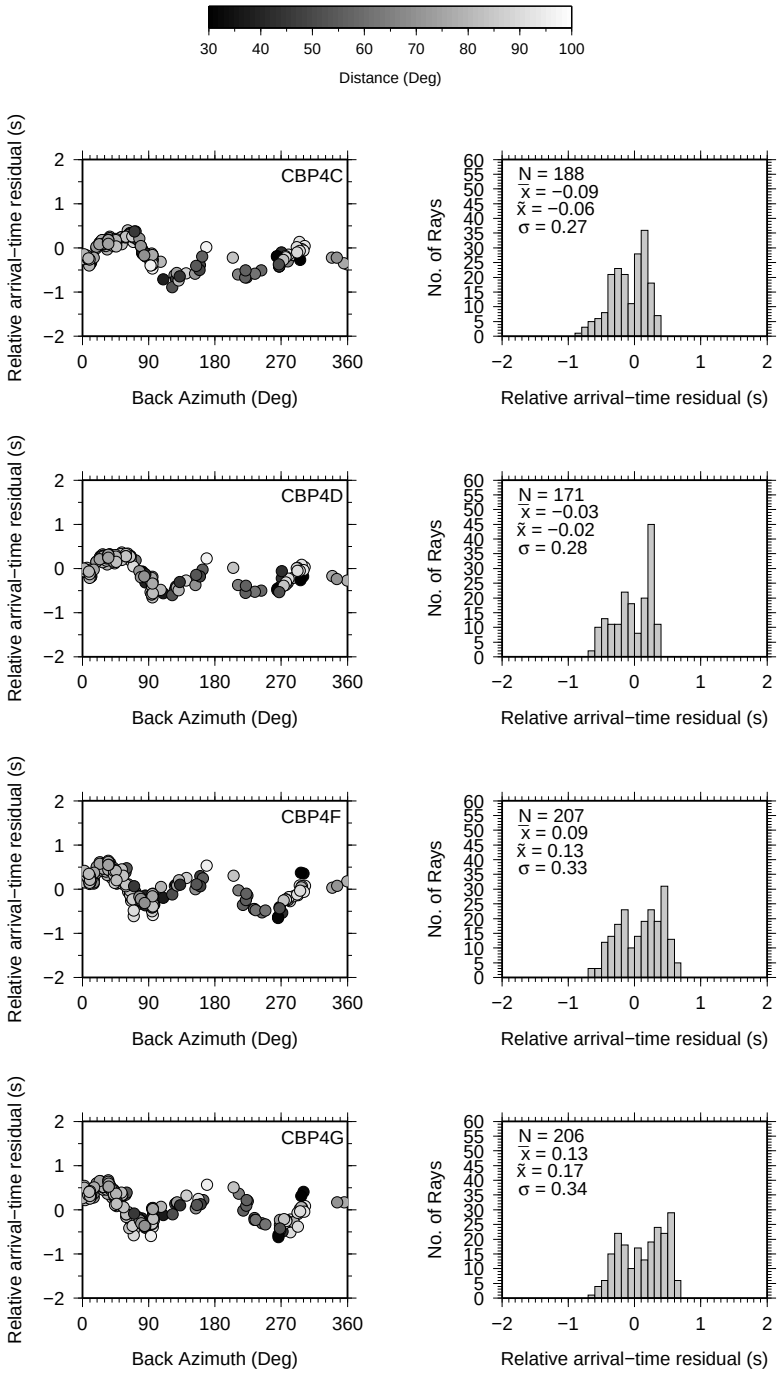

Figure C.10: P-wave relative arrival-time residuals for stations CBP4C, CBP4D, CBP4F and CBP4G

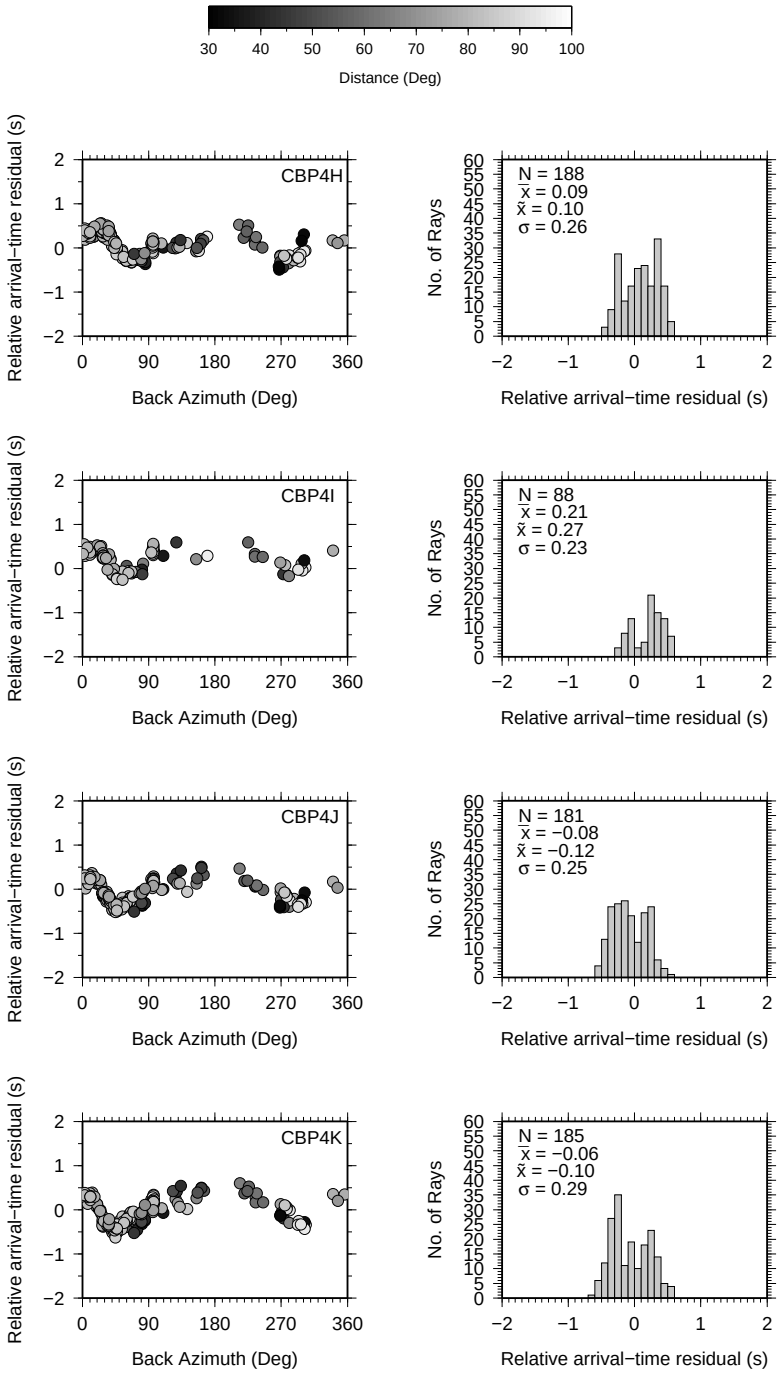

Figure C.11: P-wave relative arrival-time residuals for stations CBP4H, CBP4I, CBP4J and CBP4K

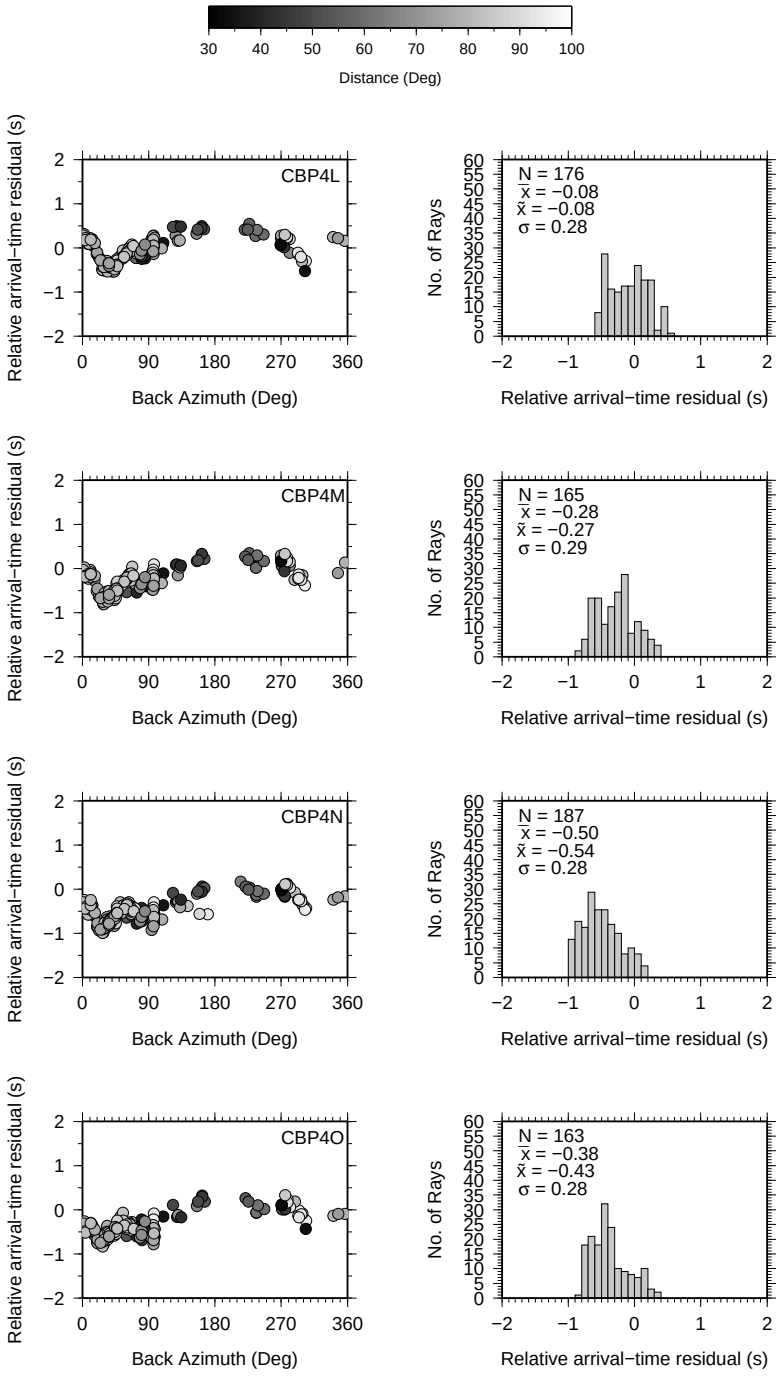

Figure C.12: P-wave relative arrival-time residuals for stations CBP4L, CBP4M, CBP4N and CBP4O

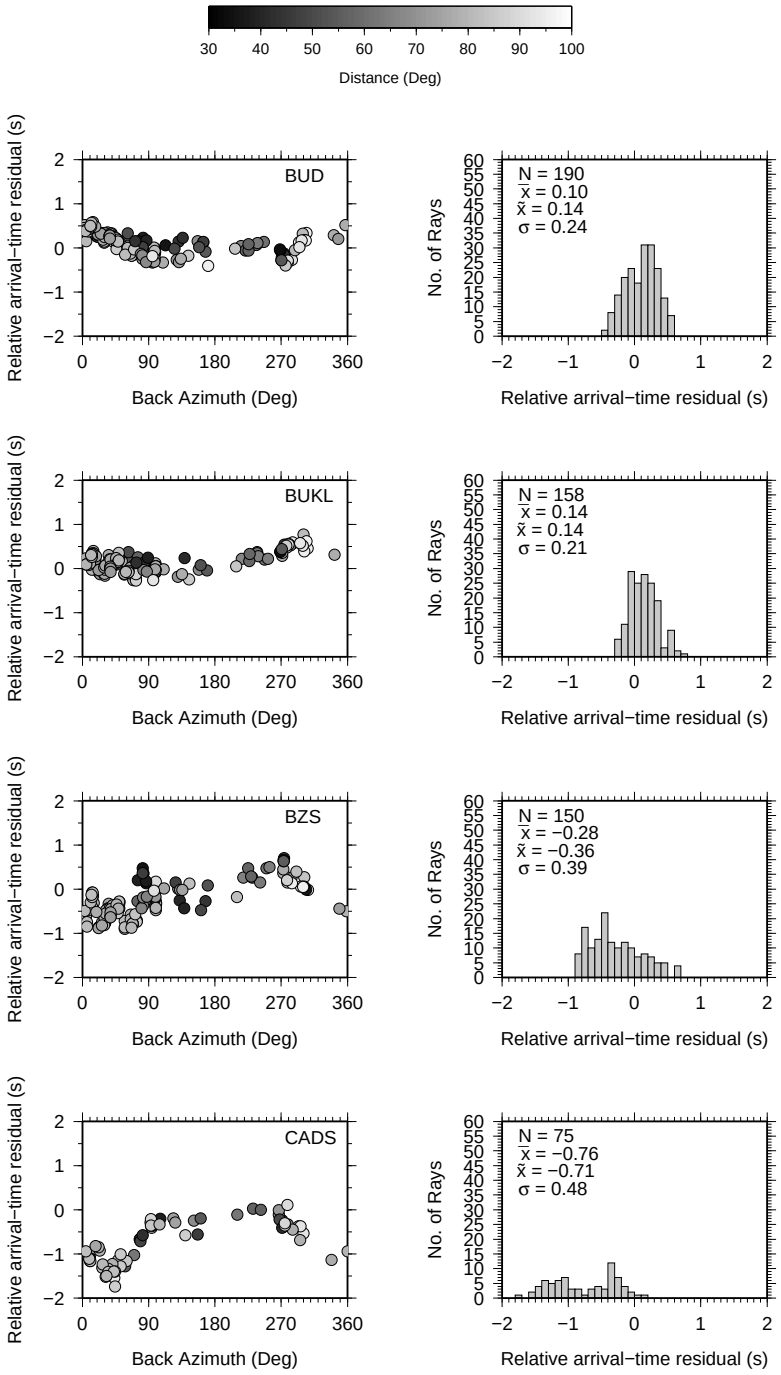

Figure C.13: P-wave relative arrival-time residuals for stations BUD, BUKL, BZS and CADS

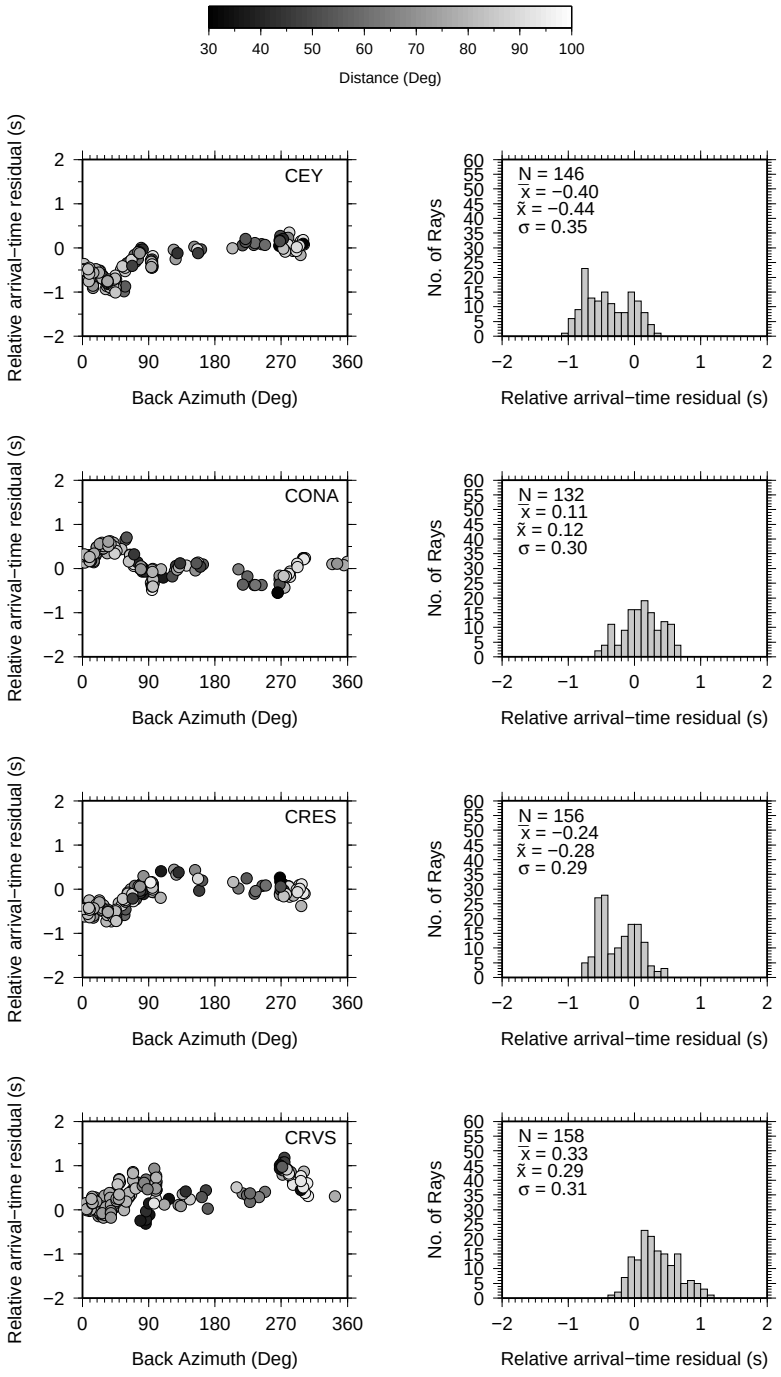

Figure C.14: P-wave relative arrival-time residuals for stations CEY, CONA, CRES and CRVS

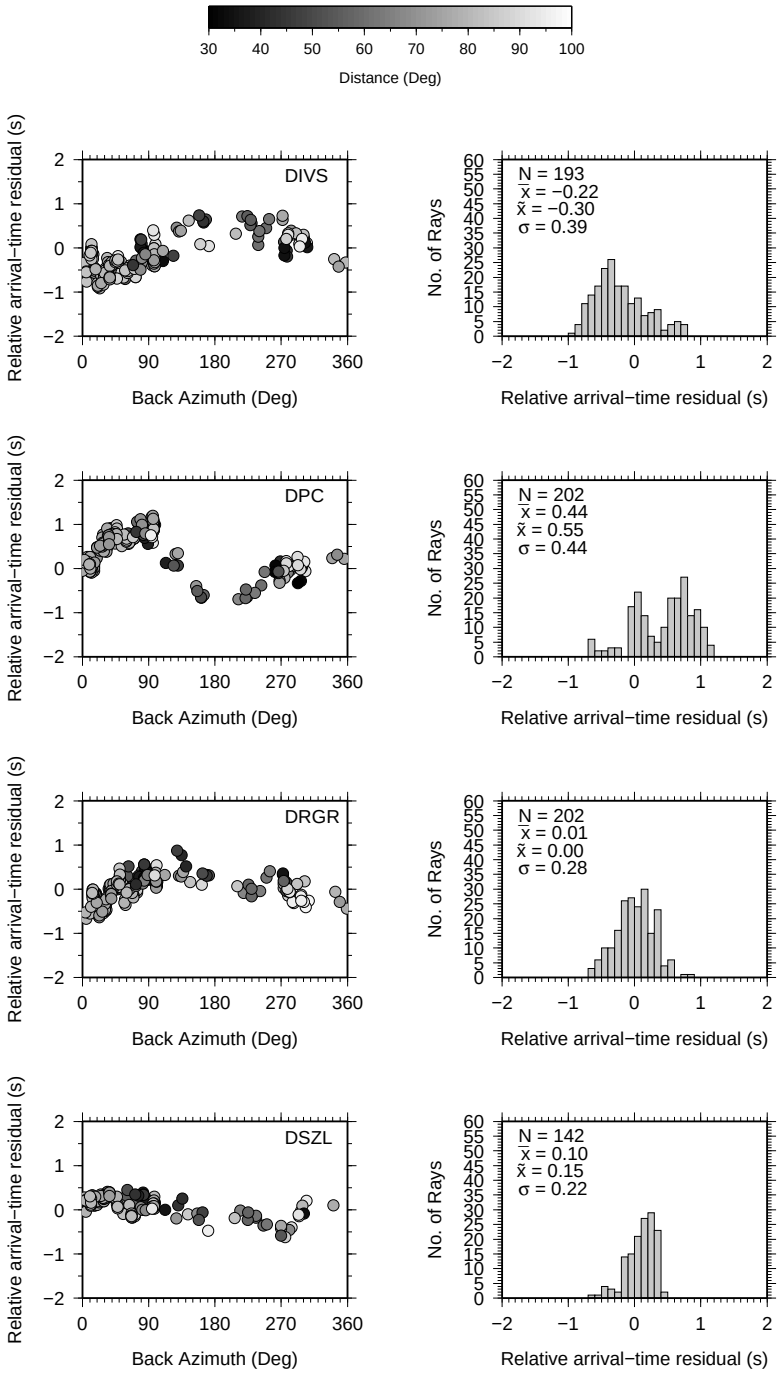

Figure C.15: P-wave relative arrival-time residuals for stations DIVS, DPC, DRGR and DSZL

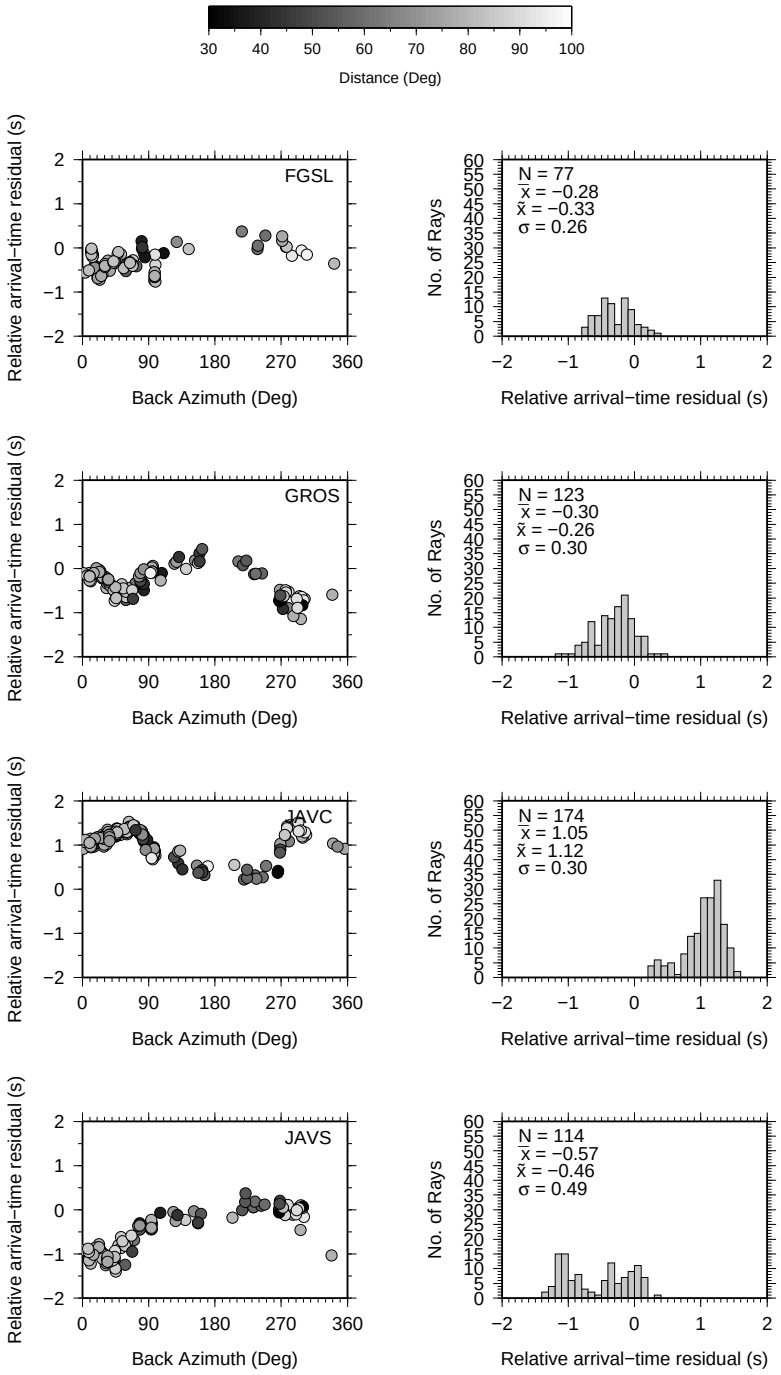

Figure C.16: P-wave relative arrival-time residuals for stations FGSL, GROS, JAVC and JAVS

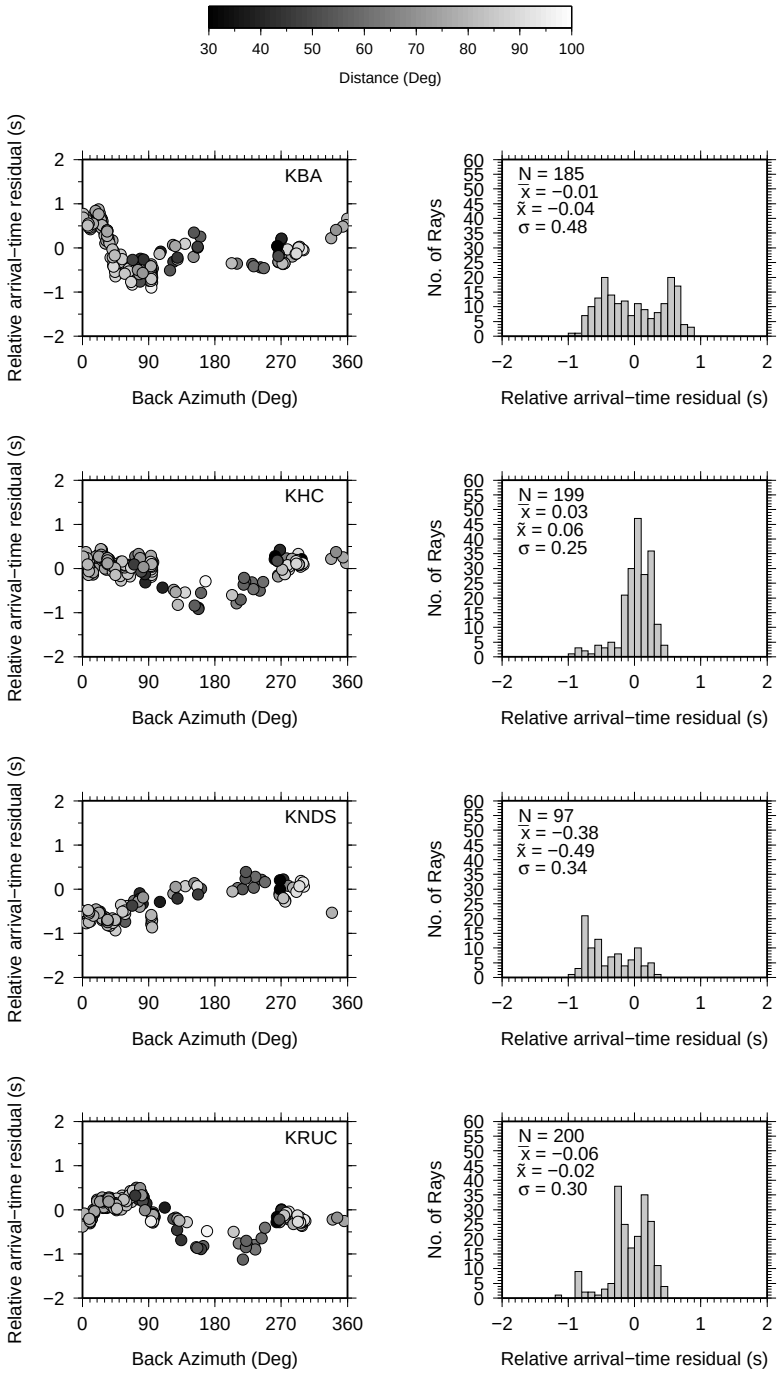

Figure C.17: P-wave relative arrival-time residuals for stations KBA, KHC, KNDS and KRUC

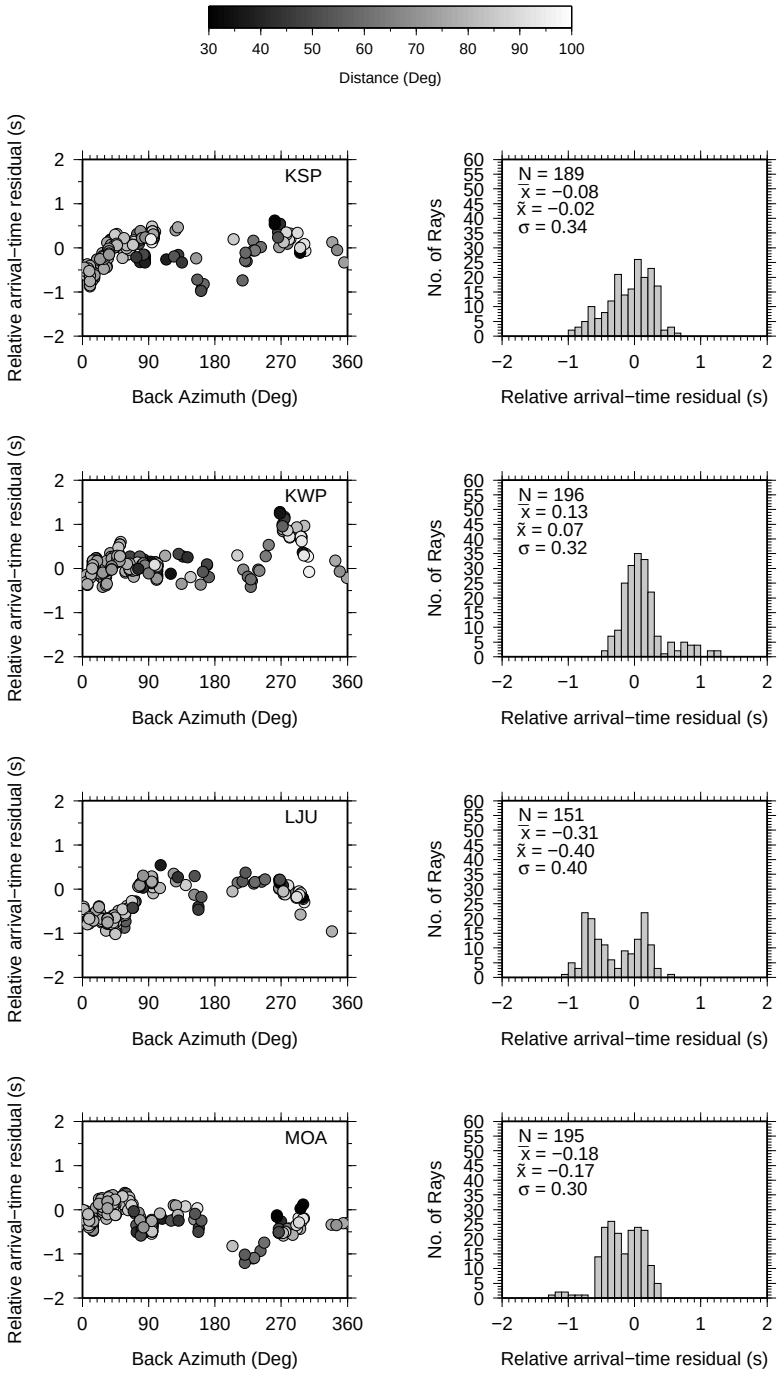

Figure C.18: P-wave relative arrival-time residuals for stations KSP, KWP, LJU and MOA

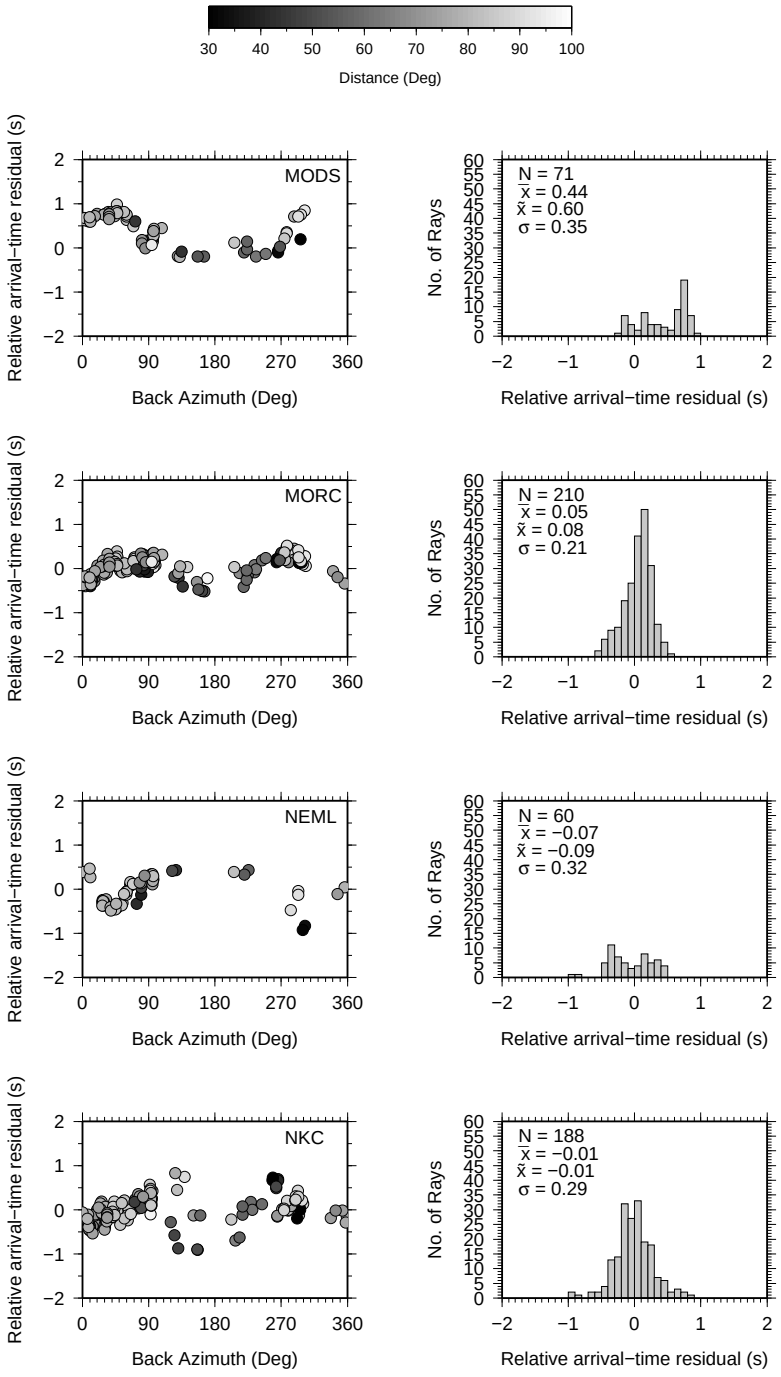

Figure C.19: P-wave relative arrival-time residuals for stations MODS, MORC, NEML and NKC

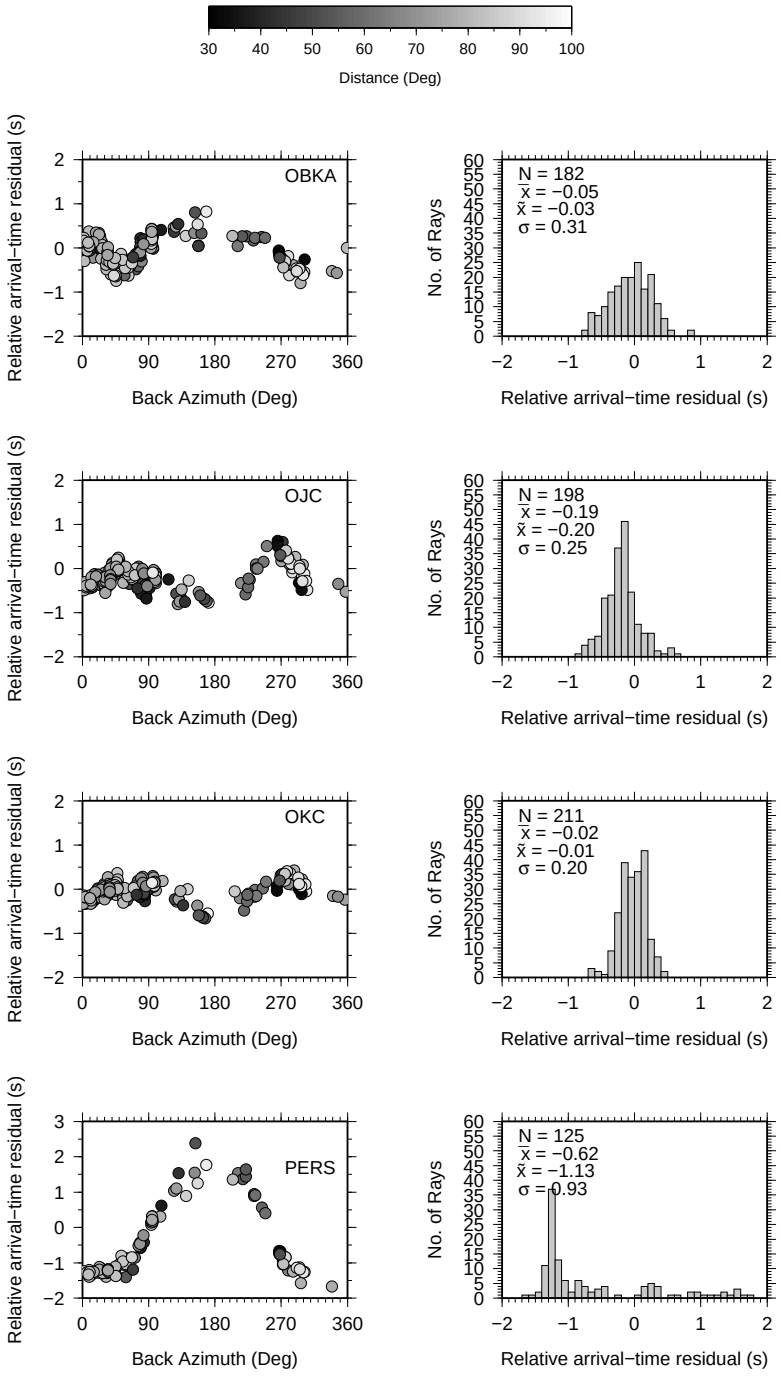

Figure C.20: P-wave relative arrival-time residuals for stations OBKA, OJC, OKC and PERS

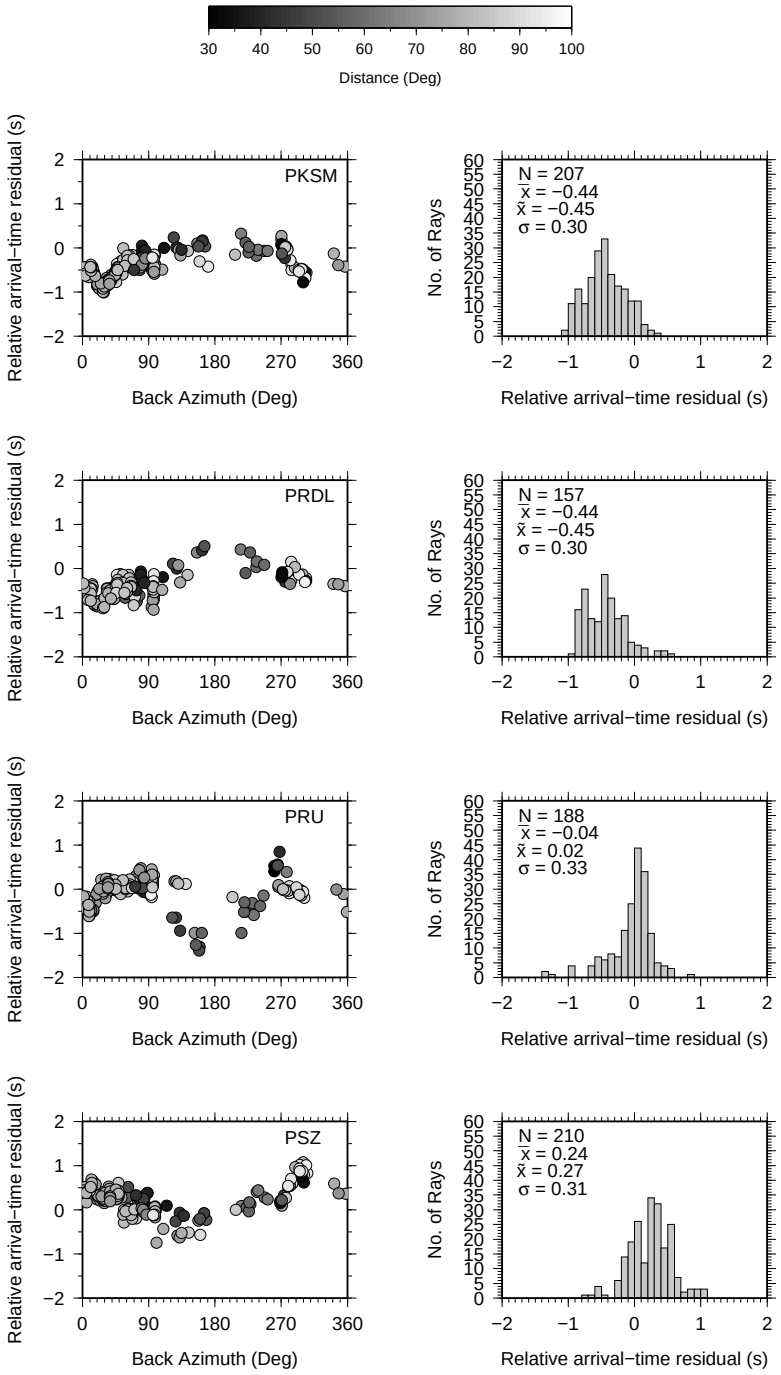

Figure C.21: P-wave relative arrival-time residuals for stations PKSM, PRDL, PRU and PSZ

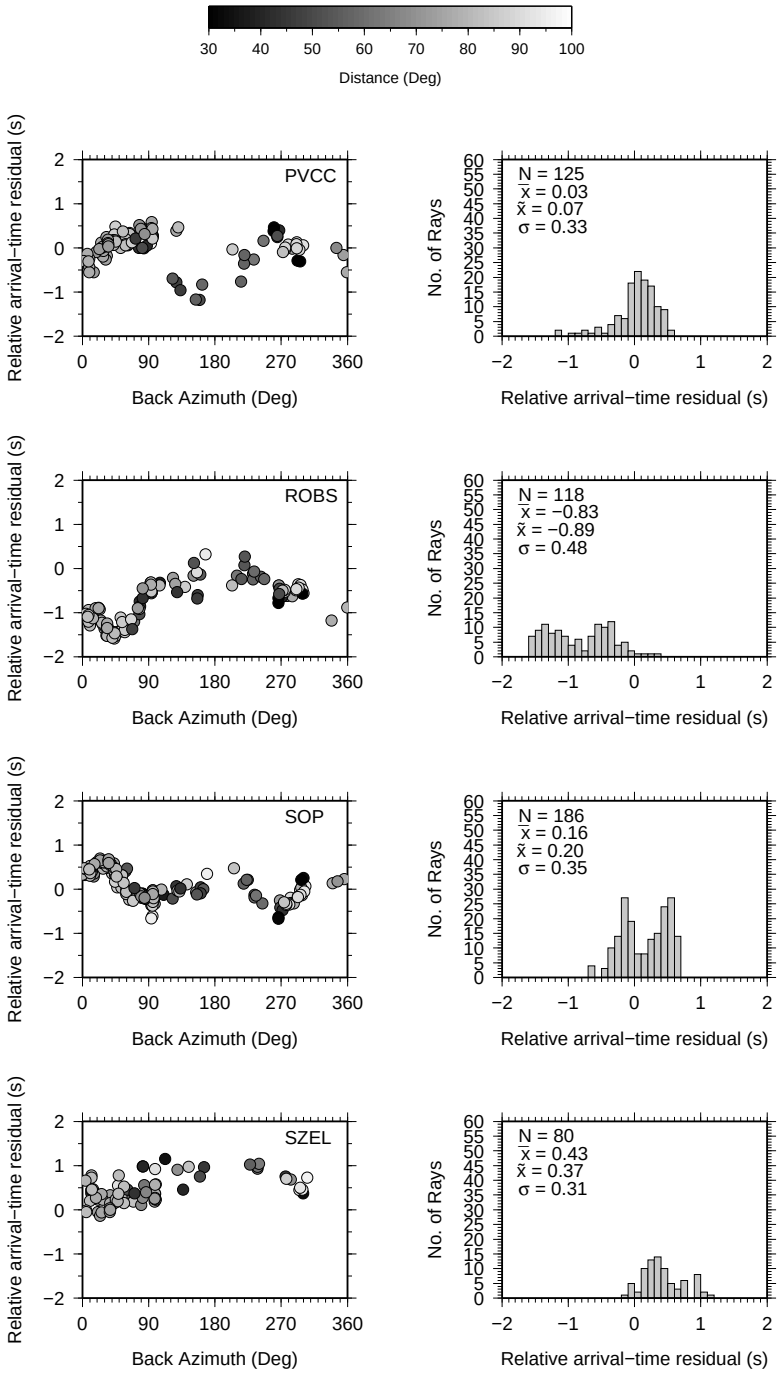

Figure C.22: P-wave relative arrival-time residuals for stations PVCC, ROBS, SOP and SZEL

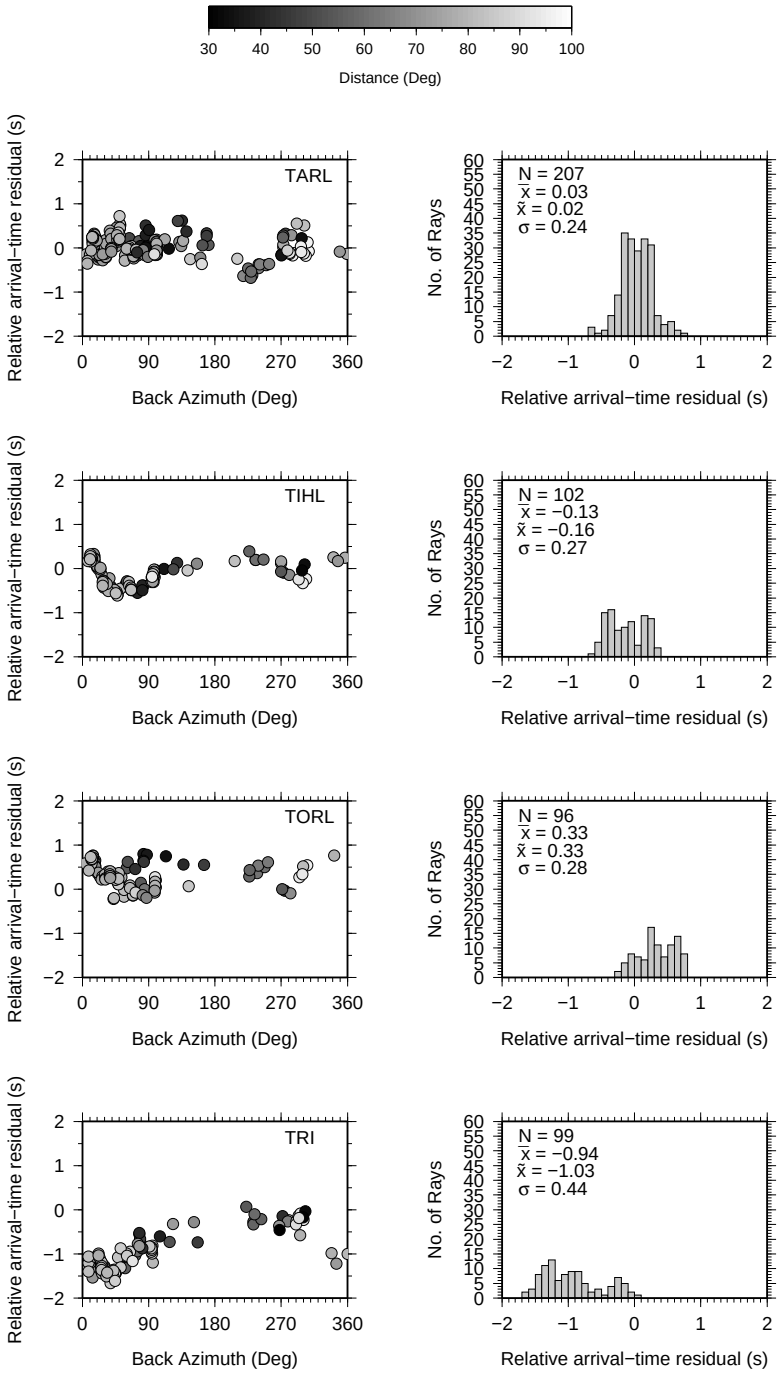

Figure C.23: P-wave relative arrival-time residuals for stations TARL, TIHL, TORL and TRI

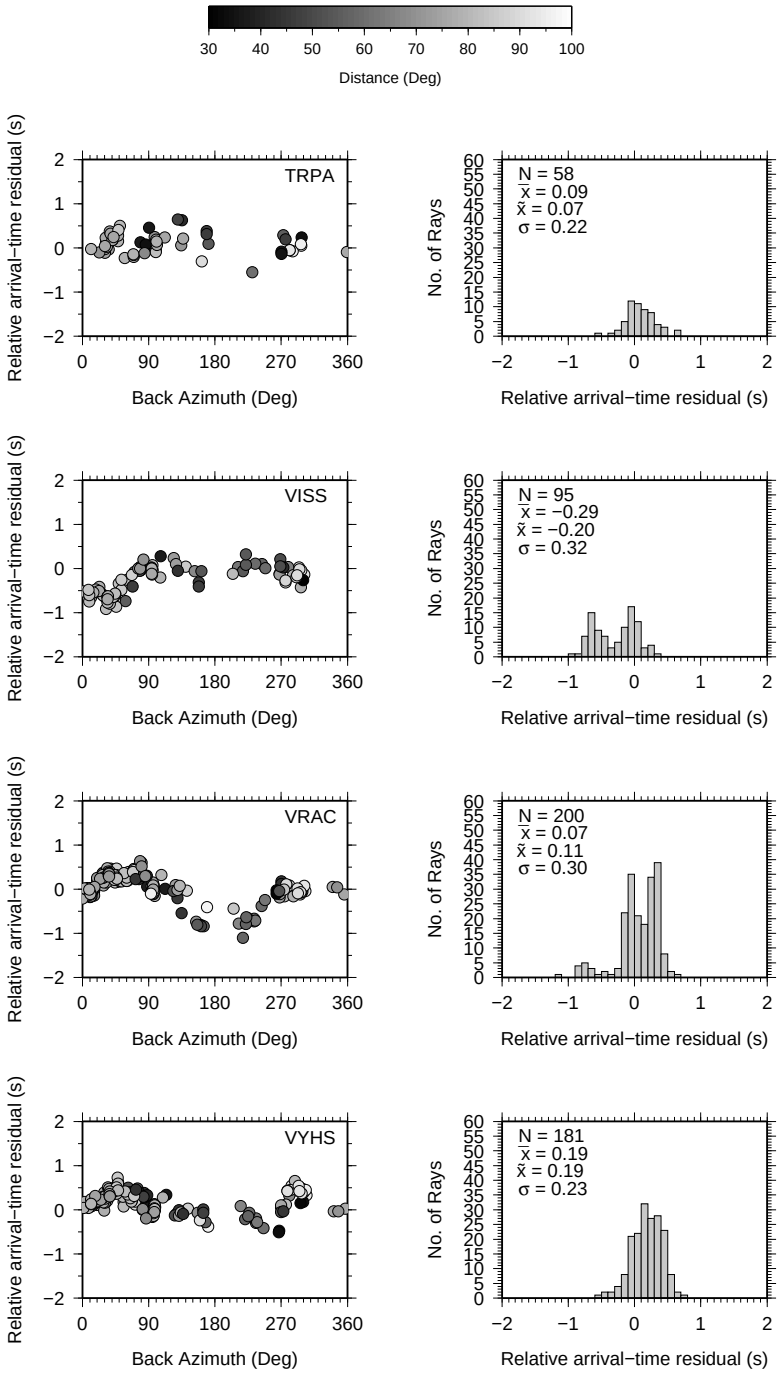

Figure C.24: P-wave relative arrival-time residuals for stations TRPA, VISS, VRAC and VYHS

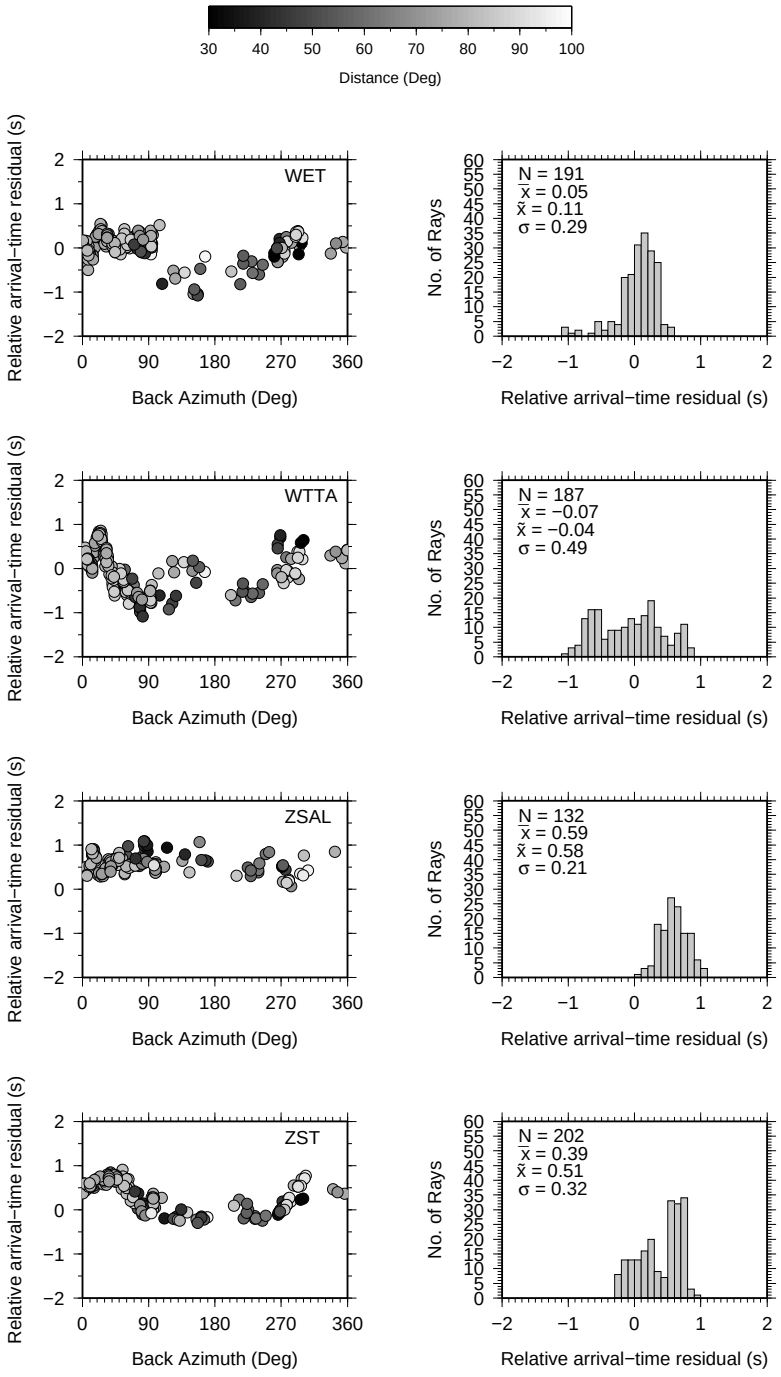

Figure C.25: P-wave relative arrival-time residuals for stations WET, WTTA, ZSAL and ZST

C.2 S-wave relative arrival-time residuals

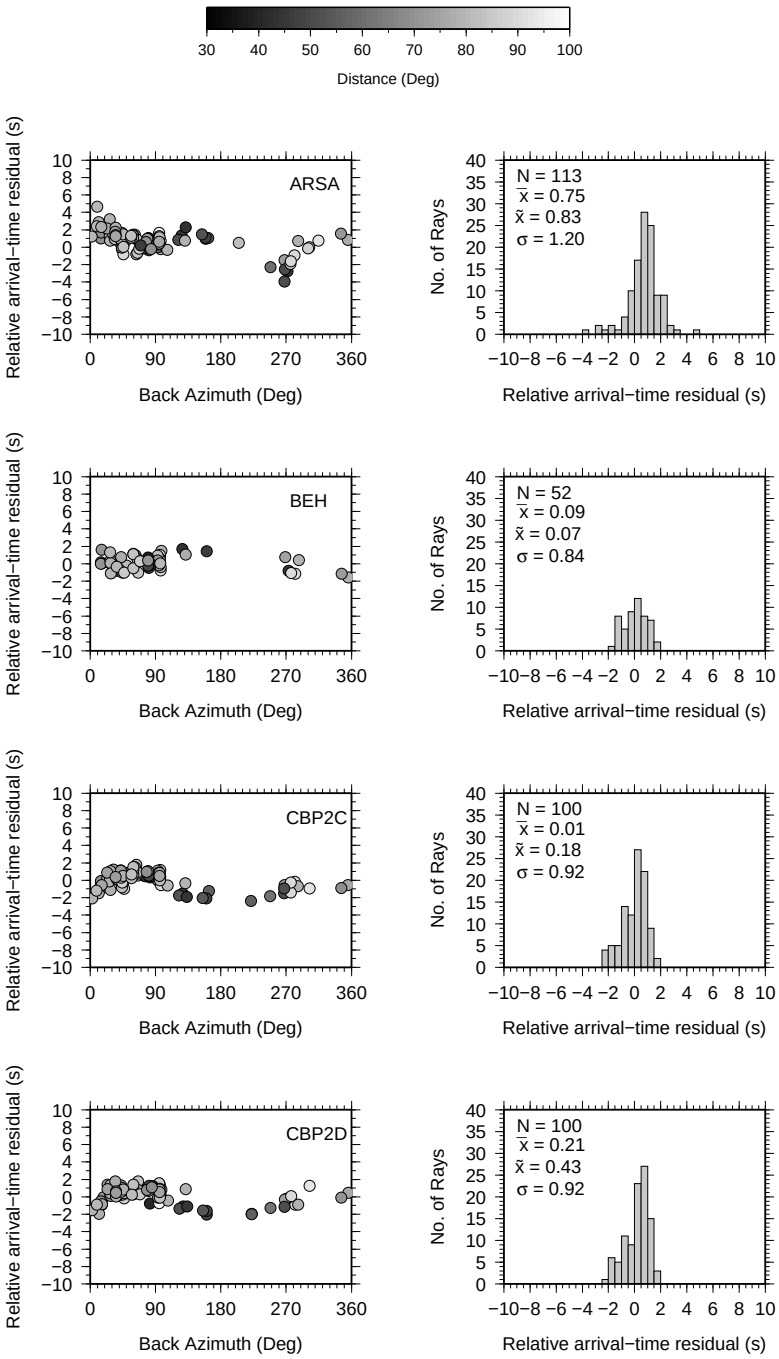

Figure C.26: S-wave relative arrival-time residuals for stations ARSA, BEH, CBP2C and CBP2D

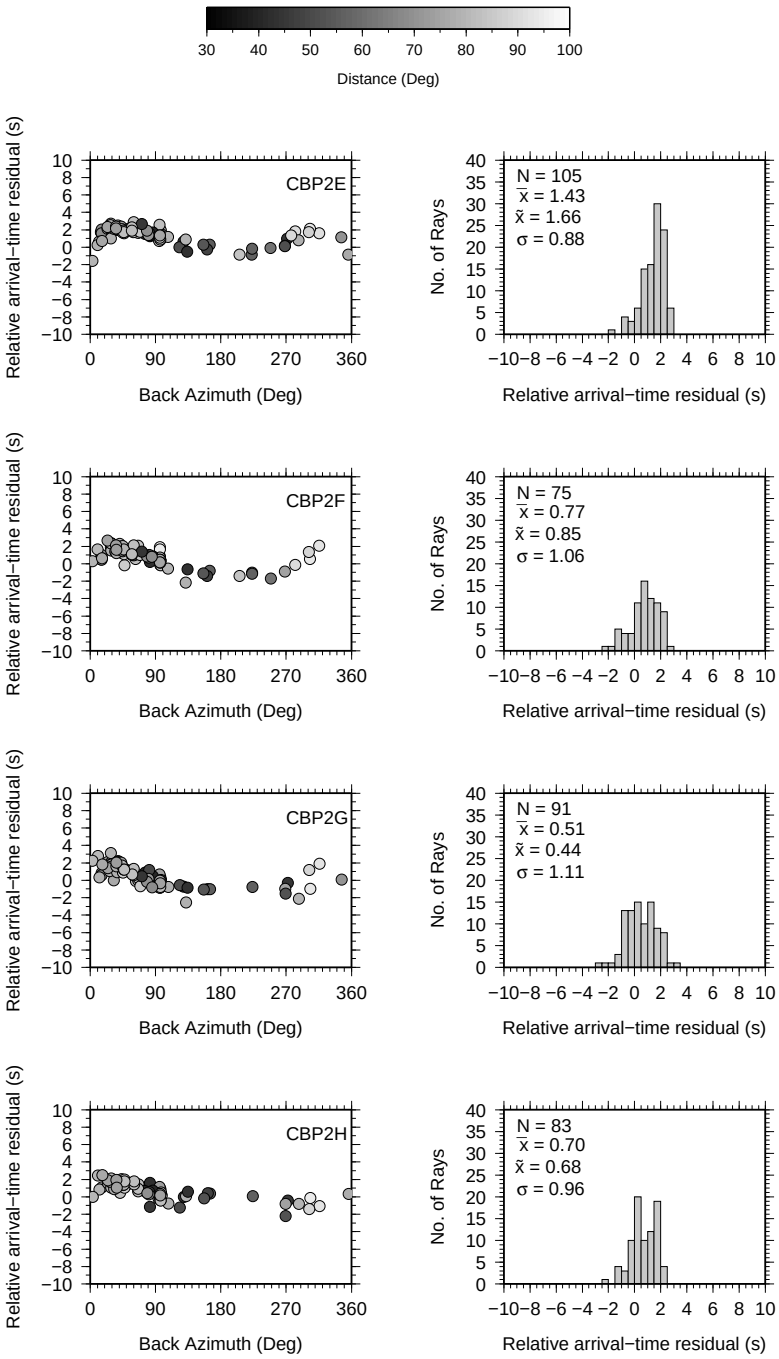

Figure C.27: S-wave relative arrival-time residuals for stations CBP2E, CBP2F, CBP2G and CBP2H

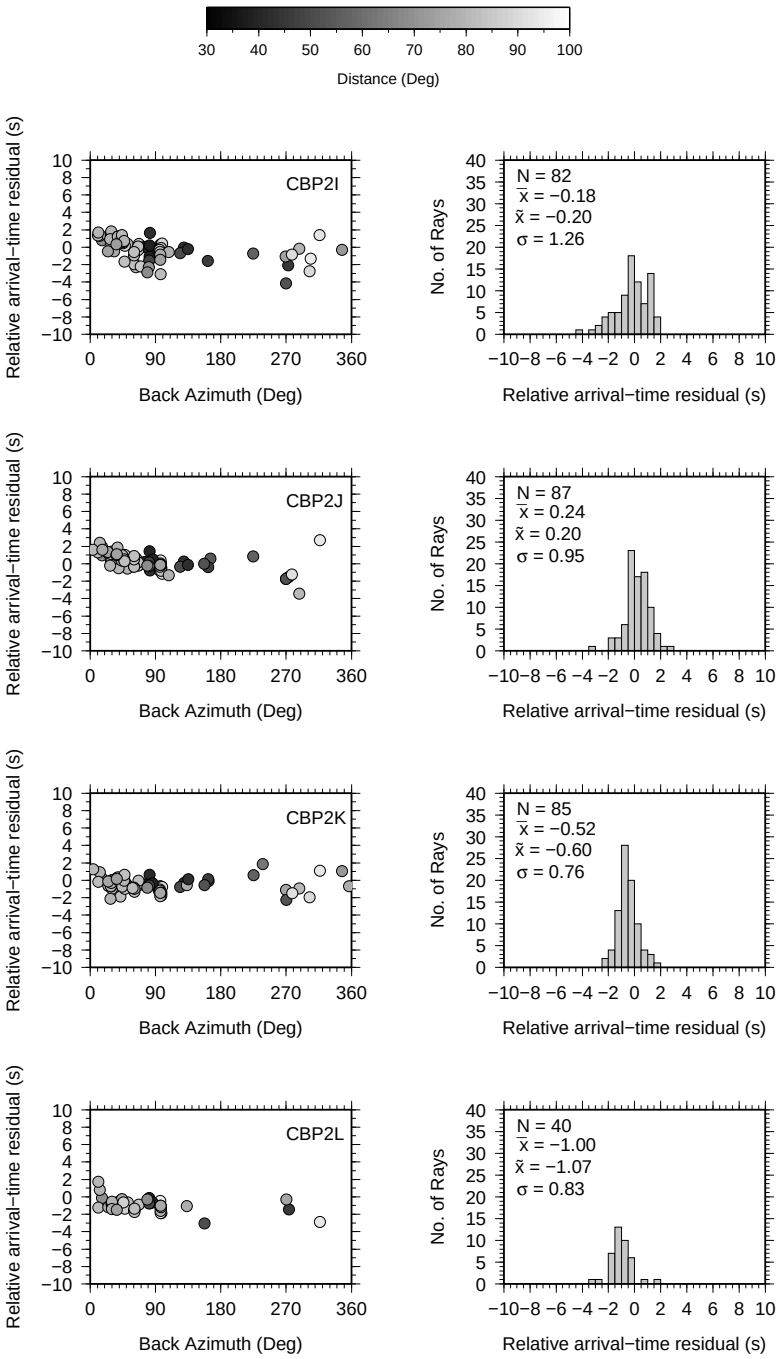

Figure C.28: S-wave relative arrival-time residuals for stations CBP2I, CBP2J, CBP2K and CBP2L

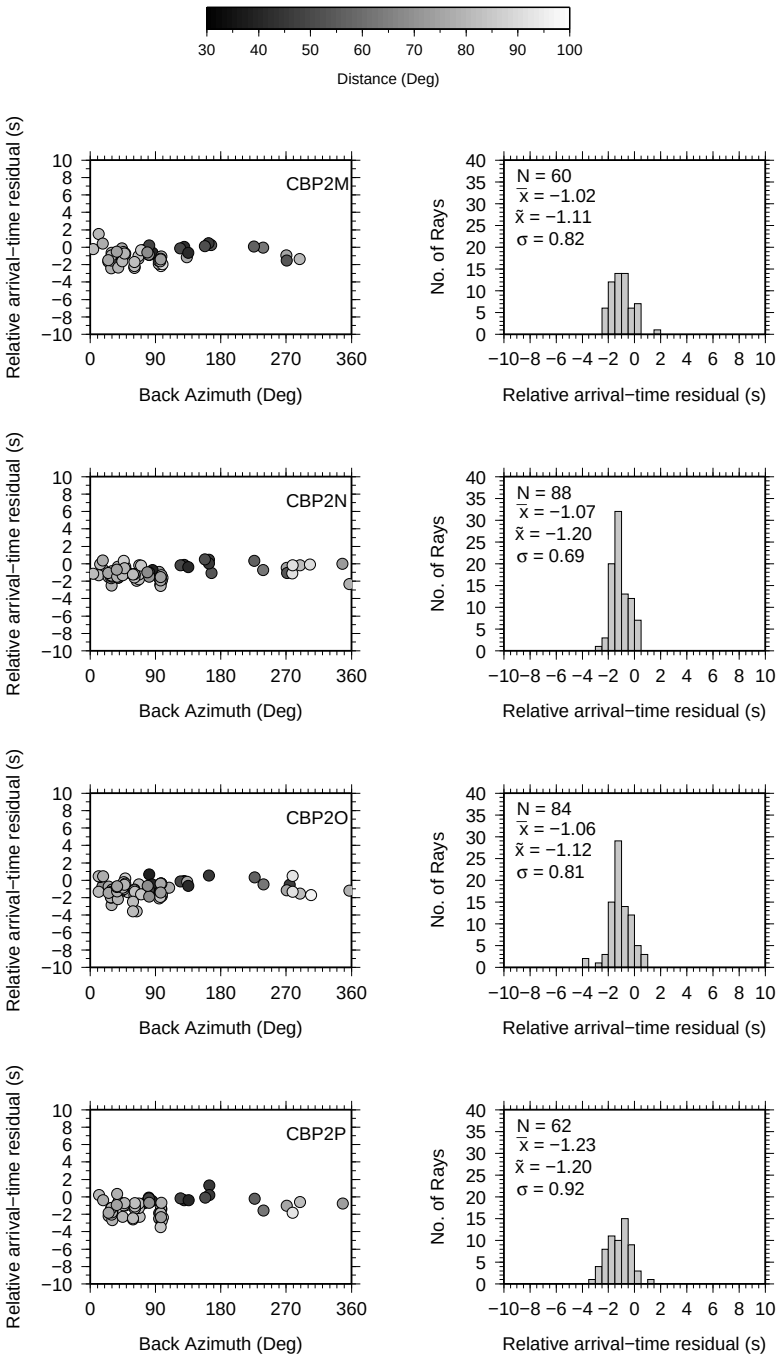

Figure C.29: S-wave relative arrival-time residuals for stations CBP2M, CBP2N, CBP2O and CBP2P

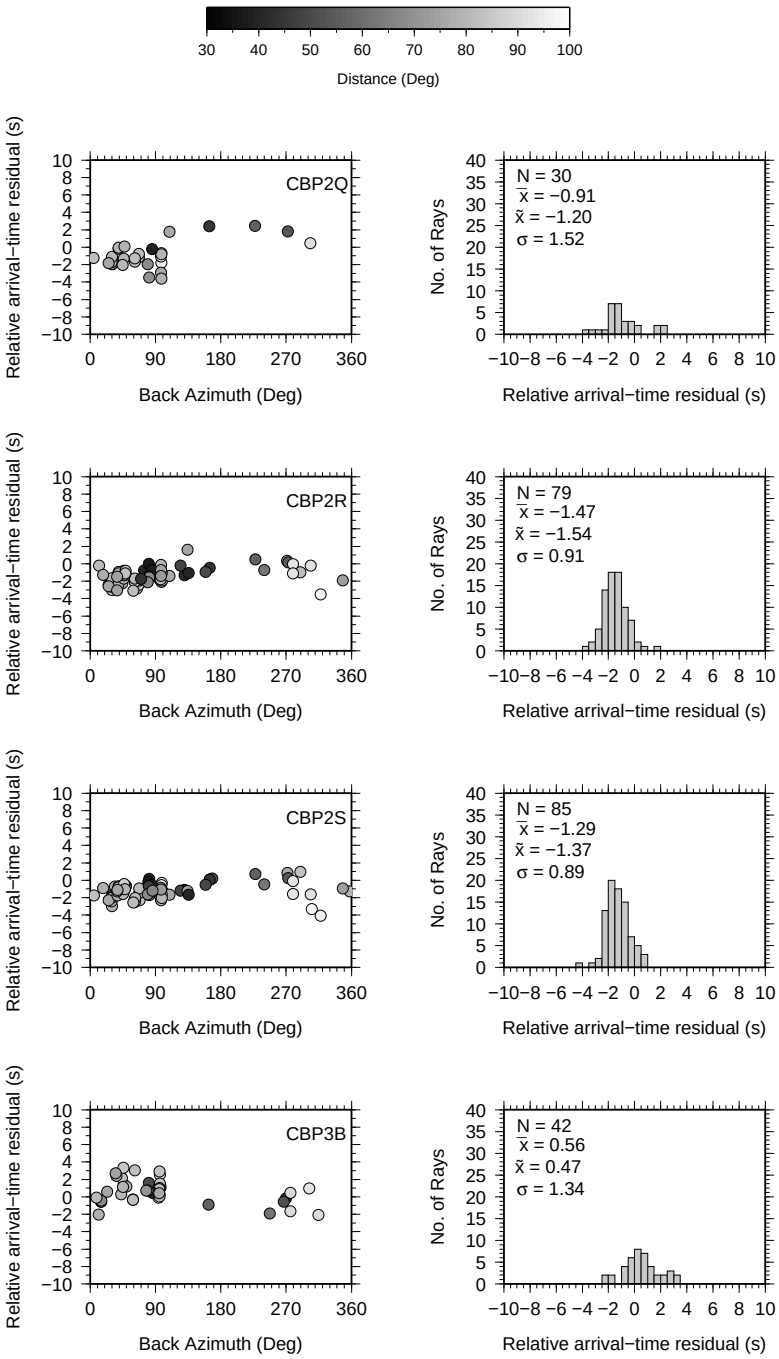

Figure C.30: S-wave relative arrival-time residuals for stations CBP2Q, CBP2R, CBP2S and CBP3B

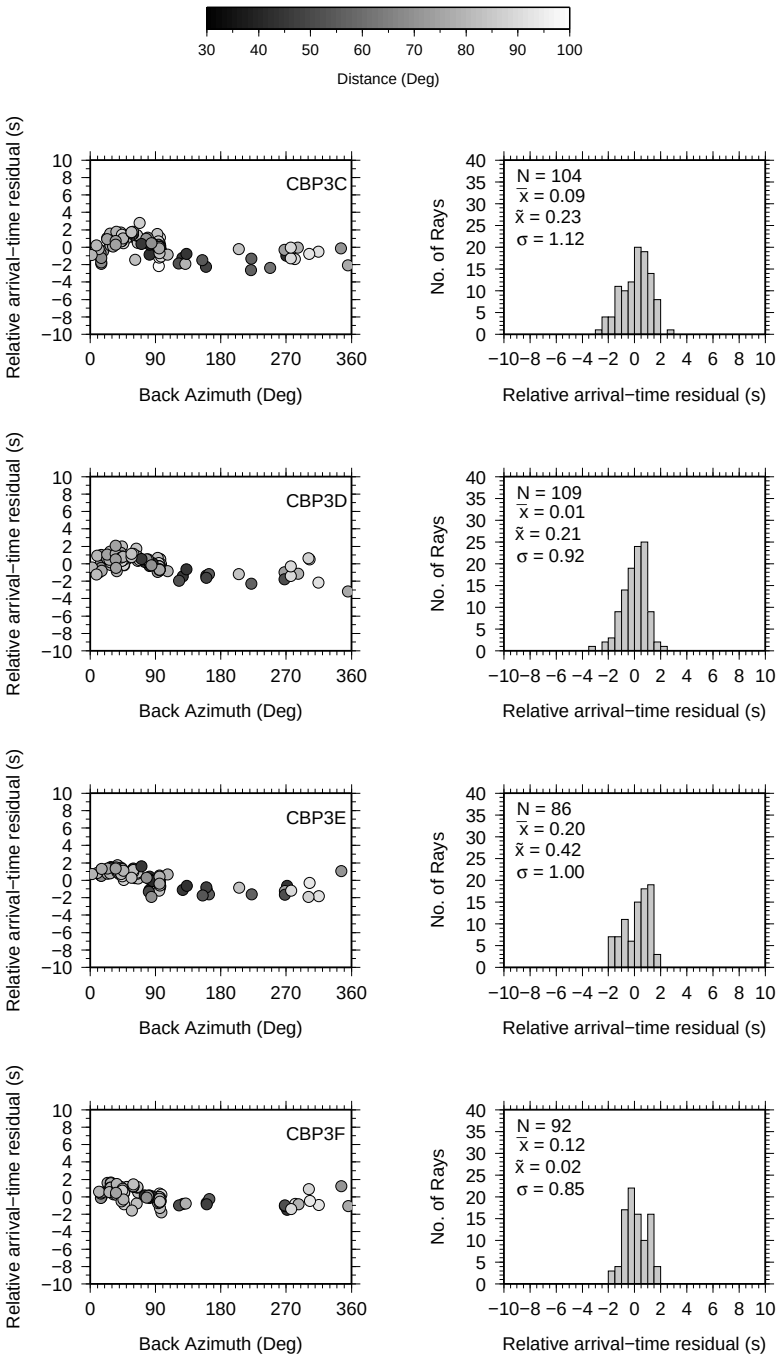

Figure C.31: S-wave relative arrival-time residuals for stations CBP3C, CBP3D, CBP3E and CBP3F

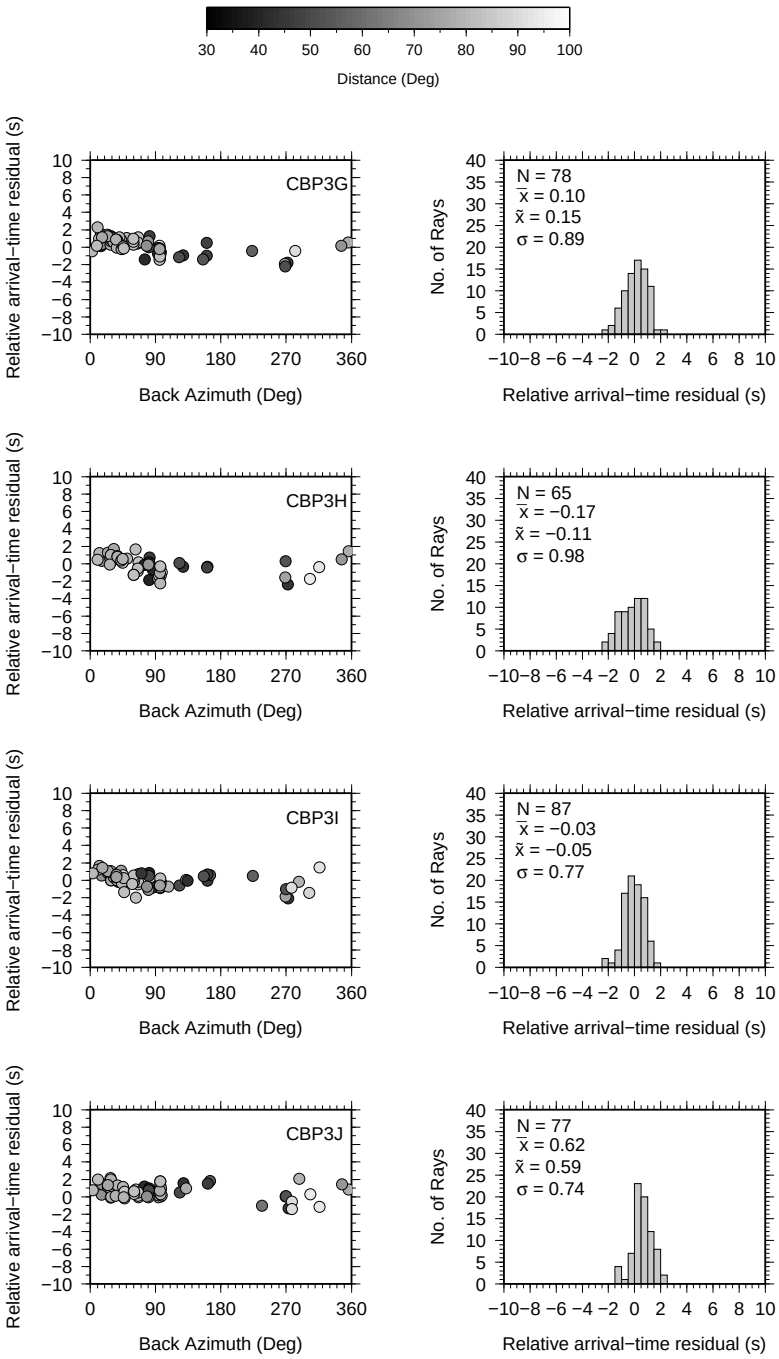

Figure C.32: S-wave relative arrival-time residuals for stations CBP3G, CBP3H, CBP3I and CBP3J

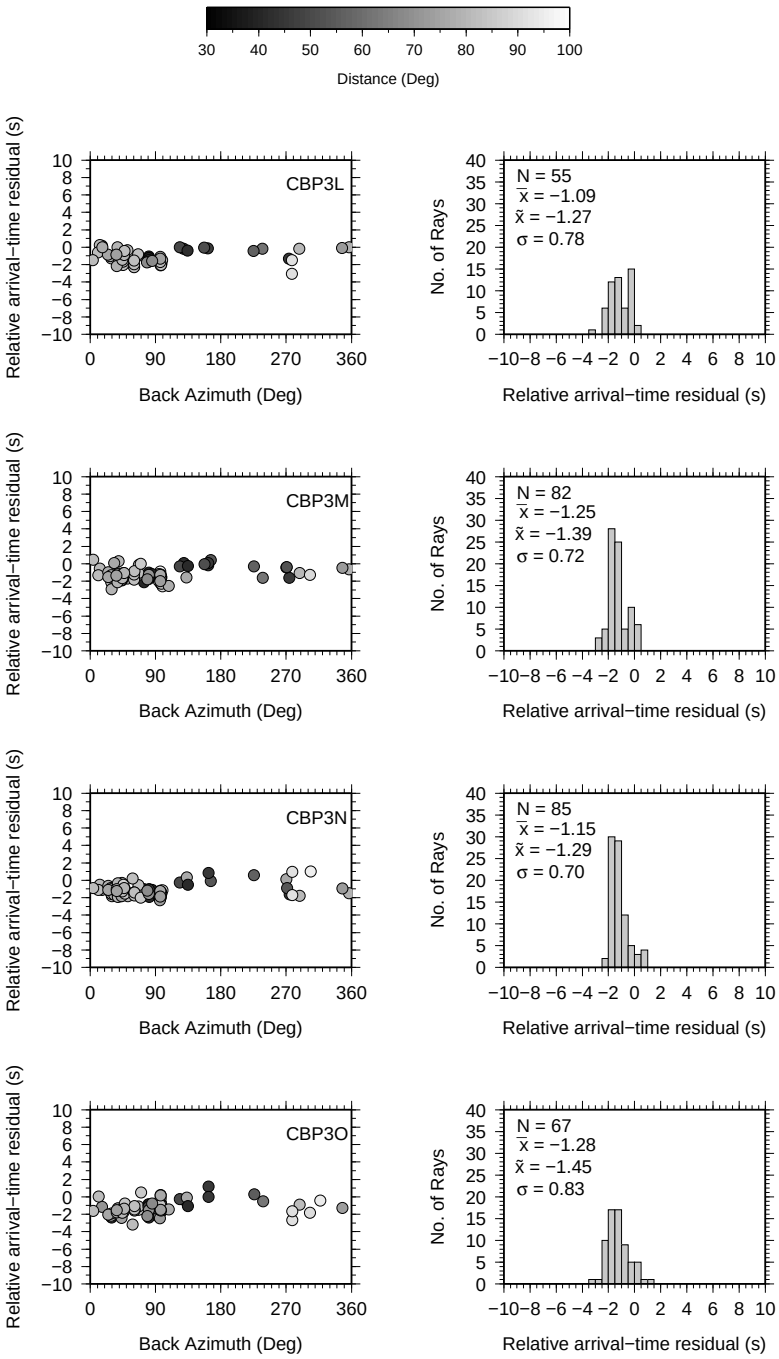

Figure C.33: S-wave relative arrival-time residuals for stations CBP3L, CBP3M, CBP3N and CBP3O

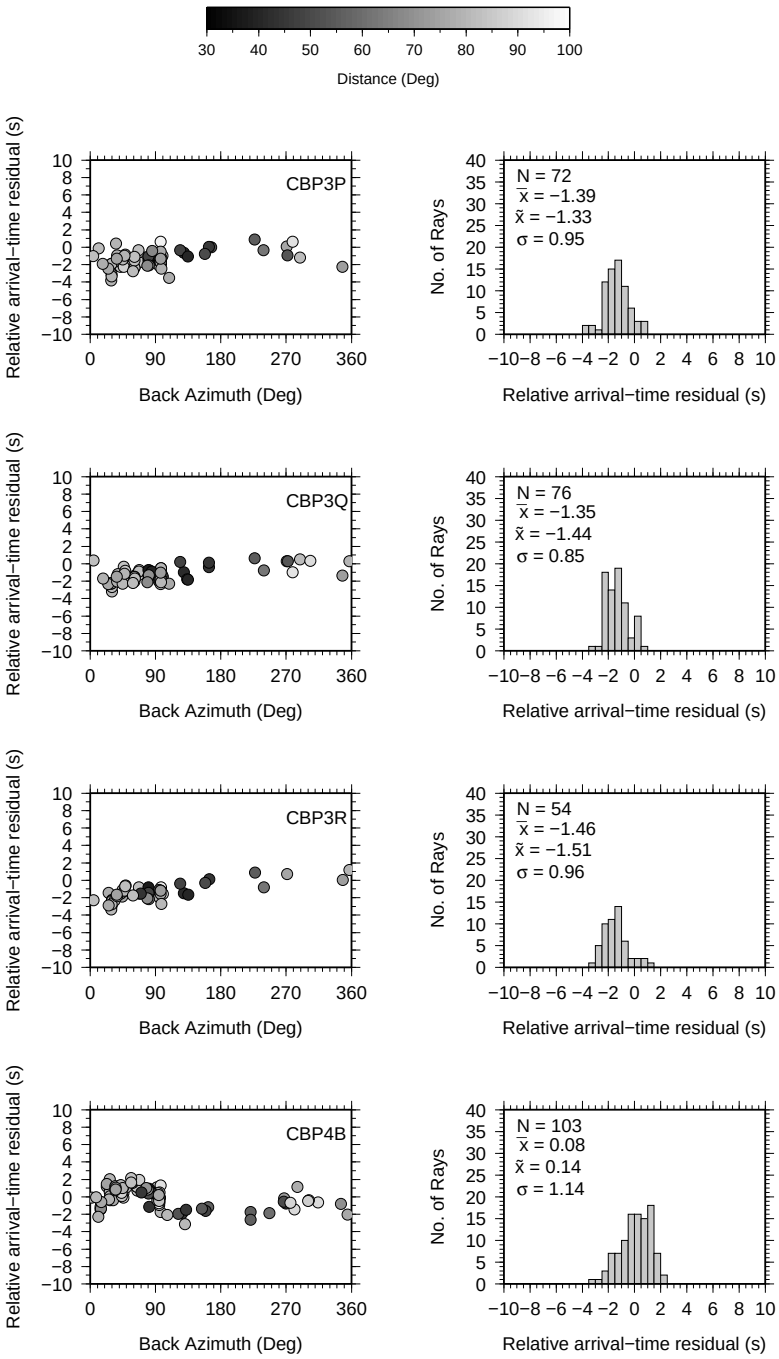

Figure C.34: S-wave relative arrival-time residuals for stations CBP3P, CBP3Q, CBP3R and CBP4B

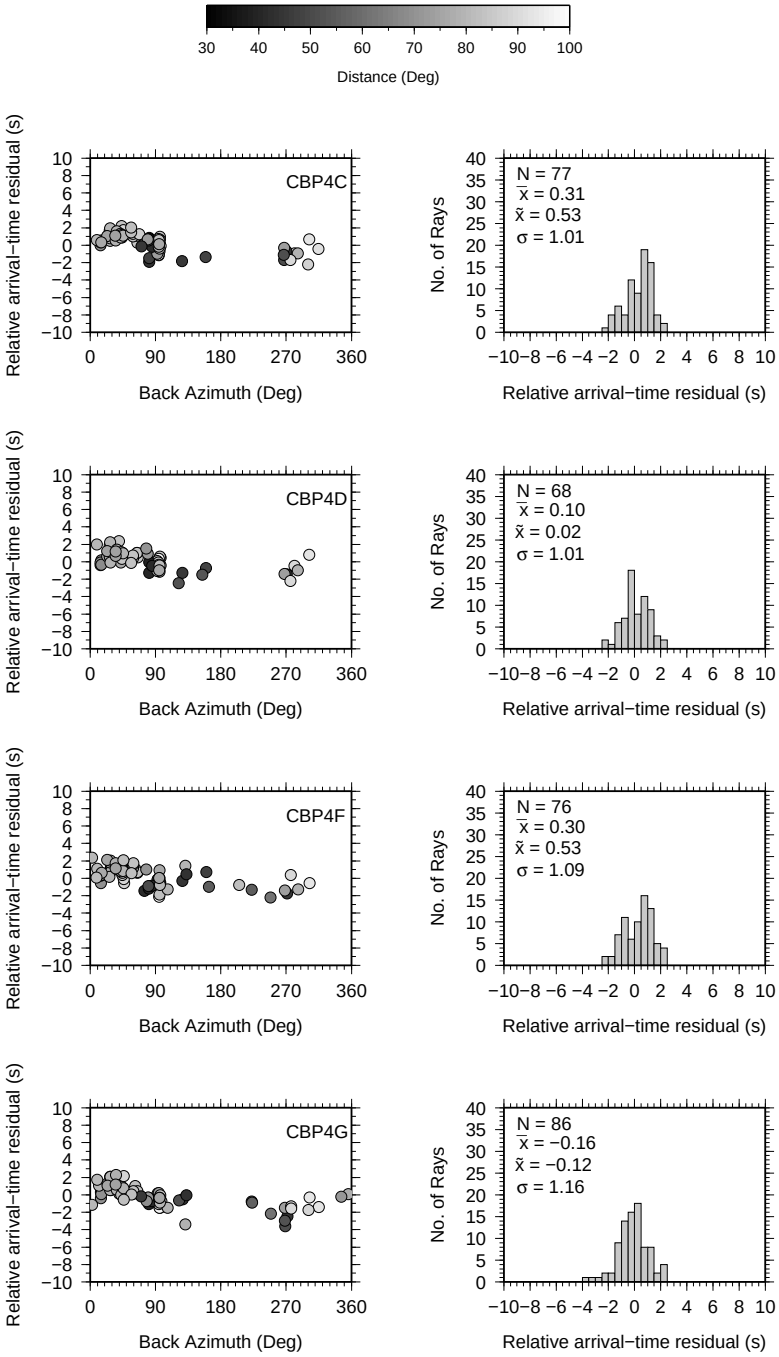

Figure C.35: S-wave relative arrival-time residuals for stations CBP4C, CBP4D, CBP4F and CBP4G

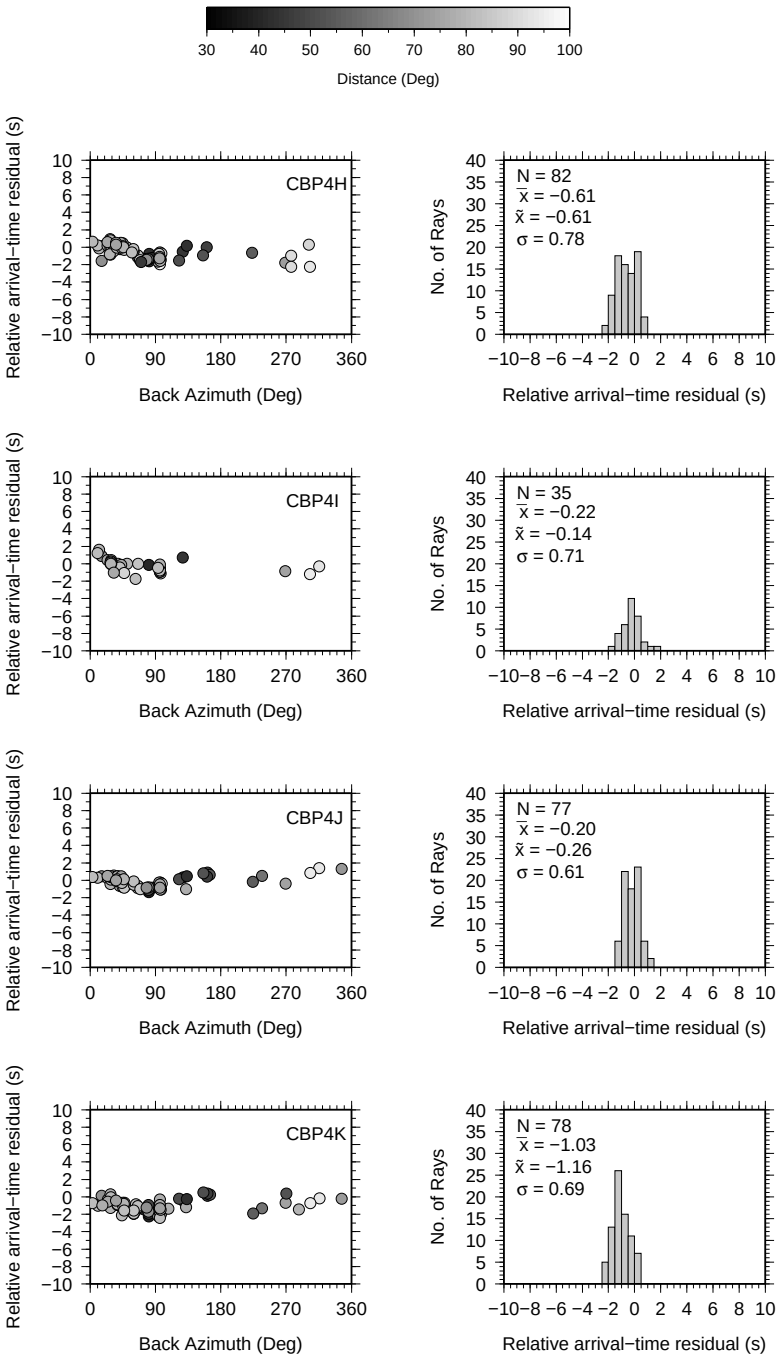

Figure C.36: S-wave relative arrival-time residuals for stations CBP4H, CBP4I, CBP4J and CBP4K

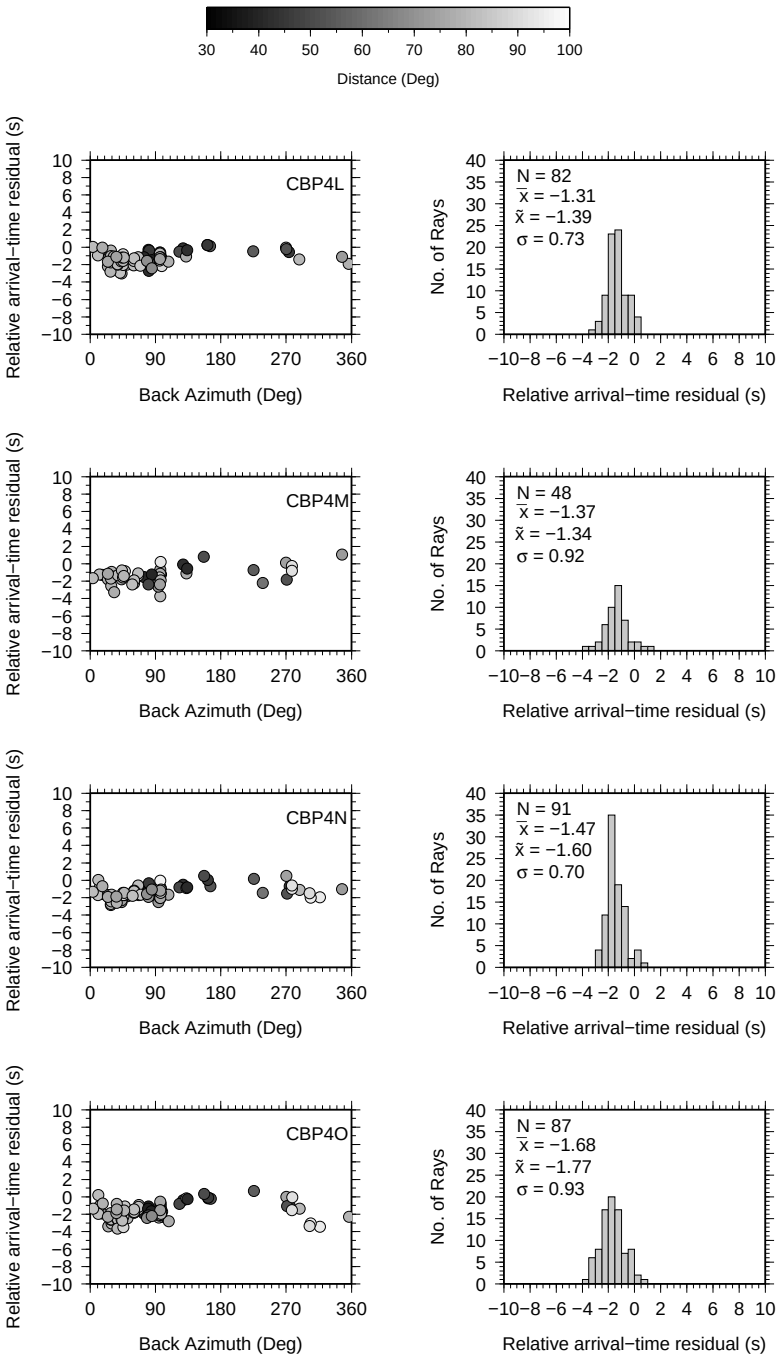

Figure C.37: S-wave relative arrival-time residuals for stations CBP4L, CBP4M, CBP4N and CBP4O

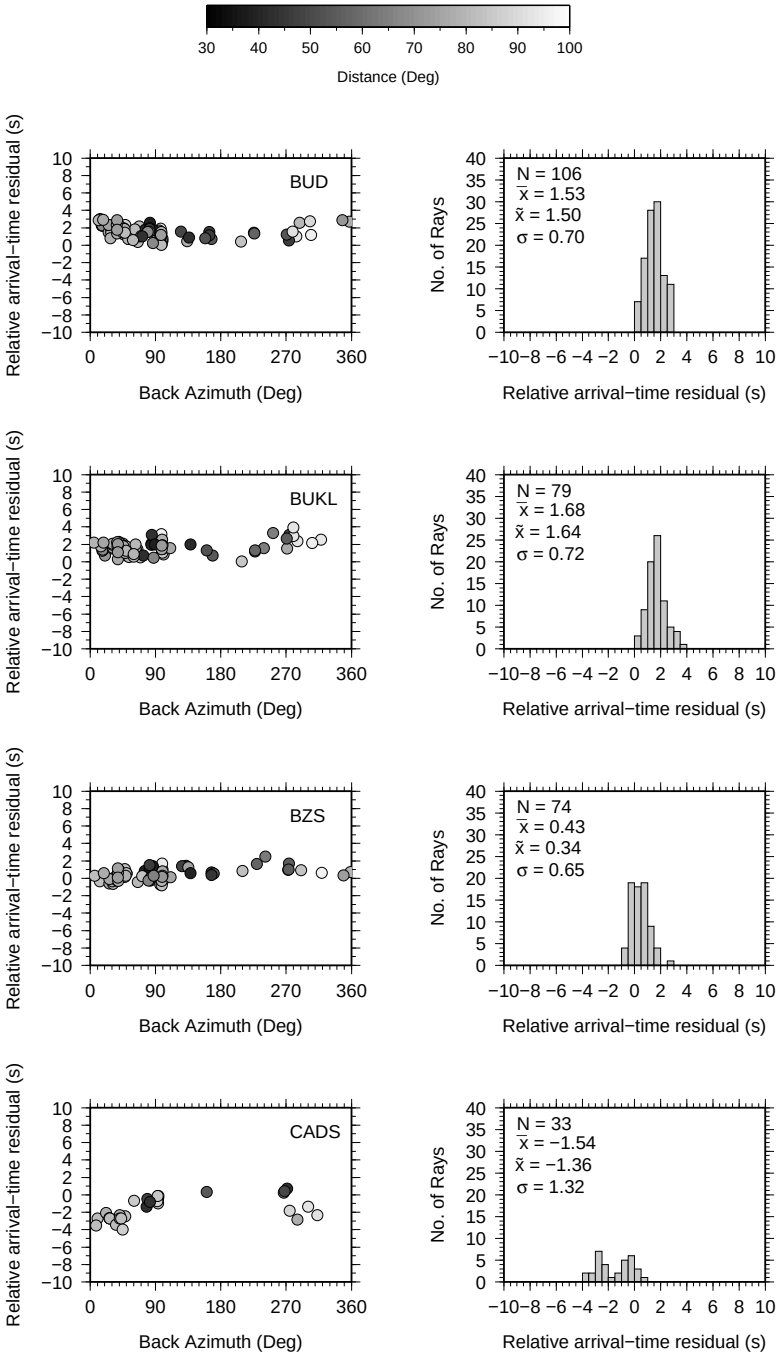

Figure C.38: S-wave relative arrival-time residuals for stations BUD, BUKL, BZS and CADS

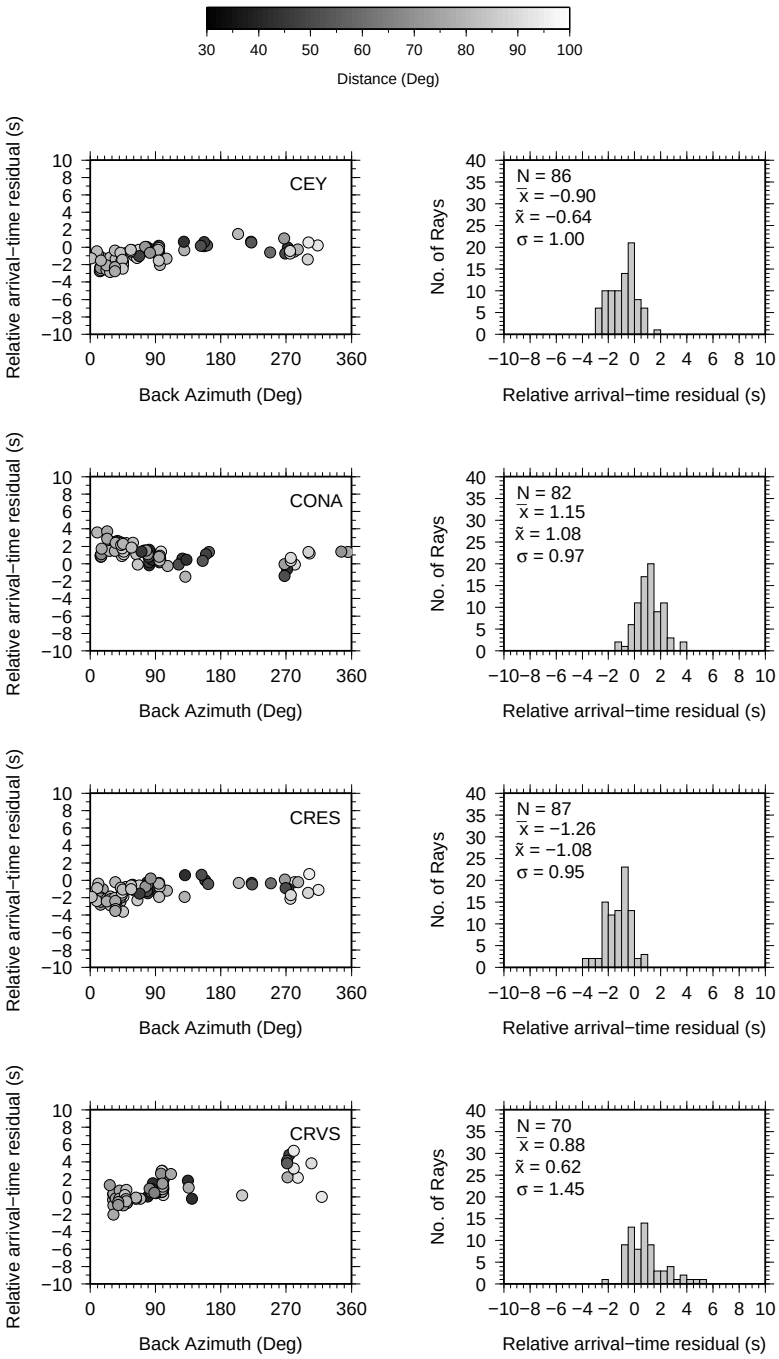

Figure C.39: S-wave relative arrival-time residuals for stations CEY, CONA, CRES and CRVS

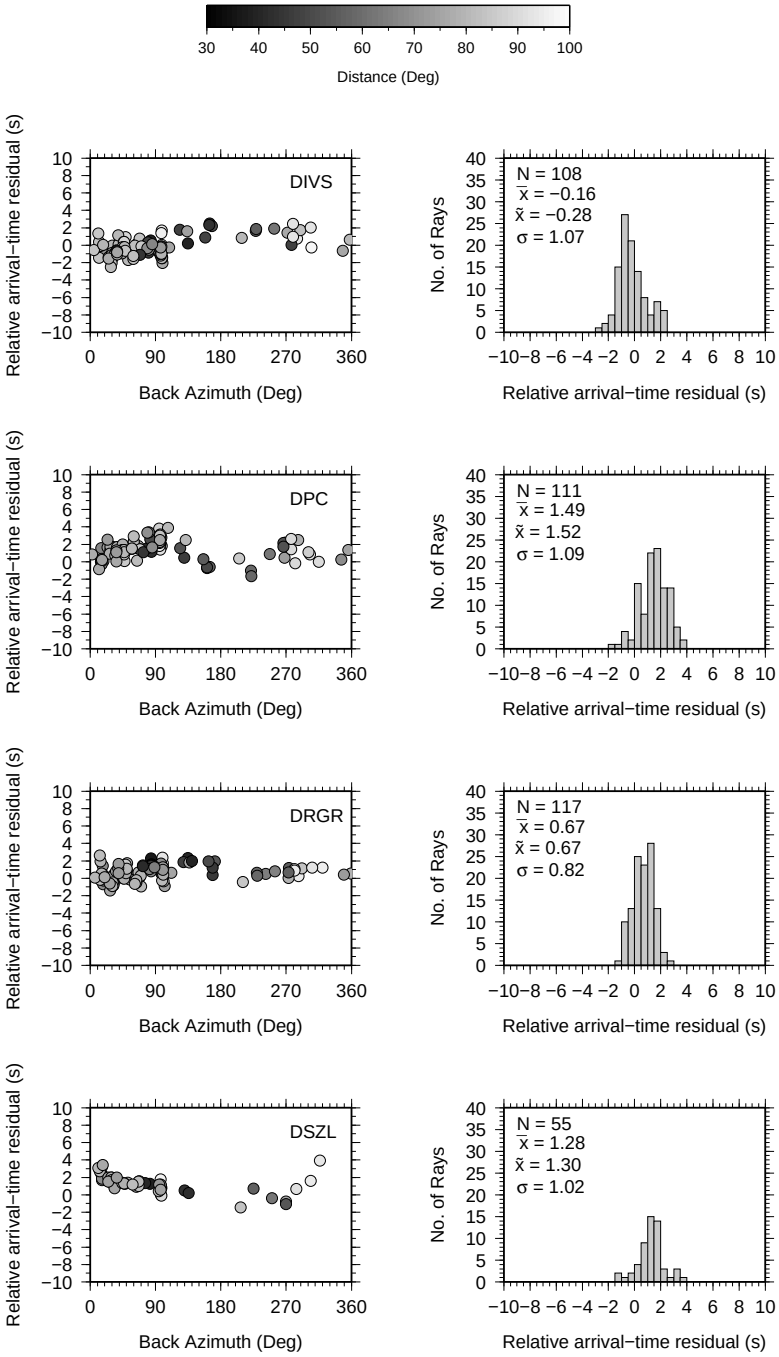

Figure C.40: S-wave relative arrival-time residuals for stations DIVS, DPC, DRGR and DSZL

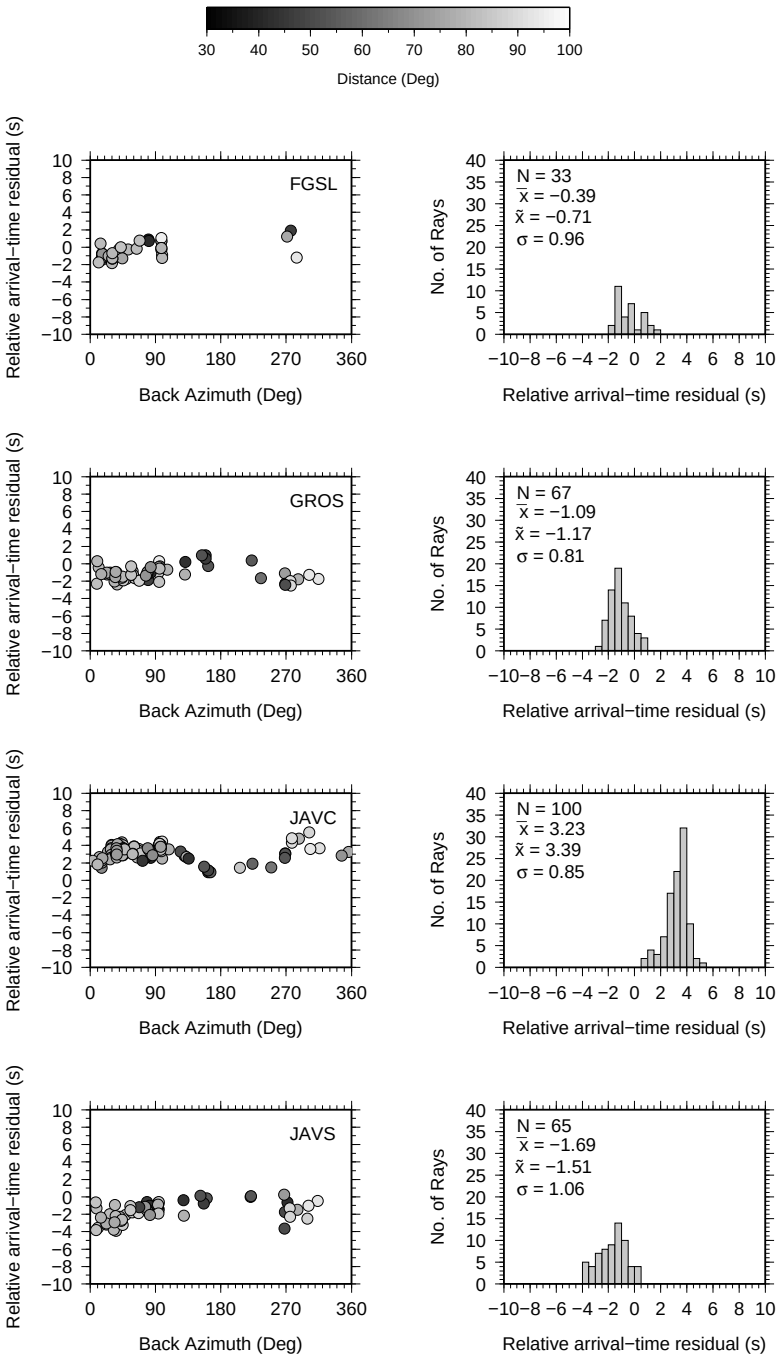

Figure C.41: S-wave relative arrival-time residuals for stations FGSL, GROS, JAVC and JAVS

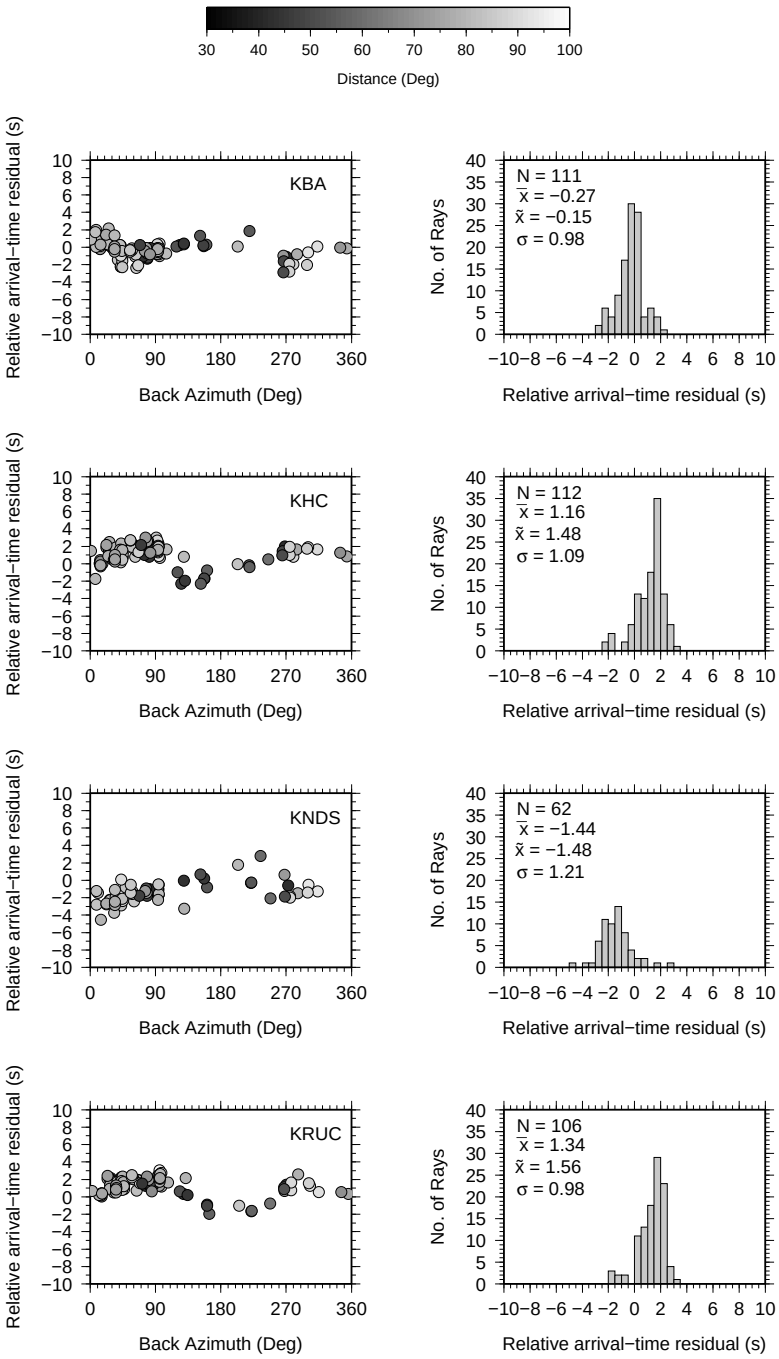

Figure C.42: S-wave relative arrival-time residuals for stations KBA, KHC, KNDS and KRUC

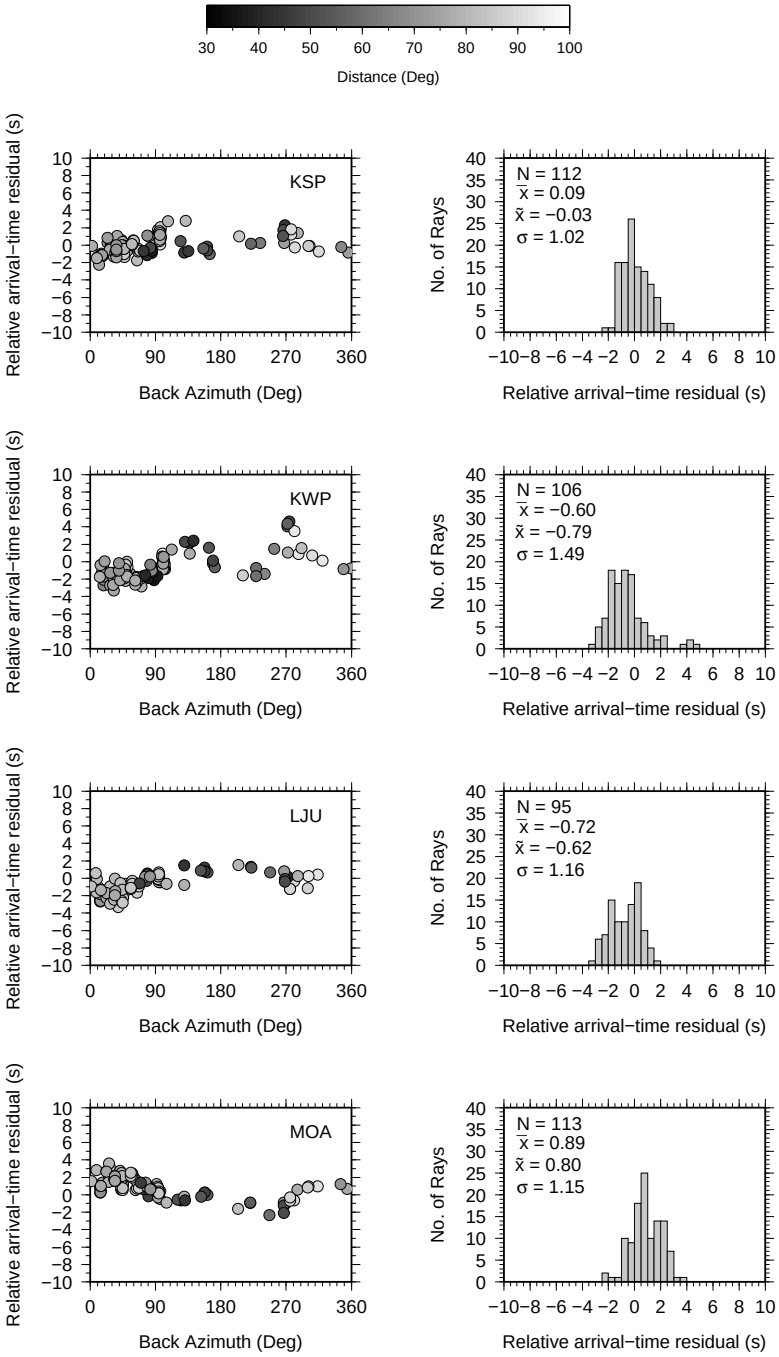

Figure C.43: S-wave relative arrival-time residuals for stations KSP, KWP, LJU and MOA

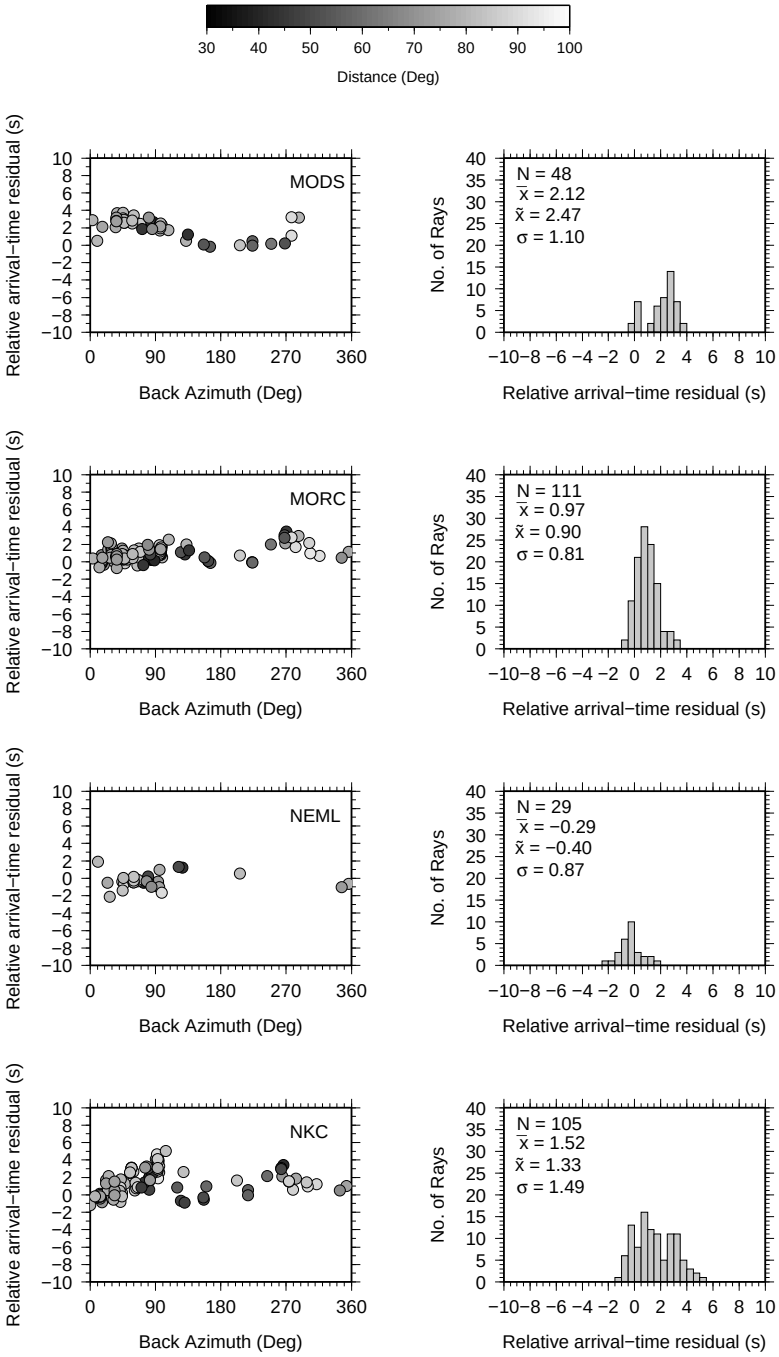

Figure C.44: S-wave relative arrival-time residuals for stations MODS, MORC, NEML and NKC

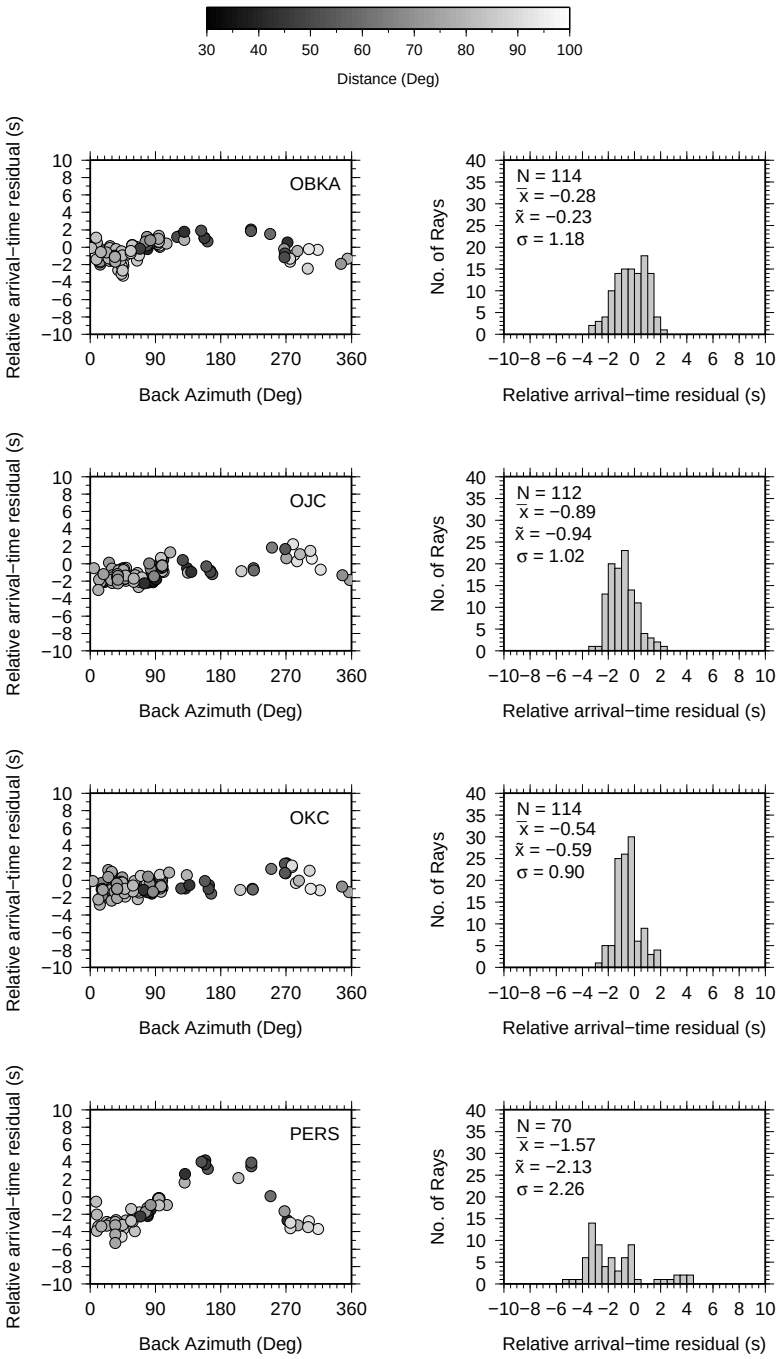

Figure C.45: S-wave relative arrival-time residuals for stations OBKA, OJC, OKC and PERS

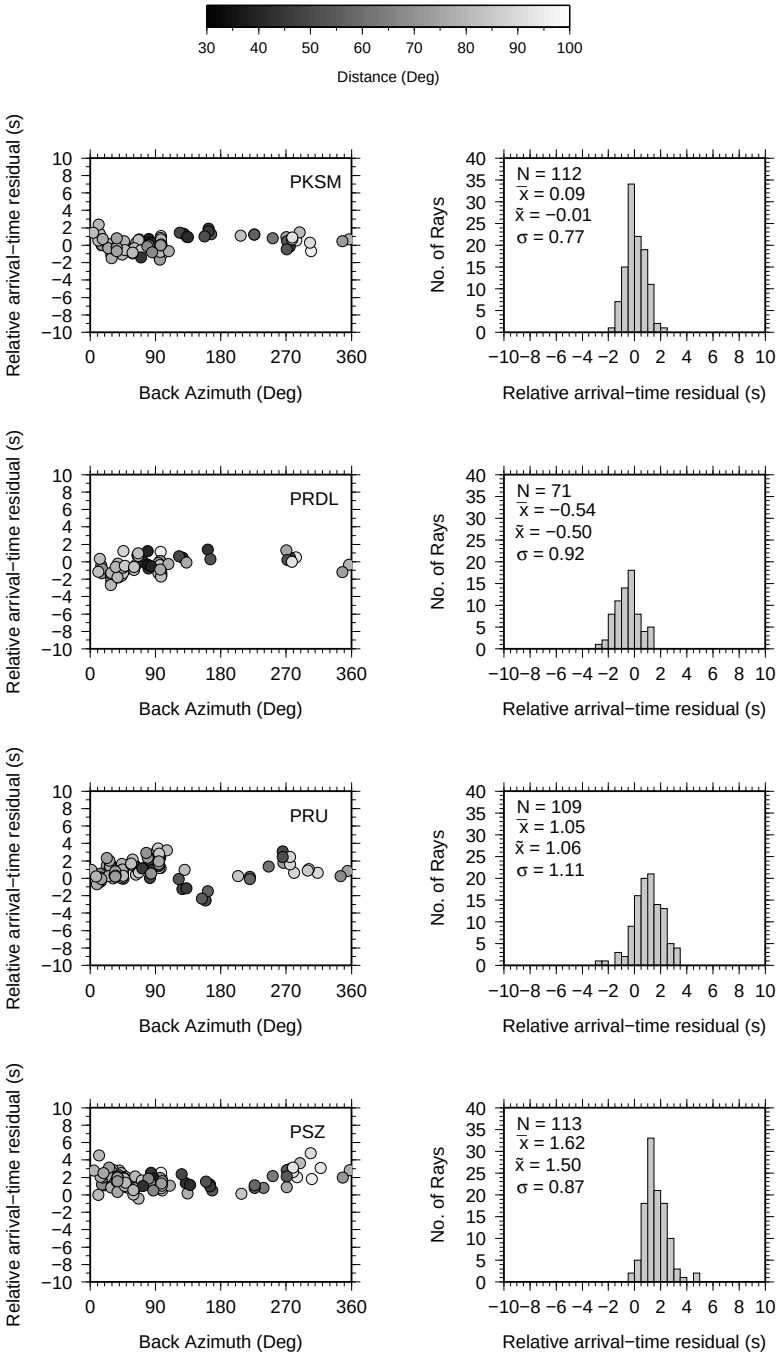

Figure C.46: S-wave relative arrival-time residuals for stations PKSM, PRDL, PRU and PSZ

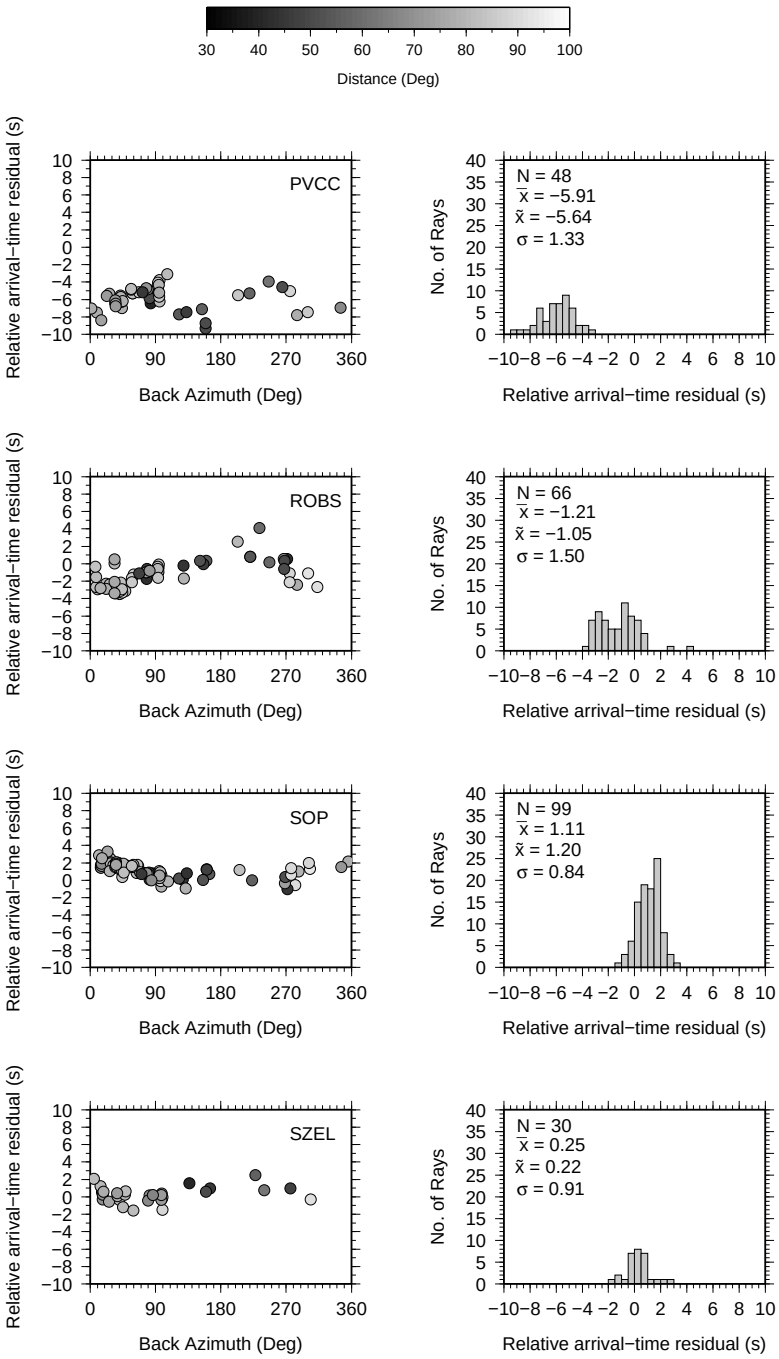

Figure C.47: S-wave relative arrival-time residuals for stations PVCC, ROBS, SOP and SZEL

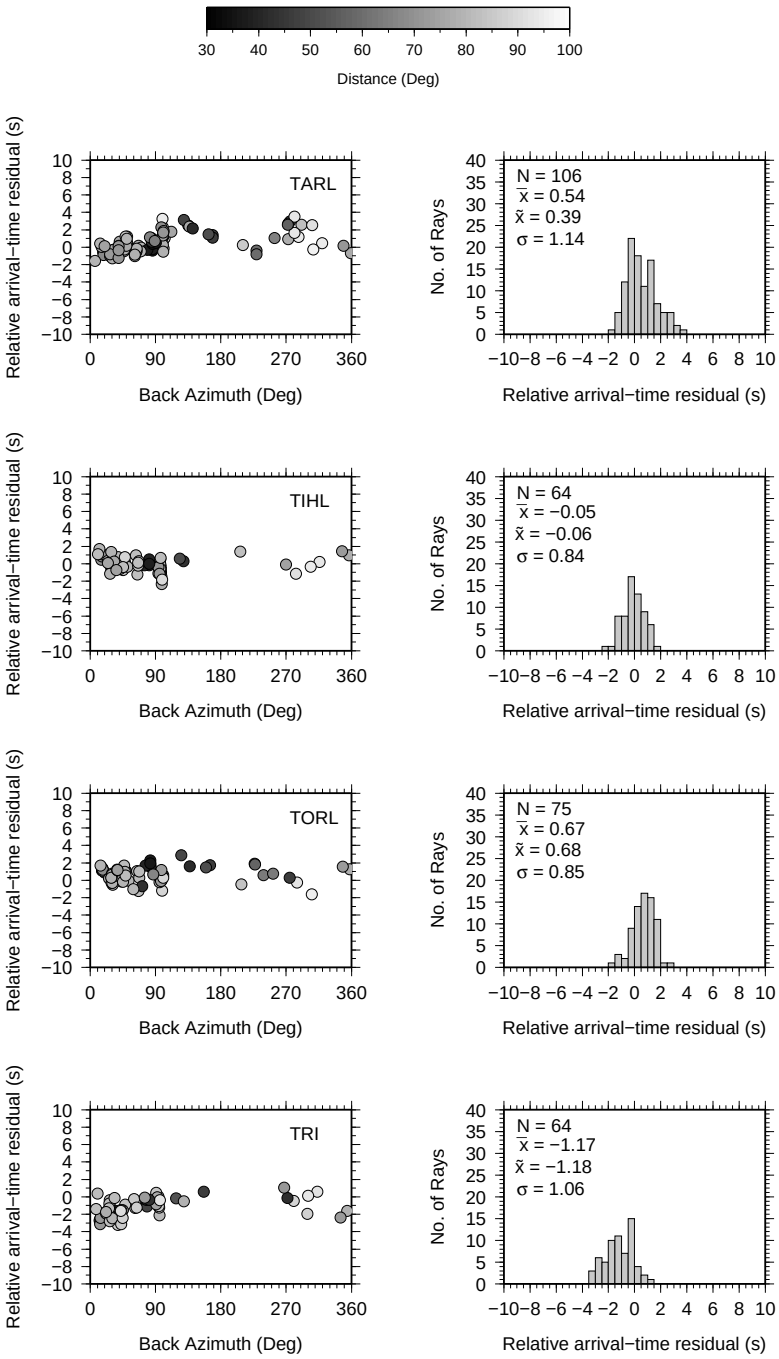

Figure C.48: S-wave relative arrival-time residuals for stations TARL, TIHL, TORL and TRI

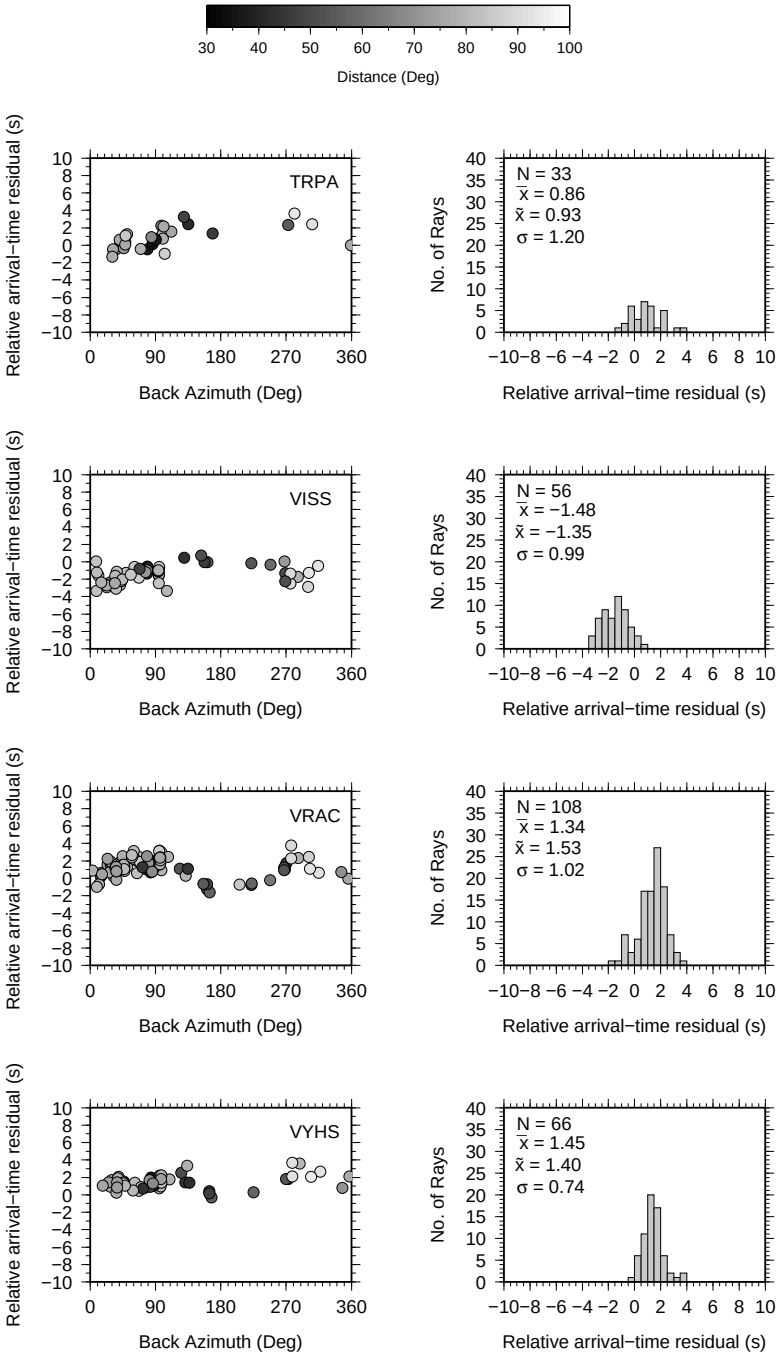

Figure C.49: S-wave relative arrival-time residuals for stations TRPA, VISS, VRAC and VYHS

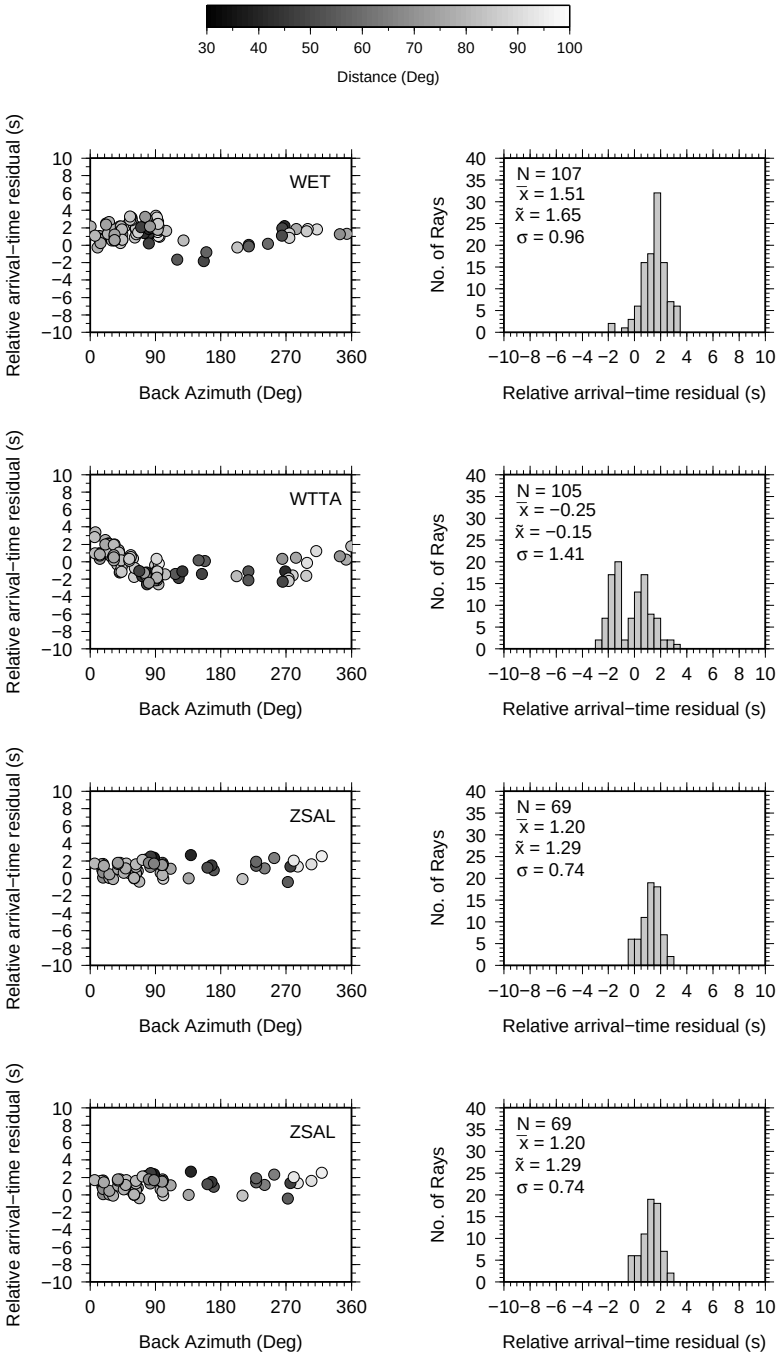

Figure C.50: S-wave relative arrival-time residuals for stations WET, WTTA, ZSAL and ZSAL

Appendix D

Supplementary CD contents

The contents of the supplementary CD are as follows:

- Crustalcorrection.dat - time correction applied to each P-wave relative arrival-time residual in chapter 6. The file contains the ray number, the event time and the associated station name with the correction time.
- PCBPS.mod - binary model before interpolation of the preferred P-wave solution model.
- SCBPS.mod - binary model before interpolation of the preferred S-wave solution model.
- Pwavemovie.mp4 - video through the P-wave tomographic model (PCBPS)
- Swavemovie.mp4 - video through the S-wave tomographic model (SCBPS)
- GPSplots/ - directory containing GPS continuity plots for each site of the HST array labelled by station. See appendix A for an example and description of the plot.
- Dando2010.pdf - electronic copy of this manuscript.

References

Ádám, A., 1996. Regional magnetotelluric (MT) anisotropy in the Pannonian Basin (Hungary), *Acta Geodaetica et Geophysica Hungarica*, **31**, 191–215.

Allen, R., Nolet, G., Morgan, W., Vogfjörd, K., Bergsson, B., Erlendsson, P., Foulger, G., Jakobsdóttir, S., Julian, B., Pritchard, M., Ragnarsson, S., & Stefánsson, R., 2002. Imaging the mantle beneath iceland using integrated seismological techniques, *Journal of Geophysical Research*, **107**(B12,2325), doi:10.1029/2001JB000595.

Arrowsmith, S., 2003. *A tomographic investigation of upper mantle processes beneath the British Isles*, Ph.D. thesis, School of Earth and Environment, Univeristy of Leeds.

Arrowsmith, S., Kendall, M., White, N., VanDecar, J., & Booth, D., 2005. Seimic imaging of a hot upwelling beneath the British Isles, *Geology*, **33**, 345–348.

Babuška, V. & Plomerová, J., 1988. Subcrustal continental lithosphere: a model of its thickness and anisotropic structure, *Physics of the Earth and Planetary Interiors*, **51**, 130–132.

Babuška, V., Plomerová, J., & Šílený, J., 1987. Structural model of the subcrustal lithosphere in central Europe, in *The Composition, Structure and Dynamics of the Lithosphere-Asthenosphere System*, vol. 16 of **Geodynamics Series**, pp. 239–251, eds Froidevaux, C. & Fuchs, K., American Geophysical Union.

Bada, G., Horváth, F., Cloetingh, S., & Coblentz, D. D., 2001. Role of topography-induced gravitational stresses in basin inversion: The case study of the Pannonian basin, *Tectonics*, **20**(3), 343–363.

Bada, G., Horváth, F., Dövényi, P., Szafián, P., Windhoffer, G., & Cloetingh, S., 2007. Present-day stress field and tectonic inversion in the pannonian basin, *Global and Planetary Change*, **58**, 165–180.

Bassin, C., Laske, G., & Masters, G., 2000. The current limits of resolution for surface wave tomography in north america, *EOS Trans American Geophysical Union*, **81**, F897.

Bastow, I., 2005. *Upper–Mantle Seismic Structure in a Region of Incipient Continental Break–up: Northern Ethiopian Rift*, Ph.D. thesis, School of Earth and Environment, Univeristy of Leeds.

Bastow, I., Nyblade, A., Stuart, G., Rooney, T., & Benoit, M., 2008. Upper mantle seismic structure beneath the Ethiopian hot spot: Rifting at the edge of the African low-velocity anomaly, *Geochemistry Geophysics Geosystems*, **9**(12), doi:10.1029/2008GC002107.

Behm, M., 2006. *Accuracy and resolution of a 3D seismic model of the Eastern Alps*, Ph.D. thesis, Vienna University of Technology.

Behm, M., Brückl, E., Chwatel, W., & Thybo, H., 2007a. Application of stacking and inversion techniques to three-dimensional wide-angle reflection and refraction seismic data of the Eastern Alps, *Geophysical Journal International*, **170**, 275–298.

Behm, M., Brückl, E., Mitterbauer, U., & CELEBRATION 2000 and ALP 2002 Working Groups, 2007b. A new seismic model of the Eastern Alps and its relevance for geodesy and geodynamics, *Vermessung & Geoinformation*, **2**, 121–133.

Bérczi, I., Hámor, G., Jámbor, A., & Szentgyörgyi, K., 1988. Neogene sedimentation in Hungary, in *The Pannonian Basin. A study in basin evolution*, vol. 45 of **AAPG Memoir**, pp. 57–67, eds Royden, L. & Horváth, F., The American Association of Petroleum Geologists and the Hungarian Geological Society.

Bielik, M., Alasonati-Tašárová, Z., Zeyen, H., Dérerová, J., Afonso, J., & Csicsay, K., 2010. Improved geophysical image of the Carpathian-Pannonian Basin region, *Acta Geodaetica et Geophysica Hungarica*, **45**(3), 284–298.

Bijwaard, H. & Spakman, W., 2000. Non-linear global P-wave tomography by iterated linearized inversion, *Geophysical Journal International*, **141**, 71–82.

Brückl, E., Bleibinhaus, F., Gosar, A., Grad, M., Guterech, A., Hrubcová, P., Keller, G. R., Majdański, M., Šumanovac, F., Tiira, T., Yliniemi, J., Hegedus, E., & Thybo, H., 2007. Crustal structure due to collisional and escape tectonics in the Eastern Alps region based on profiles alp01 and alp02 from the ALP 2002 seismic experiment, *Journal of Geophysical Research*, **112**(B06308), doi:10.1029/2006JB004687.

Cammarano, F., Goes, S., Vacher, P., & Giardini, D., 2003. Inferring upper-mantle temperatures from seismic velocities, *Physics of the Earth and Planetary Interiors*, **138**, 197–222.

Cao, A. & Levander, A., 2010. High-resolution transition zone structures of the Gorda Slab beneath the western United States: Implications for deep water subduction, *Journal of Geophysical Research*, **115**, doi:10.1029/2009JB006876.

Chalot-Prat, F. & Boullier, A., 1997. Metasomatism in the subcontinental mantle beneath the Eastern Carpathians (Romania): new evidence from trace element geochemistry, *Contributions to Mineral Petrology*, **129**(4), 284–307.

Chalot-Prat, F. & Girbacea, R., 2000. Partial delamination of continental mantle lithosphere, uplift-related crust-mantle decoupling, volcanism and basin formation: a new model for the Pliocene-Quaternary evolution of the southern East-Carpathians, Romania, *Tectonophysics*, **327**, 83–107.

Chang, S.-J., van der Lee, S., Flanagan, M., Bedle, H., Marone, F., Matzel, E., Pasyanos, M., Rodgers, A., Romanowicz, B., & Schmid, C., 2010. Joint inversion for three-dimensional S velocity mantle structure along the Tethyan margin, *Journal of Geophysical Research*, **115**(B08309), doi:10.1029/2009JB007204.

Channell, J. & Kozur, H., 1997. How many oceans? Meliata, vardar, and Pindos oceans in Mesozoic Alpine paleogeography, *Geology*, **25**(2), 183–186.

Coppens, F., 1985. First arrival picking on common-offset trace collections for automatic estimation of static correction, *Geophysical Prospecting*, **33**, 1212–1231.

Corver, M., Doust, H., van Wees, J., Bada, G., & Cloetingh, S., 2009. Classification of rifted sedimentary basins of the Pannonian Basin System according to structural genesis, evolutionary history and hydrocarbon maturation zones, *Marine and Petroleum Geology*, **26**, 1452–1464.

Crotwell, H. & Owens, T., 2005. Automated receiver function processing, *Seismological Research Letters*, **76**(6), 702–709.

Crotwell, H., Owens, T., & Ritsema, J., 1999. The TauP toolkit: flexible seismic traveltime and raypath utilities, *Seismological Research Letters*, **70**, 154–160.

Csontos, L. & Nagymarosy, A., 1998. The Mid-Hungarian line: a zone of repeated tectonic inversions, *Tectonophysics*, **297**, 51–71.

Csontos, L., Nagymarosy, A., Horváth, F., & Kovác, M., 1992. Tertiary evolution of the Intra-carpathian area: a model, *Tectonophysics*, **208**, 221–241.

Davies, J. & von Blanckenburg, F., 1995. Slab breakoff: A model of lithosphere detachment and its test in the magmatism and deformation of collisional orogens, *Earth and Planetary Science Letters*, **129**, 85–102.

de Kool, M., Rawlinson, N., & Sambridge, M., 2006. A practical grid-based method for tracking multiple refraction and reflection phases in three-dimensional heterogeneous media, *Geophysical Journal International*, **167**, 253–270.

Dérerová, J., Zeyen, H., Bielik, M., & Salman, K., 2006. Application of integrated geophysical modeling for determination of the continental lithospheric thermal structure in the eastern Carpathians, *Tectonics*, **25**, doi:10.1029/2005TC001883.

Diehl, T., Ritter, J., & the CALIXTO Group, 2005. The crustal structure beneath SE Romania from teleseismic receiver functions, *Geophysical Journal International*, **163**, 238–251.

Dövényi, P., Horváth, F., Liebe, O., Galfi, J., & Erki, I., 1983. Geothermal conditions of Hungary, *Geophysical Transactions*, **29**, 3–114.

Downes, H., Pantó, G., Póka, T., Mattey, D., & Greenwood, P., 1995. Calc-alkaline volcanics of the Inner Carpathian arc, Northern Hungary: new geochemical and oxygen isotopic results, *Acta Vulcanologica*, **7**(2), 29–41.

Engdahl, E., van der Hilst, R., & Buland, R., 1998. Global teleseismic earthquake relocation with improved travel times and procedures for depth determination, *Bulletin of the Seismological Society of America*, **88**(3), 722–743.

Evans, J. & Achauer, U., 1993. Teleseismic tomography using the ACH method: theory and application to continental scale studies, in *Seismic Tomography: Theory and Practice*, pp. 319–360, eds Iyer, H. & Hirahara, K., Chapman & Hall.

Fowler, C. & Nisbit, E., 1982. The thermal background to metamorphism - ii: Simple two-dimensional conductive models, *Geoscience Canada*, **9**(4), 208–214.

Frisch, W., Kuhlemann, J., Dunkl, I., & Brügl, A., 1998. Palinspastic reconstruction and topographic evolution of the Eastern Alps during late Tertiary tectonic extrusion, *Tectonphysics*, **297**, 1–15.

Geissler, W., Kind, R., & Yuan, X., 2008. Upper mantle and lithospheric heterogeneities in central and eastern Europe as observed by teleseismic receiver functions, *Geophysical Journal International*, **174**, 351–376.

Gerner, P., Bada, G., Dövényi, P., Müller, B., Oncescu, M., Cloetingh, S., & Horváth, F., 1999. Recent tectonic stress and crustal deformation in and around the Pannonian Basin: data and models, in *The Mediterranean Basins: Tertiary Extension within the Alpine Orogen*, vol. 156 of **Geological Society of London Special Publications**, pp. 269–294, eds Durand, B., Jolivet, L., Horváth, F., & Séranne, M., Geological Society of London.

Goes, S., Govers, R., & Vacher, P., 2000. Shallow mantle temperatures under Europe from P and S wave tomography, *Journal of Geophysical Research*, **105**(B5), 11153–11169.

Göğüş, O. & Pysklywec, R., 2008. Near-surface diagnostics of dripping or delaminating lithosphere, *Journal of Geophysical Research*, **113**(B11404), doi:10.1029/2007JB005123.

Grad, M., Guterch, A., Keller, R., Janik, T., Hegedüs, E., Vozár, J., Ślączka, A., Tiira, T., & Yliniemi, J., 2006. Lithospheric structure beneath trans-Carpathian transect from Precambrian platform to Pannonian basin: CELEBRATION 2000 seismic profile CEL05, *Journal of Geophysical Research*, **111**(B03301), doi:10.1029/2005JB003647.

Grad, M., Guterch, A., Keller, G., POLONAISE'97, & Working Groups, C., 2007. Variations in lithospheric structure across the margin of Baltica in Central Europe and the role of the Variscan and Carpathian orogenies, in *The 4D Framework of Continental Crust*, vol. Memoir 200, pp. 341–356, The Geological Society of America.

Grad, M., Tiira, T., & Group, E. W., 2009. The moho depth map of the european plate, *Geophysical Journal International*, **176**, 279–292.

Graeber, F., Houseman, G., & Greenhalgh, S., 2002. Regional teleseismic tomography of the western lachlan orogen and the newer volcanic province, southeast australia, *Geophysical Journal International*, **149**, 249–266.

Granet, M., Wilson, M., & Achauer, U., 1995. Imaging a mantle plume beneath the French Massif Central, *Earth and Planetary Science Letter*, **136**, 281–296.

Grenerczy, G. & Kenyeres, A., 2006. Crustal deformation between adria and the european platform from space geodesy, in *The Adria microplate: GPS geodesy, tectonics and hazards*, vol. 61 of **NATO Science Series IV: Earth and Environmental Sciences**, pp. 321–334, eds Pinter, N., Grenerczy, G., Weber, J., Stein, S., & Medak, D., Springer.

Gubbins, D., 2004. *Time series analysis and inverse theory for geophysicists*, Cambridge University Press.

Guterch, A., Grad, M., Špičák, A., Brückl, E., Hegedüs, E., Keller, G., Thybo, H., 2000, C., 2002, A., & Groups, S. . W., 2003. An overview of recent seismic refraction experiments in central Europe, *Studia Geophysica et Geodaetica*, **47**, 651–657.

Guterch, A., Grad, M., Keller, G., POLONAISE'97, CELEBRATION 2000, ALP2002, & Working Groups, S. ., 2004. Huge contrasts of the lithospheric structure revealed by new generation seismic experiments in Central Europe, *Prezeglad Geologiczny*, **52**(8/2), 753–760.

Hammond, J., 2007. *Imaging the upper–mantle beneath the Seychelles: Architecture of a microcontinent*, Ph.D. thesis, School of Earth and Environment, Univeristy of Leeds.

Harangi, S., Wilson, M., & Tonarini, S., 1995. Petrogenesis of Neogene potassic volcanic rocks in the Pannonian Basin, *Acta Vulcanologica*, **7**(2), 125–134.

Hétenyi, G. & Bus, Z., 2007. Shear wave velocity structure and crustal thickness in the Pannonian Basin from receiver function inversions at four permanent stations in Hungary, *Journal of Seismology*, **11**, 405–414.

Hetényi, G., Stuart, G., Houseman, G., Horváth, F., Hegedüs, E., & Brückl, E., 2009. Anomalously deep mantle transition zone below Central Europe: Evidence of lithospheric instability, *Geophysical Research Letters*, **36**, doi:10.1029/2009GL040171.

Hirschmann, M., Aubaud, M., & Withers, A., 2005. Storage capacity of h_2o in nominally anhydrous minerals in the upper mantle, *Earth and Planetary Science Letters*, **236**, 141–158.

Horváth, F., 1993. Towards a mechanical model for the formation of the Pannonian basin, *Tectonophysics*, **226**, 333–357.

Horváth, F., 1995. Phases of compression during the evolution of the Pannonian Basin and its bearing on hydrocarbon exploration, *Marine and Petroleum Geology*, **12**, 837–844.

Horváth, F. & Berckhemer, H., 1982. Mediterranean backarc basins, in *Alpine-Mediterranean Geodynamics*, vol. 7 of **Geodynamics Series**, pp. 141–173, eds Berckhemer, H. & Hsü, K., American Geophysical Union.

Horváth, F. & Cloetingh, S., 1996. Stress induced late stage subsidence anomalies in the Pannonian Basin, *Tectonophysics*, **266**, 287–300.

Horváth, F. & Tari, G., 1999. IBS Pannonian Basin project; a review of the main results and their bearings on hydrocarbon exploration, in *The Mediterranean basins : Tertiary Extension within the Alpine Orogen*, vol. 156, pp. 195–213, eds Durand, B., Jolivet, L., Horváth, F., & Séranne, M., Geological Society, London.

Horváth, F., Dövényi, P., & Laczó, I., 1986. Geothermal effect of magmatism and its contribution to the maturation of organic matter in sedimentary basins, in *Paleogeothermics (Lecture Notes in Earth Sciences)*, vol. 5, pp. 173–183, eds Buntebarth, G. & Stegena, L., Springer-Verlag.

Horváth, F., Bada, G., Szafián, P., Tari, G., Ádám, A., & Cloetingh, S., 2006. Formation and deformation of the Pannonian Basin: constraints from observational data, in *European Lithosphere Dynamics*, vol. 32 of **Geological Society of London Memoirs**, pp. 191–206, eds Gee, D. & Stephenson, R., Geological Society of London.

Houseman, G. A. & Gemmer, L., 2007. Intra-orogenic extension driven by gravitational instability: Carpathian-Pannonian orogeny, *Geology*, **35**(12), 1135–1138.

Huismans, R. S., Podladchikov, Y. Y., & Cloetingh, S., 2001. Dynamic modelling of the transition from passive to active rifting, application to the Pannonian basin, *Tectonics*, **20**, 1021–1039.

Huismans, R. S., Podladchikov, Y. Y., & Cloetingh, S. A. P. L., 2002. The Pannonian basin: Dynamic modelling of the transition from passive to active rifting, *EGU Stephan Mueller Special Publication Series*, **3**, 41–63.

eds Hurtig, E., Cermák, V., Haenel, R., & Zui, V., 1992. *Geothermal Atlas of Europe*, Hermann Haack.

eds Iyer, H. & Hirahara, K., 1993. *Seismic tomography: Theory and practice*, Chapman & Hall.

Jackson, I., , & Rigden, S., 1998. Composition and temperature of the Earth's mantle: Seismological models interpreted through experimental studies of Earth materials, in *The Earth's Mantle: Composition, Sturcture and Evolution*, pp. 405–460, ed. Jackson, I., Cambridge University Press.

Kanasewich, E., 1981. *Time sequence analysis in geophysics*, The University of Alberta Press, 3rd edn.

Kennett, B. & Engdahl, E., 1991. Traveltimes for global earthquake location and phase identification, *Geophysical Journal International*, **105**, 429–465.

Kennett, B. & Sambridge, M., 1988. Subspace methods for large inverse problems with multiple parameter classes, *Geophysical Journal*, **94**, 237–247.

Kennett, B., Engdahl, E., & Buland, R., 1995. Constraints on seismic velocities in the Earth from traveltimes, *Geophysical Journal International*, **122**, 108–124.

Kilényi, É., Kröll, A., Oberhauer, D., Šefara, J., Steinhauser, P., Szabó, Z., & Wessely, G., 1991. Pre-Tertiary basement contour map of the Carpathian basin beneath Austria, Czechoslovakia and hungary, *Geophysical Transactions*, **36**, 15–36.

Koulakov, I., Kaban, M., Tesauro, M., & Cloetingh, S., 2009. P- and s-velocity anomalies in the upper mantle beneath Europe from tomographic inversion of isc data., *Geophysical Journal International*, **179**, 345–366.

Kovács, A. C., 2009. Personal Communication.

Kovács, I. & Szabó, C., 2008. Middle Miocene volcanism in the vicinity of the Middle Hungarian zone: Evidence for an inherited enriched mantle source, *Journal of Geodynamics*, **45**, 1–17.

Kovács, I., Csontos, L., Szabó, C., Bali, E., Falus, G., Benedek, K., & Zajacz, Z., 2007. Paleogene-early Miocene igneous rocks and geodynamics of the Alpine-Carpathian-Pannonian-Dinaric region: An integrated approach, *Geological Society of America*, **Special Paper 418**, 93–112.

Kovács, S., 1984. North Hungarian facies types: A review, *Acta Geologica Hungarica*, **27**, 251–264.

Kováčs, M., Nagymarosy, A., Oszczypko, N., Slaczka, A., Csontos, L., Marunteanu, M., Matenco, L., & Márton, E., 1998. Palinspastic reconstruction of the Carpathian-Pannonian region dureing the Miocene, in *Geodynamic evolution of the Western Carpathians*, pp. 189–217, ed. Rakús, M., Dionyz Stúr.

Kozlovskaya, E., Elo, S., Hjelt, S.-E., Yliniemi, J., Pirttijärvi, M., & SSTWG, 2004. 3D density model of the crust if southern and central Finalnd obtained from joint interpretation of SVEKALAPKO crustal P-wave velocity model and gravity data, *Geophysical Journal International*, **158**, 827–848.

Laske, G. & Masters, G., 1997. A global digital map of sediment thickness, *EOS Trans. AGU*, **78**, F483.

Lenkey, L., Dövényi, D., Horváth, F., & Cloetingh, S., 2002. Geothermics of the Pannonian basin and its bearing on the neotectonics, *Stephen Mueller Special Publication Series*, **3**, 29–40.

Leonard, M., 2000. Comparison of manual and automatic onset time picking, *Bulletin of the Seismological Society of America*, **90**, 1384–1390.

Leonard, M. & Kennett, B., 1999. Multicomponent autoregressive techniques for the analysis of seismograms, *Physics of the Earth and Planetary Interiors*, **113**, 247–267.

Lévêque, J., Rivera, L., & Wittlinger, G., 1993. On the use of the checker-board test to assess the resolution of tomographic inversions, *Geophysical Journal International*, **115**, 313–318.

Lexa, J. & Konečný, V., 1998. Geodynamic aspects of the neogene to quaternary volcanism, in *Geodynamic development of the Western Carpathians*, pp. 143–154, GSSR, Bratislava.

Lippitsch, R., Kissling, E., & Ansorge, J., 2003. Upper mantle structure beneath the alpine orogen from high-resolution teleseismic tomography, *Journal of Geophysical Research*, **180**, doi:10.1029/2002JB002016.

Lombardi, D., Braunmiller, J., Kissling, E., & Giardini, D., 2009. Alpine mantle transition zone imaged by receiver functions, *Earth and Planetary Science Letters*, **278**, 163–174.

Lorinczi, P. & Houseman, G., 2009. Lithospheric gravitational instability beneath the Southeast Carpathians, *Tectonophysics*, **474**, 322–336.

Lorinczi, P. & Houseman, G., 2010. Geodynamical models of lithospheric deformation, rotation and extension of the Pannonian Basin of Central Europe, *Tectonophysics*, **492**, 73–87.

Marotta, A., Fernàndez, M., & Sabadini, R., 1999. The onset of extension during lithospheric shortening: a two dimensional thermomechanical model for lithospheric unrooting, *Geophysical Journal International*, **139**, 98–114.

Martin, M., Ritter, J. R., & the CALIXTO working group, 2005. High–resolution teleseismic body–wave tomography beneath SE Romania - I. implication for three–dimensional versus one–dimensional crustal correction strategies with a new crustal velocity model, *Geophysical Journal International*, **162**, 448–460.

Martin, M., Ritter, J. R., & the CALIXTO working group, 2006. High–resolution teleseismic body–wave tomography beneath SE Romania - II. imaging a slab detachment scenario, *Geophysical Journal International*, **164**, 579–595.

Márton, E. & Fodor, L., 1995. combination of palaeomagnetic and stress data–a case study frin North Hungary, *Tectonophysics*, **242**, 99–114.

Matenco, L. & Bertotti, G., 2000. Tertiary tectonic evolution of the external East Carpathians (Romania), *Tectonophysics*, **316**, 255–286.

McNamara, D. & Boaz, R., 2005. Seismic noise analysis system: A stand-alone software package, Tech. rep., USGS.

Mitterbauer, U. & Brückl, E., in preparation. ALPASS teleseismic tomography, personal communictation, TU-Wien.

Mooney, W., Laske, G., & Masters, G., 1998. CRUST5.1: A global crustal model of 5 x 5, *Journal of Geophysical Research*, **103**, 727–747.

Morita, Y. & Hamaguchi, H., 1984. Automatic detection of onset time of seismic waves and its confidence interval using the autoregressive model fitting, *Zisin*, **37**, 281–293.

Nagymarosy, A. & Müller, P., 1988. Some aspects of Neogene biostratigraphy in the Pannonian Basin, in *The Pannonian Basin. A study in basin evolution*, vol. 45 of **AAPG Memoir**, pp. 69–77, eds Royden, L. & Horváth, F., The American Association of Petroleum Geologists and the Hungarian Geological Society.

Nakajima, J., Matsuzawa, T., Hasegawa, A., & Zhao, D., 2001. Three-dimensional structure of v_p, v_s, and v_p/v_s beneath northeastern Japan: Implications for arc magmatism and fluids, *Journal of Geophysical Research*, **106**, 21843–21857.

Nemcock, M., Pospisil, L., Lexa, J., & Donelick, R., 1998. Tertiary subduction and slab break-off model of the Carpathian-Pannonian region, *Tectonophysics*, **295**, 307–340.

ed. Nolet, G., 1987. *Seismic tomography*, D. Riedel Publishing Company.

ed. Nolet, G., 2008. *A Breviary of Seismic tomography*, Cambridge University Press.

Nolet, G. & Zielhuis, A., 1994. Low S velocities under the Tornquist-Teisseyre zone: Evidence for water injection into the transition zone by subduction, *Journal of Geophysical Research*, **99**(B8), 15813–15820.

Oszcypko, N., 2006. Late Jurassic-Miocene evolution of the Outer Carpathian fold-and-thrust belt and its foredeep basin (Western Carpathians, Poland), *Geological Quarterly*, **50**(1), 169–194.

Pecskay, Z., Lexa, J., Szakács, A., Balogh, K., Seghedi, I., Konecny, V., Kovács, M., Márton, E., Kaliciak, M., Széki-Fux, V., Póka, T., Gyarmati, P., & Edelstein, O., 1995. Space and time distribution of Neogene-Quaternary volcanism in the Carpatho-Pannonian region, *Acta Vulcanologica*, **7**(2), 15–28.

Peterson, J., 1993. Observations and modelling of seismic background noise, *USGS Open file Report*, pp. 93–322.

Pichon, X. L. & Angelier, J., 1979. The Hellenic arc and trench system: a key to the neotectonic evolution of the Mediterraniean area, *Tectonophysics*, **60**, 1–42.

Piromallo, C. & Morelli, A., 2003. P wave tomography of the mantle under the Alpine–Mediterranean area, *Journal of Geophysical Research*, **108**, doi:10.1029/2002JB001757.

Platt, J. & Vissers, R., 1989. Extensional collapse of thickened continental lithosphere: a working hypothesis for the Alboran Sea and the Gibralter arc, *Geology*, **17**, 540–543.

Plomerová, J., Achauer, U., Babuška, V., Vecsey, L., & working group, B., 2007. Upper mantle beneath the Eger Rift (Central Europe): plume or asthenosphere upwelling?, *Geophysical Journal International*, **169**, 675–682.

Pollack, H., Hurter, S., & Johnson, J., 1993. Heat loss from the Earth's interior: analysis of the global data set, *Reviews of Geophysics*, **31**, 267–280.

Posgay, K., Bodoky, T., Hegedüs, E., Kovácsvölgyi, S., Lenkey, L., Szafián, P., Takács, E., Tímár, Z., & Varga, G., 1995. Asthenospheric structure beneath a Neogene basin in southeast Hungary, *Tectonophysics*, **252**, 467–484.

Posgay, K., Kovács, A., Csabafi, R., Bodoky, T., Hegedüs, E., , Fancsik, T., & Rigler, B., 2008. A CEL07 mélyszeizmikus szelvény újraértékelése, *Magyar Geofizika*, **48**(3), 233–244.

Pospíšil, L., Ádám, A., Bimka, J., Bodlak, P., Bodoky, T., Dövényi, P., Granser, H., Hegedüs, E., Joó, I., Kendzera, A., Lenkey, L., M.Nemčok, Pylypyshyn, B., Sedlák, J., Stanley, W., Starodub, G., Szalaiová, V., Šály, B., Šutora, A., Várga, G., & Zsíros, T., 2006. Crustal and lithospheric structure of the Carpathian-Pannonian region - a geophysical perspective: Regional geophysical data of the Carpathian-Pannonian lithosphere, in *The Carpathians and their Foreland: Geology and Hydrocarbon Resources*, vol. 84 of **AAPG Memoir**, pp. 651–697, eds Golonka, J. & Picha, F., AAPG.

Poupinet, G., Arndt, N., & Vacher, P., 2003. Seismic tomography beneath stable tectonic regions and the origin and compostion of the continental lithospheric mantle, *Earth and Planetary Science Letters*, **212**, 89–101.

Ratschbacher, L., Frisch, W., Linzer, H.-G., & Merle, O., 1991. Lateral extrusion in the eastern Alps, part 2: structural analysis, *Tectonics*, **10**(2), 257–271.

Rawlinson, N. & Kennett, B., 2004. Rapid estimation of relative and absolute delay times across a network by adaptive stacking, *Geophysical Journal International*, **157**, 332–340.

Rawlinson, N. & Sambridge, M., 2003. Seismic traveltime tomography of the crust and lithosphere, *Advances in Geophysics*, **46**, 81–197.

Rawlinson, N., Reading, A., & Kennett, B., 2006. Lithospheric structure of Tasmania from a novel form of teleseismic tomography, *Journal of Geophysical Research*, **111**(B02301), doi:10.1029/2005JB003803.

Reusch, A., Nyblade, A., Wiens, D., Shore, P., Ateba, B., Tabod, C., & Nnange, J., 2010. Upper mantle structure beneath Cameroon from body wave tomography and the origin of the Cameroon Volcanic Line, *Geochemistry Geophysics Geosystems*, **11**(10), doi:10.1029/2010GC003200.

Ritter, J., Jordan, M., Christensen, U., & Achauer, U., 2001. A mantle plume below the Eifel volcanic fields, Germanay, *Earth and Planetary Science Letters*, **186**, 7–14.

Romanowicz, B., 1991. Seismic tomography of the Earth's mantle, *Annual Reviews of Earth and Planetary Sciences*, **19**, 77–99.

Rondenay, S., Bostock, M., Hearn, T., White, D., & Ellis, R., 2000. Lithospheric assembly and modeification of the se canadian shiels: Abitibi-grenville telesismic experiment, *Journal of Geophysical Research*, **105**(B6), 13735–13754.

Royden, L., Horváth, F., & Burchfiel, B., 1982. Transform faulting, extension and subduction in the Carpathian Pannonian region, *Geological Society of America Bulletin*, **93**, 717–725.

Royden, L., Horváth, F., & Rumpler, J., 1983a. Evolution of the Pannonian Basin System 1. Tectonics, *Tectonics*, **2**(1), 63–90.

Royden, L., Horváth, F., Nagymarosy, A., & Stegena, L., 1983b. Evolution of the Pannonian Basin System 2. Subsidence and thermal history, *Tectonics*, **2**(1), 91–137.

Sanders, C., Andriessen, P., & Cloetingh, S., 1999. Life cycle of the East Carpathian orogen: Erosion history of a double vergent critical wedge assessed by fission track thermochronology, *Journal of Geophysical Research*, **104**(B12), 29095–29112.

Scales, J., 1987. Tomographic inversion via the conjugate gradient method, *Geophysics*, **52**(2), 179–184.

Schott, B. & Schmeling, H., 1998. Delamination and detachment of a lithospheric root, *Tectonophysics*, **296**, 225–247.

Seghedi, I., Downes, H., Szakács, A., Mason, P., Thirlwall, M., Roşu, E., Pécskay, Z., Márton, E., & Panaiotu, C., 2004. Neogene-quaternary magmatism and geodynamics in the Carpathian-Pannonian region: a synthesis, *Lithos*, **72**, 117–146.

Sleeman, R. & van Eck, T., 1999. Robust automatic p-phase picking: an online implementation in the analysis of broadband seismogram recordings, *Physics of the Earth and Planetary Interiors*, **113**, 265–275.

Smyth, J. & Frost, D., 2002. The effect of water in the 410-km discontinuity: An experimental study, *Geophysical Research Letters*, **29**(10), doi:10.1029/2001GL014418.

Sol, S., Thompson, C. J., Kendall, J. M., White, D., VanDecar, J. C., & Asude, I., 2002. Seismic tomographic images of the cratonic upper mantle beneath the Western Superior Province of the Canadian Shield–a remnant Archaen slab, *Physics of the Earth and Planetary Interiors*, **134**, 53–69.

Środa, P., 2010. The bright spot in the west carpathian upper mantle: a trace of the tertiary plate collision - and a caveat for a seismologist, *Geophysics Journal International*, **182**, 1–10.

Stegena, L., Géczy, B., & Horváth, F., 1975. Late Cenozoic evolution of the Pannonian Basin, *Tectonophysics*, **26**, 71–90.

Săndulescu, M., 1988. Cenozoic tectonic history of the Carpathians, in *The Pannonian Basin. A study in basin evolution*, vol. 45 of **AAPG Memoir**, pp. 17–25, eds Royden, L. & Horváth, F., The American Association of Petroleum Geologists and the Hungarian Geological Society.

Szafián, P. & Horváth, F., 2006. Crustal structure in the Carpatho-Pannonian region: insights from three-dimensional gravity modelling and their geodynamic significance, *International Journal of Earth Sciences*, **95**, 50–67.

Szafián, P., Horváth, F., & Cloetingh, S. A. P. L., 1997. Gravity constraints on the crustal structure and slab evolution along the transcarpathian transect, *Tectonophysics*, **272**, 233–247.

Szafián, P., Tari, G., Horváth, F., & Cloetingh, S. A. P. L., 1999. Crustal structure of the Alpine-Pannonian transition zone: a combined seismic and gravity structure, *International Journal of Earth Sciences*, **88**, 98–210.

Tari, G., Dövényi, P., Dunkl, I., Horváth, F., Lenkey, L., Stefanescu, M., Szafián, P., & Tóth, T., 1999. Lithospheric strucure of the Pannonian basin derived from seismic, gravity and geothermal data, *Geological Society of London, Special Publication*, **156**, 215–250.

Tašárová, A., Afonso, J., Bielik, M., Götze, H.-J., & Hók, J., 2009. The lithospheric strucure of the Western Carpathian-Pannonian Basin region based on the CELEBRATION 2000 seismic experiment and gravity modelling, *Tectonophysics*, **475**, 454–469.

Tesauro, M., Kaban, M., & Cloetingh, S., 2008. EuCRUST-07: A new reference model for the European crust, *Geophysical Research Letters*, **35**, doi:10.1029/2007GL032244.

Tilmann, F., 1999. *The Seismic Structure of the Upper Mantle beneath Hawaii*, Ph.D. thesis, Univeristy of Cambridge.

Tilmann, F., Benz, H., Priestley, K., & Okubo, P., 2001. P-wave velocity structure of the uppermost mantle beneath Hawaii from traveltime tomography, *Geophysical Journal International*, **146**, 594–606.

Tomek, C., 1993. Deep-crustal structure beneath the Central and Inner West Carpathians, *Tectonophysics*, **226**, 417–431.

Ulrych, J., Pivec, E., Lang, M., Balogh, K., & Kropáček, V., 1999. Cenozoic intraplate volcanic rock series of the Bohemain Massif: a review, *Geolines*, **9**, 123–129.

Ustaszewski, K., Schmid, S., Fügenschuh, B., Tischler, M., Kissling, E., & Spakman, W., 2008. A map-view restoration of the Alpine-Carpathian-Dinaridic system for the Early Miocene, *Swiss Journal of Geocsciences*, **101**, 273–294.

van der Hilst, R., Engdahl, E., & Spakman, W., 1993. Tomographic inversion of P and pP data for aspherical mantle structure below the northwest Pacific region, *Geophysical Journal International*, **115**, 264–302.

VanDecar, J., James, D., & Assumpção, M., 1995. Seismic evidence for a fossil mantle plume beneath South America and implications for plate driving forces., *Nature*, **378**, 25–31.

VanDecar, J. C., 1991. *Uppper Mantle Structure of the Cascadia subduction zone from non-linear teleseismic travel-time inversion*, Ph.D. thesis, Univeristy of Washington.

VanDecar, J. C. & Crosson, R. S., 1990. Determination of teleseismic relative phase arrival times using multi-channel cross-correlation and least squares, *Bulletin of the Seismological Society of America*, **80**, 150–169.

Waldhauser, F., Lippitsch, R., Kissling, E., & Ansorge, J., 2002. High-resolution teleseismic tomography of upper-mantle structure using an a priori three-dimensional crustal model, *Geophysical Journal International*, **150**, 403–414.

Wéber, Z., 2002. Imaging P_n velocities beneath the Pannonian basin, *Physics of the Earth and Planetary Interiors*, **129**, 283–300.

Wilson, M. & Downes, H., 2006. Tertiary-Quaternary intra-plate magmatism in Europe and its relationship to mantle dynamics, in *European Lithosphere Dynamics*, vol. 32 of **Geological Society of London Memoirs**, pp. 146–166, eds Gee, D. & Stephenson, R., Geological Society of London.

Wortel, M. & Spakman, W., 2000. Subduction and slab detachment in the mediterranean-carpathian region, *Science*, **290**, 1910–1917.

Zeyen, H., Dérerová, J., & Bielik, M., 2002. Determination of the continental lithospheric thermal structure in the Western Carpathians: integrated modelling of surface heat flow, gravity anomalies and topography, *Physics of the Earth and Planetary Interiors*, **134**, 89–104.